Linear and Non-linear Interactions Involving Large-scale Structures in Turbulence

Thesis by
Yuting Huang

In Partial Fulfillment of the Requirements for the
Degree of
Doctor of Philosophy

CALIFORNIA INSTITUTE OF TECHNOLOGY
Pasadena, California

2025
Defended August 20, 2024

Yuting Huang
ORCID: 0000-0002-9457-7964

ACKNOWLEDGEMENTS

First, I want to thank my advisor, Prof. Beverley McKeon, for the entire amazing PhD experience. In the last card the research group wrote to Beverley before moving to Stanford, I wrote that Beverley made my time at Caltech so enjoyable that I almost did not want to leave. This is truly spoken from my heart. Thank you for all the guidance and support during my six years at Caltech, through the smooth and rough of turbulence research.

Next, I would like to thank my thesis and candidacy committee members, Professors Tony Leonard, John Dabiri, Tim Colonius, and Guillaume Blanquart, for sharing their valuable expertise and insights. I would also like to thank my collaborators, Dr. Dea Wangsawijaya and Prof. Nicholas Hutchins from the University of Melbourne, for providing the experimental data and the inspiring discussions. I am also extremely grateful for the insights, support, and above all, patience of Prof. Greg Chini from the University of New Hampshire. It is both a pleasure and an honor working with you all. I am also grateful for the funding from the U.S. Office of Naval Research that made this work possible.

The McKeon research group is another big reason for my enjoyable time at Caltech. Thank you all so much for the discussions of math and turbulence in our windowless offices, which helped me so much with my research. I am especially indebted to Simon Toedtli, who patiently helped me with setting up the simulations, answered my many questions, and provided valuable insights into the data processing. Outside of research, we also had so much fun together. From the escape room to the Spartan race or experiencing different food during supper clubs, the group has made my graduate school experience so colorful. Above all, what I will miss the most is the amazing and thought-provoking lunch discussions, from technologies to social issues, or the most random philosophical questions. I am so grateful for being surrounded by so many talented and friendly colleagues.

The group could not operate without the support of all the amazing GALCIT administrators, who have made the department a truly enjoyable place to work. I am especially grateful to Liza Bradulina, who catered to all our needs and kept everything running smoothly behind the scenes.

I am also extremely grateful for my friends outside of Caltech. To my many long-time friends since our undergraduate time, although some of us might be thousands

of miles apart, thank you all so much for supporting me during my journey, sharing my joy, easing my anxiety, working on fun projects together, and going on exciting trips. To my friends in Pasadena, thank you for providing me with the much-needed distractions from research: going to movies, theme parks, hiking trips, and many more. I will miss these fun times together.

Lastly and most importantly, I would like to thank my mom and dad. Without their 28 years of love and support, I would not be writing this today. I love you both.

ABSTRACT

This thesis performs a linear resolvent analysis (McKeon and Sharma, 2010), and a novel quantitative non-linear analysis of the triadic interactions, to study the large-scale structures in wall-bounded turbulence.

First, resolvent analysis is applied to a flow over spanwise periodic roughness, to model the large-scale counter-rotating rolls. The experimental data (Wangsawijaya et al., 2020) is utilized to examine both the predictive and data compression capabilities of the resolvent. The improvements by the inclusion of an eddy viscosity and a crude boundary geometry model are also demonstrated. Standard resolvent is able to qualitatively predict the shape of the counter-rotating rolls. The inclusion of eddy viscosity improves the quantitative predictions and combined with the boundary geometry model is able to efficiently represent the data with small differences using only a fraction of the degree of freedom.

Next, we developed a novel framework to quantitatively analyze the triadic non-linear contributions in a turbulent channel. We incorporated the linear resolvent operator to provide the missing link from energy transfer between modes to the effect on the spectral turbulent kinetic energy. The coefficients highlight the importance of interactions involving large-scale structures, for both the large and small-scale forcing and response, providing a natural connection to the modeling assumptions of the quasi-linear (QL) and generalized quasi-linear (GQL) analyses. Specifically, it is revealed that QL and GQL are efficiently capturing important triadic interactions in the flow, and the inclusion of small amounts of wavenumbers into the GQL large-scale base flow quickly captures most of the important triadic interactions.

Finally, by performing spatio-temporal analyses of the triadic contributions to a single mode, we demonstrated the spatio-temporal nature of the triadic interactions and the effect of the resolvent operator. It is shown that the energetic triadic interactions are concentrated in temporal frequencies around a plane where all three wavespeeds are the same, allowing for a truncation of the important triadic interactions. We also demonstrated the linear amplification mechanism of the resolvent, allowing certain triadic interactions to generate a stronger response even with a weak forcing, underscoring the different perspectives offered by the inclusion of the linear resolvent operator into the analyses of the non-linear triadic interactions.

PUBLISHED CONTENT AND CONTRIBUTIONS

Huang, Y., Hutchins, N., and McKeon, B. J. (2024). "Reduced Order Mddeling of Flow Over Spanwise Periodic Rough Surfaces". International Mechanical Engineering Congress and Exposition 2024 (accepted).
Y.H. performed the linear analyses, processed the data, created the figures, and was the primary author of the paper.

Huynh, D. P., Huang, Y., and McKeon, B. J. (May 2021). "Experiments and Modeling of a Compliant Wall Response to a Turbulent Boundary Layer with Dynamic Roughness Forcing". *Fluids* 6.55, p. 173. DOI: 10.3390/fluids6050173. URL: https://www.mdpi.com/2311-5521/6/5/173.
Y.H. participated in the development of the methodology, performed the data and resolvent analyses, and participated in the writing of the manuscript.

TABLE OF CONTENTS

LIST OF ILLUSTRATIONS

LIST OF TABLES

Chapter 1

INTRODUCTION

From running water faucets to sailing cargo ships and soaring airplanes, from the geological movements that produce weather on Earth to the astrological formation of galaxies, turbulence is everywhere. In many engineering applications, turbulence is often associated with an increase in friction drag on vehicle surfaces, which accounts for more than 50% of the total drag force on modern airliners and even more for large oil tankers and submarines (Marusic et al., 2010a). It is also estimated that about 5% of the CO_2 produced by mankind is the result of wall-bounded turbulence (Jiménez, 2013). However, despite more than a century of research, turbulence remains a challenging problem for both engineers and scientists.

At the core of the mathematical descriptions of fluid motions is the Navier-Stokes equations (NSE), which govern the evolution of fluid flows through the conservation of mass and momentum. In the case of incompressible flows of interest in this thesis, the Reynolds number Re, a non-dimensional number, parameterizes the NSE. The Reynolds number, which is the ratio between inertial to viscous forces, is the key parameter that separates laminar and turbulent flow. At low Reynolds numbers, the flow remains laminar, and begins to transition to turbulence when the Reynolds number exceeds a critical value. The friction Reynolds number, Re_τ, describes the ratio between the largest length scales in the flow to the smallest length scales of the flow and is on the order of $10^4 - 10^6$ for flows in industrial applications and environmental/atmospheric flows. This huge separation between the smallest and largest length scales in the flow is extremely challenging for experimental measurements, requiring both a huge facility and accurate small-scale measurements, and even more so for computational studies. Direct numerical simulations (DNS), where the smallest length scales in the flow are resolved, require computational resources that scale with Re_τ^4. Wall-resolved large eddy simulations (LES), where the effect of unresolved small scales on the large scales are modeled, are estimated to scale as $Re_\tau^{1.8}$ and wall-modeled LES to scale as $Re_\tau^{0.2}$ (Smits and Marusic, 2013). In addition to the computation costs, the amount of data generated from high Reynolds number simulations also becomes a burden for storage, transfer, and analysis. The state-of-the-art DNS are performed with $Re_\tau \approx 5200$ for a channel flow (Lee and Moser, 2015), still lower than the Re_τ of typical industrial relevant flows. More

geometrically challenging studies such as boundary layers are often limited to even lower Reynolds numbers.

In addition, the complexities in the boundary conditions beyond those of the canonical smooth wall no-slip and no-penetration conditions introduce additional challenges. For example, surface features are known to have the capability of altering the near-wall turbulent flow and therefore changing the turbulent drag significantly, and are of great industrial interest. Schultz et al. (2011) studied the US Navy Arleigh Burke-class destroyers and showed that the biofouling level typically found on the hull resulted in an increase of 10.3% in fuel consumption, equating approximately $92M per year of extra fuel. On the other hand, numerous studies on surface features have shown that well-designed geometries such as riblets have the potential to reduce turbulent drag. The experimental work by Bechert et al. (1997) showed that with carefully optimized dimensions, simple blade riblets achieved a 9.9% drag reduction. If this drag reduction can be applied to the shipping industry, the marine bunkers alone can result in a saving of $8 billion in 2018 and a significant reduction in carbon emission (*World Oil Outlook* 2018). In attempts to control the turbulence or reduce the drag, recent studies have also utilized a number of different boundary conditions, such as compliant walls (Luhar et al., 2015; Wang et al., 2020; Huynh et al., 2021), opposition control (Luhar et al., 2014; Toedtli et al., 2019; Toedtli et al., 2020), and spanwise oscillation of the surface (Marusic et al., 2021). These different types of boundary conditions all increase the challenges in both experimental and numerical studies.

However, turbulence, despite appearing to be highly randomized at first glance, actually contains many robust and dominant structures upon detailed examination (Smits et al., 2011). These structures, known as coherent structures, are dynamically important in wall-bounded turbulent flows (Marusic et al., 2010b; Jiménez, 2018). The previously discussed challenges in high Reynolds number turbulence motivate the need for extracting these coherent structures from the flow. These coherent structures can be extracted from available data using data-driven tools such as proper orthogonal decomposition (POD), dynamic mode decomposition (DMD), or spectral proper orthogonal decomposition (SPOD). POD modes are spatially coherent structures that can optimally capture the flow energy, DMD modes are the approximate eigenmodes of the Koopman operator, and SPOD modes are coherent in both space and time (Lumley, 1970; Schmid, 2010; Taira et al., 2017; Towne et al., 2018). These data-driven methods are extremely useful in extracting structures from large

amounts of data obtained from experiments or simulations, without using the governing equations (potentially unknown in other fields). In this thesis, however, we will focus mainly on equation-driven methods, which have the advantage of requiring much less data by utilizing the known governing equations. Specifically, we will utilize the linear resolvent analysis (McKeon and Sharma, 2010), which requires only a mean profile, and explore methods to enhance its capabilities through the incorporation of some information about the non-linearity.

The beauty and complexity of turbulent fluid flow arise largely from the non-linear convective terms in the NSE and these non-linear terms remain an essential and challenging part of our understanding of turbulence. The most important role of the non-linearity is the transfer of energy between the vast range of scales in turbulence (Jiménez, 2012). Recent experimental studies on turbulence control by Marusic et al. (2021) demonstrated that actuating the near wall small scales directly, although capable of drag reduction, is unable to result in a net power saving due to the high actuation power, while actuating the large scales results in a net power saving. The large-scale actuation also leads to a broadband attenuation of turbulent fluctuations, a result of the energy transfer through non-linear interactions. This is just one example of the importance of the relatively less understood non-linearity in turbulence and motivates the more detailed quantitative study of the non-linear interactions in this thesis.

The goal of this thesis is to contribute to the advancement of modeling and understanding of turbulence in mainly two ways. First, we aim to extend the capabilities of linear analysis by incorporating some non-linear modeling and also analyze the predictive and data compression capabilities. Secondly, by analyzing the non-linear interactions in turbulence, we aim to improve the understanding of the non-linear mechanisms and provide a quantitative tool to characterize the importance of different types of interactions. This will be useful in identifying improved modeling of the non-linearity for future modeling and computational studies.

1.1 Linear Analysis

Although turbulence is a non-linear phenomenon, linear dynamics still play an important role (Kim and Lim, 2000; Jiménez, 2013). Early works started with linear stability theory, where the flow is linearized around a base flow. With the assumption of infinitesimal perturbations around the base flow, the non-linear terms can be neglected, and an eigenvalue problem can be derived to study the time-

asymptotic stability of the perturbations (Schmid and Henningson, 2001). However, linear stability theory fails to predict the correct critical Reynolds number in some flows due to the linearized Navier-Stokes operator being non-normal. The non-normal operator, having non-orthogonal eigenvectors, leads to possible transient growth even when all eigenmodes are asymptotically stable, and can trigger non-linear mechanisms leading to transition to turbulence (Trefethen et al., 1993; Schmid and Henningson, 2001; Schmid and Brandt, 2014). Following the work on transient growth, Farrell and Ioannou (1993), Jovanović and Bamieh (2005), and Hwang and Cossu (2010) studied the Navier-Stokes operator under external stochastic forcing for Couette, Poiseuille and turbulent channel flows. These studies analyzed the properties of the linear resolvent operator, which is a transfer function that maps the input forcing to the output velocity responses. McKeon and Sharma (2010) extended the use of the resolvent analysis to turbulent flows and treated the non-linear convective terms in the NSE as forcing to the linear operator.

1.1.1 Resolvent Analysis

The resolvent analysis of McKeon and Sharma (2010) utilizes a turbulent mean profile for the construction of the linear operator and analyzes the turbulent perturbations around this mean. Instead of studying external forcing, the non-linear terms in the NSE are considered as endogenous forcing, forming a closed, self-sustaining loop for the governing equations. The linear resolvent operator is a transfer function between the non-linear forcing $\boldsymbol{f}$ and the velocity responses $\boldsymbol{u}$. The velocities then feedback to the system through the non-linearity as illustrated in Figure 1.1.

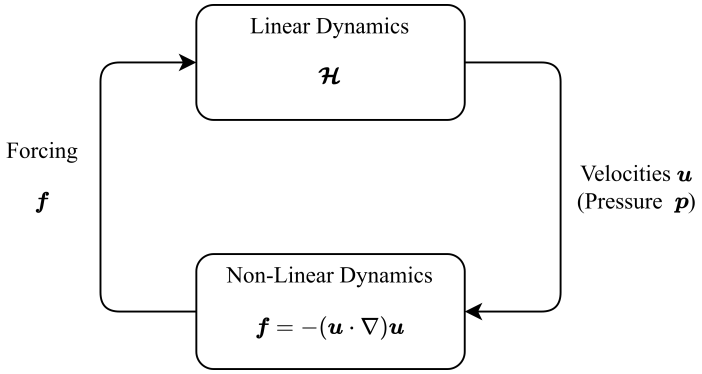

Figure 1.1: Input-output framework of the resolvent analysis.

A singular value decomposition (SVD) is then performed on the resolvent operator to obtain the left and right singular vectors, ranked by the singular values. The left and

right singular vectors are the response and forcing modes that form spatio-temporal basis functions for the response and forcing respectively, and the singular values represent the linear energy amplification of the resolvent for each mode. Previous studies have shown that the resolvent operator is low-rank at most of the energetic regions of the flow, with the first (few) singular values being dominant. Therefore, low-rank approximations using the first (few) response modes are able to qualitatively reproduce key coherent structures and statistics of turbulent flows (McKeon and Sharma, 2010; Moarref et al., 2013; Sharma et al., 2017; McKeon, 2017). For flows with a single non-homogeneous direction such as pipes and channels, the resolvent modes can be generated within seconds on a laptop and are efficient basis functions for representing the dominant structures, and therefore are useful low-cost tools that can provide predictive and reduced order modeling capabilities (McKeon, 2017).

1.1.2 Modeling Boundary Conditions in Resolvent Analysis

The resolvent analysis is originally developed for smooth wall boundary conditions with no-slip and no-penetration at the wall in McKeon and Sharma (2010). Recent studies have extended the analysis to more complex boundary conditions, for example compliant walls, where a linearized relationship between the velocities and pressure is utilized at the boundaries (Luhar et al., 2015; Huynh et al., 2021) or opposition control, where the wall-normal velocity at the boundary is set to be negatively proportional to the wall-normal velocity at a sensing location (Luhar et al., 2014; Toedtli et al., 2019; Toedtli et al., 2020). Additionally, Chavarin and Luhar (2020) introduced the volume penalization method (Khadra et al., 2000) into the resolvent to study the drag-reducing capabilities of streamwise aligned riblets. In this analysis, a permeability function is added to the resolvent. This permeability function is set to infinite in the solid region, driving the velocities to 0, and set to 0 in the fluid region, recovering the original resolvent operator. This method enables the resolvent to model general surface geometries and will be explored in Chapter 3 of this thesis.

1.1.3 Resolvent Analysis with Multiple Non-homogeneous Coordinates

Additionally, the resolvent analysis has been extended to more complex flow cases where more than one non-homogeneous direction is present. For example, resolvent analysis has been applied to turbulent jets (Schmidt et al., 2018; Towne et al., 2018; Pickering et al., 2021), streamwise developing boundary layers (Sipp and Marquet, 2013; Rigas et al., 2021; Barthel et al., 2022), cavity flow (Gómez et al., 2016)

and airfoils (Yeh and Taira, 2019). For these studies, in the non-homogeneous directions, the flow is discretized in the physical domain instead of performing the Fourier analysis. This results in a larger resolvent matrix and higher computation costs, which will be further discussed in Chapter 2.

Of particular interest to this thesis is the work of Rosenberg and McKeon (2019a), Chavarin and Luhar (2020) and Padovan et al. (2020). These studies enhanced the linear analyses with additional non-linearity important to the problem being studied. For example, when analyzing spanwise periodic exact coherent states in (Rosenberg and McKeon, 2019a) or streamwise aligned, spanwise periodic riblets in Chavarin and Luhar (2020), the authors utilized a base flow that is periodic in the spanwise direction to extend the resolvent analysis with non-linearity that couples different spanwise wavenumbers through this base flow. On the other hand, Padovan et al. (2020) utilized a base flow that is periodically in time and introduced the harmonic resolvent, which allows for non-linear cross-frequency interactions. These studies differ from the aforementioned cases due to the periodicity in these non-homogeneous directions, which still enables the Fourier transform to be applied. In this thesis, a spanwise periodic resolvent will be utilized in Chapter 3 to study flow over spanwise periodic rough surfaces.

1.1.4 Eddy Viscosity in Resolvent Analysis

The non-linearity in the resolvent analysis may be treated crudely as a broadband input to analyze the properties of the linear operator or with more sophistication such as a colored forcing arising from nonlinear modal interactions to address the turbulence closure problem (McKeon, 2017). The eddy viscosity, a model for the mean Reynolds stresses, is originally derived to provide closure for the Reynolds-averaged Navier-Stokes equations (Reynolds and Tiederman, 1967). It introduces extra viscosity to model the energy transfer from the large scales to the small scales, where the majority of the viscous dissipation occurs, known as the energy cascade (Jiménez, 2012). The eddy viscosity is a widely used method to include a partial model for the nonlinear forcing in the linearized equations of the resolvent formulation. Previous studies have demonstrated the improvements obtained by the inclusion of eddy viscosity, especially alleviating the tendency in the standard resolvent to over-predict the streamwise velocity while under-predicting spanwise and wall-normal velocities, resulting in the generation of more efficient resolvent basis functions (del Álamo and Jiménez, 2006; Hwang and Cossu, 2010; Huynh et al., 2021; Fan et al., 2024; Illingworth et al., 2018; Symon et al., 2021; Morra et al.,

2021). Recent studies have also developed an eddy viscosity model for turbulent boundary layers (Fan et al., 2024), and utilized data-driven approaches to obtain optimal eddy viscosity profiles (Pickering et al., 2021). In Chapter 3 of this thesis, we utilize the resolvent with eddy viscosity to model a flow over spanwise periodic roughness and evaluate the increase in predictive accuracy and data compression capabilities.

1.2 Non-linearity in Turbulence

Non-linearity is essential in turbulence. In turbulence, energy is transferred from the large scales to the small scales and dissipated at the small scales through viscosity. This is known as the energy cascade (Jiménez, 2012) and relies on the non-linear terms to transfer energy between different scales. However, the non-linear terms, due to the quadratic nature and the presence of gradients are very difficult to characterize until recent advancements in numerical simulations. Recent studies first utilized statistics of the flow response to infer the forcing statistics. Moarref et al. (2014) utilized an optimization algorithm to compute the forcing required to match the DNS energy spectra, and McMullen et al. (2020) performed a similar convex optimization but instead utilized the Orr-Sommerfeld and Squire decomposition of the resolvent operator. Zare et al. (2017) showed that white-in-time (uncorrelated) forcing is insufficient for capturing the turbulent statistics, necessitating a color-in-time forcing, obtained using optimization to complete the partially known covariance matrix. More recent studies such as Morra et al. (2021) and Nogueira et al. (2021) directly computed the forcing statistics in a turbulent channel flow and turbulent Couette flow from simulation data. The authors were able to verify the linear relationship between the velocity and forcing cross-spectral density. It was also observed that due to the low-rank nature of the linear resolvent operator, a low-rank approximation can capture the bulk of the response, while the linearly optimal forcing modes are not representative of the true nonlinear forcing. Despite recent advancements, the non-linearity is still relatively less understood, especially the triadic interactions that are essential for the understanding of it.

1.2.1 Triadic Interactions

Under a classical Reynolds decomposition, i.e. the definition of turbulent fluctuations relative to a temporally- or spatio-temporally-averaged mean field, the quadratic non-linearities in the incompressible NSE manifest themselves as a convolution of triadically compatible, i.e. resonant, interactions in the Fourier domain, linking a

pair of interacting scales to nonlinearity at a third scale. Such interactions have been studied in the spatial domain (e.g. Cheung and Zaki, 2014) and in the context of spatial and spectral fluxes, for example, Marati et al. (2004). The coherence between spatial scales can also be studied through the skewness of the velocity and amplitude modulation of the small scales by large ones, e.g. Marusic et al. (2010a), both of which can be expressed as a measure of the relative phase between modes (Duvvuri and McKeon, 2015). Similarly, Schmidt (2020) proposed the bispectral mode decomposition to study coherence in the velocity signals among spatial triads and analyzed the interacting frequency components using maxima in the mode bispectrum. Karban et al. (2023) have investigated the key triads underpinning minimal Couette flow. Cho et al. (2018) investigated triadic interactions in the spanwise direction and their contributions to spectral energy transfer in a turbulent channel flow, and revealed that the dominant transfer mechanism is the classical energy cascade, with evidence of inverse cascade near the wall.

However, previous studies on triadic interactions have mostly focused on the energy transfer between scales without sufficient analysis linking the energy transfer to the change of spectral turbulence kinetic energy (TKE) or the change in the velocity response. In this thesis, we aim to include the linear resolvent operator into the analysis of non-linear energy transfer, to quantitatively characterize the spatio-temporal nature of the triadic interactions and their influence on the resulting velocity response.

1.2.2 Quasi-linear and Generalized Quasi-linear Analysis

One approach to reduce the cost and complexity associated with the nonlinear terms in the NSE is to employ a quasi-linear (QL) model, in which the resolved nonlinear interactions are restricted to those either involving or resulting in the zero streamwise wavenumber (streamwise constant modes) (Farrell and Ioannou, 2007). This results in fully non-linear governing equations for the means flow (the streamwise constant modes), where all triadic interactions are retained, and linear governing equations for the perturbations, where the interactions between small-scale perturbations are neglected (or modeled). The approach rests on the admitted interactions capturing the key elements of the nonlinearity, while the remaining unresolved interactions are neglected or approximated with a suitable model (Gayme et al., 2010; Farrell and Ioannou, 2012). Self-sustaining simulations can be achieved with flow features that resemble those obtained from direct numerical simulations (DNS), thus providing a cost-efficient model alternative to DNS of the full NSE (Thomas et al., 2015; Farrell

et al., 2016).

Generalized quasi-linear (GQL) analysis is an extension to QL: instead of only including the streamwise constant mode in the base flow, the streamwise large-scales, with streamwise wavenumber $k_x \leq \Lambda$, are included into the base flow. Similar to QL, the governing equations are non-linear for the base flow (large scales), and are linear for the perturbations (small scales) around the base flow. Compared to QL, more modes in GQL are included in the base flow, and therefore undergo non-linear interactions and constitute the resolved modes. Additionally, due to the presence of non-zero wavenumbers in the base flow, the small scales are now capable of spectrally non-local energy redistribution between each other through scattering off non-zero wavenumbers in the base flow. GQL can also be interpreted as an interpolation between QL ($\Lambda = 0$) and DNS ($\Lambda \to \infty$), serving as a systematic way of improving QL (Marston et al., 2016). Farrell and Ioannou (2007) and Marston et al. (2016) demonstrated the success of GQL on zonal jets in atmospheric turbulence, which are 2D jets with dominating large-scale modes. Hernández et al. (2022a) demonstrated the success of GQL in the streamwise direction for a turbulent channel flow at $Re_\tau \approx 1700$, and later also in the spanwise direction (Hernández et al., 2022b). The authors showed that QL in a turbulent channel flow is not sufficient to capture the turbulent statistics while including a few modes in GQL can rapidly improve the performance. However, the authors also demonstrated that GQL requires more resolved wavenumbers in the spanwise direction to achieve similar performance compared to the streamwise direction. Finally, the selection of Λ in GQL currently largely relies on trials and comparisons with the baseline direct numerical simulations (DNS) or large eddy simulations (LES), and could benefit from a quantitative analysis of the important triadic interactions. To our knowledge, the importance of the resolved nonlinear interactions relative to the unresolved (neglected or modeled) ones in QL and GQL has not been fully quantified or explained, which is one motivation for the present work.

1.3 Thesis Outline

In this thesis, we will focus on the linear and non-linear interactions involving large-scale structures. In Chapter 2, we will start with the mathematical formulation for the linear resolvent analysis that is central to the entire thesis, including a discussion of the role of the non-linear forcing and models for it. Chapter 3 will explore the linear resolvent analysis, including enhancements of eddy viscosity and a crude boundary geometry model. The resolvent is applied to an experimental data set

over a spanwise periodic rough surface and the predictive and data compression capabilities are studied, highlighting the improvements offered by the additional models. Chapters 4 to 6 focus on the non-linear interactions. Chapter 4 presents the simulation data, including details of the temporal filter, temporal Fourier analysis, and verification of the data processing methods. Chapter 5 presents a novel method to quantify the importance of different triadic interactions on the forcing and response. The results highlight the importance of large-scale structures in triadic interactions and provide a natural connection to the QL and GQL frameworks. Chapter 6 presents analyses of triadic interactions that contribute to a representative mode of the near-wall cycle. The results demonstrate the spatio-temporal nature of the triadic interactions and the effect of the linear resolvent operator. We conclude in Chapter 7 with a discussion of the significance of our results and directions for future research.

Chapter 2

RESOLVENT ANALYSIS AND NON-LINEAR INTERACTIONS IN TURBULENCE

In this chapter, we start by formulating the resolvent analysis, followed by a discussion of the non-linear forcing in Fourier space, which highlights the triadic interactions. Finally, we discuss methods that can be used to (partially) model the non-linear forcing including the eddy viscosity model and the 2D resolvent.

2.1 Resolvent Formulation

We consider an incompressible, fully developed, turbulent channel or turbulent boundary layer, with the streamwise, wall-normal and spanwise coordinates given by x, y, z, and the corresponding velocity components u, v, w, as shown in Figure 2.1. Vectors $\boldsymbol{x} = [x, y, z]$ and $\boldsymbol{u} = [u, v, w]$ are the spatial coordinate and velocity vectors receptively. Normalization of the coordinates and velocities are performed using the outer scales: channel half height h, channel centerline velocity U_{CL} or boundary layer thickness δ_{98}, and boundary layer free stream velocity U_∞ unless otherwise specified.

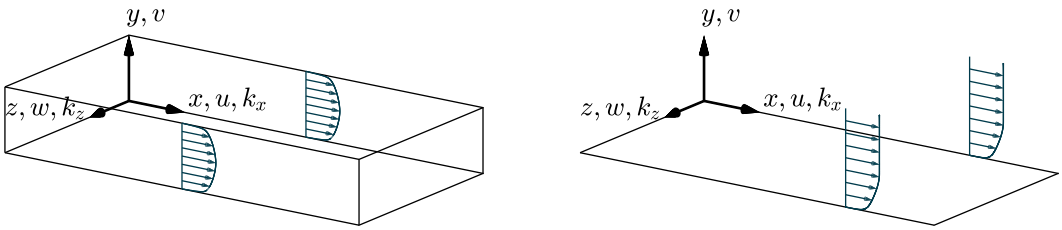

Figure 2.1: Sketch of a turbulent channel flow (left) and a turbulent boundary layer (right), with the coordinate system and the spatio-temporal mean profile $\overline{U}(y)$.

The flow field is then decomposed into a mean profile and the fluctuations around the mean. For a fully developed channel flow studied in Chapters 4-6 with homogeneous streamwise and spanwise directions, the spatio-temporal mean profile $\overline{U}(y)$, obtained by averaging in x, z, t is a natural selection. On the other hand, for spatially developing flows, previous studies have applied the global resolvent analysis to study flows such as jets (Schmidt et al., 2018; Towne et al., 2018; Pickering et al., 2021), streamwise developing boundary layers (Sipp and Marquet, 2013; Rigas et al., 2021;

Barthel et al., 2022), cavity flow (Gómez et al., 2016), and airfoils (Yeh and Taira, 2019). In these studies, the streamwise developing flow is discretized in the physical domain for both the streamwise direction and the wall normal direction (or radial direction in the case of jets) and the streamwise developing mean profile is used. In Chapter 3, a boundary layer is analyzed with the quasi-parallel flow assumption applied in the streamwise direction by neglecting the streamwise development of the flow, mainly due to the fact that experimental data is only available at a single streamwise location.

A boundary layer with quasi-parallel assumption or a channel flow is decomposed into the spatio-temporal mean profile $\overline{U}(y)$, averaged in x, z, t and shown in Figure 2.1, and the perturbations $\boldsymbol{u}(x, y, z, t)$ relative to the spatio-temporal mean. The perturbation equations can then be obtained by subtracting the mean equations from the full Navier-Stokes equations (NSE):

$$\nabla \cdot \boldsymbol{u} = 0, \tag{2.1}$$

$$\frac{\partial \boldsymbol{u}}{\partial t} + (\boldsymbol{u} \cdot \nabla)\overline{U} + (\overline{U} \cdot \nabla)\boldsymbol{u} = -\nabla p + \frac{1}{Re}\nabla^2 \boldsymbol{u} + \boldsymbol{f}, \tag{2.2}$$

where p is the pressure fluctuations and $\boldsymbol{f}$ is the non-linear forcing defined in physical space as:

$$\boldsymbol{f}(\boldsymbol{x}, t) = -\boldsymbol{u}(\boldsymbol{x}, t) \cdot \nabla \boldsymbol{u}(\boldsymbol{x}, t). \tag{2.3}$$

The nonlinear forcing is a result of grouping all terms that are non-linear with respect to the perturbations stemming from the non-linear convection term in the NSE. It may be treated crudely as a broadband input to analyze the properties of the linear operator or with more sophistication such as a data-driven forcing (Towne et al., 2020) or an eddy viscosity to address the turbulence closure problem (Hwang and Cossu, 2010; McKeon, 2017).

A Fourier decomposition is then employed in the homogeneous directions of x, z, and t:

$$\boldsymbol{u}(\boldsymbol{x}, t) = \iiint_{-\infty}^{\infty} \boldsymbol{u}(\boldsymbol{k}, y) e^{i(k_x x + k_z z - \omega t)} dk_x dk_z d\omega, \tag{2.4}$$

where we have introduced a wavenumber-frequency triplet $\boldsymbol{k} = [k_x, k_z, \omega]$. Here k_x, k_z are the streamwise, spanwise wavenumbers, and ω is the temporal frequency.

The Fourier-transformed perturbation equations are then written in an input-output form, where the non-linear term $\boldsymbol{f} = [f_x, f_y, f_z]^T$ is considered as an input forcing

to the resolvent operator $\mathcal{H}_p(\boldsymbol{k}, y)$:

$$\begin{bmatrix} \boldsymbol{u}(\boldsymbol{k}, y) \\ p(\boldsymbol{k}, y) \end{bmatrix} = \mathcal{H}_p(\boldsymbol{k}, y)\ \boldsymbol{f}(\boldsymbol{k}, y). \tag{2.5}$$

2.1.1 The Resolvent Operator

Following McKeon and Sharma (2010), the primitive form resolvent operator $\mathcal{H}_p(\boldsymbol{k}, y)$, which maps the forcing $\boldsymbol{f}$ to the velocity and pressure $[\boldsymbol{u}, p]^T$ can be written as:

$$\mathcal{H}_p(\boldsymbol{k}, y) = \left(-i\omega \begin{bmatrix} \boldsymbol{I} & \\ & 0 \end{bmatrix} - \begin{bmatrix} \mathcal{L}_{\boldsymbol{k}} & -\nabla_{\boldsymbol{k}} \\ \nabla_{\boldsymbol{k}}^{\mathrm{T}} & 0 \end{bmatrix} \right)^{-1} \begin{bmatrix} \boldsymbol{I} \\ 0 \end{bmatrix}, \tag{2.6}$$

with $\boldsymbol{I}$ as the 3×3 identity matrix, $\nabla_{\boldsymbol{k}} = [ik_x, \frac{d}{dy}, ik_z]^{\mathrm{T}}$, $\nabla_{\boldsymbol{k}}^{\mathrm{T}}$ the Fourier-transformed gradient and divergence operators, and $\mathcal{L}_{\boldsymbol{k}}$ defined as:

$$\mathcal{L}_{\boldsymbol{k}} = \begin{bmatrix} -ik_x\overline{U} + \frac{\Delta_{\boldsymbol{k}}}{Re} & -\frac{d\overline{U}}{dy} & 0 \\ 0 & -ik_x\overline{U} + \frac{\Delta_{\boldsymbol{k}}}{Re} & 0 \\ 0 & 0 & -ik_x\overline{U} + \frac{\Delta_{\boldsymbol{k}}}{Re} \end{bmatrix}, \tag{2.7}$$

where $\Delta_{\boldsymbol{k}} = \frac{d^2}{dy^2} - k_x^2 - k_z^2$ is the Fourier-transformed Laplacian. Note that the primitive form resolvent operator $\mathcal{H}_p(\boldsymbol{k}, y)$ defined in equation (2.6) is a 4×3 operator, mapping the three forcing components to the three velocity components plus the pressure. Since pressure is not studied in this thesis, the last row of $\mathcal{H}_p$ can be removed to obtain the 3×3 operator, $\mathcal{H}(\boldsymbol{k}, y)$, mapping the three forcing components to the three velocity components without giving the pressure.

Alternatively, similar to Moarref et al. (2013), the wall normal velocity v and wall normal vorticity $\eta = ik_z u - ik_x w$ can be used to eliminate the pressure and rewrite the NSE into:

$$\begin{bmatrix} -i\omega\Delta_{\boldsymbol{k}} - \mathcal{L}_{OS} & 0 \\ ik_z\frac{d\overline{U}}{dy} & -i\omega + \mathcal{L}_{SQ} \end{bmatrix} \begin{bmatrix} v(\boldsymbol{k}, y) \\ \eta(\boldsymbol{k}, y) \end{bmatrix} = \begin{bmatrix} -ik_x\frac{d}{dy} & -k^2 & -ik_z\frac{d}{dy} \\ ik_z & 0 & -ik_x \end{bmatrix} \boldsymbol{f}(\boldsymbol{k}, y) = \boldsymbol{B}\boldsymbol{f}, \tag{2.8}$$

where $k^2 = k_x^2 + k_z^2$, and the Orr-Sommerfeld and Squire operators defined as:

$$\mathcal{L}_{OS} = ik_x\frac{d^2\overline{U}}{dy^2} - ik_x\overline{U}\Delta_{\boldsymbol{k}} + \frac{\Delta_{\boldsymbol{k}}^2}{Re}, \tag{2.9}$$

$$\mathcal{L}_{SQ} = ik_x\overline{U} - \frac{\Delta_{\boldsymbol{k}}}{Re}. \tag{2.10}$$

The inverted matrix can then be written as:

$$\mathcal{H}' = \begin{bmatrix} -i\omega\Delta_{\boldsymbol{k}} - \mathcal{L}_{OS} & 0 \\ ik_z \frac{d\overline{U}}{dy} & -i\omega + \mathcal{L}_{SQ} \end{bmatrix}^{-1} = \begin{bmatrix} \mathcal{H}_{vv} & 0 \\ \mathcal{H}_{\eta v} & \mathcal{H}_{\eta\eta} \end{bmatrix}, \tag{2.11}$$

with the submatrices computed using:

$$\mathcal{H}_{vv} = \left(-i\omega\Delta_{\boldsymbol{k}} - \mathcal{L}_{OS}\right)^{-1}, \tag{2.12}$$

$$\mathcal{H}_{\eta\eta} = \left(-i\omega + \mathcal{L}_{SQ}\right)^{-1}, \tag{2.13}$$

$$\mathcal{H}_{\eta v} = -ik_z \mathcal{H}_{\eta\eta} \left(\frac{d\overline{U}}{dy}\right) \mathcal{H}_{vv}. \tag{2.14}$$

Finally, the velocities can be recovered from the wall-normal vorticity by:

$$\boldsymbol{u}(\boldsymbol{k}, y) = \frac{1}{k^2} \begin{bmatrix} ik_x \frac{d}{dy} & -ik_z \\ k^2 & 0 \\ ik_z \frac{d}{dy} & ik_x \end{bmatrix} \begin{bmatrix} v(\boldsymbol{k}, y) \\ \eta(\boldsymbol{k}, y) \end{bmatrix} = \boldsymbol{A} \begin{bmatrix} v(\boldsymbol{k}, y) \\ \eta(\boldsymbol{k}, y) \end{bmatrix}. \tag{2.15}$$

Combining $\boldsymbol{A}$, $\mathcal{H}'$, $\boldsymbol{B}$ defined in equations (2.15), (2.11), and (2.8), the resolvent operator $\mathcal{H}$ that maps the forcing $\boldsymbol{f}$ to the velocities $\boldsymbol{u}$ can be alternatively written as:

$$\mathcal{H} = \boldsymbol{A}\mathcal{H}'\boldsymbol{B}, \tag{2.16}$$

which differs from the primitive form resolvent operator $\mathcal{H}_p$ only in that $\mathcal{H}$ does not produce the pressure fluctuations, and is the same as $\mathcal{H}_p$ with the last row removed. However, equation (2.16) has the advantage that utilizing the block triangular structure, individual sub-blocks can be inverted on their own, resulting in the inversion of two 1×1 operators instead of one 4×4 operator, which is more computationally efficient.

2.1.2 Singular Value Decomposition of the Resolvent Operator

The discrete resolvent operator $\mathcal{H}(\boldsymbol{k}, y)$ is constructed using N Chebyshev collocation points in y for a channel or a rational transformed Chebyshev grid for a boundary layer. A singular value decomposition (SVD) can then be performed on the discrete operator:

$$\mathcal{H}(\boldsymbol{k}, y) = \sum_q \psi_q(\boldsymbol{k}, y)\sigma_q(\boldsymbol{k})\phi_q^*(\boldsymbol{k}, y), \tag{2.17}$$

where ψ_q are the singular response modes (henceforth referred to as resolvent modes), σ_q are the (ordered) singular values, and ϕ_q are the singular forcing modes.

Superscript $*$ denotes a complex conjugate. Velocity Fourier modes can then be expressed as:

$$\boldsymbol{u}(\boldsymbol{k}, y) = \sum_{q} \chi_q(\boldsymbol{k}) \sigma_q(\boldsymbol{k}) \psi_q(\boldsymbol{k}, y), \tag{2.18}$$

where $\chi_q(\boldsymbol{k}) = \phi_q^*(\boldsymbol{k}, y)\boldsymbol{f}(\boldsymbol{k}, y)$ are the non-linear weights obtained by projecting the nonlinear forcing (if known) onto the singular forcing modes. Without detailed knowledge of the non-linear forcing, the non-linear weights can be determined using data-driven methods such as the least squares regression explored in detail in Chapter 3. Other methods of obtaining the non-linear weights include optimization algorithms, where the non-linear weights are computed by minimizing the difference between the resolvent represented statistics and the available DNS statistics (typically the energy spectra) (Moarref et al., 2014; McMullen, 2020). Alternatively, the resolvent based estimation, which performs a least squares regression on the cross-spectral density (CSD), can be utilized to estimate the CSD for unknown locations or states from available data, essentially obtaining the CSD of the non-linear weights χ (Towne et al., 2020; Amaral et al., 2021). Finally, Barthel (2022) performed non-linear interactions using the resolvent modes, obtaining a set of polynomial equations for χ, which were solved using convex optimization.

The computation of the resolvent modes can be performed separately at each wavenumber-frequency triplet of interest. The analysis at each triplet costs less than a second on a laptop computer for the cases considered in this study employing a quasi-parallel flow assumption, making the resolvent a low-cost computational tool for modeling and data compression.

2.2 Non-linear Forcing in the Navier-Stokes Equations

The non-linear (quadratic) terms $\boldsymbol{f}$ are defined in physical space in equation 2.3 through a point-wise multiplication, while in (discrete) Fourier space the non-linear forcing at a wavenumber-frequency triplet $\boldsymbol{k}_3$ can be written in terms of a convolution of the velocity fields and velocity gradients at $\boldsymbol{k}_1$ and $\boldsymbol{k}_2$:

$$\boldsymbol{f}(\boldsymbol{k}_3, y) = -\sum_{\boldsymbol{k}_1+\boldsymbol{k}_2=\boldsymbol{k}_3} \boldsymbol{u}(\boldsymbol{k}_1, y) \cdot \nabla \boldsymbol{u}(\boldsymbol{k}_2, y). \tag{2.19}$$

The requirement of $\boldsymbol{k}_1 + \boldsymbol{k}_2 = \boldsymbol{k}_3$ is the triadic compatibility or resonance constraint, a result of the quadratic nature of the non-linearity.

In the resolvent formulation, the Fourier-transformed NSE are written in an input-output form, where $\boldsymbol{f}(\boldsymbol{k}, y)$ is considered an input forcing to the resolvent operator

$\mathcal{H}(\boldsymbol{k}, y)$ as shown in equation (2.5). It can be seen that the linear operator does not modify the scale of the input, such that each wavenumber-frequency triplet operates independently from each other. On the other hand, equation (2.19) shows that the non-linear forcing is responsible for the coupling of different scales, and therefore the distribution of energy between scales.

The triadic interactions are visually depicted in Figure 2.2, where the velocity fields at $\boldsymbol{k}_1$ non-linearly interacts with the velocity gradients at $\boldsymbol{k}_2$, generating part of the forcing at $\boldsymbol{k}_3 = \boldsymbol{k}_1 + \boldsymbol{k}_2$. The full forcing is a convolution sum of all pairs of $\boldsymbol{k}_1$ and $\boldsymbol{k}_2$ that are triadically compatible with $\boldsymbol{k}_3$, which is then passed through the linear resolvent operator to generate the velocity response at $\boldsymbol{k}_3$. This triadic interaction will be explored further in Chapter 5.

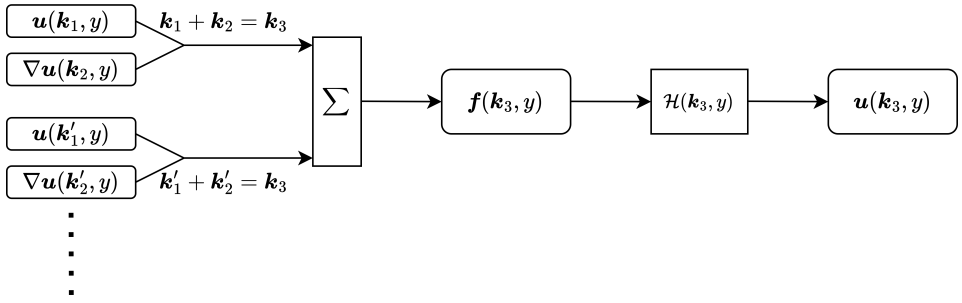

Figure 2.2: Diagram for the triadic interactions. The velocity and velocity gradient at $\boldsymbol{k}_1$ and $\boldsymbol{k}_2$ interact non-linearly to generate part of the forcing at $\boldsymbol{k}_3 = \boldsymbol{k}_1 + \boldsymbol{k}_2$. The full forcing is a convolution sum of all pairs of $\boldsymbol{k}_1$ and $\boldsymbol{k}_2$ that are triadically compatible with $\boldsymbol{k}_3$, which forces the resolvent operator to generate the response.

2.2.1 Helmholtz Decomposition

The non-linear forcing can be decomposed into irrotational and solenoidal parts (Rosenberg, 2018; Morra et al., 2021):

$$\boldsymbol{f}(\boldsymbol{k}, y) = \boldsymbol{f}_i(\boldsymbol{k}, y) + \boldsymbol{f}_s(\boldsymbol{k}, y) = \nabla\xi(\boldsymbol{k}, y) + \nabla \times \boldsymbol{\zeta}(\boldsymbol{k}, y), \tag{2.20}$$

where the irrotational part $\boldsymbol{f}_i(\boldsymbol{k}, y)$ can be written as the gradient of a scalar field and the solenoidal part $\boldsymbol{f}_s(\boldsymbol{k}, y)$ can be written as the curl of a vector field. Therefore, the irrotational part of the forcing can be absorbed into the gradient of the pressure fluctuations, and have no effect on the resulting velocity fields.

Additionally, the $\boldsymbol{B}(\boldsymbol{k}, y)$ matrix defined in equation (2.8) is used to eliminate the pressure term in the NSE to arrive at the velocity-vorticity formulation of the NSE

in equation (2.8). As similarly derived in Morra et al. (2021), it can be show that $\boldsymbol{B}(\boldsymbol{k}, y)$ also eliminates the irrotational part of the forcing in the same manner:

$$\boldsymbol{B}(\boldsymbol{k},\boldsymbol{y})\boldsymbol{f}_i(\boldsymbol{k}, y) = \begin{bmatrix} -ik_x\frac{d}{dy} & -k^2 & -ik_z\frac{d}{dy} \\ ik_z & 0 & -ik_x \end{bmatrix} \begin{bmatrix} ik_x \\ \frac{d}{dy} \\ ik_z \end{bmatrix} \xi(\boldsymbol{k}, y) = 0. \tag{2.21}$$

Combining with equation (2.16), we can arrive at:

$$\boldsymbol{u}(\boldsymbol{k}, y) = \mathcal{H}(\boldsymbol{k}, y)\boldsymbol{f}(\boldsymbol{k}, y) = \mathcal{H}(\boldsymbol{k}, y)\boldsymbol{f}_s(\boldsymbol{k}, y). \tag{2.22}$$

In other words, without studying the pressure in this thesis, the irrotational part of the forcing is naturally eliminated when multiplied by the resolvent operator, and only the solenoidal part of the forcing is active.

2.2.2 Energy Transfer by the Non-linear Forcing

We start by defining the spectral turbulence kinetic energy (TKE) as $e(\boldsymbol{k}, y) = |u(\boldsymbol{k}, y)|^2 + |v(\boldsymbol{k}, y)|^2 + |w(\boldsymbol{k}, y)|^2$, which is the energy of Fourier modes at given $\boldsymbol{k}$. An equation for the spectral TKE can be written as:

$$\underbrace{\mathrm{Re}\left\{u^*(\boldsymbol{k}, y)v(\boldsymbol{k}, y)\overline{U}'(y)\right\}}_{\text{Production}} + \underbrace{\frac{k^2}{Re}e(\boldsymbol{k}, y) + \frac{1}{Re}\frac{d}{dy}u_i^*(\boldsymbol{k}, y)\frac{d}{dy}u_i(\boldsymbol{k}, y)}_{\text{Viscous Dissipation}}$$

$$+\underbrace{\mathrm{Re}\left\{\frac{d}{dy}\left[v^*(\boldsymbol{k}, y)p(\boldsymbol{k}, y)\right]\right\}}_{\text{Pressure Transport}} - \underbrace{\frac{1}{2}\frac{1}{Re}\frac{d^2}{dy^2}e(\boldsymbol{k}, y)}_{\text{Viscous Transport}} = \underbrace{\mathrm{Re}\left\{u_i^*(\boldsymbol{k}, y)f_i(\boldsymbol{k}, y)\right\}}_{\text{Turbulent Transport}}, \tag{2.23}$$

where $\mathrm{Re}\{\cdot\}$ indicates the real part, and the summation notation is used with the subscripts i. The derivation is given in appendix A.1.

The turbulent transport term can be alternatively written as:

$$\begin{aligned} u_i^*(\boldsymbol{k}, y)f_i(\boldsymbol{k}, y) =& \boldsymbol{u}^*(\boldsymbol{k}, y)\boldsymbol{f}(\boldsymbol{k}, y) \\ =& -\boldsymbol{u}^*(\boldsymbol{k}, y)\sum_{\boldsymbol{k}_1+\boldsymbol{k}_2=\boldsymbol{k}} \boldsymbol{u}(\boldsymbol{k}_1, y)\cdot\nabla\boldsymbol{u}(\boldsymbol{k}_2, y), \end{aligned} \tag{2.24}$$

which shows that the turbulent transport is the only term that involves the non-linear forcing, and therefore the only term that transports energy between different wavenumber-frequency triplets $\boldsymbol{k}$. Additionally, Schmid and Henningson (2001) and Barthel (2022) have demonstrated that the non-linear turbulent transport is energy conserving on a triad by triad basis.

Alternatively, the resolvent formulation $\boldsymbol{u}(\boldsymbol{k}, y) = \mathcal{H}(\boldsymbol{k}, y)\ \boldsymbol{f}(\boldsymbol{k}, y)$ can be utilized to obtain:

$$\begin{aligned} e(\boldsymbol{k}, y) =& \boldsymbol{u}^*(\boldsymbol{k}, y)\ \mathcal{H}(\boldsymbol{k}, y)\boldsymbol{f}(\boldsymbol{k}, y) \\ =& -\boldsymbol{u}^*(\boldsymbol{k}, y)\ \mathcal{H}(\boldsymbol{k}, y) \sum_{\boldsymbol{k}_1+\boldsymbol{k}_2=\boldsymbol{k}} \boldsymbol{u}(\boldsymbol{k}_1, y) \cdot \nabla \boldsymbol{u}(\boldsymbol{k}_2, y). \end{aligned} \tag{2.25}$$

The formulation of equations (2.23) and (2.25), both derived from the NSE, are mathematically equivalent, yet they have slightly different interpretation. Equation (2.23) is an energy balance equation. The energy transported into or out of $\boldsymbol{k}$ through non-linear interactions (the turbulent transport term), is balanced by 4 other mechanisms, and is therefore not directly correlated to the increase or decrease of the spectra TKE at this $\boldsymbol{k}$. Equation (2.25) on the other hand, considers the non-linearity as a forcing that drives the turbulent perturbations and activates the linear mechanisms of production, pressure, and viscosity (all contained in the linear resolvent operator $\mathcal{H}$), therefore providing a direct link between the non-linearity and the spectral TKE.

2.3 Methods to Partially Model the Non-linear Forcing

We briefly introduce two methods to model part of the non-linear forcing in the resolvent that will be explored in this study: an eddy viscosity model and the 2D resolvent.

2.3.1 Eddy Viscosity Model

The energy cascade is an important feature in turbulence where energy at the large scales is transferred to the small scales through non-linear interactions and dissipated at the small scale by viscosity (Jiménez, 2012). As a result, for the large-scale structures, the viscosity alone is insufficient for modeling the energy dissipation, and an additional model that captures the extraction of energy by the Reynolds stress is desired.

The eddy viscosity, a model for the mean Reynolds stresses in terms of the mean velocity gradient, is originally derived to provide closure for the Reynolds-averaged Navier-Stokes equations (Reynolds and Tiederman, 1967). An analytical model for

the channel flow is given by:

$$\nu_T(y) = \frac{1}{2}\left\{1+\left[\frac{\kappa Re_\tau}{3}\left(2y-y^2\right)\left(3-4y+2y^2\right)\left(1-\exp\left(\frac{(|y-1|-1)\,Re_\tau}{A}\right)\right)\right]^2\right\}^{1/2}+\frac{1}{2}, \tag{2.26}$$

where $\nu_T(y)$ is the total effective viscosity, which includes both the molecular and eddy viscosity, and is normalize by the molecular viscosity ν. κ is the Karman constant, A is a constant in van Driest's wall law, and $y \in [0, 2]$ is the wall normal coordinate for the channel, normalized by channel half height, with walls located at $y = 0$ and $y = 2$. Reynolds and Hussain (1972) later utilized this eddy viscosity model to relate the oscillating Reynolds stress to the oscillating strain rate in a turbulent channel flow with waves induced by vibrating ribbons. Many recent studies have further utilized the eddy viscosity as a method to introduce a partial model for the nonlinear Reynolds stress in the linearized equations of the resolvent formulation, with the goal of generating more efficient resolvent basis functions (del Álamo and Jiménez, 2006; Hwang and Cossu, 2010; Huynh et al., 2021; Fan et al., 2024; Illingworth et al., 2018; Symon et al., 2021). In these previous works, the viscous term in the original momentum equations are replaced to include the eddy viscosity:

$$\frac{1}{Re}\nabla^2\boldsymbol{u} \longrightarrow \frac{1}{Re}\nabla\cdot\left[\nu_T\left(\nabla\boldsymbol{u}+\nabla\boldsymbol{u}^T\right)\right]. \tag{2.27}$$

The results showed that the standard resolvent tends to over predict the streamwise velocity u while under predicts v and w, while the inclusion of the eddy viscosity profile improves the performance. However, Illingworth et al. (2018) showed that this scale independent eddy viscosity profile (no dependency on $\boldsymbol{k}$) only works to improve the resolvent performance for the large scale structures, while for the intermediate and small scales, this is not a suitable model.

In the language of section 2.2, the eddy viscosity is modeling the interaction between two small scales (large $\boldsymbol{k}_1, \boldsymbol{k}_2$) affecting a large scale (small $\boldsymbol{k}_3$), visually represented by the Feynman diagram in Figure 2.3. This method of enhancing the resolvent with eddy viscosity is explored in details in Chapter 3.

2.3.2 2D Resolvent Analysis

A similar class of problems involving flows with periodic spanwise or temporal variations such as spanwise periodic exact coherent states (Rosenberg and McKeon,

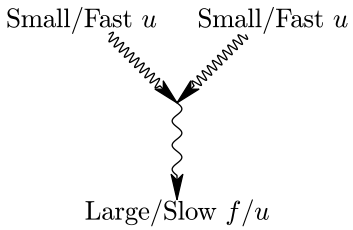

Figure 2.3: Feynman diagram depicting the type of triadic interaction modeled by the eddy viscosity.

2019a), spanwise varying riblets (Chavarin and Luhar, 2020) or airfoils with temporal periodicity (Padovan et al., 2020) can be studied using the 2D resolvent analysis, which utilizes mean profiles with a spanwise or temporal variation. Owing to the periodicity, the analysis can still be performed in Fourier domain for the spanwise or temporal coordinate. However, wavenumber-frequency triplets at different k_z or ω are now non-linearly coupled together through the mean profile, and must be solved simultaneously, unlike the 1D resolvent analysis. The 2D resolvent are including triadic interactions between the large/slow scales contained in the mean profile and any scale of interest, depicted in Figure 2.4.

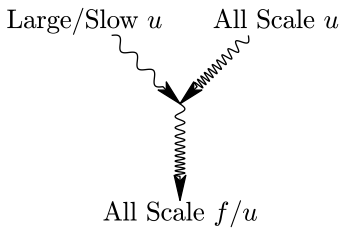

Figure 2.4: Feynman diagram depicting the type of triadic interaction modeled by the 2D resolvent.

Of particular interest to this work is the method presented in Chavarin and Luhar (2020), where the volume penalization formulation is used in the resolvent framework to study the drag reducing abilities of streamwise aligned, spanwise periodic riblets. This formulation allows for the inclusion of a boundary geometry in the resolvent, allowing for non-linear interactions between modes through the imposed boundary geometry. This method is adapted for this study, without utilizing a spanwise varying mean velocity profile, and only utilizes the volume penalization to model the effect of the boundary geometry. We start by considering the perturbation

momentum equation with a volume penalization term:

$$\frac{\partial \boldsymbol{u}}{\partial t} + (\boldsymbol{u} \cdot \nabla)\overline{U} + (\overline{U} \cdot \nabla)\boldsymbol{u} = -\nabla p + \frac{1}{Re}\nabla^2 \boldsymbol{u} + \boldsymbol{f} - K^{-1}\boldsymbol{u}, \tag{2.28}$$

where the parameter $K(y, z) \rightarrow \infty$ in the fluid region, therefore recovering the original NSE, and $K(y, z) \rightarrow 0$ in the solid region, to force the flow velocity to 0. We then apply a Fourier transform in the spanwise direction on the volume penalization term:

$$K^{-1}(y, z) = \sum_{m=-M}^{M} a_m(y) \exp\{im \cdot k_{z0} \cdot z\}, \tag{2.29}$$

where k_{z0} is the spanwise fundamental wavenumber of the surface geometry. With a streamwise and temporally constant surface geometry, the wavenumber frequency triple of the surface can be defined as $\boldsymbol{k}_0 = [0, k_{z0}, 0]$. After the Fourier transform, the volume penalization term becomes a convolution, which can be incorporated into the resolvent analysis by modifying equation (2.5):

$$\mathcal{H}(\boldsymbol{k}, y)^{-1} \begin{bmatrix} \boldsymbol{u}(\boldsymbol{k}, y) \\ p(\boldsymbol{k}, y) \end{bmatrix} - \sum_m a_m \, \boldsymbol{u}(\boldsymbol{k} - m\boldsymbol{k}_0, y) = \boldsymbol{f}(\boldsymbol{k}, y), \tag{2.30}$$

where multiple triplets of interest are coupled together through the boundary geometry described by a_m. However, the coupling of the triplets indicates that the resolvent analysis has to be performed for multiple triplets simultaneously, therefore increasing the computation cost. This method will be explored in Chapter 3 to model the surface geometry of interest.

Finally, we briefly discuss the increase of computation costs associated with the biglobal and 2D resolvent analysis. Starting with the 1D resolvent analysis, the linear system is of size $N_q N_y$ where N_q is the number of state variables and N_y the number of discretization points in the wall normal direction y. Using M streamwise discretization points for the global resolvent or M k_z or ω Fourier modes in the 2D resolvent, the linear system becomes size MN_qN_y. The computation cost scales with the size of the system with power $1 < a \leq 3$, $O\left(\left(MN_qN_y\right)^a\right)$, with the value of a depending on the numerical algorithm (Duff et al., 2017). Recent studies have made improvements to the algorithm to reduce computation costs. For example, Moarref et al. (2013) utilized the randomized SVD and reported a cost reduction by a factor of two, and Ribeiro et al. (2020) utilized sketching of the linear operator combined with randomized SVD to achieve an order-of-magnitude cost reduction. Sparse differentiation schemes can also be used to sparsify the operator and utilize

sparse matrix solvers (Mattsson and Nordström, 2004; Barthel et al., 2022; Gomez, 2024). Kamal et al. (2020) and Towne et al. (2022) developed a method using spatial marching to approximate the resolvent modes for flows with slowly varying mean profile instead of matrix inversions. Barthel et al. (2022) developed the variational resolvent analysis which removes the dependency on the inversion of the linear operator, achieving an order-of-magnitude cost reduction. In Chapter 3, symmetries in the resolvent are utilized for the computation of the 2D resolvent mode, improving the computation efficiency, while other algorithms are not utilized due to the manageable computation costs.

Chapter 3

RESOLVENT MODELING OF A FLOW OVER SPANWISE PERIODIC ROUGH SURFACE

In this chapter[1], we utilize the resolvent analysis on a experimental data set[2] of a turbulent boundary layer with spanwise alternating rough surface, where large-scale flow structures are observed. We start with a brief discussion of the experimental data set and the mean profile used for the construction of the resolvent matrix. We then discuss a method to reconstruct the flow field using resolvent modes and explore the validity of using an eddy viscosity as a partial non-linear model to enhance the resolvent and a 2D resolvent model that includes a crude model for the boundary geometry. Next, we present the results of the least squares regression using the resolvent modes on the experimental data, showcasing both the predictive and reduced-order modeling capabilities of the resolvent, followed by a brief discussion of future modeling directions.

3.1 Experimental Study of a Flow Over Spanwise Periodic Rough Surfaces

In this chapter, data from the experimental studies of Wangsawijaya et al. (2020), involving a turbulent boundary layer over a spanwise varying rough surface is analyzed. The experiments were performed on a streamwise aligned rough surface constructed out of strips of alternating cardboard (smooth patch) and sandpaper (rough patch) of equal width S, forming a surface with a spanwise wavelength of $2S$. This chapter focuses on the case of $S = 100$ mm, with a Reynolds number of $Re \approx 7.27 \times 10^4$. All velocity measurements are taken 4 meters downstream with both hot-wire anemometry (HWA) and stereoscopic particle image velocimetry (SPIV).

The HWA data provided by Wangsawijaya et al. (2020) were taken with hotwires on a grid with 31 logarithmically spaced wall-normal (y) locations, 12 spanwise (z) locations across a half-wavelength, and reflected across $z = 0$ owing to the presumed periodicity in the spanwise direction. The measurements were then time-averaged to obtain the mean streamwise velocity profile in the $y - z$ plane. The SPIV data

[1] Part of this chapter has been published in Huang et al. (2024).

[2] The author would like to thank Dr. Dea Wangsawijaya and Dr. Nicholas Hutchins for making the experimental data available and the valuable insights.

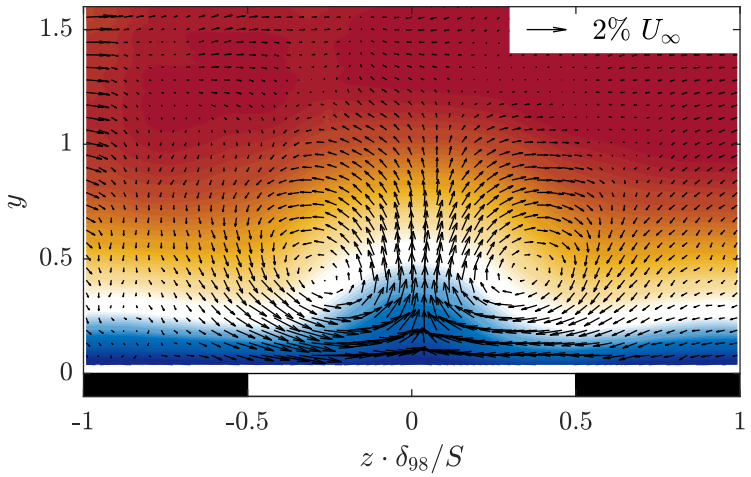

Figure 3.1: Temporal mean velocity $\overline{\overline{\boldsymbol{U}}}(y,z) = \overline{\boldsymbol{U}}(y) + \widetilde{\boldsymbol{U}}(y,z)$ from SPIV, with the contour plot showing the streamwise component and the quiver plot showing the spanwise and wall-normal components. The white and black patches at the bottom of the figure correspond to smooth and rough strips, respectively. The spanwise coordinate z is re-normalized with the strip width S, while maintaining the aspect ratio of the figure. Figure from Wangsawijaya et al. (2020), reproduced with permission.

was post-processed on a uniform grid of 144 $(y) \times 209$ (z) measurement points across one wavelength $(2S)$ of the spanwise varying rough surface. The streamwise velocity component agrees well between both datasets, with HWA providing finer grid resolution near the wall, and SPIV providing data for the wall-normal and spanwise velocity components.

A triple decomposition is performed on the flow field normalized by the free stream velocity U_∞:

$$\hat{\boldsymbol{u}}(x,y,z,t) = \overline{\boldsymbol{U}}(y) + \widetilde{\boldsymbol{U}}(y,z) + \boldsymbol{u}'(x,y,z,t), \tag{3.1}$$

where $\overline{\boldsymbol{U}}(y)$ is the spatio-temporal mean obtained by averaging in z,t, with the measurements taken at a single streamwise x location. Note that the perturbation defined for the resolvent in Chapter 2 includes two terms from this triple decomposition: $\boldsymbol{u}(x,y,z,t) = \widetilde{\boldsymbol{U}}(y,z) + \boldsymbol{u}'(x,y,z,t)$. The temporal mean $\overline{\overline{\boldsymbol{U}}}(y,z) = \overline{\boldsymbol{U}}(y) + \widetilde{\boldsymbol{U}}(y,z)$ is obtained by averaging in time, from which the spanwise varying component of the temporal mean $\widetilde{\boldsymbol{U}}(y,z)$, induced by the periodic rough surface, can be computed. $\overline{\overline{\boldsymbol{U}}}(y,z)$ is shown in Figure 3.1, and a pair of counter-rotating rolls near the transition regions between the smooth and rough strips can be observed. This dominant large-scale structure induced by the surface geometry motivates the use of a few resolvent modes to model the flow and extract this feature.

The goal of this chapter is to utilize knowledge of the spatio-temporal mean $\overline{\boldsymbol{U}}(y)$ to obtain information about the spanwise variations of the temporal mean $\widetilde{\boldsymbol{U}}(y,z)$, rather than utilizing the temporal mean $\overline{\overline{\boldsymbol{U}}}(y,z) = \overline{\boldsymbol{U}}(y) + \widetilde{\boldsymbol{U}}(y,z)$ to study the turbulent perturbations $\boldsymbol{u'}(x,y,z,t)$, such as the work of Chavarin and Luhar, 2020.

3.2 Spatio-temporal Mean Profile for Resolvent Construction

For the construction of the resolvent operator, a mean profile is a required input. Here we use the spatio-temporal mean, $\overline{U}(y)$, noting that this does not explicitly account for the spanwise variation associated with the roughness strips, which is the target of our modeling effort. Due to the limited resolution of the experimental measurements near the wall, the experimental profiles cannot be directly used for the resolvent computations. However, an analytical model for the spatio-temporal mean with a few tuning parameters can be used to generate a profile that best fits the experimental results. The profile of Chauhan et al. (2009) is used in this chapter and is composed of the law of the wall, a buffer region, the log law, and a wake profile, with Re_τ, log layer shift and wake strength being the tuning parameters. The optimal parameters are found by minimizing the difference with the spatio-temporal mean from HWA as it provides data closer to the wall than SPIV. The resulting optimal analytical profile is compared to both HWA and SPIV results in Figure 3.2, where little difference is observed in the majority of the boundary layer. The larger differences at locations close to the wall could be attributed to difficulties in obtaining accurate near-wall measurements in the experiments, and potentially the lack of boundary geometry information in the analytical model. However, these differences are not expected to significantly influence the resolvent output.

3.3 Resolvent Modeling of the Experimental Data

We start by impose the no-slip and no-penetration conditions at $y = 0$ for the resolvent, i.e. the smooth wall boundary condition, and seek to approximate the influence of the complex rough wall geometry via the resolvent model. With a focus on modeling the $\widetilde{\boldsymbol{U}}(y,z)$ component, which contains the largest structures in the streamwise direction, we utilize the $k_x = 0$ (streamwise constant) and $\omega = 0$ (temporally constant) resolvent modes with $k_z = p \cdot k_{z0}$, $p = 1, 2\ldots$, where $k_{z0} = 2\pi\delta_{98}/(2S)$ is the spanwise fundamental wavenumber of the periodic rough surface. Inserting $k_x = \omega = 0$ into equations (2.5)-(2.7), and multiplying the z

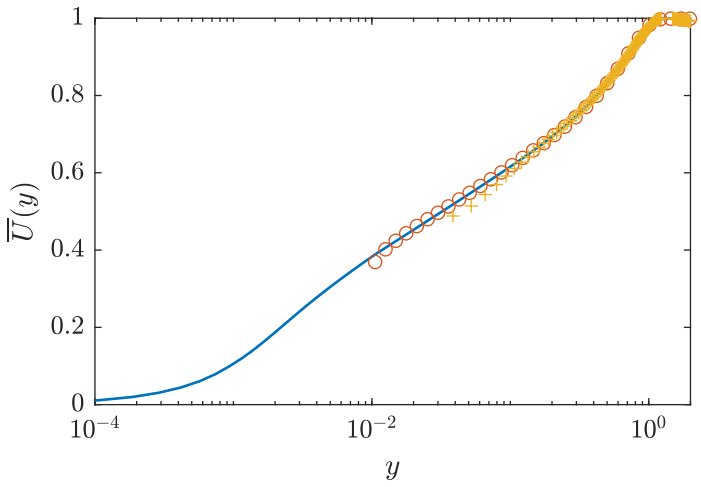

Figure 3.2: Comparison of the spatio-temporal mean profiles $\overline{U}(y)$ between the analytical profile (solid blue lines), the experimental results of HWA (red circles), and SPIV (yellow crosses).

momentum equation with i, the resolvent formulation can be further simplified into:

$$\begin{bmatrix} u(\boldsymbol{k},y) \\ v(\boldsymbol{k},y) \\ iw(\boldsymbol{k},y) \\ p(\boldsymbol{k},y) \end{bmatrix} = \begin{bmatrix} -\frac{\Delta_{\boldsymbol{k}}}{Re} & \frac{d\overline{U}}{dy} & 0 & 0 \\ 0 & -\frac{\Delta_{\boldsymbol{k}}}{Re} & 0 & \frac{d}{dy} \\ 0 & 0 & -\frac{\Delta_{\boldsymbol{k}}}{Re} & -k_z \\ 0 & \frac{d}{dy} & k_z & 0 \end{bmatrix}^{-1} \begin{bmatrix} f_x(\boldsymbol{k},y) \\ f_y(\boldsymbol{k},y) \\ if_z(\boldsymbol{k},y) \\ 0 \end{bmatrix}, \tag{3.2}$$

resulting in a real resolvent matrix and further reducing the computation cost.

Utilizing equation (2.18) and the inverse Fourier transform with N_{k_z} spanwise Fourier modes and N_{svd} singular vectors in the SVD, $\widetilde{\boldsymbol{U}}(y,z)$ can be written as an expansion:

$$\widetilde{\boldsymbol{U}}(y,z) = \sum_{p=1}^{N_{k_z}} \sum_{q=1}^{N_{svd}} 2 \cdot Real\left(\chi_{p,q}\sigma_{p,q}\psi_{p,q}(y) \cdot e^{ip\cdot k_{z0}\cdot z}\right), \tag{3.3}$$

where the subscript p is used as a short hand for quantities at $\boldsymbol{k} = [0,\ p\cdot k_{z,0},\ 0]$. Only the positive k_z modes are included in this equation, with the hermitian symmetry utilized for the negative k_z resolvent modes. The non-linear weights $\chi_{p,q}$ will be obtained via least squares regression using the experimental data later in this chapter.

3.3.1 Partially Modeling the Non-linear Forcing with Eddy Viscosity

As presented in section 2.3, the eddy viscosity is a well know method to incorporate part of the non-linear forcing to improve the resolvent analysis. Following Fan et al. (2024), an analytic approximation for the turbulent eddy viscosity for a boundary layer is constructed by combining the approximation for turbulent channels by Reynolds and Tiederman (1967) near the wall where the dynamics is expected to be similar between a boundary layer and a channel, and a model based on Prandtl's mixing-length hypothesis in the outer region:

$$\nu_T(y) = \begin{cases} \frac{1}{2}\left\{1 + \left[\frac{\kappa Re_\tau}{3}\left(2y - y^2\right)\left(3 - 4y + 2y^2\right)\left(1 - \exp\left(\frac{-yRe_\tau}{A}\right)\right)\right]^2\right\}^{1/2} + \frac{1}{2}, & \text{for } y \leq 0.7, \\ Re \cdot l_m^2 \left|\frac{d\overline{U}}{dy}\right| + 1, & \text{for } y \geq 0.7, \end{cases} \tag{3.4}$$

where $\nu_T(y)$ is the total effective viscosity, combining the molecular and eddy viscosity, normalized by the molecular viscosity ν. The mixing length l_m is chosen such that the profile is continuous at the matching location of $y = 0.7$, and the constants $\kappa = 0.426$ and $A = 25.4$ are chosen following previous studies (del Álamo and Jiménez, 2006). In this form, the wall normal coordinate y is normalized with boundary layer thickness δ_{98} with the wall located at $y = 0$. The spatio-temporal averaged Reynolds stress $-\overline{uv}$ from the SPIV measurements is compared with the predicted stress using the eddy viscosity model $Re^{-1}(\nu_T - 1)(d\overline{U}/dy)$ in Figure 3.3(a), where reasonable agreement is observed. However, in this study, the resolvent is tasked with the generation of spanwise varying modes. To understand the performance of eddy viscosity for spanwise varying modes, the temporal-averaged, spanwise varying $-\widetilde{uv}(k_z)$ Reynolds stress at different spanwise wavenumbers are compared between the SPIV measurements and the corresponding predictions using the eddy viscosity profile in Figure 3.3(b) for $k_z = p \cdot k_{z0}$ with $p = 1 - 4$. It can be observed that the overall structure of the $-\widetilde{uv}(k_z)$ Reynolds stress is well captured at all four wavenumbers, indicating that the eddy-viscosity profile is a decent model for the large-scale modes considered in this study. Better agreement could be obtained by tuning the parameters in the eddy viscosity model or utilizing data-driven approaches to obtain optimal eddy viscosity profiles, which are shown in Pickering et al. (2021) to improve the large scale structures obtained from the resolvent analysis. However the additional required experimental measurements

would impact the simplicity of the model we seek.

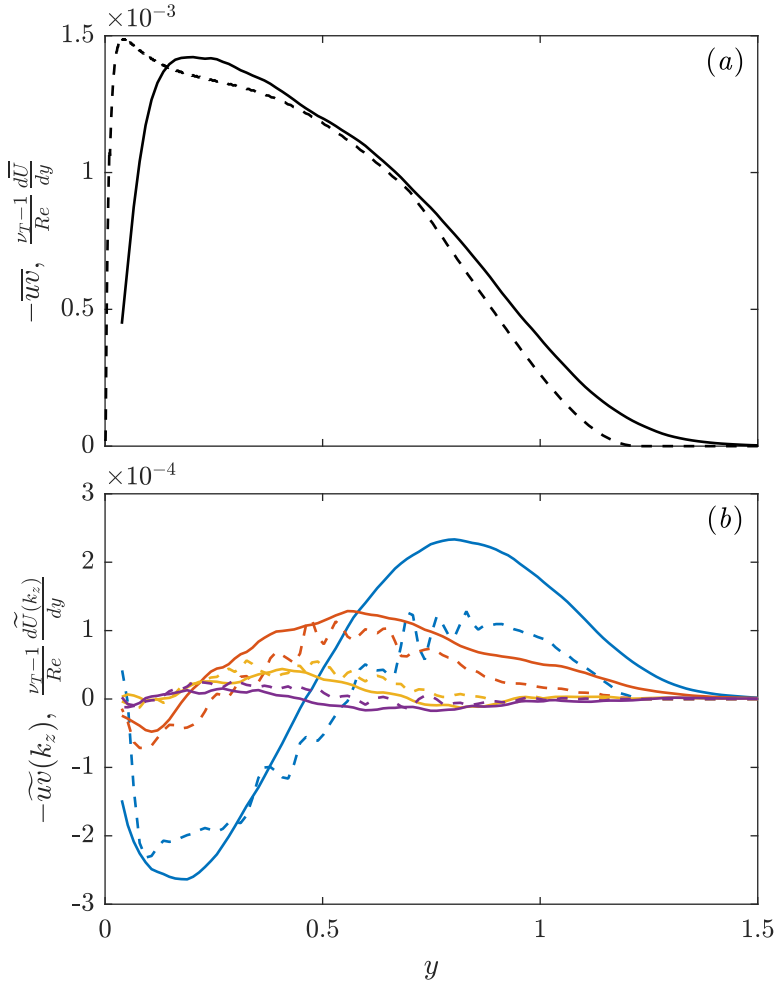

Figure 3.3: Comparison of experimental Reynolds stress $-\overline{uv}$ and $-\widetilde{uv}(k_z)$ (solid lines) with the modeled Reynolds stress using the eddy viscosity profile and the SPIV mean velocity gradient (dashed lines) for (a) the spatio-temporal averaged, and (b) the spanwise varying components at 4 different k_z values. In subplot (b), the blue, red, yellow, and purple lines correspond to $k_z = p \cdot k_{z0}$ with $p = 1, 2, 3, 4$, respectively.

Different from previous studies, where the eddy viscosity is included in all 3 momentum equations, in this study, we only include the eddy viscosity in the x momentum equation for the following reasons. First, the original Reynolds-Tiederman eddy viscosity model was developed only for the $\overline{uv}$ Reynolds stress (Reynolds and Tiederman, 1967), and is demonstrated to agree well with the $\overline{uv}$ Reynolds stress in previous computational studies (Fan et al., 2024; Hou et al., 2006), with experimental results in Figure 3.3, while little evidence showing the success of utilizing it for

the other Reynolds stress components exist. Secondly, the $\overline{uw}$ and $\overline{vw}$ components are significantly smaller in magnitude than $\overline{uv}$; therefore, it is justifiable to neglect those in the eddy viscosity enhancement of the resolvent. Finally, previous studies utilizing eddy viscosity enhanced resolvent all focused on convecting modes, where the wavespeeds $c = \omega/k_x$ are non-zero. These modes are characterized by a strong critical layer mechanism within the boundary layer (McKeon, 2017), while the stationary modes studied here do not. Including the eddy viscosity in all three momentum equations as the previous studies results in an overly viscous boundary layer compared to the free stream. As a result, only the viscous operator $\frac{\Delta_k}{Re}$ in the x momentum equation is replaced by:

$$\frac{\nu_T \Delta_k^2}{Re} + \frac{1}{Re}\frac{d\nu_T}{dy}\frac{d}{dy}, \tag{3.5}$$

to include the eddy viscosity while the y and z momentum equations are unchanged.

3.3.2 Enhancing the Resolvent with Boundary Geometry Modeling

As previously introduced in section 2.3.2, the spanwise periodic 2D resolvent with volume penalization is a useful method to encode boundary geometry into the resolvent framework. However, different from previous work such as Chavarin and Luhar (2020) or Rosenberg and McKeon (2019a) where a spanwise varying mean profile $\overline{\overline{\boldsymbol{U}}}(y,z)$ is used to construct the 2D resolvent, we utilize only the spatio-temporal mean $\overline{U}(y)$ in the resolvent construction, as the spanwise varying component is the target of our modeling effort. In addition, with the eddy viscosity demonstrated to be a suitable model for the modes of interest in the previous section, we retain the eddy viscosity model as previously described.

A crude model for the boundary geometry is employed by modeling the rough patches of the spanwise varying surface as streamwise aligned riblets. The riblet tips are set to line up with the smooth surface at $y = 0$ and the riblet height set to $0.1\delta_{98}$, which are reasonably representative of the experimental setup. On the other hand, each rough strip is modeled with three streamwise aligned riblets, which is a simplification of the actual geometry by ignoring the streamwise variation of the rough surface and using a spanwise grain size larger than the actual rough surface. The volume penalization coefficient in equation (2.28) is set to 10^{-4} in the solid region. The Fourier transform of $K^{-1}(y,z)$ in the spanwise direction utilizes $M = 28$ in equation (2.29) to obtain a_m, and the resulting distribution of $K^{-1}(y,z)$ is plotted in Figure 3.4. In the figure, the dark regions, with large K^{-1} values represent the solid region, while the white region with $K^{-1} \approx 0$ represents the fluid region. In

the figure, above $y = 0$ where no solid exist, $K^{-1} = 0$, and the original resolvent is recovered. Below $y = 0$, the alternating smooth and rough surface can be observed, with the vertical dashed lines demarcating the transition between. The smooth strips ($z \cdot \delta_{98}/S \in [-0.5, 0.5]$) are represented by a continuous piece of solid, and the rough strips ($z \cdot \delta_{98}/S \in [-1.5, -0.5] \cup [0.5, 1.5]$) represented by alternating solid and fluid regions in the form of square riblets. The transition between solid and fluid regions results in a step change in K^{-1}, causing Gibbs phenomenon in the Fourier representation, observed as the imperfect transitions in Figure 3.4.

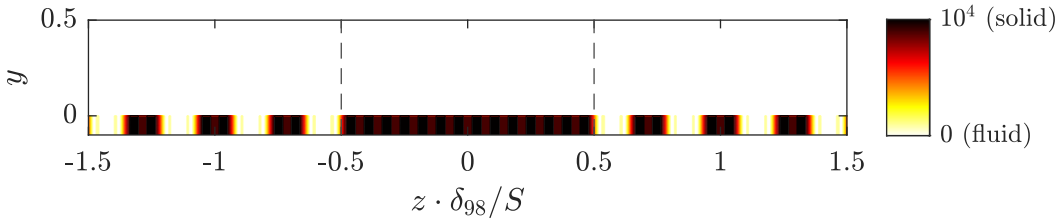

Figure 3.4: Volume penalization coefficient $K^{-1}(y, z)$ in the y-z plane. Area with large values indicate the solid region and small values indicate the fluid region. The vertical dash lines demarcate the transition between rough and smooth strips, with the smooth strip in the middle ($z \in [-0.5, 0.5]$).

It should be noted that the eddy viscosity models the effect of interacting small scales on the large scales being studied, and the 2D resolvent models the interaction between the large scales being studied and the large scales of the boundary geometry affecting another large scale, as demonstrated in sections 2.3. Therefore, the two methods are modeling different types of non-linear interactions, are not conflicting, and can be included together. To the best of the author's knowledge, this is the first study to combine the eddy viscosity with a spanwise varying 2D resolvent analysis.

Similar to Chavarin and Luhar (2020), the 2D resolvent is then discretized using a split domain grid in y, with 30 Chebyshev collocation point below $y = 0$, and a rational transformed 401 point Chebyshev grid above $y = 0$. The values and derivatives at $y = 0$ are matched between the two domains and a no-slip boundary condition is applied to the bottom of the domain at $y = -0.1$. The resolvent operator is then constructed for modes at $k_z = p \cdot k_{z0}$ with $p = 1, 2, \ldots M$, with diagonal blocks being 1D resolvent with the addition of a_0, and off-diagonal blocks including the a_m coefficients. The 2D resolvent matrix is larger than the 1D resolvent and takes a longer time to compute. To reduce computation costs, the matrix sizes are reduced by computing the symmetric (about $z = 0$) and anti-symmetric modes separately,

with the entire computation completed under 1 hour on a desktop machine. Further efficiency improvements can be utilized such as taking advantage of the sparse matrix, using randomized resolvent analysis (Ribeiro et al., 2020) or variational resolvent analysis (Barthel et al., 2022).

3.4 Least Squares Regression Using Resolvent Modes

To determine the non-linear weights in the resolvent $\chi_{p,q}$ used for the construction of $\widetilde{\boldsymbol{U}}(y,z)$ in equation (3.3), a weighted least squares regression is used to obtain the solution that best fits the experimental data. For the HWA data, with a non-uniform measurement grid, the resolvent response modes are first transformed into physical space onto the experimental grid. The resolvent modes are orthonormal to each other with respect to the $L2$ norm: $\int_0^\infty \int_{-\infty}^\infty \cdot \, dzdy$. The integration weights are obtained using a trapezoid rule and used as the least square weights to account for the non-uniform experimental grid. For the SPIV data, with a uniform grid, the experimental results are Fourier transformed in the spanwise direction, and least squares is performed for each spanwise wavenumber k_z in the Fourier space.

In order to select the most suitable combination of N_{k_z} and N_{svd} in equation (3.3), the least squares analysis is performed using different combinations of $N_{k_z} = 1 \sim 8$ and $N_{svd} = 1 \sim 4$ on the streamwise velocities from HWA. The resulting RMS error in $\widetilde{U}(y,z)$ over the $y-z$ plane together with the maximum relative error compared to the HWA measurements are computed and plotted in Figure 3.5 for a portion of the studied cases. The RMS error decreases monotonically as the number of modes increases, since it is minimized by the least squares regression, while the maximum relative error does not necessarily decay monotonically. As N_{k_z} increases, the reduction of RMS error plateaus at $N_{k_z} = 3$, while the maximum relative error shows a minimum point at $N_{k_z} = 4$. On the other hand, as N_{svd} increases, the RMS error decreases but the maximum relative error increases. Using both studies, $N_{k_z} = 4,\ N_{svd} = 2$ is selected to achieve a relatively good balance of both types of error.

A total of five cases are analyzed to study the predictive and data compression capabilities of the resolvent and analyze the improvements provided by the inclusion of the eddy viscosity and the boundary geometry. The standard resolvent modes are used for case 1, the eddy viscosity enhanced resolvent modes are used for cases 2 and 3a/b, and the 2D resolvent with eddy viscosity enhancement for case 4. Cases 1 and 2 use the HWA data which only has streamwise velocity measurements to analyze

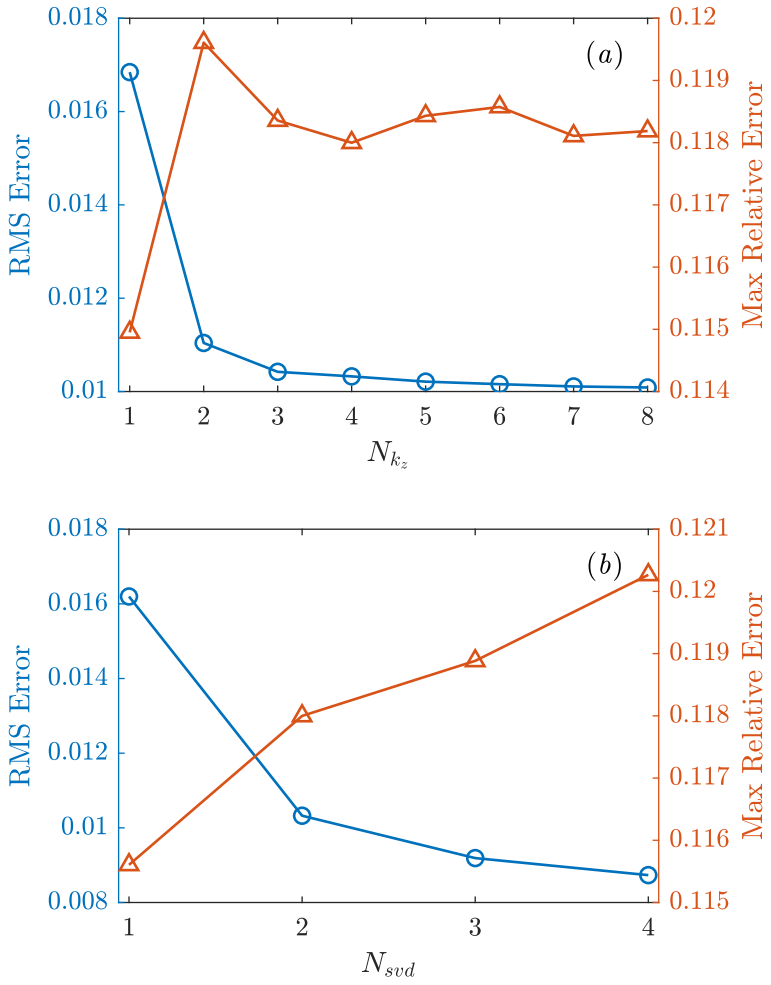

Figure 3.5: RMS error (blue circles) and maximum relative error (red triangles) in the streamwise direction compared to the HWA measurements using (*a*) $N_{svd} = 2$ with $N_{k_z} = 1 \sim 8$ and (*b*) $N_{k_z} = 4$ with $N_{svd} = 1 \sim 4$.

the predictive capability of the wall-normal and spanwise velocity components and cases 3a/b, 4 use the PIV data with all 3 velocity components to study the data compression capability. The four cases are summarized in table 3.1.

Table 3.1: Summary of the five studied cases.

Case	Resolvent Formulation	N_{k_z}	N_{svd}	Input data
1	Standard	4	2	HWA $\widetilde{U}(y,z)$
2	Eddy Viscosity	4	2	
3a	Eddy Viscosity	4	2	SPIV $\widetilde{U},\widetilde{V},\widetilde{W}$
3b	Eddy Viscosity	10	8	
4	2D with Eddy Viscosity	–	40	

3.4.1 Standard Resolvent Approximating the Counter Rotating Rolls

We start by utilizing the standard resolvent modes and only the streamwise velocity measurements from HWA to explore the predictive capabilities of the resolvent analysis. The resolvent reconstructed velocities are plotted in Figure 3.6(a), with the streamwise velocity as a contour plot and the wall-normal and spanwise velocities as overlaying vector plots. Figure 3.6(b) shows the difference between the resolvent reconstructed streamwise velocity and that from the HWA: $\overline{\overline{U}}_{res}(y,z) - \overline{\overline{U}}_{HWA}(y,z)$ and Figure 3.6(c) shows the relative error: $\left[\overline{\overline{U}}_{res} - \overline{\overline{U}}_{HWA}\right] / \overline{\overline{U}}_{HWA}$, where ±2% relative errors are highlighted with black dashed contour lines, and ±5% relative errors with black solid contour lines. From the error plots, it is clear that the resolvent modes can faithfully represent the streamwise velocity field with less than 2% error in the majority parts of the flow field, with the exception of larger errors located mainly in regions close to the wall. This is expected, as the oversimplified smooth wall resolvent analysis employed here does not use the correct boundary conditions at the wall. In addition, for the near wall region where the effect of the roughness is expected to be the strongest, the experiments do not offer enough data points to ensure the analytical spatial-temporal mean $\overline{U}(y)$ used for constructing the resolvent is a good representation of the near wall region. The resulting streamwise velocity field has an RMS error of 0.0103, a maximum difference of 0.0544, and a maximum relative error of 11.8%.

The wall-normal and spanwise velocities $\widetilde{V}(y,z)$ and $\widetilde{W}(y,z)$ plotted in Figure 3.6(a) are predicted from the streamwise velocity measurements using resolvent modes. Compared with the SPIV results shown in Figure 3.1, the location, shape, and direction of the counter-rotating rolls match with the SPIV results fairly well. However, the $\widetilde{V}, \widetilde{W}$ velocities are roughly 2 orders of magnitude smaller than the experimental results, highlighted by the 0.02% U_∞ arrow size legend in Figure 3.6(a) instead of the 2% U_∞ arrow size legend in Figure 3.1. This is a known issue observed in Moarref et al. (2014) that the standard resolvent over-predicts the $\overline{uu}$ spectrum and under-predicts the $\overline{vv}$ and $\overline{uv}$ spectra.

3.4.2 Improving Predictions with Eddy Viscosity

In order to improve the under-predicted $\widetilde{V}$ and $\widetilde{W}$ magnitudes, the resolvent modes generated with the eddy viscosity are used in case 2. The least squares regression is performed in the same manner as case 1 on the streamwise data from HWA, and the reconstructed results are plotted in Figure 3.6(d). The streamwise velocity difference and relative errors are plotted in Figure 3.6(e-f), with very similar behaviors

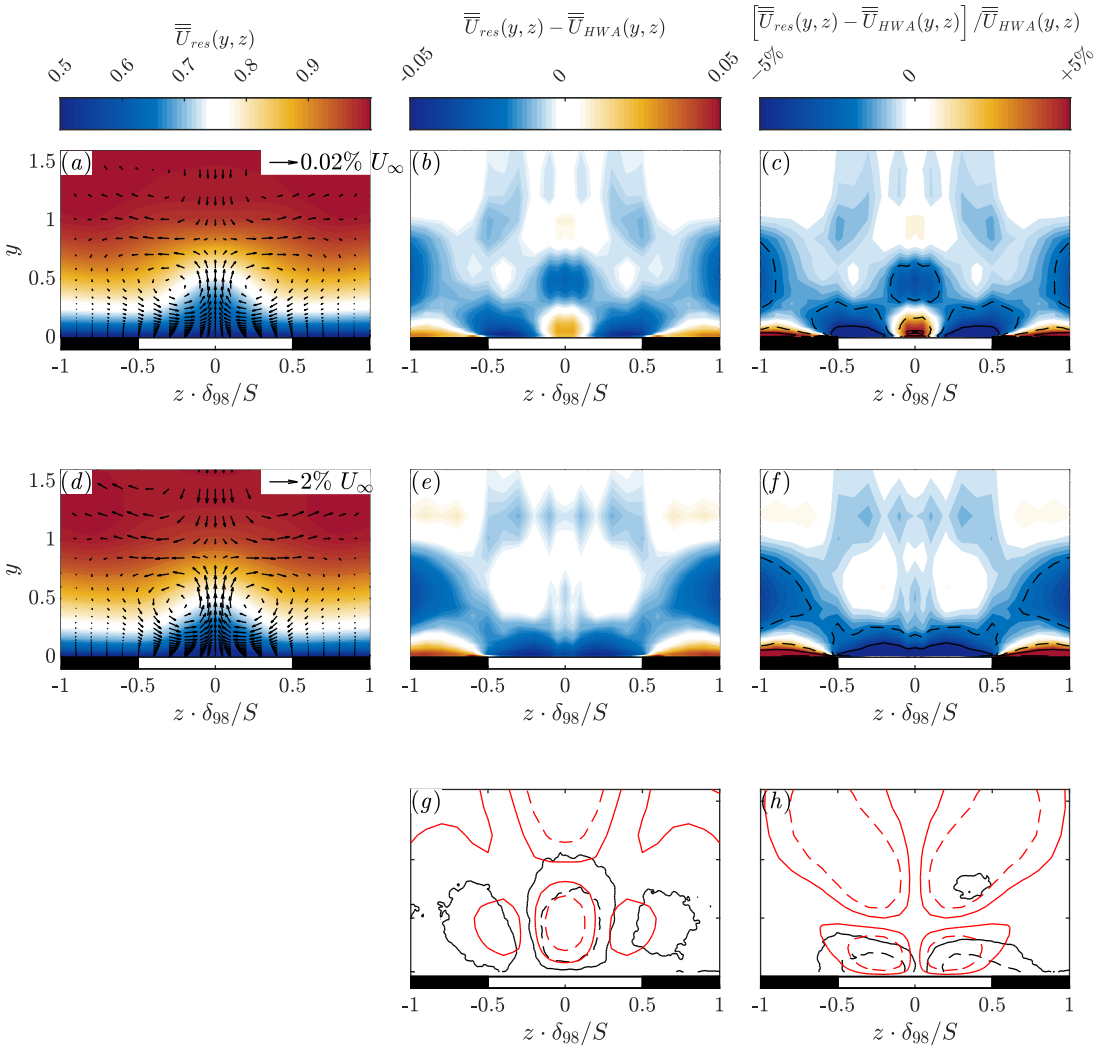

Figure 3.6: Resolvent reconstructed temporal mean profile $\overline{\overline{\boldsymbol{U}}}(y,z)$ and associated errors compared to the experimental data for case 1 (*a-c*) and case 2 (*d-h*). Subplots in the first column (*a, d*) are the resolvent reconstructed temporal mean profile, with the streamwise component $\overline{\overline{U}}(y,z)$ plotted as a contour plot sharing the legend on top. $\widetilde{V}(y,z)$ and $\widetilde{W}(y,z)$ components are plotted as quiver plots on top of the contour plots. Filled contour plots in the second column (*b, e*) are the differences in the streamwise component between the resolvent and the HWA data: $\overline{\overline{U}}_{res} - \overline{\overline{U}}_{HWA}$, with a common legend on top. Filled contour plots in the third column (*c, f*) are the relative differences in the streamwise component, with a common legend on top. The dashed contour lines mark the 2% relative error, and solid lines mark the 5% error. The contour line plot (*g*) is a comparison between the resolvent reconstruction (red contour lines) and the SPIV data (black contour lines) of $\widetilde{V}(y,z)$. Solid contour lines are for ±0.2 of the maximum value of each dataset and dashed contour lines are for ±0.5. Subplot (*h*) is for $\widetilde{W}(y,z)$, with the same format as subplot (*g*).

compared to case 1. The resulting streamwise velocity field has an RMS error of 0.0117, a maximum difference of 0.0568, and a maximum relative error of 17.1%, which are almost the same, but slightly worse than the results from case 1.

However, for the $\widetilde{V}$ and $\widetilde{W}$ velocity components, case 2 maintains the mostly correct location, shape, and direction predictions of the counter-rotating rolls from the previous case, while improving the magnitude predictions. The $\widetilde{V}(y,z)$ and $\widetilde{W}(y,z)$ predictions are now on the same order of magnitude as the experimental results. The experimental and resolvent predicted $\widetilde{V}(y,z)$ have maximum amplitudes of 0.0205 and 0.0171 respectively, showing good agreement. On the other hand, the experimental and resolvent predicted $\widetilde{W}(y,z)$ have maximum amplitudes of 0.0332 and 0.0098, and, although still being under-predicted, are nevertheless an improvement from the previous case without eddy viscosity.

To quantitatively compare the $\widetilde{V}(y,z)$ distributions, contour lines for $\widetilde{V}(y,z)$ are plotted with the experiments in black, and the resolvent predictions in red for comparison in Figure 3.6(g). The solid lines are contour levels of ± 0.2 of the maximum amplitude of each dataset, and the dashed lines are for contour levels of ± 0.5. The $\widetilde{V}$ distribution reasonably agrees between the experimental measurements and the resolvent predictions, roughly matching the location of the upwards motion in the middle and the downwards motion near the transition region. However, near the edge of the boundary layer ($y \approx 1$), the resolvent predicted a non-negligible downward motion which is not observed in the experimental results. For $\widetilde{W}(y,z)$, Figure 3.6(f) is plotted in the same format. A strong $\widetilde{W}$ component is observed near the wall in the experimental results, which is generated through the imbalance of wall shear stress generation of the rough patches and the smooth patches (Wangsawijaya et al., 2020). This uncaptured physics is most likely the reason behind the near wall peak in $\widetilde{W}$ not being captured accurately by the resolvent modes and the under-prediction of the maximum amplitude of $\widetilde{W}$, which is located near the wall in the experimental results.

3.4.3 Reduced Order Modeling Using Resolvent with Eddy Viscosity

Next, in cases 3a/b, the reduced order modeling ability of the resolvent with eddy viscosity is explored. The least squares regression is now performed using all three velocity components from the SPIV measurements. The RMS values for $\widetilde{U}(y,z)$, $\widetilde{V}(y,z)$, $\widetilde{W}(y,z)$ are 0.028, 0.0045, 0.0054 from the SPIV measurements. Therefore, to account for the lower magnitude of $\widetilde{V}$ and $\widetilde{W}$, they are given weights of 5 in the

least squares regression, so that all three velocity components are optimized roughly evenly. In addition, due to the slight asymmetry across $z = 0$ for the SPIV data, $\chi_{p,q}$ retains the complex form in equation (3.3), with small imaginary parts (from components asymmetric about $z = 0$) relative to the real parts (from components symmetric about $z = 0$). Case 3a uses $N_{k_z} = 4$ and $N_{svd} = 2$, the same as cases 1 and 2, while case 3b uses $N_{k_z} = 10$ and $N_{svd} = 8$. For case 3a, the total degrees of freedom is reduced to eight complex mode weights from the SPIV measurement grid of 144×209 with three velocity components, which equates to 0.018% of the original degree of freedom. For case 3b, the reduced degree of freedom equates 0.18% of the original experimental results. The results are plotted in Figure 3.7 using the same formats as Figure 3.6, with case 3a plotted in (*a-e*) and case 3b in (*f-j*).

For case 3a, the error in the streamwise direction increased slightly compared with cases 1 and 2, due to the least squares optimizing for $\widetilde{V}$ and $\widetilde{W}$ as well. However, the relative error remains around 2% for the majority parts of the flow except for the near wall region. On the other hand, improvements in the $\widetilde{V}$ distributions can be observed for case 3a, with the location of the up and downwards motions matching better with the experimental results. Furthermore, the large downward motion located near $y = 1$ observed in case 2 is reduced, matching better with the experimental observations. For $\widetilde{W}$, with the near wall peaks not being captured by the resolvent modes, the improvements in the distribution are relatively minimal.

For case 3b, with a 10 times increase in the number of resolvent modes used, improvements are observed for all three velocity components. The $\widetilde{U}$ error is further reduced, with a RMS error of 0.0114, a maximum difference of 0.0613, and a maximum relative error of 12.4%. The distribution of $\widetilde{V}$ and $\widetilde{W}$ are improved as well, matching the experimental results quite well. However, it should be pointed out that the $\widetilde{V}$ and $\widetilde{W}$ amplitudes are still under-predicted, with values of 0.0137 and 0.0106, compared to the experimental values of 0.0205 and 0.0332.

Finally, it should be pointed out that with more data utilized in case 3a and 3b (more grid points in the SPIV and all three velocity components), the risk of rank deficiency (difficulties in distinguishing multiple resolvent modes on the experimental grid) is less than in cases 1 and 2 where the HWA data is used, allowing for case 3b with $N_{k_z} = 10$ and $N_{svd} = 8$ to be explored. However, the grid used to generate the resolvent modes is much finer than both experimental results, and N_{k_z}, N_{svd} cannot be indefinitely increased without running into issues with rank deficiency in the

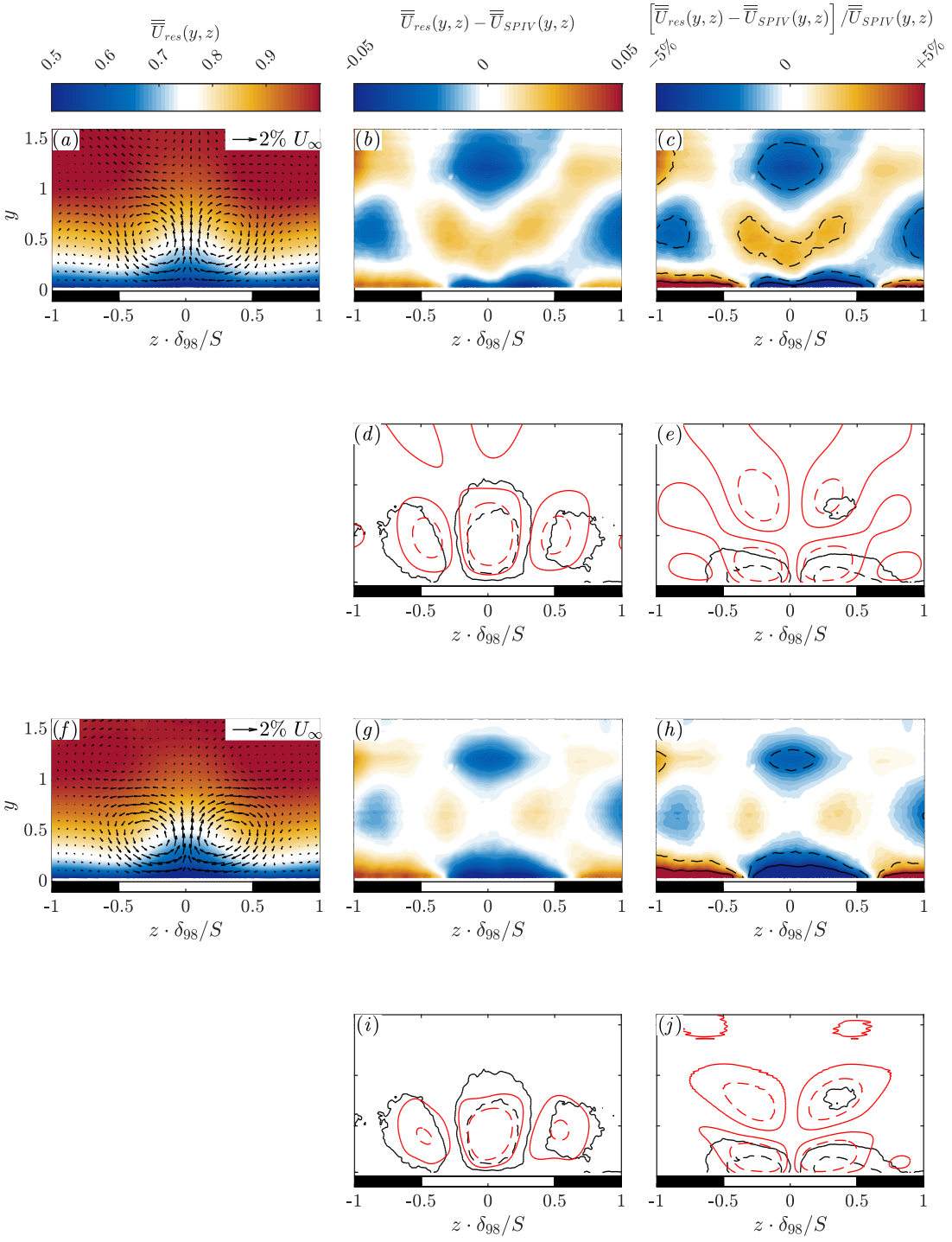

Figure 3.7: Resolvent reconstructed temporal mean profile $\overline{\overline{\boldsymbol{U}}}(y,z)$ and associated errors compared to the experimental SPIV data for case 3a (*a-e*) and case 3b (*f-j*), with the same format as Figure 3.6.

least squares regression.

3.4.4 Reduced Order Modeling Using 2D Resolvent

Finally, in case 4, the reduced order modeling ability of the 2D resolvent with eddy viscosity and boundary geometry modeling is studied. For the 2D resolvent, each resolvent mode consists of multiple spanwise wavenumbers. The modes are therefore inverse Fourier transformed in the spanwise direction and the least squares regression is performed using all three velocity components from the SPIV measurements on the measurement grid in physical space. The same as in case 3a/b, $\widetilde{V}$ and $\widetilde{W}$ are given weights of 5 in the least squares regression. Different from previous cases, the number of Fourier modes N_{k_z} is now set by the 2D resolvent formulation, and the total number of modes used for the least squares regression is controlled by $N_{svd} = 40$ alone. Using 40 symmetric (about $z = 0$) and 40 anit-symmetric (about $z = 0$) modes, the total degree of freedom is 80, which is 0.089% of the original SPIV degree of freedom. The resulting resolvent reconstruction with the associated comparisons and errors are plotted in Figure 3.8.

In the streamwise difference and relative error plots of Figure 3.8(b, c), it can be observed that the difference is reduced compared to previous cases, with a RMS error of 0.0089, and a maximum relative error of 6.7%. But more importantly, the wall-normal and spanwise components $\widetilde{V}(y, z)$ and $\widetilde{W}(y, z)$ see a big improvement, not only improving the location and distribution as seen in Figure 3.8(d, e), but also the magnitude of the reconstructed velocities as evident from Figure 3.8(f-k). $\widetilde{V}(y, z)$ now has relatively small differences throughout the domain, and $\widetilde{W}(y, z)$ has small differences except near the wall, where improvements from previous cases can be observed, but still with relatively large differences.

3.5 Discussion

The results showcased the ability to use the resolvent analysis to predict the wall-normal and spanwise temporal mean velocity components from just the streamwise temporal mean measurements. The resolvent modes used for the predictions are generated without directly encoding the rough wall boundary conditions, yet the predictions (cases 1 and 2) are in good agreement with the experiments, especially when the eddy viscosity is included. However, it should be noted that although the resolvent modes do not contain information on the spanwise varying structure of the rough wall, that information is partially encoded into the streamwise temporal mean $\widetilde{U}(y, z)$, which is a direct result of the spanwise varying surface geometry.

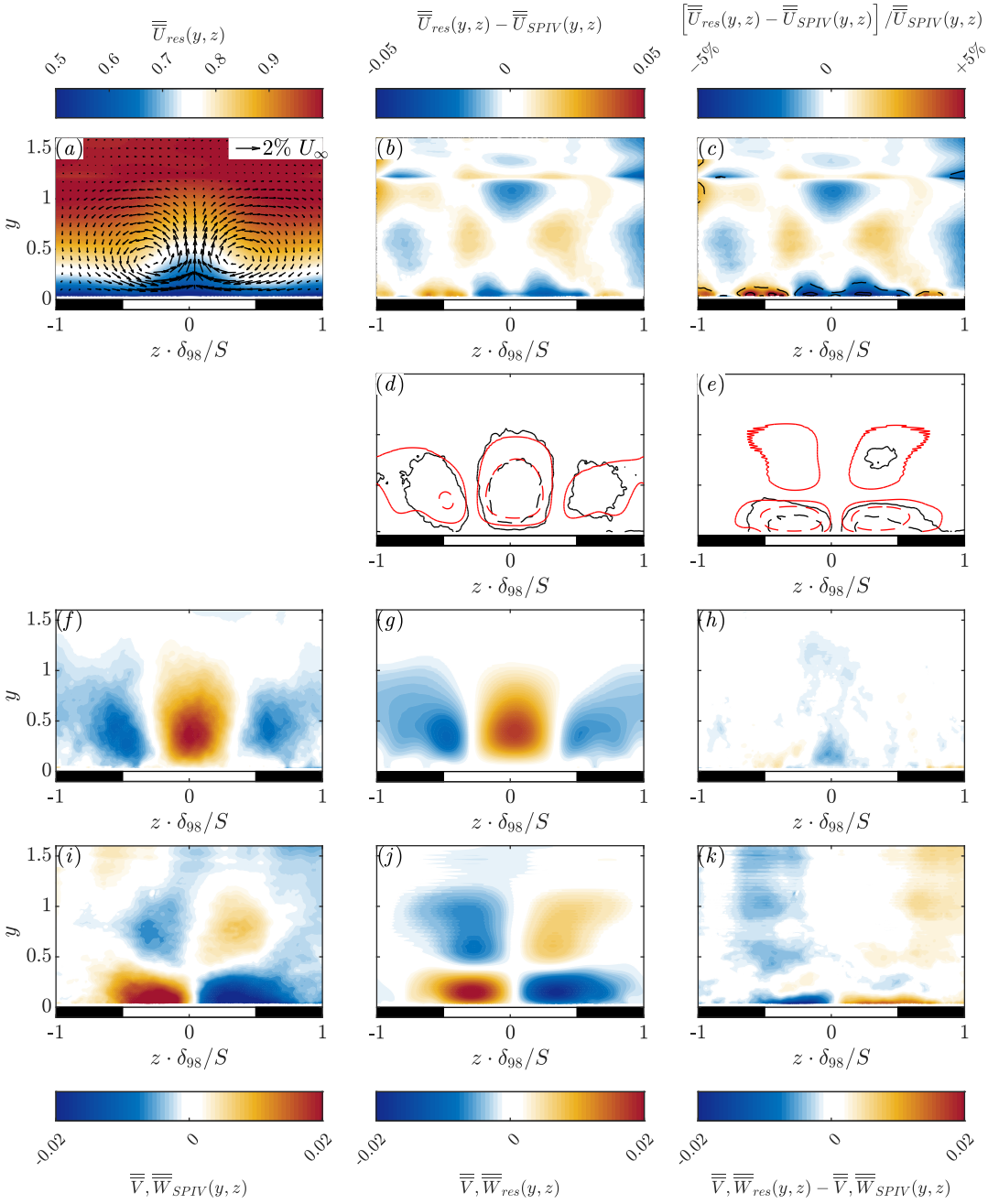

Figure 3.8: Resolvent reconstructed temporal mean profile $\overline{\overline{\boldsymbol{U}}}(y,z)$ and associated errors compared to the experimental SPIV data for case 4, using the 2D resolvent with eddy viscosity. Subplots (b, c) are the difference and relative errors in the streamwise direction in the same format as Figure 3.6(b, c). Subplots (d, e) are contour line comparisons for $\widetilde{V}(y,z)$ and $\widetilde{W}(y,z)$ in the same format as Figure 3.6(g, h). For subplot (f-k), the three columns are SPIV measurement, resolvent reconstruction, and the difference, each column sharing the colorbar at the bottom, with the third row (f-h) for $\widetilde{V}(y,z)$ and the fourth row (i-k) for $\widetilde{W}(y,z)$.

Therefore, the least squares regression, which uses $\widetilde{U}(y,z)$, encodes information about the surface geometry into the resolvent predictions, which contributes to the success of predicting the counter-rotating rolls observed in the experiments.

However, for cases 1-3, a portion of the near-wall physics is not included in the resolvent model using a smooth wall boundary condition, resulting in relatively big differences located near the wall. First of all, the near wall portion of the spatio-temporal mean profile $\overline{U}(y)$ used to construct the resolvent operator is extrapolated from the experimental measurements in the log region using an analytical profile. Therefore, the near wall behavior of $\overline{U}(y)$ cannot be verified and might be missing important physics such as the virtual origin induced by the rough wall geometry. More importantly, it has been proposed that the counter-rotating rolls are the result of an imbalance of shear stress generated between the rough and smooth patches, where turbulence is transferred from high-stress areas to low-stress areas, inducing the observed flow pattern (Wangsawijaya et al., 2020). This imbalance of stress is not included in the resolvent modeling with a smooth wall boundary condition and is likely the culprit behind the under-prediction of the spanwise velocities near the wall as observed in Figure 3.7(*e, j*).

When including just a crude model for the boundary geometry in case 4 using the 2D resolvent, an improvement was observed in Figure 3.8, with better agreeing $\widetilde{V}(y,z)$ and $\widetilde{W}(y,z)$ magnitudes and improved agreement in all 3 velocity components near the wall. This again showcases the importance of the wall geometry and the resulting non-linear coupling in this problem being studied. However, the imbalanced shear stress is still not included in the current study, and could be the cause of the slightly under-predicted $\widetilde{W}(y,z)$ near the wall in case 4.

3.6 Conclusion and Future Directions

In this chapter, the predictive and data compression capabilities of the resolvent framework without utilizing detailed knowledge of the surface geometry are studied using experimental data with spanwise varying rough surfaces. The standard resolvent modes are able to approximate the location, shape, and direction of the counter-rotating rolls, while under-predicting the magnitude. The addition of an eddy viscosity into the resolvent framework improved the amplitude predictions and is able to generate modes that can efficiently represent all three velocity components from the experiments with a reduction in degree of freedom to 0.018% and 0.18% of the original experimental results. The 2D resolvent with eddy viscosity, which

includes a crude model of the surface geometry, is able to further improve the effectiveness of the resolvent modes especially near the wall, and is able to represent all three velocity components with relatively small differences using only 0.089% of the original degree of freedom. For the large scale structures being studied, the inexpensive linear resolvent analysis performed well in both modeling the structure and being used as basis functions for data compression, especially when including an eddy viscosity to model the non-linear Reynolds stress and with the inclusion of a crude boundary geometry model.

It should be emphasized again, that the goal of this chapter is to utilize knowledge of the spatio-temporal mean $\overline{\boldsymbol{U}}(y)$ to obtain information about the spanwise variations of the temporal mean $\widetilde{\boldsymbol{U}}(y,z)$. Both $\overline{\boldsymbol{U}}(y)$ and the modeling target of this study $\widetilde{\boldsymbol{U}}(y,z)$ are required in 2D resolvent studies that utilize the temporal mean $\overline{\overline{\boldsymbol{U}}}(y,z) = \overline{\boldsymbol{U}}(y) + \widetilde{\boldsymbol{U}}(y,z)$ to study the turbulent perturbations $\boldsymbol{u'}(x,y,z,t)$, for example Chavarin and Luhar, 2020. The results from this study can also be utilized in future 2D resolvent studies, especially for 2D/3C type studies (Gayme et al., 2011), to extend experimental data closer to the wall, alleviating the difficulties in obtaining accurate experimental data close to the wall.

For future studies, one improvement that can be applied to the current study is a better eddy viscosity profile. The profile currently in use, although continuous, has a discontinuous first derivative, which causes Gibbs oscillation when differentiating spectrally with the Chebshev differentiation matrices. An eddy viscosity profile that blends the two profiles together more smoothly, giving a continuous first derivative, can alleviate this issue.

Further studies on the effect of the boundary geometry model in the case of the 2D resolvent are also important. The height of the riblets, the number of riblets and the shape of the riblets can all be modified to better match the experimental setup, such as using triangular riblets of smaller spanwise sizes. The effect on the performance of the resulting resolvent modes is of great interest, and could potentially provide more physical insight into the effect of different roughness geometries on the flow.

Finally, it will also be valuable to explore methods that allow for encoding the spanwise variation of the wall shear stress, which is the proposed mechanism that generates the flow structure of interest (Wangsawijaya et al., 2020), into the 2D resolvent. This could further improve the near-wall performance of the method, and provide more evidence for the proposed theory.

Chapter 4

DIRECT NUMERICAL SIMULATION OF A TURBULENT CHANNEL

This chapter describes the Direct Numerical Simulation (DNS)[1] of a turbulent channel flow, including the data acquisition and the preliminary signal analyses that laid the groundwork for the subsequent analyses of the non-linear interactions in Chapters 5 and 6. We start with an overview of the simulation algorithm and parameters, with verification of the statistics against previous studies. Next, the temporal filter, which is necessary to prevent aliasing in the non-linear forcing is introduced, followed by a description of the temporal Fourier analysis using the Welch method with proper corrections for the effect of the window function. Finally, we end this chapter with a verification of the temporal Fourier analysis.

4.1 Simulation Overview

The simulation is carried out using a modified DNS code of Flores and Jiménez (2006). The channel geometry is plotted in Figure 2.1(a), with a channel half height of h, a domain size of $4\pi h \times 2\pi h$, and a friction Reynolds number $Re_\tau = u_\tau h/\nu$ of approximately 551. The code uses a spectral discretization in the streamwise (x) and spanwise (z) directions, with the non-linear terms computed in the physical space with 2/3 dealiasing, and a compact finite differences scheme in the wall-normal direction (y). Quantities normalized with inner-units, using the viscous length scale $\delta_\nu = \nu/u_\tau$ and friction velocity u_τ are indicated with superscripts '+'. Otherwise, normalization is performed with channel center-line velocity U_{cl} and channel half-height h. The simulation parameters are similar to previous studies and are compared to studies of Lee and Moser (2015) and Flores and Jiménez (2006) in table 4.1. Although the simulation box size of $4\pi h \times 2\pi h$ is relatively small, it is a commonly utilized size in previous studies, and is less expensive for computation and data storage. The maximum wavenumbers retained by the DNS are $k_x = \pm 127.5$, $k_z = \pm 255$. The time stepping is performed using a third-order Runge-Kutta scheme with constant step sizes of $\Delta t = 0.00185$, and sampled every 20 time steps with a sampling time of $\Delta t_s = 0.0369$, both normalized by U_{cl} and h. The

[1]The author would like to thank Dr. Simon Toedtli for the valuable guidance provided on the setup of the DNS.

sample rate is selected to capture most of the energetic frequencies while keeping the data size manageable. A total of 6144 DNS snapshots are collected, with a total eddy turnover time of $Tu_\tau/h = 10.78$. Turbulence statistics are in good agreement with previous studies as shown in Figure 4.1 for the spatio-temporal mean profile and in Figure 4.2 for the temporal averaged uu and uv power spectra. All analyses performed on the DNS data set, including the resolvent analysis, utilize identical spatial grids and spatial differentiation schemes as the DNS, while in the temporal domain, a Fourier analysis is utilized instead of time stepping, the implementation of which is discussed later in this chapter.

Table 4.1: Comparison of simulation parameters used by Lee and Moser (2015) (LM15), Flores and Jiménez (2006) (FJ06) and the current study. L_x, L_z are the box size in the streamwise and spanwise directions, with grid spacing in inner scale given by Δx^+ and Δz^+. Δy_w^+ and Δy_c^+ are the wall normal grid spacing at the wall and at the channel centerline, with a total of N_y grid points. Tu_τ/h is the total simulation time.

	Re_τ	L_x/h	L_z/h	Δx^+	Δz^+	Δy_w^+	Δy_c^+	N_y	Tu_τ/h
LM15	544	8π	3π	8.9	5.0	0.019	4.5	384	13.6
FJ06	556	4π	2π	10.2	–	0.8	7.0	–	–
Current Study	551	4π	2π	9.0	4.5	0.69	6.0	272	10.78

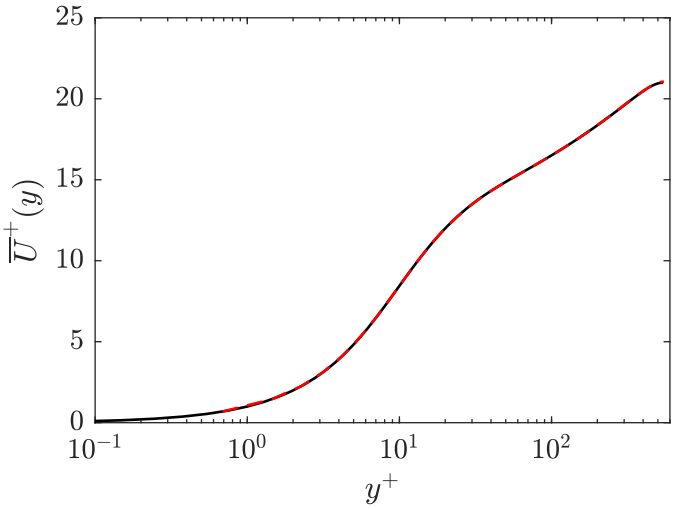

Figure 4.1: Comparison of the spatio-temporal mean in inner scales $\overline{U}^+(y^+)$ between the results of Lee and Moser (2015) (black solid line) and the current DNS study (red dashed line).

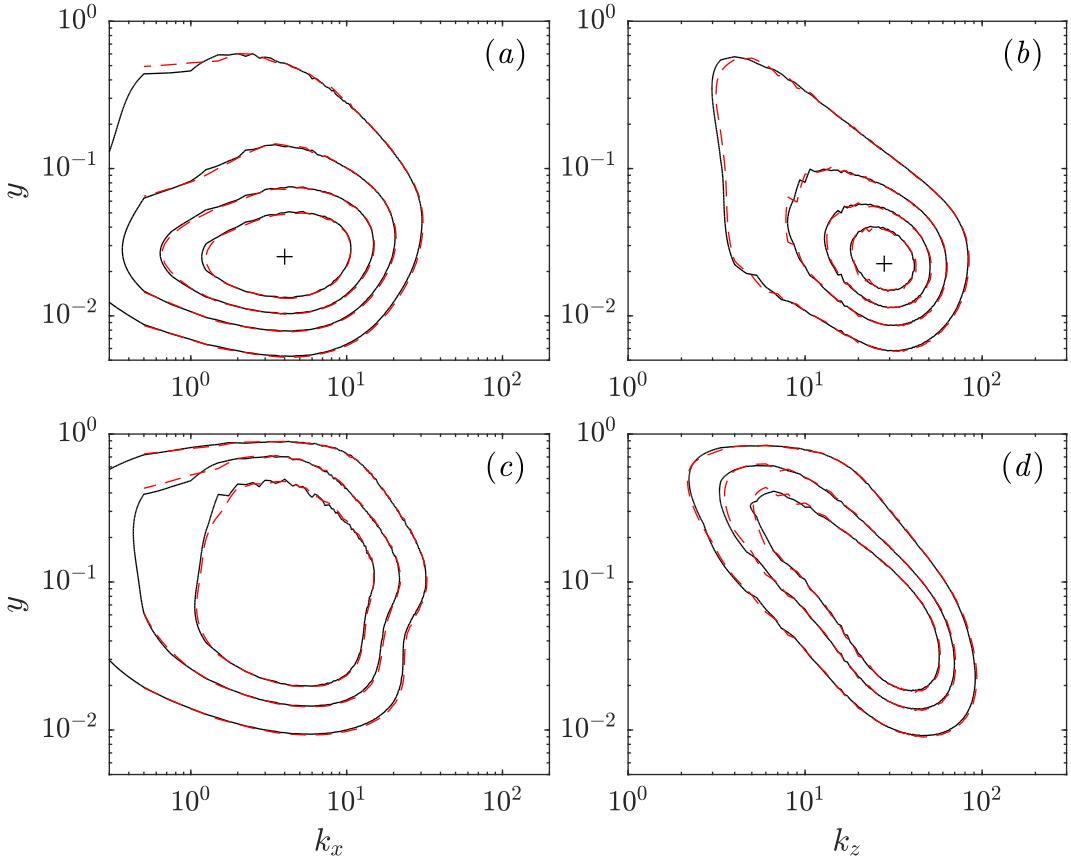

Figure 4.2: Comparison of the temporal averaged pre-multiplied power spectra between the results of Lee and Moser (2015) (black solid lines) and the current DNS study (red dashed lines) in outer scales. The *uu* power spectra is plotted in (*a*) k_x-y plane and (*b*) k_z-y plane. The *uv* power spectra is plotted in (*c*) k_x-y plane and (*d*) k_z-y plane. Contour lines are plotted at the same levels between the results of Lee and Moser (2015) and the current study. The + markers in figure (*a*) located at $k_x = 4$ and in figure (*b*) at $k_z = 28$ mark the peak in the *uu* power spectra, which are the representative wavenumbers for the near wall cycle.

4.2 Temporal Filtering to Remove Temporal Aliasing in the Forcing

Although the selected sampling rate captures most of the energetic frequencies of the velocity fluctuations, it is insufficient to capture all the frequencies of the non-linear forcing, due to the quadratic nature resulting in higher frequencies. To prevent aliasing, a temporal filter is required to limit the frequency content before down sampling during the DNS run.

A low pass filter (LPF) with cutoff frequency f_c is inserted into the DNS before sampling the velocities, and only frequencies in the range of $[-f_R, f_R]$ from the temporal Fourier transform of the sampled data are retained (discussed later in

section 4.3). The resolved frequency range is required to be smaller than the cutoff frequencies $f_R \leq f_c$, and additional requirements come from consideration of the quadratic forcing terms. Assuming a LPF with infinite roll-off at f_c, the non-linear forcing will have its highest frequency at $2f_c$ aliasing to $2f_c - 2f_{s,NQ}$, which should remain outside of the resolved zone:

$$2f_c - 2f_{s,NQ} \leq -f_R, \tag{4.1}$$

where $f_{s,NQ} = \frac{1}{2\Delta t_s}$ is the sampling Nyquist frequency. When setting $f_R = f_c$, the 2/3 dealiasing result of $f_R \leq \frac{2}{3} f_{s,NQ}$ is obtained, similar to that used in the spatial dimensions. However, to account for the LPF having a finite roll-off at the cutoff frequency, some buffer is introduced by selecting:

$$f_R = \frac{1}{2} f_{s,NQ}. \tag{4.2}$$

This filter design is guaranteed to remove all aliasing in the forcing under the worst-case scenario. Practically, very little energy content is present for the forcing at the very high frequencies, and the filter criterion could be relaxed slightly to retain more of the higher frequencies, with the trade-off of allowing small amounts of energy at the high frequencies to cause aliasing.

Additionally, no phase distortion of the filtered signal is desired, requiring a linear phase filter, where the filter phase response is a linear function of frequencies. This results in a filtered signal with all frequencies having the same constant time delay compared to the unfiltered signal, or in other words, no phase distortion (see appendix A.2). An order 2000 filter is designed using MATLAB fircls1 function (MATLAB, 2023), with the maximum amplitude deviation set to 10^{-4} for the pass band $[0, f_R]$, and 10^{-3} for the stop band. The resulting filter amplitude and phase are plotted in Figure 4.3, which shows the resolved frequency range with very little amplitude deviation from 1 and a perfectly linear phase response.

To demonstrate the necessity and effect of the filter, two short DNS runs are conducted with the same parameters as the main computation. The first run does not include the LPF, while the second one includes the LPF as described above. The two runs are initialized using the same initial conditions with the time delay induced by the LPF properly corrected, ensuring the two runs are properly aligned in time. The power spectra of the wall-normal velocity and vorticity forcing f_v and f_{ω_y} are computed for both runs and compared in Figures 4.4 and 4.5 at $y = 0.91$ ($y^+ = 500$). f_v and f_{ω_y} are the forcing utilized in the velocity-vorticity resolvent

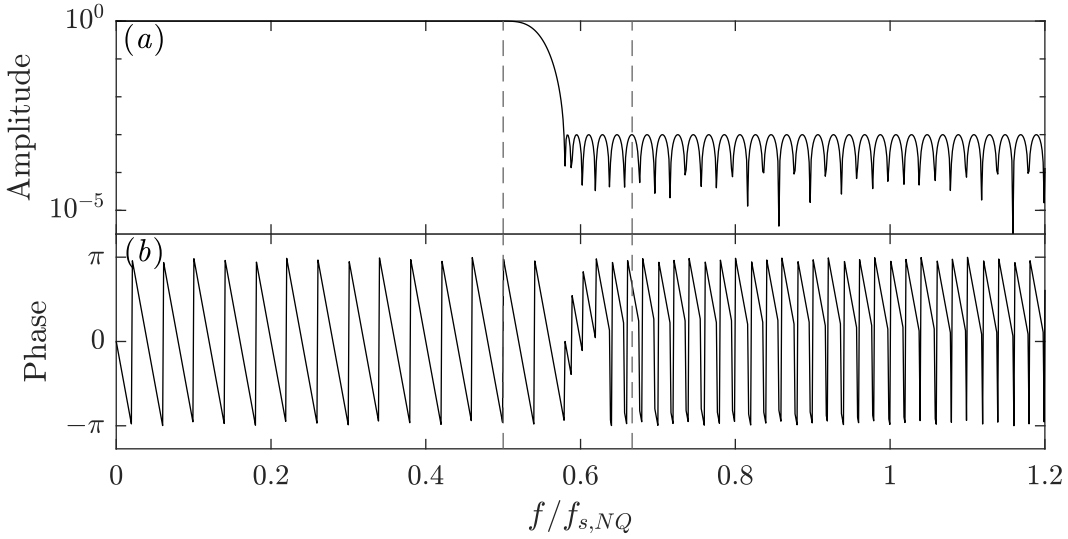

Figure 4.3: (*a*) Amplitude and (*b*) phase for the order 2000 linear-phase low pass filter. The vertical lines correspond to the resolved frequency range $f_R = \frac{1}{2} f_{s,NQ}$, and the largest frequency that does not cause aliasing $\frac{2}{3} f_{s,NQ}$.

formulation introduced in equation (2.8), which is defined as:

$$\begin{bmatrix} f_v \\ f_{\omega_y} \end{bmatrix} = \begin{bmatrix} -ik_x \frac{d}{dy} & -k^2 & -ik_z \frac{d}{dy} \\ ik_z & 0 & -ik_x \end{bmatrix} \boldsymbol{f}(\boldsymbol{k}, y) = \boldsymbol{B}\boldsymbol{f}(\boldsymbol{k}, y). \tag{4.3}$$

The is the solenoidal part of the forcing, which excludes the irrotational part that is not responsible for driving the velocities (see the Helmholtz decomposition discussed in section 2.2.1, Rosenberg and McKeon (2019b), and Morra et al. (2021)).

In Figures 4.4 and 4.5, the black dash lines denote the critical layer, where the wavespeed $c = \omega/k_x$ is equal to the local spatio-temporal means velocity $c = \overline{U}(y)$ (McKeon and Sharma, 2010). The frequencies beyond the sampling Nyquist frequency are aliased to the resolved frequency range, which manifests as the "S" shaped part of the dashed lines in Figures 4.4 and 4.5, due to the log scaled axes. The energy in the forcing can be seen to concentrate around the critical layer consistent with previous studies (Rosenberg, 2018). Starting from $k_x \approx 40$, significant energy content can be observed near the aliased "S" shaped part of the dashed lines in the unfiltered results presented in the first column. This aliased energy content corrupts the results starting from $k_x \approx 40$, showing the necessity of the LPF in the DNS for studying the non-linear forcing. From the power spectra of the filtered run presented in the second column of Figures 4.4 and 4.5, and the difference between the filtered and unfiltered results presented in the third column, it can be observed that the

aliased energy in the forcing is completely removed by the introduction of the LPF, while the non-aliased energy is correctly preserved.

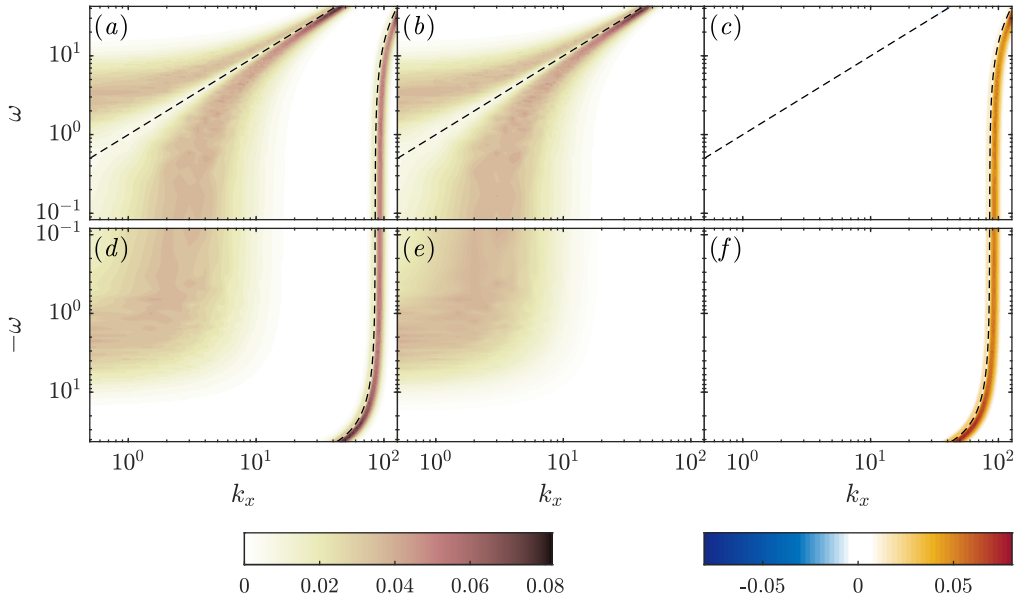

Figure 4.4: The wall normal velocity forcing f_v power spectra in $k_x - \omega$ space at $y = 0.91$ ($y^+ = 500$) for (*a, d*) the unfiltered DNS, and (*b, e*) the filtered DNS. The third column (*c, f*) is the difference between the unfiltered and filtered spectra. The top row (*a-c*) is for positive ω and the bottom row (*d-f*) for negative ω. The black dashed line in all six subplots denote the critical layer $c = \omega/k_x = \overline{U}(y = 0.91)$ with the ω frequencies beyond the sampling Nyquist frequency aliasing into the resolved frequency range, manifesting as the "S" shaped part of the dashed lines.

It is also observed that the aliased energy predominately resides in regions with $k_x \geq 40$ for $y^+ = 500$ as shown in Figures 4.4 and 4.5. Therefore, removing all k_x wavenumbers above a critical value $k_{x,c}$ could potentially be utilized as an alternative method to inserting a LPF into the DNS code. This critical streamwise wavenumber $k_{x,c}$ differs for each wall-normal location, and can be best estimated using the critical layer location: $k_{x,c}(y) = \omega_{s,NQ}/\overline{U}(y)$, where $\omega_{s,NQ}$ is the sampling Nyquist frequency. However, this method will not remove the aliased energy as cleanly as the LPF, and does not guarantee the complete removal of all aliased energy. In cases where rerunning the simulation with a LPF in the code is not feasible, this might serve as an alternative method.

4.3 From Time to Frequency

To perform the spatio-temporal analyses, the time domain DNS data needs to be transformed into the Fourier domain. For this purpose, the Welch method is applied

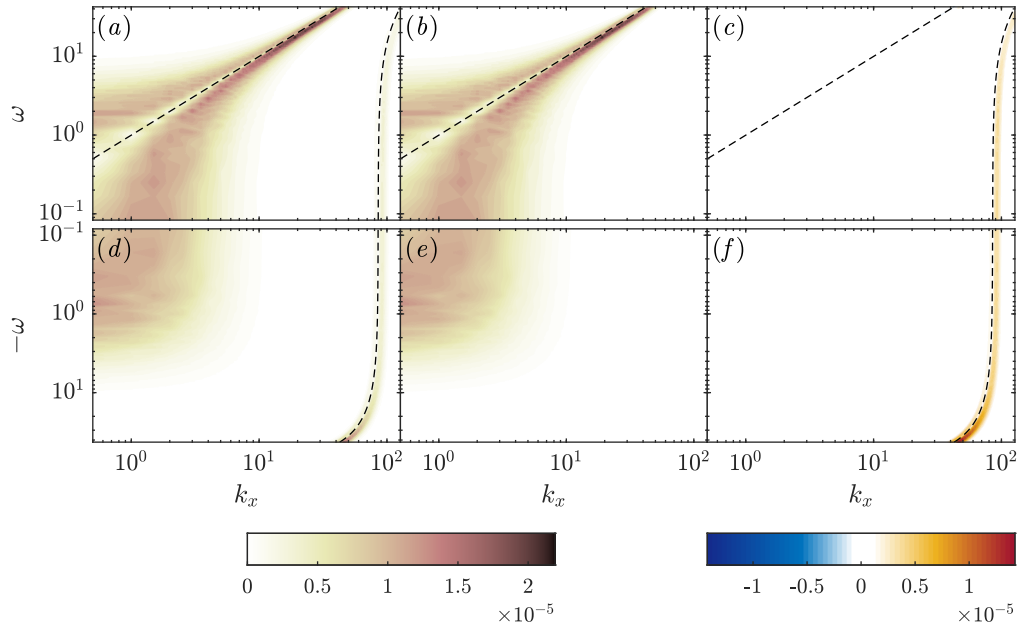

Figure 4.5: The wall normal vorticity forcing f_{ω_y} power spectra in $k_x - \omega$ space at $y = 0.91$ ($y^+ = 500$) in the same format at Figure 4.4.

where the 6,144 DNS snapshots are segmented into 5 segments of 2,048 snapshots each, with 50% overlap. The Hann window function is then applied to each temporal segment before taking the temporal Fourier transform, and the frequencies between $\pm\omega_R = \pm 2\pi f_R = \pm 42.53$ are retained. Finally, the results are averaged across all 5 temporal segments, the validity of which is discussed in appendix A.3 for the quantities of interest in Chapter 5. To analyze the effect of the window function, similar to Nogueira et al. (2021) and Morra et al. (2021), the momentum equation is multiplied by the window function $w(t)$, and the spatial dimensions are temporarily ignored as they do not play a role in this analysis of the temporal window function:

$$w(t)\frac{\partial}{\partial t}\boldsymbol{u}(t) + w(t)\mathcal{L}\boldsymbol{u}(t) = w(t)\boldsymbol{f}(t). \tag{4.4}$$

In this equation, $\mathcal{L}$ is the linear part of the Navier-Stokes operator, and the equation can then be rewritten as:

$$\frac{\partial}{\partial t}\left[w(t)\boldsymbol{u}(t)\right] + \mathcal{L}\left[w(t)\boldsymbol{u}(t)\right] - \boldsymbol{u}(t)\frac{d}{dt}w(t) = \left[w(t)\boldsymbol{f}(t)\right]. \tag{4.5}$$

Performing the Fourier transform in time on the signals with the window function applied: $\boldsymbol{u}(\omega) = \mathcal{F}\left[w(t)\boldsymbol{u}(t)\right], \boldsymbol{f}(\omega) = \mathcal{F}\left[w(t)\boldsymbol{f}(t)\right]$ and defining the spurious forcing: $\boldsymbol{s}(\omega) = \mathcal{F}\left[\boldsymbol{u}(t)\frac{d}{dt}w(t)\right]$, the above equation can be rewritten using the resolvent operator $\mathcal{H}$:

$$\boldsymbol{u}(\omega) = \mathcal{H}\left(\boldsymbol{f}(\omega) + \boldsymbol{s}(\omega)\right), \tag{4.6}$$

which can be reorganized as:

$$\tilde{\boldsymbol{u}}(\omega) = \boldsymbol{u}(\omega) - \mathcal{H}\boldsymbol{s}(\omega) = \mathcal{H}\boldsymbol{f}(\omega). \tag{4.7}$$

$\tilde{\boldsymbol{u}}(\omega)$ are the velocity Fourier modes corrected for the spurious forcing due to the window function, which satisfies the input-output form of the resolvent analysis introduced in equation (2.5).

Additionally, the forcing Fourier modes, $\boldsymbol{f}(\omega) = \mathcal{F}\left[w(t)\boldsymbol{f}(t)\right]$, can be computed in two equivalent ways:

$$\boldsymbol{f}(\omega) = \mathcal{F}\left[w(t)\boldsymbol{u}(t)\cdot\nabla\boldsymbol{u}(t)\right] = \mathcal{F}\left[\sqrt{w(t)}\boldsymbol{u}(t)\right] * \mathcal{F}\left[\sqrt{w(t)}\nabla\boldsymbol{u}(t)\right], \tag{4.8}$$

where $*$ denotes the convolution operator. The first method computes $\boldsymbol{f}(t)$ in physical time, then applies the window function and takes the Fourier transform, while the second method computes $\boldsymbol{f}(\omega)$ in the Fourier space through a convolution. Note that to ensure the equivalence between the two methods, the second method requires the use of the $\sqrt{w(t)}$ as the window function applied to the velocity and velocity gradients.

The N-point periodic Hann window function is utilized in the analyses, where $N = 2048$ is the length of each temporal segment. In discrete space, $n = 0, \ldots, N-1$, and the window function, its time derivative, and its square root are written as:

$$w[n] = \sin^2\left(\frac{\pi n}{N}\right), \tag{4.9}$$

$$w'[n] = \frac{2\pi}{N\Delta t_s}\sin\left(\frac{\pi n}{N}\right)\cos\left(\frac{\pi n}{N}\right), \tag{4.10}$$

$$\sqrt{w[n]} = \sin\left(\frac{\pi n}{N}\right). \tag{4.11}$$

The window function and Fourier transform are applied to the streamwise velocity modes to compute the streamwise power spectra $\phi_{uu}(c, y; k_x)$, plotted as a function of k_x, y, and the wavespeed $c = \omega/k_x$ for two representative large scales: $k_x = 0.5, 1$ in Figure 4.6(a) and (b), and a representative small scale at $k_x = 30$ in Figure 4.6(c). The black dashed lines in each subplot show the streamwise mean velocity profile, $\overline{U}(y)$. It can be observed that the energy contained in the large scales is distributed in y, extending almost throughout the entire channel height, and predominantly located at high wavespeeds. On the other hand, the small scales (large k_x) have most of the energy located at smaller wavespeeds and have an energy distribution that is mostly localized near the wall and in a y range that is centered around the local mean velocity.

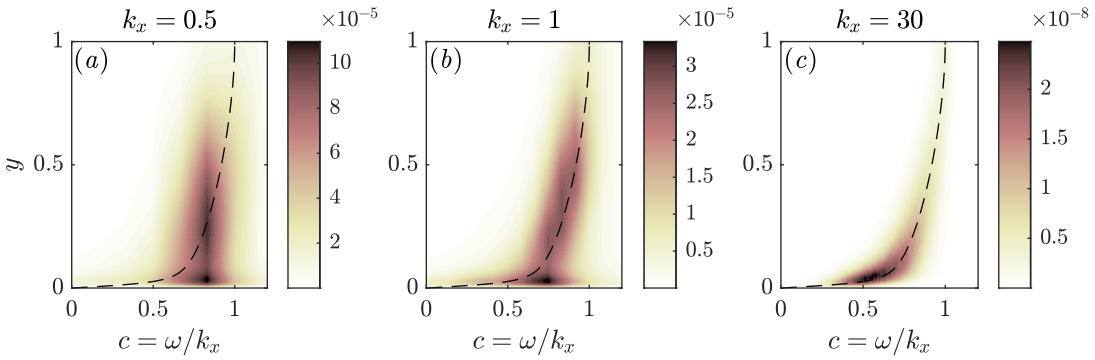

Figure 4.6: Contour plots of streamwise power spectra as a function of k_x, y, and the wavespeed $c = \omega/k_x$. Figures (*a, b*) are the large scales with $k_x = 0.5, 1$, and (*c*) is a small scale with $k_x = 30$. The black dash lines are the spatio-temporal averaged streamwise velocity profile $\overline{U}(y)$ and are also marking the critical layer locations.

4.4 Verification of Temporal Fourier Analysis

Finally, for verification of the temporal Fourier analysis, the following two quantities are computed utilizing the Welch method and the Hann window function described in section 4.3 for all wavenumber-frequency triplets $\boldsymbol{k}$:

$$V(\boldsymbol{k}) = \mathbb{E}\left\{\langle \tilde{\boldsymbol{u}}(\boldsymbol{k}, y),\ \mathcal{H}(\boldsymbol{k}, y)\boldsymbol{f}(\boldsymbol{k}, y)\rangle_y\right\}, \tag{4.12}$$

$$E_u(\boldsymbol{k}) = \mathbb{E}\left\{\langle \tilde{\boldsymbol{u}}(\boldsymbol{k}, y),\ \tilde{\boldsymbol{u}}(\boldsymbol{k}, y)\rangle_y\right\}, \tag{4.13}$$

where $\mathbb{E}\{\cdot\}$ is the expected value operator, indicating an average over all temporal segments. $E_u(\boldsymbol{k})$ is defined as the spectral turbulent kinetic energy of $\tilde{\boldsymbol{u}}(\boldsymbol{k})$ at a given wavenumber-frequency triplet $\boldsymbol{k}$ and the weighted inner product $\langle a(y),\ b(y)\rangle_y$ is defined as the integral over a certain y range in the continuous domain and approximated in the discrete space using a weight matrix W with the appropriate integration coefficients on the diagonal:

$$\langle a(y),\ b(y)\rangle_y = \int_y a^*(y)b(y)\,\mathrm{d}y \approx a^*Wb, \tag{4.14}$$

with the superscript $(\cdot)^*$ indicating the conjugate transpose. Utilizing equation (4.7), the two quantities should be equal with $V(\boldsymbol{k})/E_u(\boldsymbol{k}) = 1$. A similar demonstration of this agreement between $\tilde{\boldsymbol{u}}$ and $\mathcal{H}\boldsymbol{f}$ is performed in Morra et al. (2021), where the agreement is characterized using the power spectral density as a function of y for selected modes. Here, we elect to demonstrate the agreement in a y-integrated sense for all computed wavenumber-frequency triplets.

In Figure 4.7, the quantities $E_u(\boldsymbol{k})$ and $V(\boldsymbol{k})/E_u(\boldsymbol{k})$ are plotted in the $k_x - k_z$ planes for two representative low frequencies $\omega = 0, 0.166$ and one high frequency

$\omega = 25.088$ to examine the agreement between $V(\boldsymbol{k})$ and $E_u(\boldsymbol{k})$. The black contour lines in all figures denote the energy level of 10^{-12}, which is a few orders of magnitude weaker than the most energetic modes in the flow. From Figure 4.7(d) and (e), it can be observed that for the low frequencies, $V(\boldsymbol{k})$ and $E_u(\boldsymbol{k})$ agree very well with each other, especially in the high energy regions enclosed by the black contour lines. As the frequency increases, the agreement degrades. Although still in relatively good agreement in the high energy regions, the low energy regions start to show increasing errors. This behavior is expected for mainly two reasons: first, as the frequency increases, the spectral TKE of the modes decreases, leading to higher sensitivity to numerical errors when normalizing by the spectral TKE in $V(\boldsymbol{k})/E_u(\boldsymbol{k})$. Additionally, high frequency modes are expected to receive more contributions from the non-linear interactions involving high frequencies (further demonstrated in later sections), part of which are removed by the low pass filter for sampling, resulting in larger errors. The consequence of these errors will be further analyzed in Chapter 5 for the quantities of interest. Finally, although only the results averaged over all temporal segments are shown in Figure 4.7, the agreement for each temporal segment is roughly the same as the averaged results.

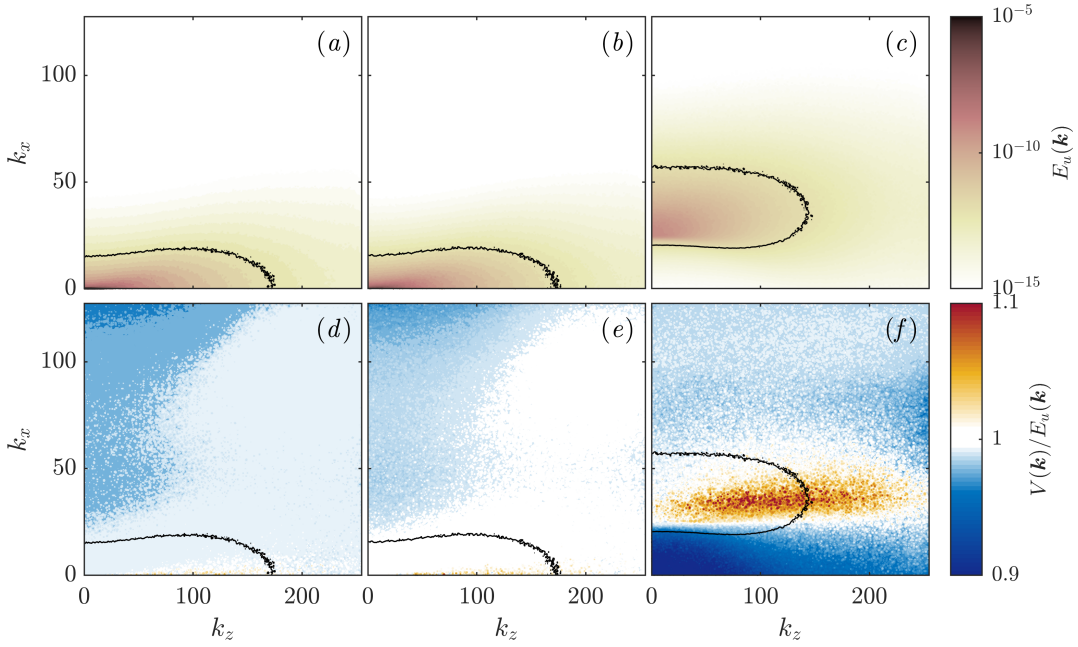

Figure 4.7: Contour plots of the comparison between $E_u(\boldsymbol{k})$ and $V(\boldsymbol{k})$. The top row (a - c) are $E_u(\boldsymbol{k})$, the spectral turbulent kinetic energy of $\tilde{\boldsymbol{u}}$ with a log scale colorbar, and the bottom row (d - f) are $V(\boldsymbol{k})/E_u(\boldsymbol{k})$ with a linear colorbar. The three columns are $\omega = 0, 0.166, 25.088$, and the black contour lines in all subplots are the energy level of 10^{-12}.

4.5 Conclusion

In this chapter, the modified direct numerical simulation necessitated by the non-standard data requirements is discussed. The Fourier space analysis benefits from the constant time stepping of the DNS which provides equally spaced time snapshots. Additionally, the high sampling rate allows for the resolving of most dynamically relevant temporal frequencies and the large amount of snapshots allows for the averaging over multiple temporal segments for improved convergence. Finally, a low pass filter in time is inserted into the DNS code prior to down-sampling to remove aliasing, which is a method not utilized in previous numerical simulations. These modifications to the DNS result in a good agreement between the left and right hand sides of the input-output formulation: $\tilde{\boldsymbol{u}} = \mathcal{H}\boldsymbol{f}$. This good agreement is demonstrated in this chapter for a range of wavenumber-frequency triplets, validating our numerical simulation and Fourier analysis.

Chapter 5

SPATIO-TEMPORAL CHARACTERISTICS OF THE TRIADIC INTERACTIONS

In this chapter, the non-linear triadic interactions are analyzed to provide new insights. We start by defining the forcing and response coefficients for each triadic interaction, which are used to quantify the importance in terms of the amount of contribution to the forcing and the velocity responses. We then discuss the physical interpretation and properties of the coefficients, followed by the relation to the bispectrum. We then compute these coefficients for the turbulent channel DNS introduced in Chapter 4, and analyze the different types of triadic interactions. Finally, the coefficients are utilized to quantitatively analyze the triadic interactions captured in quasi-linear and generalized quasi-linear analyses[1].

5.1 Formulation

As introduced in section 2.2, equation (2.5) shows that the linear resolvent operator does not modify the scale of the input, while equation (2.19) shows that the non-linear forcing is responsible for the coupling of different scales, and therefore the distribution of energy between scales. The triadic interactions are visually depicted in Figure 5.1. First, the velocity fields at $\boldsymbol{k}_1$ non-linearly interact with the velocity gradients at $\boldsymbol{k}_2$, generating part of the forcing at $\boldsymbol{k}_3 = \boldsymbol{k}_1 + \boldsymbol{k}_2$. This triadic contribution to the forcing is studied using the forcing coefficients $P(\boldsymbol{k}_1, \boldsymbol{k}_2)$ (defined later). The forcing at $\boldsymbol{k}_3$ is then passed through the linear resolvent operator to generate the velocity response at the same wavenumber-frequency triplet $\boldsymbol{k}_3$. This triadic contribution to the velocity response, which involves both the non-linear convolution and the linear resolvent operator, is studied using the response coefficients $R(\boldsymbol{k}_1, \boldsymbol{k}_2)$ (also defined later).

5.1.1 Triadic Contributions to the Forcing

The contribution from the interaction between a pair of triplets $\boldsymbol{k}_1$ and $\boldsymbol{k}_2$ to the resulting forcing at $\boldsymbol{k}_3 = \boldsymbol{k}_1 + \boldsymbol{k}_2$, can be quantified through a forcing coefficient

[1]The author would like to thank Dr. Gregory Chini for the valuable insights provided on quasi-linear and generalized quasi-linear analyses.

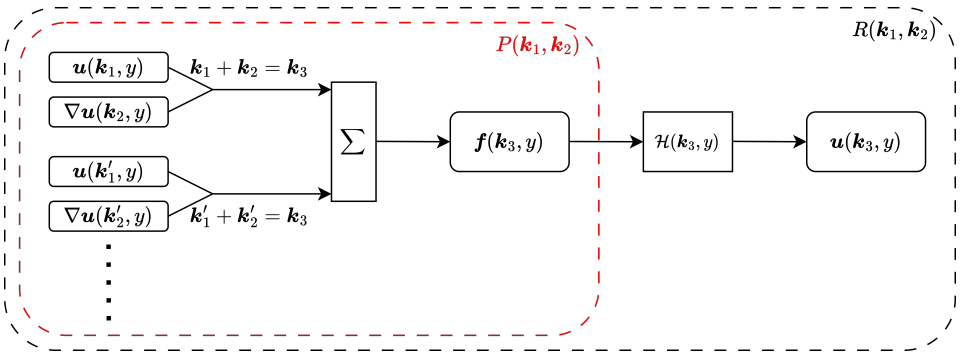

Figure 5.1: Diagram for the triadic interactions. The red inner box contains the triadic contributions to the non-linear forcing, studied using the coefficients $P(\boldsymbol{k}_1, \boldsymbol{k}_2)$, and the black outer box contains the triadic contributions to the response, studied using the coefficients $R(\boldsymbol{k}_1, \boldsymbol{k}_2)$.

$P(\boldsymbol{k}_1, \boldsymbol{k}_2)$:

$$P(\boldsymbol{k}_1, \boldsymbol{k}_2) = -\mathbb{E}\left\{\langle \boldsymbol{f}(\boldsymbol{k}_1 + \boldsymbol{k}_2, y),\ \boldsymbol{u}(\boldsymbol{k}_1, y) \cdot \nabla \boldsymbol{u}(\boldsymbol{k}_2, y)\rangle_y\right\}, \tag{5.1}$$

which is the inner product between $-\boldsymbol{u}(\boldsymbol{k}_1, y) \cdot \nabla \boldsymbol{u}(\boldsymbol{k}_2, y)$ and $\boldsymbol{f}(\boldsymbol{k}_3, y) = \boldsymbol{f}(\boldsymbol{k}_1 + \boldsymbol{k}_2, y)$. The inner product $\langle a(y),\ b(y)\rangle_y$ is previously defined in equation (4.14) and $\mathbb{E}\{\cdot\}$ is the expected value operator, indicating an average over all temporal segments (or different realizations). In this chapter, three separate wall-normal (y) ranges will be used, loosely corresponding to the near-wall $y^+ \in (0, 30)$, overlap $y^+ \in (30, 200)$, and wake regions $y^+ \in (200, 550)$, to study the wall-normal variations of these coefficients.

The intentionally un-normalized coefficients take the forcing magnitude into consideration, e.g. a large fractional contribution to a small magnitude forcing is treated as unimportant. Note that these coefficients, defined for DNS Fourier modes, differ from those, e.g. in McKeon (2017), which are defined for the interactions between resolvent modes. To facilitate computation and visualization of $P(\boldsymbol{k}_1, \boldsymbol{k}_2)$, we define P_{k_x}, P_{k_z}, and P_ω by summation in 4 of the 6 dimensions:

$$P_{k_x}(k_{x1}, k_{x2}) = \sum_{k_{z1}} \sum_{k_{z2}} \sum_{\omega_1} \sum_{\omega_2} P(\boldsymbol{k}_1, \boldsymbol{k}_2), \tag{5.2a}$$

$$P_{k_z}(k_{z1}, k_{z2}) = \sum_{k_{x1}} \sum_{k_{x2}} \sum_{\omega_1} \sum_{\omega_2} P(\boldsymbol{k}_1, \boldsymbol{k}_2), \tag{5.2b}$$

$$P_\omega(\omega_1, \omega_2) = \sum_{k_{x1}} \sum_{k_{x2}} \sum_{k_{z1}} \sum_{k_{z2}} P(\boldsymbol{k}_1, \boldsymbol{k}_2). \tag{5.2c}$$

P_{k_x} defined in equation (5.2a) describes the interaction in the streamwise direction between k_{x1} and k_{x2}, summed over all possible k_z and ω interactions. Similarly,

$P_{k_z}(k_{z1}, k_{z2})$ describes the interaction between k_{z1} and k_{z2}, and P_ω describes the interaction between ω_1 and ω_2.

Using the Hermitian symmetry of the velocity Fourier modes, it can be shown that the forcing coefficients are also Hermitian functions. However, they are asymmetric about their two arguments, due to the action of the velocity gradient tensor. The forcing coefficient satisfies:

$$P(\boldsymbol{k}_1, \boldsymbol{k}_2) = P^*(-\boldsymbol{k}_1, -\boldsymbol{k}_2) \neq P(\boldsymbol{k}_2, \boldsymbol{k}_1), \tag{5.3}$$

with P_{k_x}, P_{k_z}, and P_ω satisfying the same property. We retain the two separate coefficients associated with each combination of $(\boldsymbol{k}_1, \boldsymbol{k}_2)$ to maximize the information about the dominant interactions within each triad, which will be lost under a combined symmetric coefficient.

Utilizing equation (2.19), we can obtain the summation property of the forcing coefficient:

$$\sum_{\boldsymbol{k}_1} P(\boldsymbol{k}_1, \boldsymbol{k}_3 - \boldsymbol{k}_1) = \langle \boldsymbol{f}(\boldsymbol{k}_3, y),\ \boldsymbol{f}(\boldsymbol{k}_3, y) \rangle_y \,, \tag{5.4}$$

where the right-hand side of the equation is the spectral energy of the forcing at $\boldsymbol{k}_3$, and is a real positive quantity. As a result, the forcing coefficients can be interpreted as the triadic contributions to the forcing spectral energy. The positive and negative real parts of the coefficients represent energy injection and extraction respectively, while the complex parts of the coefficients cancel out due to the Hermitian symmetry described in equation (5.3), resulting in a real positive sum. Similar properties can be obtained for P_{k_x}, P_{k_z} and P_ω:

$$\sum_{k_{x1}} P_{k_x}(k_{x1}, k_{x3} - k_{x1}) = \sum_{k_{z3}} \sum_{\omega_3} \mathbb{E}\left\{ \langle \boldsymbol{f}(\boldsymbol{k}_3, y),\ \boldsymbol{f}(\boldsymbol{k}_3, y) \rangle_y \right\}, \tag{5.5a}$$

$$\sum_{k_{z1}} P_{k_z}(k_{z1}, k_{z3} - k_{z1}) = \sum_{k_{x3}} \sum_{\omega_3} \mathbb{E}\left\{ \langle \boldsymbol{f}(\boldsymbol{k}_3, y),\ \boldsymbol{f}(\boldsymbol{k}_3, y) \rangle_y \right\}, \tag{5.5b}$$

$$\sum_{\omega_1} P_\omega(\omega_1, \omega_3 - \omega_1) = \sum_{k_{x3}} \sum_{k_{z3}} \mathbb{E}\left\{ \langle \boldsymbol{f}(\boldsymbol{k}_3, y),\ \boldsymbol{f}(\boldsymbol{k}_3, y) \rangle_y \right\}. \tag{5.5c}$$

5.1.2 Triadic Contributions to the Velocity Response

To study the triadic contribution from the interaction between a pair of triplets $\boldsymbol{k}_1$ and $\boldsymbol{k}_2$ to the resulting velocity response at $\boldsymbol{k}_3 = \boldsymbol{k}_1 + \boldsymbol{k}_2$, including the effect of the linear resolvent operator, we will pass $-\boldsymbol{u}(\boldsymbol{k}_1, y) \cdot \nabla \boldsymbol{u}(\boldsymbol{k}_2, y)$ through $\mathcal{H}(\boldsymbol{k}_3, y)$ and then take the inner product with the resulting velocity response $\tilde{\boldsymbol{u}}(\boldsymbol{k}_3, y)$ to define

the response coefficient:

$$R(\boldsymbol{k}_1, \boldsymbol{k}_2) = -\mathbb{E}\left\{\langle \tilde{\boldsymbol{u}}(\boldsymbol{k}_1 + \boldsymbol{k}_2, y),\ \mathcal{H}(\boldsymbol{k}_1 + \boldsymbol{k}_2, y)\,[\boldsymbol{u}(\boldsymbol{k}_1, y) \cdot \nabla \boldsymbol{u}(\boldsymbol{k}_2, y)]\rangle_y\right\}, \tag{5.6}$$

where $\tilde{\boldsymbol{u}}(\boldsymbol{k}_3, y)$, defined in section 4.3, are the velocity Fourier modes with a correction to remove the effect of the window function in the temporal Fourier transform. The coefficients are again intentionally un-normalized to take the response magnitude into consideration. For the response coefficients, this also has the added benefit of rejecting the errors discussed in section 4.4, as relatively large errors are observed to predominately reside over areas with small energy, and would contribute very little to the un-normalized response coefficients defined here.

Similar to the previous section, the 2-dimensional coefficients R_{k_x}, R_{k_z}, and R_ω are defined by summation in 4 of the 6 dimensions:

$$R_{k_x}(k_{x1}, k_{x2}) = \sum_{k_{z1}} \sum_{k_{z2}} \sum_{\omega_1} \sum_{\omega_2} R(\boldsymbol{k}_1, \boldsymbol{k}_2), \tag{5.7a}$$

$$R_{k_z}(k_{z1}, k_{z2}) = \sum_{k_{x1}} \sum_{k_{x2}} \sum_{\omega_1} \sum_{\omega_2} R(\boldsymbol{k}_1, \boldsymbol{k}_2), \tag{5.7b}$$

$$R_{\omega}(\omega_1, \omega_2) = \sum_{k_{x1}} \sum_{k_{x2}} \sum_{k_{z1}} \sum_{k_{z2}} R(\boldsymbol{k}_1, \boldsymbol{k}_2). \tag{5.7c}$$

The Hermitian symmetry and the asymmetry about the two arguments are also satisfied by the response coefficient:

$$R(\boldsymbol{k}_1, \boldsymbol{k}_2) = R^*(-\boldsymbol{k}_1, -\boldsymbol{k}_2) \neq R(\boldsymbol{k}_2, \boldsymbol{k}_1), \tag{5.8}$$

with R_{k_x}, R_{k_z}, and R_ω satisfying the same property.

Utilizing equations (2.19) and (4.7), the summation properties of the response coefficient can also be obtained:

$$\sum_{\boldsymbol{k}_1} R(\boldsymbol{k}_1, \boldsymbol{k}_3 - \boldsymbol{k}_1) = \mathbb{E}\left\{\langle \tilde{\boldsymbol{u}}(\boldsymbol{k}_3, y),\ \tilde{\boldsymbol{u}}(\boldsymbol{k}_3, y)\rangle_y\right\}, \tag{5.9}$$

where the right-hand side of the equation is the spectral turbulent kinetic energy of the velocity response at $\boldsymbol{k}_3$, and is again a real positive quantity. As a result, the response coefficients can be interpreted as the triadic contributions to the spectral turbulent kinetic energy (TKE). The positive and negative real parts of the coefficients represent the injection and extraction of spectral TKE at a given wavelength or frequency, while the complex parts of the coefficients cancel out due to the Hermitian symmetry described in equation (5.8). Similar properties can be obtained for

R_{k_x}, R_{k_z}, and R_ω:

$$\sum_{k_{x1}} R_{k_x}(k_{x1}, k_{x3} - k_{x1}) = \sum_{k_{z3}} \sum_{\omega_3} \mathbb{E}\left\{\langle \tilde{\boldsymbol{u}}(\boldsymbol{k}_3, y),\ \tilde{\boldsymbol{u}}(\boldsymbol{k}_3, y)\rangle_y\right\}, \tag{5.10a}$$

$$\sum_{k_{z1}} R_{k_z}(k_{z1}, k_{z3} - k_{z1}) = \sum_{k_{x3}} \sum_{\omega_3} \mathbb{E}\left\{\langle \tilde{\boldsymbol{u}}(\boldsymbol{k}_3, y),\ \tilde{\boldsymbol{u}}(\boldsymbol{k}_3, y)\rangle_y\right\}, \tag{5.10b}$$

$$\sum_{\omega_1} R_\omega(\omega_1, \omega_3 - \omega_1) = \sum_{k_{x3}} \sum_{k_{z3}} \mathbb{E}\left\{\langle \tilde{\boldsymbol{u}}(\boldsymbol{k}_3, y),\ \tilde{\boldsymbol{u}}(\boldsymbol{k}_3, y)\rangle_y\right\}. \tag{5.10c}$$

5.1.3 Alternative Forms of the Forcing and Response Coefficients

To compute the 2-dimensional coefficients P_{k_x}, P_{k_z}, P_ω, R_{k_x}, R_{k_z}, and R_ω, the definitions presented in equations (5.2a)-(5.2c) and (5.7a)-(5.7c) cannot be directly utilized as the computation of the original six-dimensional $P(\boldsymbol{k}_1, \boldsymbol{k}_2)$ and $R(\boldsymbol{k}_1, \boldsymbol{k}_2)$ would require petabyte levels of storage with computation power and memory requirements beyond currently available systems. In this section, alternative forms of the coefficients are derived to simplify computation and provide an alternative physical interpretation of the coefficients.

Utilizing the discrete Fourier transform pairs and the orthogonality of Fourier modes, equivalent forms for the 2-dimensional coefficients P_{k_x}, P_{k_z}, and P_ω can be obtained in the (z, t), (x, t), and (x, z) domains:

$$\begin{aligned} &P_{k_x}(k_{x1}, k_{x2}) \\ &= -\frac{1}{N_z N_t} \sum_z \sum_t \mathbb{E}\left\{\langle \boldsymbol{f}(k_{x1} + k_{x2}, y, z, t),\ \boldsymbol{u}(k_{x1}, y, z, t) \cdot \nabla \boldsymbol{u}(k_{x2}, y, z, t)\rangle_y\right\} \end{aligned} \tag{5.11a}$$

$$\begin{aligned} &P_{k_z}(k_{z1}, k_{z2}) \\ &= -\frac{1}{N_x N_t} \sum_x \sum_t \mathbb{E}\left\{\langle \boldsymbol{f}(x, y, k_{z1} + k_{z2}, t),\ \boldsymbol{u}(x, y, k_{z1}, t) \cdot \nabla \boldsymbol{u}(x, y, k_{z2}, t)\rangle_y\right\} \end{aligned} \tag{5.11b}$$

$$\begin{aligned} &P_\omega(\omega_1, \omega_2) \\ &= -\frac{1}{N_x N_z} \sum_x \sum_z \mathbb{E}\left\{\langle \boldsymbol{f}(x, y, z, \omega_1 + \omega_2),\ \boldsymbol{u}(x, y, z, \omega_1) \cdot \nabla \boldsymbol{u}(x, y, z, \omega_2)\rangle_y\right\}. \end{aligned} \tag{5.11c}$$

Note that $\boldsymbol{u}(k_{x1}, y, z, t)$ here denotes the velocity Fourier transformed only in x, and differs from $\boldsymbol{u}(\boldsymbol{k}_1, y)$ in equation (5.1), which is Fourier transformed in x, z, and t. These alternative forms are in essence an extended form of the convolution theorem.

P_{k_x} and P_{k_z} can now be computed in the temporal domain, while P_ω requires a Fourier transform in time, the implementation of which is discussed in Chapter 4 section 4.3. Additionally, to ensure consistency across all three computations, P_{k_x} and P_{k_z} computed in the time domain employ the same temporal segmentation, window functions ($\sqrt{w(t)}$ for $\boldsymbol{u}$ and $\nabla\boldsymbol{u}$, $w(t)$ for $\boldsymbol{f}$ as discussed in section 4.3) and averaging over the temporal segments even though a temporal Fourier transform is not utilized. The validity of applying the Welch method, which averages over multiple temporal segments is discussed in appendix A.3.

These forms provide alternative physical interpretations of the forcing coefficients: $P_{k_x}(k_{x1}, k_{x2})$ can now be interpreted as quantifying the importance of interactions between k_{x1} and k_{x2} averaged over all spanwise locations and time instead of a summation over wavenumbers and frequencies in the Fourier domain. Similarly, P_{k_z} describes the k_z interactions averaged in x, t, and P_ω the ω interactions averaged in x and z. Additionally, for the numerical computations, these alternative forms in equations (5.11a)-(5.11c) ensure that the original 6 dimensional $P(\boldsymbol{k}_1, \boldsymbol{k}_2)$ is never computed, reducing computation cost, memory and storage requirements, enabling the computation to be completed on currently available systems.

For the response coefficients, we first simplify the notation utilizing the matrix form of the inner product with weight matrix $\boldsymbol{W}$, and introduce $\boldsymbol{h}(\boldsymbol{k}_3, y)$:

$$\boldsymbol{h}^*(\boldsymbol{k}_3, y) = \tilde{\boldsymbol{u}}^*(\boldsymbol{k}_3, y)\boldsymbol{W}\mathcal{H}(\boldsymbol{k}_3, y), \tag{5.12}$$

which is computed in the Fourier domain for each $\boldsymbol{k}_3$. The response coefficient $R(\boldsymbol{k}_1, \boldsymbol{k}_2)$ can then be rewritten as:

$$R(\boldsymbol{k}_1, \boldsymbol{k}_2) = -\mathbb{E}\left\{\boldsymbol{h}^*(\boldsymbol{k}_1 + \boldsymbol{k}_2, y)\left[\boldsymbol{u}(\boldsymbol{k}_1, y) \cdot \nabla\boldsymbol{u}(\boldsymbol{k}_2, y)\right]\right\}. \tag{5.13}$$

Substitute the inverse Fourier transforms into equations (5.7a)-(5.7c) for R_{k_x}, R_{k_z}, and R_ω and utilize the orthogonality of the Fourier modes again, and we can obtain:

$$R_{k_x}(k_{x1}, k_{x2})$$
$$= -\frac{1}{N_z N_t} \sum_z \sum_t \mathbb{E}\left\{\boldsymbol{h}^*(k_{x1} + k_{x2}, y, z, t)\boldsymbol{u}(k_{x1}, y, z, t)\nabla\boldsymbol{u}(k_{x2}, y, z, t)\right\}. \quad (5.14a)$$

$$R_{k_z}(k_{z1}, k_{z2})$$
$$= -\frac{1}{N_x N_t} \sum_x \sum_t \mathbb{E}\left\{\boldsymbol{h}^*(x, y, k_{z1} + k_{z2}, t)\boldsymbol{u}(x, y, k_{z1}, t)\nabla\boldsymbol{u}(x, y, k_{z2}, t)\right\}, \quad (5.14b)$$

$$R_{\omega}(\omega_1, \omega_2)$$
$$= -\frac{1}{N_x N_z} \sum_x \sum_z \mathbb{E}\left\{\boldsymbol{h}^*(x, y, z, \omega_1 + \omega_2)\boldsymbol{u}(x, y, z, \omega_1)\nabla\boldsymbol{u}(x, y, z, \omega_2)\right\}, \quad (5.14c)$$

all resembling the alternative forms for P_{k_x}, P_{k_z}, and P_{ω} presented in equations (5.11a)-(5.11c). These forms also provide the alternative interpretation of averaging in the physical domain instead of summation over wavenumbers and frequencies. Similarly, the alternative forms provide significant reductions in computation cost and memory requirements, with R_{k_x} and R_{k_z} computed in the time domain employing the same temporal segmentation, window functions, and averaging over the temporal segments to ensure consistency with R_{ω}. However, it should be pointed out that $\boldsymbol{h}(\boldsymbol{k}_3, y)$, due to the presence of the resolvent operator, is first computed in the Fourier domain before being inverse Fourier transformed back to the physical time domain for the computations of R_{k_x} and R_{k_z} using equations (5.14a) and (5.14b).

5.1.4 Relation to Triple Correlation and Bispectrum

The forcing and response coefficients studied here may be related to the more well-known triple correlation and bispectrum. Following Lii et al. (1976), the three-point spatial triple correlation for three state variables q_l, q_m, and q_n can be defined as:

$$R_{lmn}(\boldsymbol{r}, \boldsymbol{r'}) = \langle q_l(\boldsymbol{x})q_m(\boldsymbol{x} + \boldsymbol{r})q_n(\boldsymbol{x} + \boldsymbol{r'})\rangle_{\boldsymbol{x}}, \quad (5.15)$$

where $\langle\cdot\rangle_{\boldsymbol{x}}$ represents a spatial average. Two triple spatial Fourier transforms of $R_{lmn}(\boldsymbol{r}, \boldsymbol{r'})$ in $\boldsymbol{r}, \boldsymbol{r'}$ lead to the three-dimensional spatial bispectrum:

$$B_{lmn}(\hat{\boldsymbol{k}}, \hat{\boldsymbol{k}'}) = q_l^*(\hat{\boldsymbol{k}} + \hat{\boldsymbol{k}'})q_m(\hat{\boldsymbol{k}})q_n(\hat{\boldsymbol{k}'}). \quad (5.16)$$

The forcing coefficients proposed in this work in equation (5.1) can be seen as a spatio-temporal extension of the bispectrum, considering the spatio-temporal wavenumbers, $\boldsymbol{k}$, that is suitable for the analysis of wall-bounded flows with homogeneous directions of x, z, and t rather than the spatial wavenumbers, $\hat{\boldsymbol{k}}$. An

additional difference is that forcing coefficients in this work are specifically designed to study the contribution of an interacting pair on the resulting forcing, which to our knowledge has not been studied before. The three contributing terms to the interaction coefficients are the velocity $\boldsymbol{u}$, velocity gradient $\nabla\boldsymbol{u}$, and forcing $\boldsymbol{f}$ in contrast to previous studies that focused more on the three terms being the same flow quantity, for example, $\partial u/\partial x$ in Lii et al. (1976) to study the non-linear energy transfer between scales and velocity $\boldsymbol{u}$ in Schmidt (2020), where the bispectral mode decomposition is introduced to compute modes associated with triadic interactions through maximization of the integral bispectral density.

On the other hand, the response coefficients proposed in equation (5.6) can be considered as a weighted version of the spatio-temporal extension to the bispectrum, which includes the effect of the linear resolvent operator, acting as the weight matrix. Traditional bispectrum analyses such as $\langle u(\boldsymbol{k}_1+\boldsymbol{k}_2,y),\ u(\boldsymbol{k}_1,y)u(\boldsymbol{k}_2,y)\rangle_y$ or the extension $\langle \boldsymbol{u}(\boldsymbol{k}_1+\boldsymbol{k}_2,y),\ \boldsymbol{u}(\boldsymbol{k}_1,y)\cdot\nabla\boldsymbol{u}(\boldsymbol{k}_2,y)\rangle_y$ are directly related to the turbulent transport term in equation (2.23), and identifies the transfer of energy between different triplets. However, without the linear resolvent operator, the effects of other terms in the spectral TKE equation (2.23), such as viscosity, pressure, and production by the mean shear are not accounted for. For example, energy transfer from one pair of $(\boldsymbol{k}_1,\boldsymbol{k}_2)$ to $\boldsymbol{k}_3=\boldsymbol{k}_1+\boldsymbol{k}_2$ with energy distributed mainly at a wall-normal location with strong mean shear could potentially increase the mode amplitude at this location and induce a stronger production, resulting in some energy amplification, therefore contributing more significantly to the spectral TKE at $\boldsymbol{k}_3$, while another pair transferring energy to the same $\boldsymbol{k}_3$ but with energy distributed mainly at another y location with weak mean shear will not have this effect. The inclusion of the linear resolvent operator as a weight matrix accounts for these mechanisms, and therefore provides a new and more complete picture of the effects of the triadic energy transfer on the resulting spectral TKE. Additionally, as shown in equation (2.22), when the forcing is multiplied by the resolvent operator, the irrotational part, which does not affect the velocity response, is naturally eliminated. Therefore, the response coefficient defined in equation (5.6) naturally removes the effect of the inactive irrotational forcing, which differs from both the forcing coefficients defined in equation (5.1) and the bispectrum analyses.

5.2 Spatio-temporal Characteristics of the Nonlinear Interactions

In Figure 5.2, Feynman diagrams depicting important triadic interactions are plotted. These six different types of interactions represent different regions in Figures 5.3,

5.4, and 5.5, which are the magnitude of the streamwise, spanwise, and temporal coefficients respectively. In Figures 5.3-5.5, subplots (*a* - *d*) are the forcing coefficients and (*e* - *h*) are the response coefficients, corresponding to different y integration ranges for the inner product defined in equation (4.14): all y, followed by limits corresponding loosely to the near-wall, overlap, and wake regions.

The streamwise, spanwise wavenumbers and temporal frequency for the velocity fields, k_{x1}, k_{z1}, ω_1, are on the vertical axis of all figures, and k_{x2}, k_{z2}, ω_2 for the velocity gradients are on the horizontal axis. Lines with a slope of -1 correspond to constant $k_{x3} = k_{x1} + k_{x2}$, $k_{z3} = k_{z1} + k_{z2}$, and $\omega_3 = \omega_1 + \omega_2$ for the resulting forcing or response; the extremum values of $k_{x3} = \pm 127.5$, $k_{z3} = \pm 255$, and $\omega_3 = \pm 42.53$ reflect the maximum k_x, k_z, and ω retained by the DNS and the temporal Fourier analysis. Four quadrants of (k_{x1}, k_{x2}), (k_{z1}, k_{z2}), and (ω_1, ω_2) are shown in subplots (*a, e*) for completeness, while the symmetry discussed in equations (5.3) and (5.8) is exploited for subsequent subplots (*b* - *d*) and (*f* - *h*) in which only $k_{x1}, k_{z1}, \omega_1 \geq 0$ are shown. To highlight the details of the coefficients, the same logarithmic color scale spanning multiple orders of magnitude is used throughout the different y integration ranges. It should be noted that part of the differences in magnitude between subplots (*b* - *d*) and between subplots (*f* - *h*) are simply attributed to the different sizes of the y integration domains. The inserts in subplots (*a, e*) of Figures 5.3-5.5 are representations of the central rectangular regions enclosed in the dotted white lines using linear colorbars. The diagonal white dotted lines with -1 slopes in subplots (*a, e*) in Figures 5.3-5.5 mark the locations of $[k_{x3},\ k_{z3},\ \omega_3] = [4,\ 28,\ 2.492]$, a representative mode for the near wall cycle used in Chapter 6. This mode has a wavespeed of $c_3 = \omega_3/k_{x3} = 0.62$, and corresponds to $\lambda_x^+ = 865$, $\lambda_z^+ = 124$, $\omega_3^+ = 0.0953$, and $c_3^+ = \omega_3^+/k_{x3}^+ = 13$ in inner scales. In the inserts of subplots (*a, e*), the lines are plotted with black dashed lines instead for better contrast in the figures.

Figures 5.3-5.5 reveal three dominant bands with high magnitudes for all coefficients: the horizontal, vertical, and diagonal bands, centered around $\boldsymbol{k}_1, \boldsymbol{k}_2$, and $\boldsymbol{k}_3 \approx 0$ respectively. These bands are all nonlinear interactions involving the large/slow scales of the flow and are visually represented by Feynman diagrams in Figures 5.2(*a* - *c*).

In this chapter, we are focusing on the averaged result over all five temporal segments. In Appendix C, we will study the variation of these coefficients over the different temporal segments and demonstrate that the overall structures of these

results are robust and sufficiently converged. However, we will also demonstrate in Appendix C that some of the transitional regions between constructive and destructive interference will require more data to reduce the variations for future studies focusing on these regions.

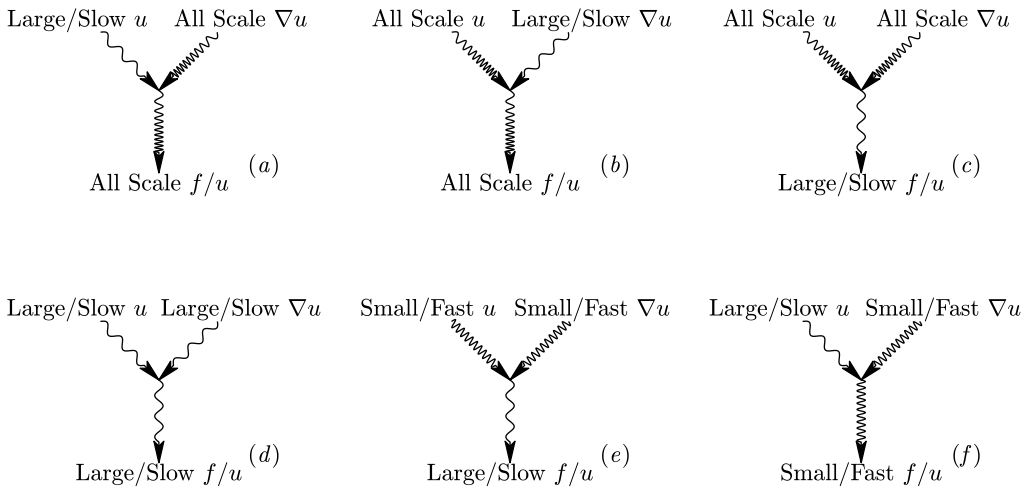

Figure 5.2: Feynman diagrams depicting the important triadic interactions observed in the forcing and response coefficients. Subplots (*a*), (*b*), (*c*) are for the horizontal, vertical, and diagonal bands of high magnitudes shown in Figures 5.3-5.5. Subplots (*d*), (*e*), and (*f*) are for the central region, the top-left corners, and the left or right corners of the horizontal bands in Figures 5.3-5.5.

5.2.1 Triadic Interactions in the Streamwise Direction

Starting with the streamwise forcing and response coefficients $\left|P_{k_x}(k_{x1}, k_{x2})\right|$ and $\left|R_{k_x}(k_{x1}, k_{x2})\right|$ in Figures 5.3(*a, e*), a dominant horizontal band is observed for the forcing, while in the response, it has relatively high magnitude without being the most dominating band. This horizontal band, centered around $k_{x1} = 0$, corresponds to the interaction between the streamwise large-scale velocity modes with velocity gradients at all scales, depicted in the Feynman diagram in Figure 5.2(*a*).

For the forcing coefficient in Figures 5.3(*a* - *d*), the high values in the horizontal band are not surprising, as the streamwise large-scale structures at $k_x = 0$ and ± 0.5 are the most energetic modes in the flow field. In addition, these modes have a tall wall-normal extent as shown in Figure 4.6, and therefore are capable of interacting with modes of any size, centered at any y location. The combined effect leads to a significant amount of forcing energy generated across a range of scales by these large-scale modes, manifesting as the energetic horizontal band. Additionally, the

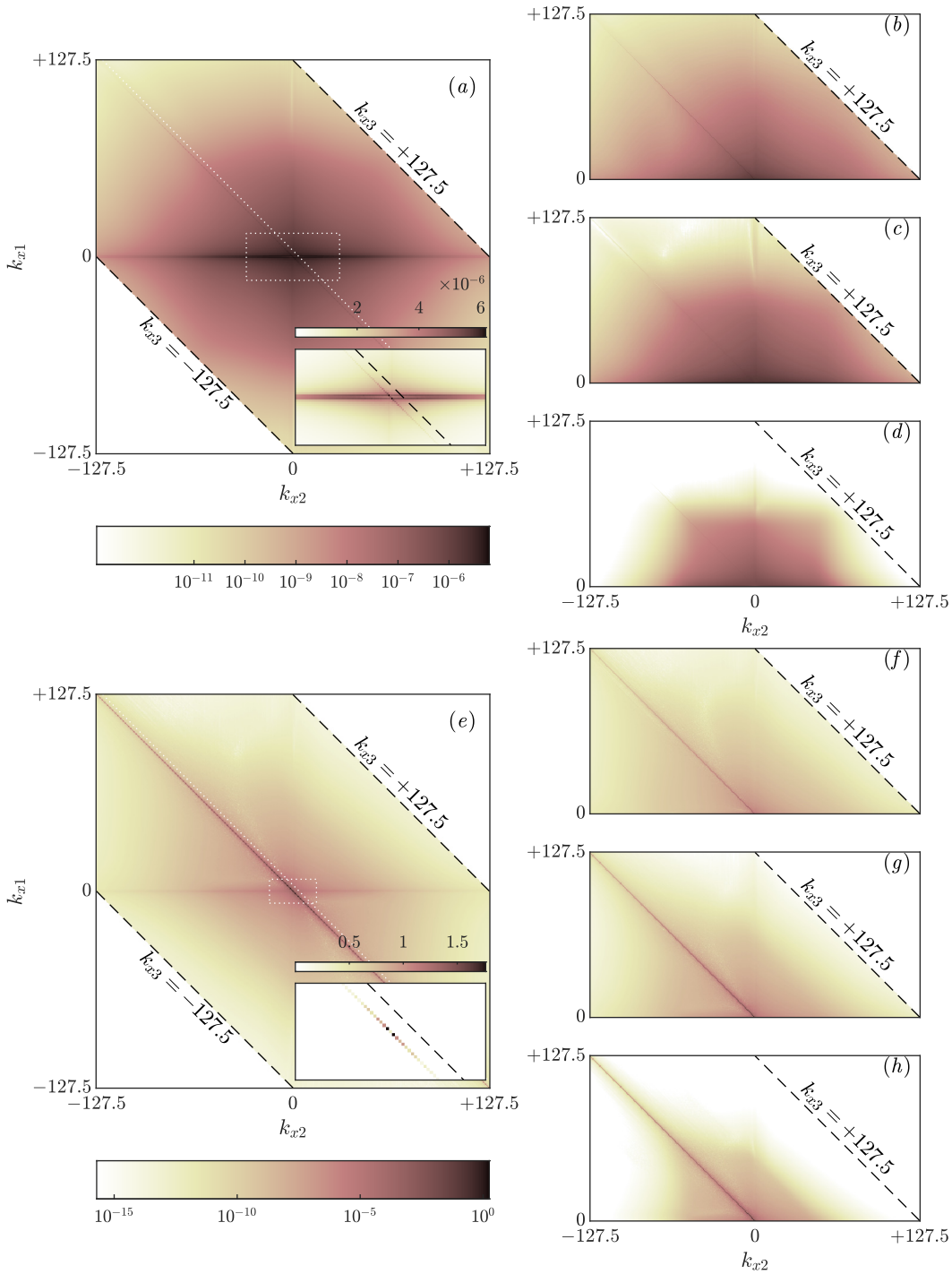

Figure 5.3: Heatmaps of the magnitude of (*a* - *d*) the streamwise forcing coefficients $\left|P_{k_x}(k_{x1}, k_{x2})\right|$, and (*e* - *h*) the streamwise response coefficients $\left|R_{k_x}(k_{x1}, k_{x2})\right|$. Subplots (*a* - *d*) except the insert shares the same logarithmic colorbar, same for subplots (*e* - *h*). The insert in (*a*) and (*e*) corresponds to representations of the rectangular regions enclosed in the dashed white lines using linear scale colorbars. The y-integration limits for the inner product in equation (4.14) are: (*a, e*) all y^+; (*b, f*) $y^+ \in (0, 30)$; (*c, g*) $y^+ \in (30, 200)$; and (*d, h*) $y^+ \in (200, 550)$. The streamwise wavenumber for the velocity fields, k_{x1}, is on the vertical axis; k_{x2} for the velocity gradient is on the horizontal axis; $k_{x3} = k_{x1} + k_{x2}$ for the resulting forcing and response is constant along lines with slopes of -1. The diagonal white dotted lines in (*a, e*) and the black dashed lines in the inserts mark the location of $k_{x3} = 4$ ($\lambda_x^+ = 865$).

values in this horizontal band decay relatively slowly as $|k_{x2}|$ increases (away from the center), due to the compensation by the gradients, despite the velocity modes becoming less energetic with increasing $|k_{x2}|$. Finally, comparing the wall-normal variation of the horizontal band across Figures 5.3(b - d), it can be observed that P_{k_x} exhibits a significant presence across all 3 y ranges due to the tall large scale modes. However, for the left and right corners of the horizontal band (large $|k_{x2}|$, Feynman diagram in Figure 5.2(f)), less energy is observed for the wake region in Figure 5.3(d), due to the small scales having less energy at regions far from the wall.

On the other hand, in Figures 5.3(e - h), the horizontal band of the response coefficient although prominent, is not the most energetic band. Further comparing the left and right corners (large $|k_{x3}|$) of the horizontal band between Figures 5.3(a) and (e), it can be observed that significant forcing is present while resulting in very little response energy. This showcases the effect of the linear resolvent operator, where the small scales are less amplified than the large scales. As a result, the horizontal band of the response coefficient R_{k_x} decays faster moving away from the center (as $|k_{x3}|$ increases), resulting in a less prominent horizontal band compared to the forcing coefficient P_{k_x}. This is consistent with Jiménez (2012), where it is demonstrated that the energy is transferred from the large scales to the small scales through nonlinear interactions and dissipated at the small scales through viscosity.

Focusing instead on the contributors to the small scales with high $|k_{x3}|$ (45° regions near the dash lines of $k_{x3} = \pm 127.5$), it can be observed that the left and right corners of the horizontal bands are the dominant contributors for both the forcing and response coefficients. These regions represent the nonlinear interactions between large-scale velocity modes (small $|k_{x1}|$) and small-scale velocity gradients (large $|k_{x2}|$), generating forcing and response at small scales (large $|k_{x3}|$), with Feynman diagram depicted in Figure 5.2(f). High values and dominant contributions to the small scales from these long-range interactions (in k_x) indicate coherence between the large and small scales, consistent with the superposition and modulation mechanisms observed in Marusic et al. (2010a).

Lower values of $\left|P_{k_x}\right|$ and $\left|R_{k_x}\right|$ are observed along the vertical band, centered around $k_{x2} = 0$, (Feynman diagram in Figure 5.2(b)). Compared to the horizontal band, in the vertical band, the modes contributing to the velocity and velocity gradient are reversed in equations (5.2a) and (5.7a) (swapping k_{x1} and k_{x2}). Spatial derivatives for the large scale are weaker and the energy of the small scales is lower than for the horizontal band, underscoring the asymmetry of interactions within a given triad.

For the diagonal band with $k_{x3} \approx 0$ (Feynman diagram in Figure 5.2(c)), a weak signature of interactions between two similar size modes generating a streamwise large-scale forcing can be observed for the forcing coefficients in Figures 5.3(a - d). For the response coefficients in Figures 5.3(e - h), this diagonal band is stronger, and is the most dominant band of R_{k_x}, due to the preferential amplification of the large scale modes by the linear resolvent operator.

Within this diagonal region, forcing coefficient P_{k_x} for interactions between two large scales in the central region (Feynman diagram in Figure 5.2(d)) is stronger than the interactions between two small scales in the corner regions (especially evident in the linear scale inserts). This is consistent with the findings of Morra et al. (2021), where it is demonstrated that large-scale forcing modes are mostly the result of interactions by large-scale structures, although with a relatively weak influence from the interactions between the smaller scales. In addition, the forcing components generated from small-scale interactions are almost non-existent in the outer region (shown in Figure 5.3(d)), due to the small scales having little energy presence far from the wall. On the contrary, the response coefficient R_{k_x}, with an energetic diagonal band extending all the way to the corners in Figures 5.3(e - h), shows that this type of interaction between small scales affecting the large scales (Feynman diagram in Figure 5.2(e)), although having a relatively weaker influence on the velocity response, is not a negligible effect. This phenomenon is also demonstrated in the work of Illingworth et al. (2018) and Chapter 3 of this thesis, where it is shown that including an eddy viscosity into the resolvent framework, which is intended to model the effect of this type of interactions, improves the performance of the resolvent analysis for the large scales. It should be pointed out that Figure 5.3 examines only the magnitude of the interaction coefficients, where large values show strong importance. The direction of energy, whether energy injection or extraction will be examined later using the phase of the coefficients, and it will be shown that this type of interaction between small scales weakens the spectral TKE of the the large scales, consistent with the energy cascade (Jiménez, 2012).

Finally, it should be noted that the three bands having peak values at $k_{x1}, k_{x2}, k_{x3} = 0$ is an artifact of the current numerical simulation. With the current x domain length of 4π, energy from the unresolved large scales manifests as streamwise constant structures at $k_x = 0$, making it the most energetic wavenumber. It should also be pointed out that these are still the mean-subtracted velocity fluctuations, that are

streamwise constant, yet non-constant in spanwise direction ($k_z \neq 0$) and/or non-constant in time ($\omega \neq 0$). For simulations with longer x domain lengths, capable of resolving the longest streaks, all three bands are likely to display dual-band structures with large values located at $k_{x1}, k_{x2}, k_{x3} = \pm k_{xl}$, where $k_{xl} \in (0, 0.5)$ is the streamwise wavenumber of the most energetic large scale streak. As the box size approaches infinity, providing higher and higher resolution for the streamwise wavenumber, these bands are expected to display some width in k_x where multiple wavenumbers very close to $\pm k_{xl}$ displaying high levels of importance, with $\pm k_{xl}$ as the peak.

5.2.2 Triadic Interactions in the Spanwise Direction

The spanwise forcing and response coefficients $\left|P_{k_z}(k_{z1}, k_{z2})\right|$ and $\left|R_{k_z}(k_{z1}, k_{z2})\right|$, in Figure 5.4, behave very similarly to the streamwise coefficients, with the exception that the three bands no longer show single-banded structures located around $k_x \approx 0$, but instead shows dual-band structures located at $k_z \approx \pm 3$. This is as expected since the large-scale structures, which are the most energetic modes in the flow field, with $k_x = 0$ and $k_x = 0.5$ are also most energetic at $k_z \approx \pm 3$. The dual-banded structures are very prominent for the energetic horizontal band of P_{k_z} and diagonal band of R_{k_z}, while less obvious for the less energetic bands.

A teardrop shaped region at high k_{z2} and k_{z3} values with very small magnitude is observed in the forcing coefficient P_{k_z} in Figures 5.4(a - d). This region is believed to be not very well converged using the current data. First of all, this region involves the highest spanwise wavenumbers in the DNS (significantly smaller scales than the near wall cycle located around $k_z = 28$ ($\lambda_z^+ \approx 100$)), and these wavenumbers are not expected to be well-resolved by the DNS due to the limited number of grid points per period. Secondly, the forcing coefficients in this region have magnitudes that are orders of magnitude smaller, making it sensitive to numerical errors. Although the corner areas of the results involving extreme k_z values are less robust quantitatively, the overall structure of the results is expected to remain consistent.

5.2.3 Triadic Interactions of the Temporal Frequencies

The overall structure of the frequency forcing and response coefficients $|P_\omega(\omega_1, \omega_2)|$ and $|R_\omega(\omega_1, \omega_2)|$ plotted in Figure 5.5 are again similar to the streamwise coefficients, with the exception that the single-banded structures in the streamwise direction now becomes multi-banded. These prominent discrete high-value lines located in the horizontal, vertical, and diagonal bands with $\omega_1, \omega_2, \omega_3 \approx 0$ are due to the

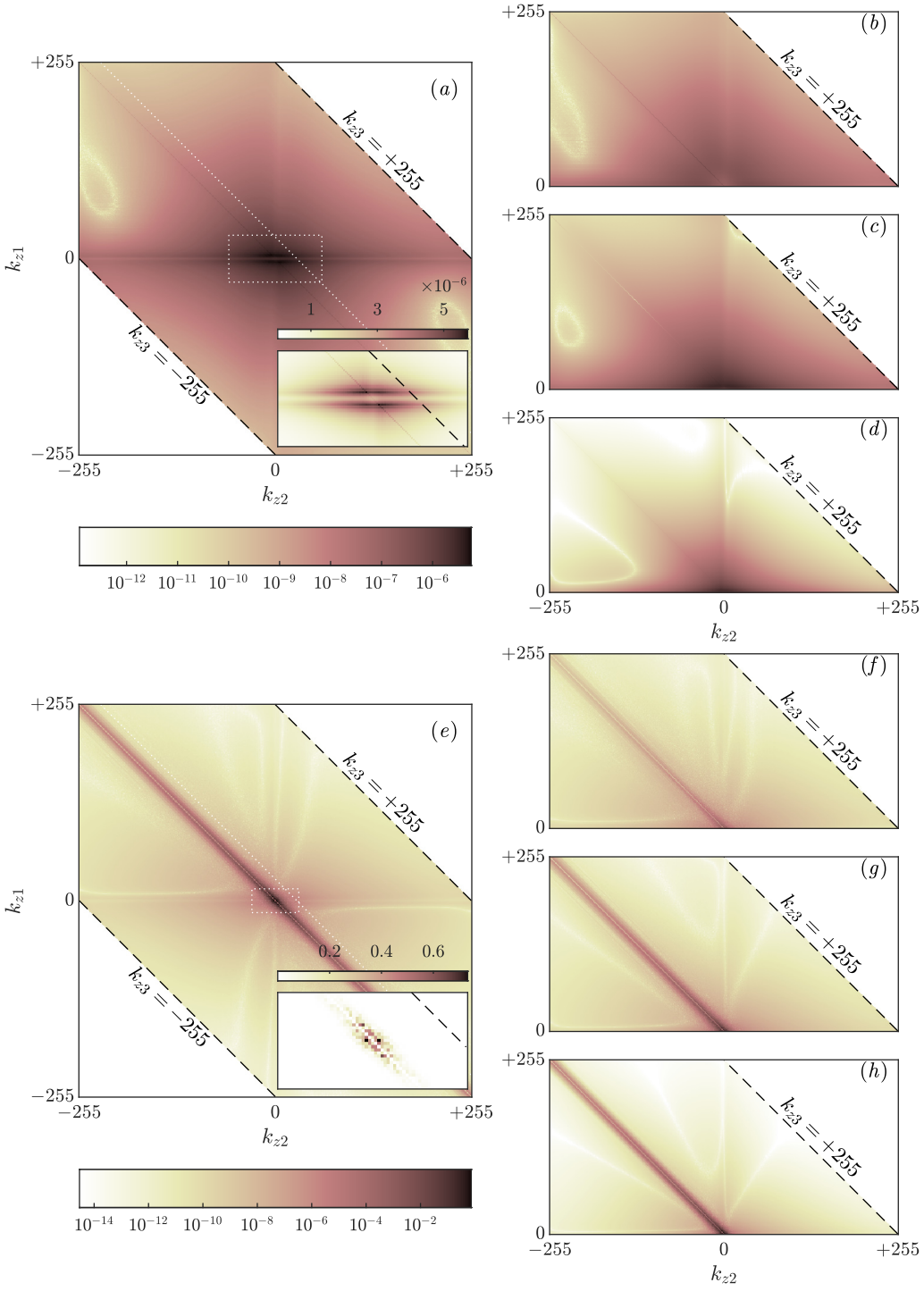

Figure 5.4: Heatmaps of the magnitude of (*a* - *d*) the spanwise forcing coefficients $\left|P_{k_z}(k_{z1}, k_{z2})\right|$, and (*e* - *h*) the spanwise response coefficients $\left|R_{k_z}(k_{z1}, k_{z2})\right|$ in the same format as Figure 5.3. The diagonal white dotted lines in (*a, e*) and the black dashed lines in the inserts mark the location of $k_{z3} = 28$ ($\lambda_z^+ = 124$).

discreteness in the streamwise wavenumber k_x, an artifact of the finite simulation domain length, as similarly demonstrated in Gómez et al. (2014). The frequency can be related to the phase speed for a given $\boldsymbol{k}$ via $\omega = c \cdot k_x$; at a given wavespeed, c, an increase in k_x to the next discrete wavenumber, with an increment of 0.5 fixed by the simulation domain length, will cause ω to increase by $0.5c$. Therefore, increments in ω are largest for large scales with high wavespeeds, appearing as discrete lines, and smaller for small scales with low wavespeeds, reflected as the smooth varying background.

A more detailed analysis reveals that the 5 most prominent lines observed in Figure 5.5 for both P_ω and R_ω are located at $\omega \approx 0$, ± 0.4, and ± 0.8. These lines correspond well with the energetic modes at $k_x = 0$, $k_x = \pm 0.5$ (with wavespeeds of $c = \omega / k_x \approx 0.8$ shown in Figure 4.6(a)) and $k_x = \pm 1$ (with $c \approx 0.8$ shown in Figure 4.6(b)) respectively. Furthermore, by observing the relative intensities between the smooth background and discrete lines across different y locations, it can be seen that the former is more prominent near the wall in Figures 5.5(b, f) where the discreteness is barely visible, while away from the wall in Figures 5.5(d, h) the opposite is true. Combined with the tall y extent for large scales and the concentration of energy near the wall for small scales, as demonstrated in Figure 4.6, these confirm that the smooth background mostly shows the triadic interactions between the small scales, while the discrete lines are mostly the result of interactions involving the large scales. Although the discreteness is an artifact of the finite simulation domain length, interactions involving large scales are expected to be important regardless of the domain length.

5.2.4 Constructive and Destructive Triadic Interactions

Both the forcing and response coefficients are complex numbers, with the magnitude providing information about the importance of a triadic interaction, while the phase provides information about constructive and destructive interference. From equations (5.10a)-(5.10c), it can be observed that the response coefficients sum up to become the spectral turbulent kinetic energy of the response modes, which are real positive quantities. Therefore, the imaginary parts of the coefficients are being canceled out by each other, while the real parts provide information about the constructive and destructive contributions to the spectral TKE. A positive real part of $R(\boldsymbol{k}_1, \boldsymbol{k}_2)$ indicates that the interaction between $\boldsymbol{k}_1$ and $\boldsymbol{k}_2$ causes an increase in spectral TKE of the response mode at $\boldsymbol{k}_3$, while a negative real part indicates a decrease of spectral TKE. To analyze the constructive and destructive interfer-

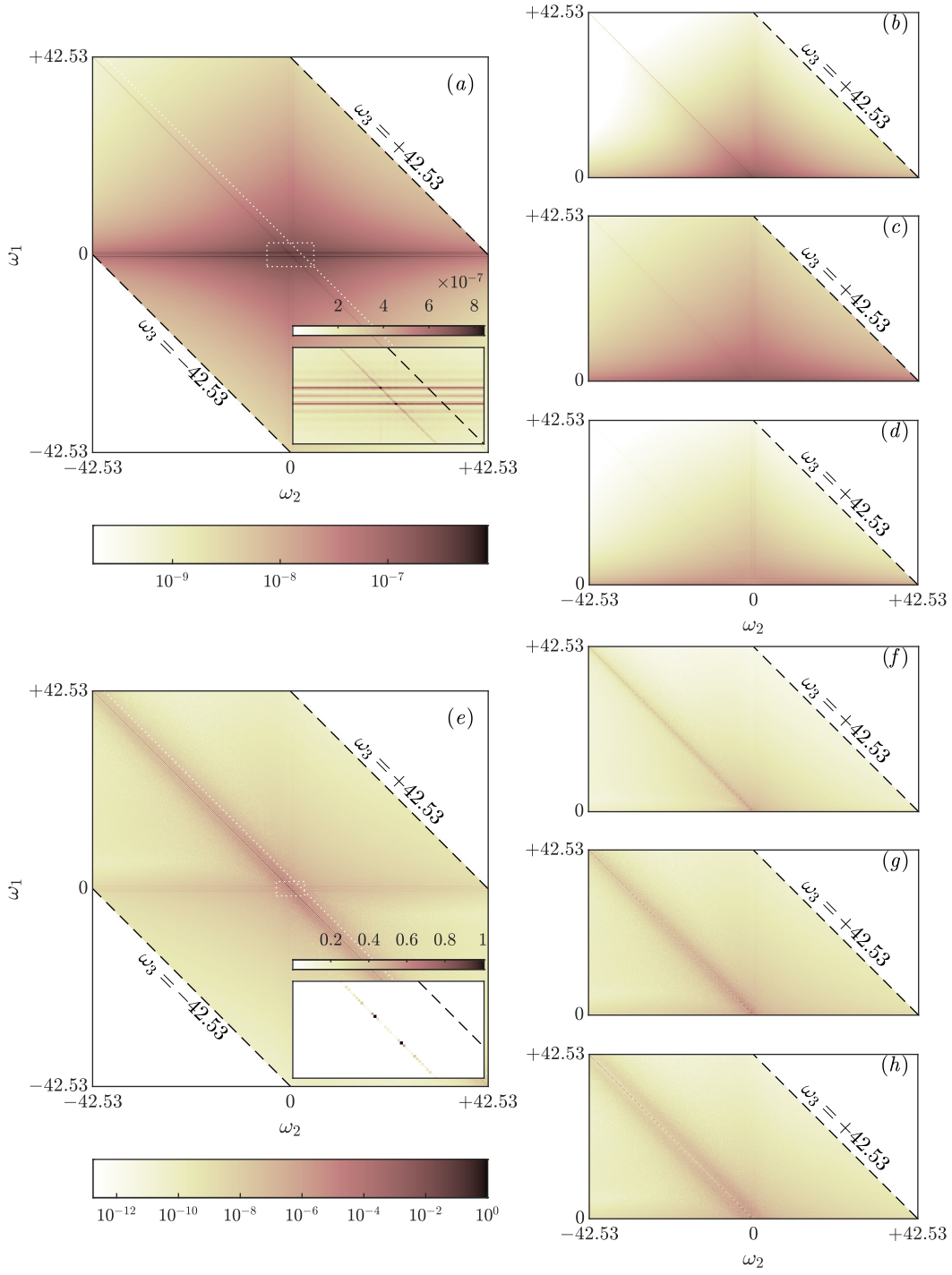

Figure 5.5: Heatmaps of the magnitude of (*a* - *d*) the temporal forcing coefficients $|P_\omega(\omega_1, \omega_2)|$, and (*e* - *h*) the temporal response coefficients $|R_\omega(\omega_1, \omega_2)|$ in the same format as Figure 5.3. The diagonal white dotted lines in (*a, e*) and the black dashed lines in the inserts mark the location of $\omega_3 = 2.492$ ($\omega_3^+ = 0.0953$).

ence, we utilized the phase angle of the response coefficients: a phase angle within $(+\pi/2, -\pi/2)$ or the right half plane of the complex plane indicates a positive real part with both positive or negative imaginary part; while a phase angle within $(+\pi/2, +\pi) \cup (-\pi, -\pi/2)$ or the left half plane indicates a negative real part. Since the sign of the imaginary part is of less interest, we utilize the absolute value of the phase angles, where $|\angle R| \in [0, \pi/2)$ indicates constructive interference or in other words, increase of spectral TKE, and $|\angle R| \in (\pi/2, \pi]$ indicates destructive interference or in other words, decrease of spectral TKE. In Figures 5.6, the absolute value of the phase of R_{k_x}, R_{k_z}, and R_ω are plotted, with phase angles close to 0 in red indicating constructive interference and phase angles close to π in blue indicating destructive interference.

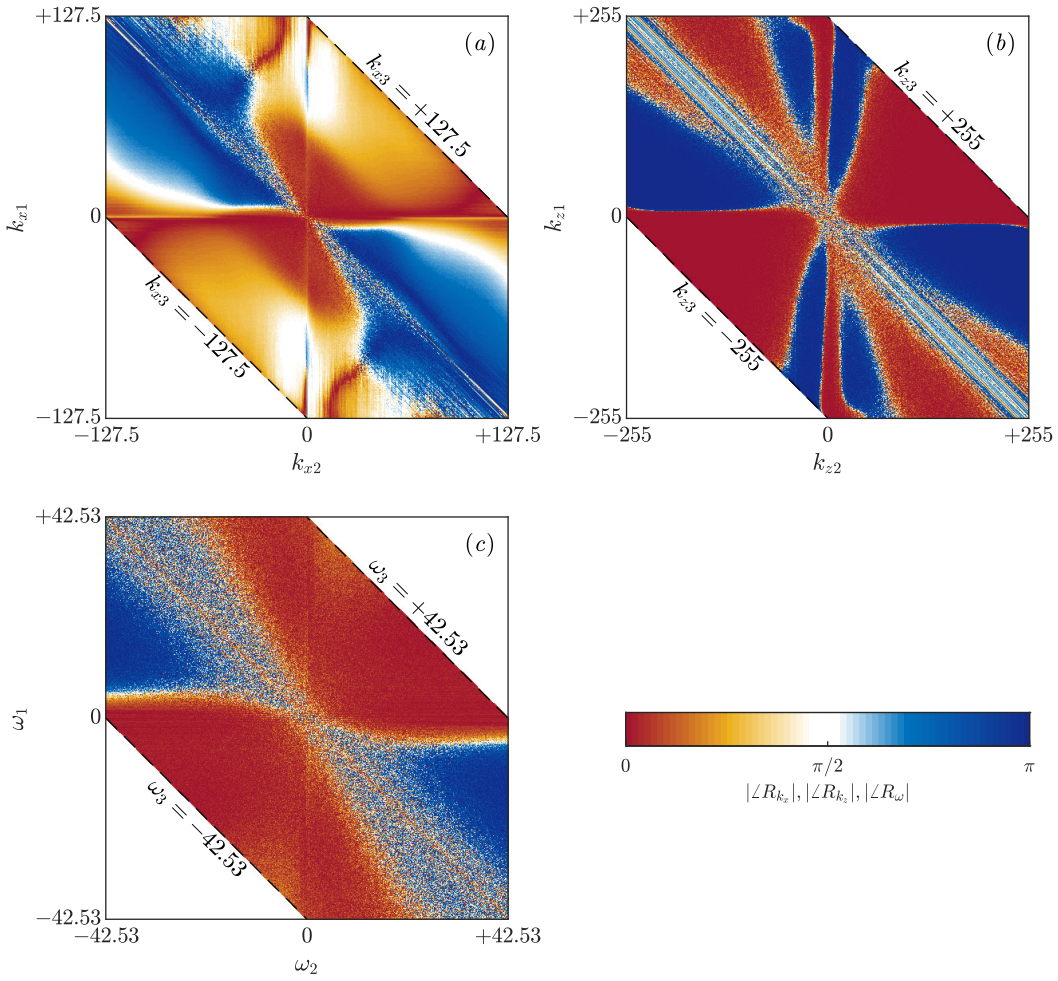

Figure 5.6: Heatmaps of the absolute values of the phase angles of the response coefficients: (*a*) $\left|\angle R_{k_x}(k_{x1}, k_{x2})\right|$, (*b*) $\left|\angle R_{k_z}(k_{z1}, k_{z2})\right|$, and (*c*) $|\angle R_\omega(\omega_1, \omega_2)|$. Phase angles close to 0 (red) indicate constructive interference, while phase angles close to π (blue) indicate destructive interference.

It should be noted that the constructive and destructive interference studied here are different from typical studies of energy transfer focusing on the turbulent transport term. As noted in equation (2.23), a non-linear energy transfer into a mode at $\boldsymbol{k}_3$ by turbulent transport does not necessarily result in an increase in spectral TKE due to the presence of other linear mechanisms. However, in this study, with both the non-linear energy transfer and linear energy amplification mechanisms studied together, constructive or destructive interference directly indicates an increase or decrease of the spectral TKE, providing a different perspective compared to energy transfer studies.

The overall structure of the phase plots can be seen as a red hour-glass structure spanning from the bottom-left to the top-right, which is obvious across all three subplots, and a blue hour-glass structure spanning from the top-left to bottom right, which is obvious for R_{k_x} and R_ω, but exhibits more complex behavior for R_{k_z}. To analyze this structure, we will focus on lines of constant $\boldsymbol{k}_3$, which are lines with slopes of -1, parallel to the dashed lines marking the extreme values of $\boldsymbol{k}_3$. Equation (5.10a) indicates that summing along this line of constant k_{x3} gives the energy of all modes at k_{x3}. Within this line, the central region with small k_{x1} and k_{x2}, representing the interactions between the large scales, generally contributes positively to the energy, while the corner regions, representing the interactions between small scales, generally reduce energy. This is consistent with the energy cascade, where turbulent kinetic energy is being generated at the large scales, transferred to small scales through triadic interactions, and dissipated at the small scales by viscosity. For the phase of R_ω, the general structure behaves similarly. However, the central region is more fuzzy while generally remaining red, contributing positively towards the energy. This is likely due to the fact that, unlike k_x where only large scales contribute towards low k_x, for ω, both large scales with high wavespeeds and small scale with low wavespeeds can contribute to low ω. This phenomenon results in the coexistence of the high-value discrete lines and the smooth varying background in the magnitude of R_ω discussed in the previous section, and mostly likely contributes to the fuzziness in the central region. For the phase of R_{k_z}, the general structure remains similar, while more complex structures exist that would require future studies.

5.3 Quasi-linear and Generalized Quasi-linear Contributions to the Forcing and Response

In Figure 5.3, we observed three regions of dominant contributions to the forcing and response, all corresponding to triadic interactions involving the streamwise large scales, consistent with the assumptions underlying QL and GQL analyses. It should be emphasized that P_{k_x} and R_{k_x} are measurements of the triadic contributions to the total forcing and response using data from the DNS, which is a different dynamical system compared to QL/GQL. Nevertheless, as all are mathematical approximations to the same physical system, the following analyses should be able to provide insights into the types non-linear interactions retained or lost in QL and GQL.

We start by decomposing the velocity $\boldsymbol{u}$ and non-linear forcing $\boldsymbol{f}$ in a manner reflecting the QL and GQL restrictions (e.g. Marston et al., 2016):

$$\begin{aligned} \boldsymbol{u} &= \bar{\boldsymbol{u}} + \tilde{\boldsymbol{u}} + \boldsymbol{u'} , \\ \boldsymbol{f} &= \underbrace{\bar{\boldsymbol{f}}}_{k_x=0} + \underbrace{\tilde{\boldsymbol{f}}}_{0<|k_x|\leq\Lambda} + \underbrace{\boldsymbol{f'}}_{|k_x|>\Lambda} . \end{aligned} \tag{5.18}$$

Here $\bar{\boldsymbol{u}}$, $\bar{\boldsymbol{f}}$ are the streamwise averages, i.e. all modes with $k_x = 0$. $\tilde{\boldsymbol{u}}$ and $\tilde{\boldsymbol{f}}$ contain the large scales with k_x less than or equal to the cut-off Λ, i.e. $0 < |k_x| \leq \Lambda$, and $\boldsymbol{u'}$, $\boldsymbol{f'}$ contain the residual, i.e. small scales with $|k_x| > \Lambda$. Note that the spatio-temporal mean profile $\overline{U}$ with $\boldsymbol{k} = (k_x, k_z, \omega) = (0, 0, 0)$ appears as part of $\bar{\boldsymbol{u}}$ under this decomposition.

The three terms may be grouped to reflect QL or GQL system formulations. In QL, $\Lambda = 0$, such that $\bar{\boldsymbol{u}}$ represents the base flow and $\boldsymbol{u'}$ the perturbation, while $\tilde{\boldsymbol{u}}$ is zero. For GQL, the base flow consists of all contributions with $k_x \leq \Lambda$, i.e. $\bar{\boldsymbol{u}} + \tilde{\boldsymbol{u}}$, and $\boldsymbol{u'}$ is the perturbation.

Figure 5.7(a) shows the triadic interactions permitted by QL/GQL in a tabular form, with the six possibilities for the velocity or the velocity gradient listed in the six columns, and the resulting forcing or response listed in the three rows. These regions of interactions are also plotted in Figure 5.7(b) in a k_{x1} vs k_{x2} plane similar to Figure 5.3. In this figure, the color green indicates interactions resolved in both QL/GQL and corresponds to three lines with k_{x1}, k_{x2}, or $k_{x3} = 0$ in Figure 5.7(b). The color blue indicates additional interactions included in GQL but not in QL, and in the limiting cases for GQL with $\Lambda = 0$, for which GQL is equivalent to QL, the blue regions disappear, and the triple decomposition collapses to a double decomposition. The color red indicates interactions that are modeled or neglected

in both QL/GQL. In the limiting case for GQL with $\Lambda \geq \max(k_x) = 127.5$, the red regions disappear, as all the non-linear interactions included in the DNS are also included in GQL. Finally, the hashed cells in Figure 5.7(a) indicate non-resonant, prohibited interactions; for example, the interaction of $\bar{\boldsymbol{u}}$ and $\bar{\boldsymbol{u}}$ (both $k_x = 0$) can contribute to $\bar{\boldsymbol{f}}, \bar{\boldsymbol{u}}$ ($k_x = 0$), but not $\tilde{\boldsymbol{f}}, \tilde{\boldsymbol{u}}$ nor $\boldsymbol{f'}, \boldsymbol{u'}$. From Figure 5.7($a$), it can be observed that all triadic interactions contributing to $\bar{\boldsymbol{f}}, \bar{\boldsymbol{u}}$ are resolved in QL/GQL, while for $\tilde{\boldsymbol{f}}, \tilde{\boldsymbol{u}}$ and $\boldsymbol{f'}, \boldsymbol{u'}$ only part of the triadic interactions are resolved.

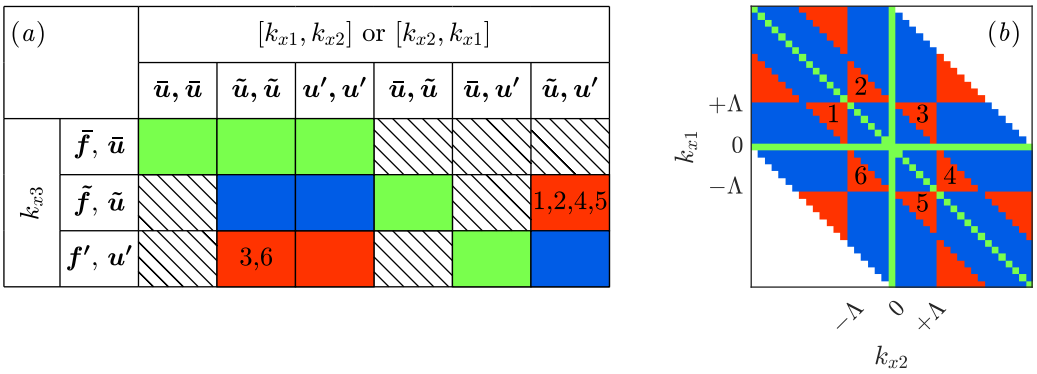

Figure 5.7: The regions of triadic interactions included in QL/GQL in (a) tabular form and (b) graphical form for comparison with Figure 5.3. The color for the table cells and figure are green for triadic interactions resolved in both QL and GQL; blue for additional triadic interactions included in GQL but not in QL; and red for triadic interactions modeled or neglected in both QL and GQL. Hashed cells in the table indicate prohibited interactions. Six special red triangular regions in the center are labeled 1-6, marking the regions that expands as Λ increases. The interaction type of each triangular region is also marked in the corresponding cell in the table.

Upon close inspection of the six red triangular regions in the center (labeled 1-6 in Figure 5.7(b)), it can be observed that the three boundaries of these triangles do not all move inwards as Λ increases. As Λ changes, an inward-moving boundary turns red regions into blue, indicating the inclusion of more triadic interactions in GQL. On the other hand, an outward-moving boundary turns a previously blue region red, indicating a loss of some previously included triadic interactions. The direction of movement of the boundary of triangular regions 1-3 are sketched in Figure 5.8. As Λ increases, only one boundary of each triangular region 1-6 moves inwards, and these triangular regions, having side lengths of Λ, increase in size and move further from the center. These triangular regions eventually reach the boundary of the figure (maximum k_x retained by the DNS), then start to decrease in size as portions of them are now outside of the figure. When Λ reaches $\max(k_x) = 127.5$, they move completely out of the figure and the GQL becomes equivalent to the DNS.

The important consequence of this is that as Λ increases, although more triadic interactions are being included globally, a portion of the previously included ones are now lost. Depending on the relative importance of the newly included and lost interactions, the increase in Λ could cause non-monotonic performance changes under certain conditions.

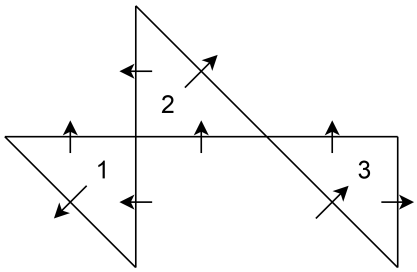

Figure 5.8: The direction of boundary movement for the red triangular regions 1-3 in the Figure 5.7 as Λ increases. Triangular regions 4-6 are the mirror images of 1-3 and are omitted in this sketch.

Comparing Figure 5.7(b) with Figure 5.3, it can be seen that the QL assumptions do indeed restrict resolved interactions to those corresponding to large forcing and response coefficients in the DNS. The blue regions in Figure 5.7(b), which are the additional interactions resolved in GQL, also correspond to large contributions to the overall forcing and response in Figure 5.3. The fractional contribution of GQL-permitted interactions to the total DNS forcing and response for varying Λ can be quantified with the following ratios:

$$\rho_f(\Lambda) = \frac{\sum_{GQL(\Lambda)} P_{k_x}(k_{x1}, k_{x2})}{\sum_{GQL(\infty)} P_{k_x}(k_{x1}, k_{x2})}, \tag{5.19}$$

$$\rho_r(\Lambda) = \frac{\sum_{GQL(\Lambda)} R_{k_x}(k_{x1}, k_{x2})}{\sum_{GQL(\infty)} R_{k_x}(k_{x1}, k_{x2})}, \tag{5.20}$$

where $\sum_{GQL(\Lambda)}$ indicates a summation in the k_{x1}, k_{x2} regions resolved by GQL with the parameter Λ (a summation over the green and blue regions in Figure 5.7(b)). As $\Lambda \to \infty$, the GQL assumptions admit the equivalent range of interactions to the DNS, with $\rho_f(\Lambda \to \infty) = \rho_r(\Lambda \to \infty) = 1$, and $\Lambda = 0$ indicates no blue region, with GQL equivalent to QL, and the ratios describing the fractional energy captured by QL.

The ratios $\rho_f(\Lambda)$ and $\rho_r(\Lambda)$ are plotted in Figure 5.9. It can be seen that for QL ($\Lambda = 0$), a small amount of forcing energy is captured while almost all the response energy is already captured. This is due to the fact that almost all the response energy

is concentrated at $k_{x3} = 0$ shown in the insert of Figure 5.3(e), and it is expected for QL to perform well for this flow. However, as discussed in the previous section, the concentration at $k_{x3} = 0$ is likely the result of a small simulation domain size. With larger domains properly resolving the streamwise large scales, the concentration is expected to be located at small but non-zero k_{x3}, which necessitates the use of GQL. In addition, $\rho_f(\Lambda)$ and $\rho_r(\Lambda)$ converge rapidly, due to the summation over regions of P_{k_x} and R_{k_x}, despite requiring a large number of snapshots for the convergence of P_{k_x} and R_{k_x} themselves. Small differences are observed in Figure 5.9 when ρ_f and ρ_r are computed using the first temporal segment rather than the average of all five temporal segments, and therefore ρ_f and ρ_r can be approximated with a short statistically steady DNS run.

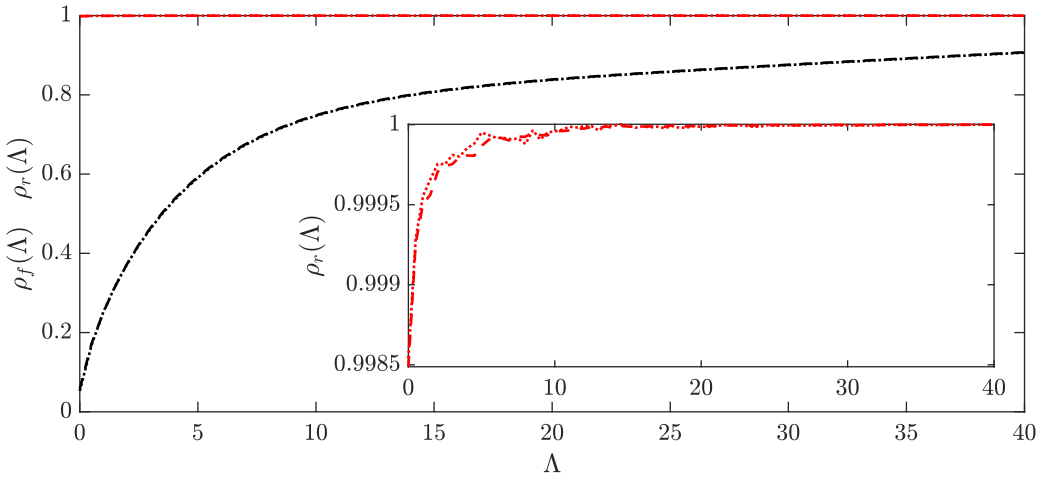

Figure 5.9: Fraction of total DNS forcing and response energy captured by interactions obeying GQL assumptions for various values of Λ. The black lines are $\rho_f(\Lambda)$ for the forcing and the red lines are $\rho_r(\Lambda)$ for the response. For both the forcing and response, the dashed lines are results computed using the coefficients averaged over all five temporal segments, while the dotted lines are the results computed using only the first temporal segment. The insert is a zoomed in view of $\rho_r(\Lambda)$.

With the previous analysis of GQL regions for all k_{x3} dominated by the mode at $k_{x3} = 0$, we now perform the analysis again for specific values of k_{x3}. The two energy ratios are redefined:

$$\gamma_f(\Lambda, k_{x3}) = \frac{\sum_{GQL(\Lambda),k_{x1}+k_{x2}=\pm k_{x3}} P_{k_x}(k_{x1}, k_{x2})}{\sum_{GQL(\infty),k_{x1}+k_{x2}=\pm k_{x3}} P_{k_x}(k_{x1}, k_{x2})}, \tag{5.21}$$

$$\gamma_r(\Lambda, k_{x3}) = \frac{\sum_{GQL(\Lambda),k_{x1}+k_{x2}=\pm k_{x3}} R_{k_x}(k_{x1}, k_{x2})}{\sum_{GQL(\infty),k_{x1}+k_{x2}=\pm k_{x3}} R_{k_x}(k_{x1}, k_{x2})}. \tag{5.22}$$

The summation $\sum_{GQL(\Lambda),k_{x1}+k_{x2}=\pm k_{x3}}$, is still the summation in the k_{x1}, k_{x2} regions resolved by GQL with the parameter Λ (green and blue regions), with the added restriction of $k_{x1} + k_{x2} = \pm k_{x3}$ (along two lines with slopes of -1 corresponding to constant $\pm k_{x3}$). The resulting ratios are plotted in Figure 5.10 for $k_{x3} = 0.5$, a representative large scale and in Figure 5.11 for $k_{x3} = 4$ ($\lambda_x^+ \approx 900$), the peak of the near wall cycle.

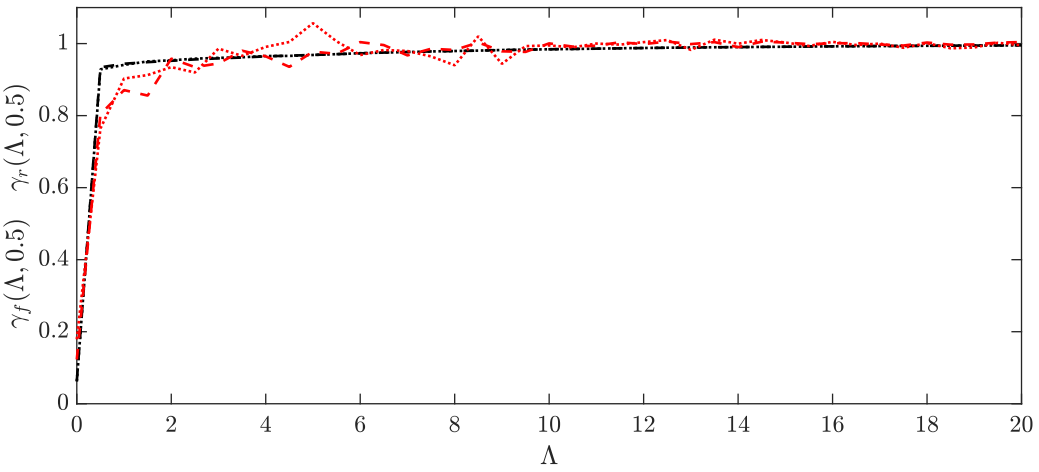

Figure 5.10: Fraction of total DNS forcing and response energy captured by interactions obeying GQL assumptions for various values of Λ and restricted to $k_{x3} = k_{x1} + k_{x2} = 0.5$, a representative large scale. The black lines are $\gamma_f(\Lambda, 0.5)$ for the forcing and the red lines are $\gamma_r(\Lambda, 0.5)$ for the response. For both the forcing and response, the dashed lines are results computed using the coefficients averaged over all 5 temporal segments, while the dotted lines are the results computed using only the first temporal segment.

For $k_{x3} = 0.5$ in Figure 5.10, it can be observed that at $\Lambda = 0$ (QL), very little energy for both the forcing and response are captured. This is expected as $k_x = 0.5$ is not contained in the large scale base flow for $\Lambda = 0$, and the only triadic interactions included are $(k_{x1}, k_{x2}) = (0, 0.5)$ and $(0.5, 0)$, which constitutes a small fraction of energy for $k_{x3} = 0.5$. Both $\gamma_f(\Lambda, 0.5)$ and $\gamma_r(\Lambda, 0.5)$ immediately jump above 0.8 starting from $\Lambda = 0.5$. For $\Lambda \geq 0.5$, the $k_x = 0.5$ modes are included in the large-scale base flow, and almost all triadic interactions contributing to $k_{x3} = 0.5$ are included except for the pairs $(k_{x1}, k_{x2}) = (\Lambda + 0.5, -\Lambda)$ and $(-\Lambda, \Lambda + 0.5)$ (the tips of triangles 2 and 4 in Figure 5.7(b)). As Λ increases, this neglected pair of interactions moves towards less energetic regions and the energy ratios quickly converge to 1, with some overshoots due to the missing of destructive interference.

For $k_{x3} = 4$ in Figure 5.11, corresponding to the peak of the near wall cycle, more

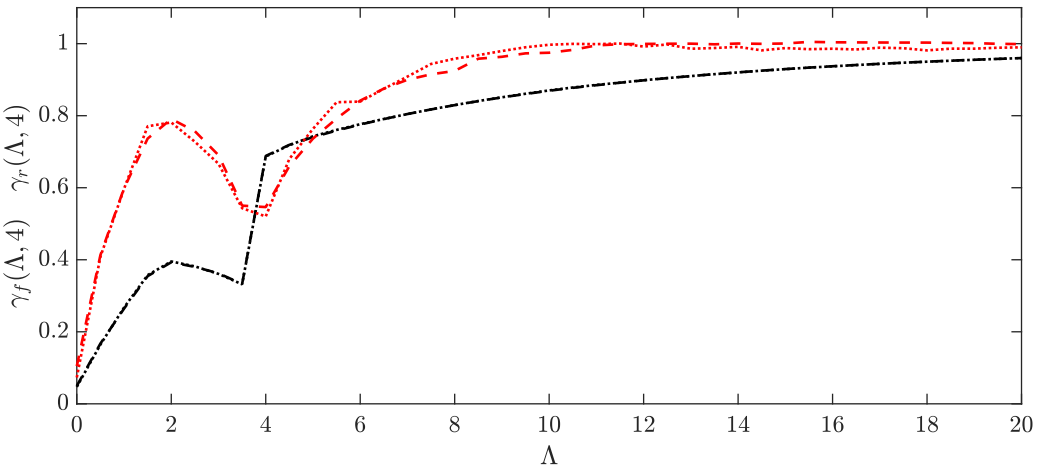

Figure 5.11: Fraction of total DNS forcing and response energy captured by interactions obeying GQL assumptions for various values of Λ and restricted to $k_{x3} = k_{x1} + k_{x2} = 4$ ($\lambda_x^+ \approx 900$), the peak of the near-wall cycle, in the same format as the previous figure.

interesting behavior is observed. The ratios start off at a low value for $\Lambda = 0$ due to the same reason as the previous case, then steadily increase till $\Lambda = 2$ before decreasing till $\Lambda = 4$, and finally increase steadily till convergence around 1. We first compute the range of triadic interactions *not* included for given Λ:

$$k_{x1} \in \begin{cases} (-\infty, -\Lambda) \cup (\Lambda, 4-\Lambda) \cup (4+\Lambda, \infty) & \text{for } \Lambda \in (0,2) \\ (-\infty, -\Lambda) \cup [4-\Lambda, \Lambda] \cup (4+\Lambda, \infty) & \text{for } \Lambda \in [2,4) \\ (\Lambda, \Lambda+4] \cup [-\Lambda, 4-\Lambda) & \text{for } \Lambda \in [4,\infty) \end{cases} . \tag{5.23}$$

It can be seen that for $\Lambda \in (0,2)$, all three ranges shrink in size as Λ increases, indicating more triadic interactions are being steadily added while none are lost. In addition, due to the small Λ, the included regions almost exclusively contribute to constructive interference, resulting in monotonically increasing γ_f and γ_r. For $\Lambda \in [2,4)$ however, the triangle 3 in Figure 5.7(b) is now one of the regions not included for $k_{x3} = 4$. As Λ increases, this red region increases in size, losing triadic interactions and causing γ_f and γ_r to decrease. Finally, for $\Lambda \geq 4$, $k_{x3} = 4$ is now included in the base flow as one of the large scales, although the ranges of not included k_{x1} remain constant in size (going across triangles 2 and 4 in Figure 5.7(b)), they get pushed out to less energetic regions, resulting in increasing γ_f and γ_r, eventually converging to 1. This phenomenon is, in fact, the standard behavior for most (if not all) $k_{x3} \geq 1.5$, where the ratios increase for $\Lambda \in (0, k_{x3}/2)$, decrease for $\Lambda \in [k_{x3}/2, k_{x3})$ and increase again for $\Lambda \in [k_{x3}, \infty)$. $k_{x3} = 0.5$ and 1 do not behave like this due to the non-existence of the first two ranges of Λ.

However, it should be noted that the non-monotonic behavior is mainly located in regions with $k_{x3} > \Lambda$, which means it mainly affects the unresolved small scales, and may or may not manifest itself in the resolved large scales.

With these studies, it can be observed that including a small number of k_x wavenumbers in the base flow using GQL is very effective at capturing the important triadic interactions for the forcing and even more effective for the response. However, the increase in Λ does not guarantee a monotonic performance increase of GQL, due to the morphing of the neglected regions of triadic interactions. Finally, we will emphasize again that all the above analyses are performed using data from the DNS, a different dynamical system compared to QL/GQL. In QL/GQL, the modes will equilibrate at different amplitudes, shapes, and potentially phases due to the different dynamics compared to the DNS. Therefore, capturing triadic interaction shown to be important by the DNS data is not a sufficient condition, yet it is beneficial and likely a necessary condition for the success of reduced models.

5.4 Conclusion and Future Directions

In this chapter, we developed a new method to characterize spatio-temporal, resonant triadic interactions, which arise due to the quadratic non-linearity in the Navier-Stokes equations viewed from the Fourier domain. We anticipate that this work will be useful in identifying improved modeling of the nonlinearity, especially in quasi-linear, generalized quasi-linear, and resolvent analyses.

We proposed forcing and response coefficients to quantify the contribution from each pair of interacting wavenumber-frequency triplets to the resulting non-linear forcing and velocity response. The response coefficients, although similar to traditional bispectrum analyses, include the linear resolvent operator, providing a new and more complete description of the effect of the triadic interactions on the resulting turbulent kinetic energy at each wavenumber-frequency triplet.

The coefficients show the importance of interactions involving large-scale structures. For the large scales, we observed that it is mainly driven by the interactions between large scales, while interactions between small scales are non-negligible energy extraction mechanisms, consistent with the energy cascade. For the small scales, it is revealed that the long-range interactions between large scales and the small scale gradients contribute significantly, consistent with the coherence revealed by amplitude modulation studies which relate large-scale fluctuations to the modulation of near-wall structures. Finally, the phases of the coefficients are also utilized to reveal

the constructive and destructive energy contributions by the triadic interactions.

Further, the subset of the total interactions that are permitted under QL and GQL reductions correspond well with regions of high amplitude forcing and response coefficients, and increasing the number of GQL-large scales, Λ, expands the permitted interactions to increase the total forcing and response energy captured. This analysis, performed only on DNS data, reinforces the modeling assumptions underlying QL and GQL approaches, albeit without analyzing the dynamics of QL/GQL.

We emphasize that ρ_f, ρ_r and γ_f, γ_r are measurements of the contribution of the interactions permitted under QL/GQL reductions to the total forcing and response calculated by DNS of the full NSE. As such, it gives an indication of a possible reason for the success of QL and GQL simulations in replicating features of wall turbulence, without consideration of the different dynamics associated with the restricted systems. Detailed analysis of changes in the neglected triadic interactions as Λ changes in GQL is also performed. Due to the morphing of the neglected regions of triadic interactions as Λ increases, certain triadic interactions can be lost while others are being included. The relative importance between the lost and newly included triadic interactions could cause non-monotonic performance in GQL as Λ increases. This is shown to have a strong effect on the unresolved small scales and may even result in complex behaviors for the resolved large scales.

For future work, it would be useful to conduct the analysis on DNS of channels with longer streamwise domains so that the large scales can be properly resolved. In addition, the application of this method to more complex flows would be of great interest and could assist in the understanding of the underlying non-linear mechanisms behind less understood flows. This method can also be applied to a QL/GQL dataset and compare the resulting triadic interactions with the results reported here to further the understanding of the underlying effect of the truncation of permitted interactions under QL/GQL. Finally, the method can be further extended to study two-point correlations in y instead of integrating in y. However, the two additional dimensions will lead to difficulties in computation and more so in data visualization.

Chapter 6

TRIADIC CONTRIBUTIONS TO THE NEAR WALL CYCLE

In the previous chapter, we performed the analyses using 2-dimensional coefficients P_{k_x}, P_{k_z}, P_ω, R_{k_x}, R_{k_z}, and R_ω, where the interactions in k_x, k_z, and ω are analyzed separately. In this chapter, we will analyze individual triadic interactions that all contribute to a single $\boldsymbol{k}_3$, a representative triplet of the near-wall cycle. We start with a brief discussion of the selection of $\boldsymbol{k}_3$, followed by three-dimensional analyses of the forcing and response coefficients that reveal relationships between interactions in the streamwise and temporal directions. Finally, three individual triadic interactions are selected to demonstrate the effect of the low-rank linear resolvent operator.

6.1 Triadic Contributions to a Single $\boldsymbol{k}_3$ Representative of the Near-wall Cycle

In this chapter, we focus on analyzing the triadic contributions to a single Fourier mode at $\boldsymbol{k}_3$. The wavenumbers $k_{x3} = 4$ and $k_{z3} = 28$ are selected to represent the near-wall cycle. They are the peaks in the pre-multiplied time-averaged streamwise power spectra in $k_x - y$ and $k_z - y$ planes, and are marked with + markers in Figures 4.2(a - b). $\omega_3 = 2.492$ is then selected for being the most energetic wavenumber at $k_{x3} = 4$, $k_{z3} = 28$. This resulting mode of $\boldsymbol{k}_3 = [4,\ 28,\ 2.492]$ has a wavespeed of $c_3 = \omega_3/k_{x3} = 0.62$, and corresponds to $\lambda_x^+ = 865$, $\lambda_z^+ = 124$, $\omega_3^+ = 0.0953$, and $c_3^+ = \omega_3^+/k_{x3}^+ = 13$ in inner scales.

Following previous notations, the velocity Fourier modes corrected for the effect of the window function at $\boldsymbol{k}_3$ are denoted as $\tilde{\boldsymbol{u}}(\boldsymbol{k}_3, y)$, and the forcing Fourier modes are denoted as $\boldsymbol{f}(\boldsymbol{k}_3, y)$. The Fourier modes themselves, obtained from finite time temporal segments, have variations in both phase and amplitude across different temporal segments (or different realizations). To improve the convergence, we will examine the energy of the forcing and velocity Fourier modes averaged across the different temporal segments, $\mathbb{E}\left\{|\boldsymbol{f}(\boldsymbol{k}_3, y)|^2\right\}$ and $\mathbb{E}\left\{|\tilde{\boldsymbol{u}}(\boldsymbol{k}_3, y)|^2\right\}$, or in other words the spectral TKE as a function of y. This process of averaging over multiple temporal segments is the Welch's method to estimate the PSD (Welch, 1967), as similarly employed in the works of Towne et al. (2018), Nogueira et al. (2021) and Morra et al. (2021). The energy of the forcing and velocity Fourier modes, $\mathbb{E}\left\{|\boldsymbol{f}(\boldsymbol{k}_3, y)|^2\right\}$ and $\mathbb{E}\left\{|\tilde{\boldsymbol{u}}(\boldsymbol{k}_3, y)|^2\right\}$, are plotted in Figure 6.1 together with $\mathbb{E}\left\{|\mathcal{H}(\boldsymbol{k}_3, y)\boldsymbol{f}(\boldsymbol{k}_3, y)|^2\right\}$ for comparison. The agreement between $\tilde{\boldsymbol{u}}(\boldsymbol{k}_3, y)$ and

$\mathcal{H}(\boldsymbol{k}_3, y)\boldsymbol{f}(\boldsymbol{k}_3, y)$, is first demonstrated in Chapter 4 Figure 4.7 in an y-integrated sense for all $\boldsymbol{k}_3$. Excellent agreement is observed for low ω_3 modes, and good agreement for high ω_3 modes except those with very little energy. In this section, we further demonstrate this excellent agreement across all y locations, for the selected $\boldsymbol{k}_3$ representing the near-wall cycle, using the bottom row of Figure 6.1, where very close alignment can be observed between the black lines for $\mathbb{E}\left\{|\tilde{\boldsymbol{u}}(\boldsymbol{k}_3, y)|^2\right\}$ and red lines for $\mathbb{E}\left\{|\mathcal{H}(\boldsymbol{k}_3, y)\boldsymbol{f}(\boldsymbol{k}_3, y)|^2\right\}$. Although only the results averaged over all temporal segments are plotted in Figure 6.1, all five individual temporal segments at this $\boldsymbol{k}_3$ exhibit similar levels of close agreement between $\tilde{\boldsymbol{u}}(\boldsymbol{k}_3, y)$ and $\mathcal{H}(\boldsymbol{k}_3, y)\boldsymbol{f}(\boldsymbol{k}_3, y)$.

As shown in equation (2.19), the forcing Fourier mode at $\boldsymbol{k}_3$ is the sum of all interactions between triadically compatible pairs of $\boldsymbol{k}_1$ and $\boldsymbol{k}_2$, with $\boldsymbol{k}_1 + \boldsymbol{k}_2 = \boldsymbol{k}_3$. Here, we introduce the notation for the individual contributions to the forcing and velocity Fourier modes by the interaction between $\boldsymbol{k}_1$ and $\boldsymbol{k}_2$:

$$\boldsymbol{f}(\boldsymbol{k}_1, \boldsymbol{k}_2, y) = -\boldsymbol{u}(\boldsymbol{k}_1, y) \cdot \nabla \boldsymbol{u}(\boldsymbol{k}_2, y), \tag{6.1a}$$

$$\tilde{\boldsymbol{u}}(\boldsymbol{k}_1, \boldsymbol{k}_2, y) = \mathcal{H}(\boldsymbol{k}_1 + \boldsymbol{k}_2, y)\boldsymbol{f}(\boldsymbol{k}_1, \boldsymbol{k}_2, y), \tag{6.1b}$$

and the energy of each term, averaged over all temporal segments, is defined as:

$$E_f(\boldsymbol{k}_1, \boldsymbol{k}_2) = \mathbb{E}\left\{\langle \boldsymbol{f}(\boldsymbol{k}_1, \boldsymbol{k}_2, y),\ \boldsymbol{f}(\boldsymbol{k}_1, \boldsymbol{k}_2, y)\rangle_y\right\}, \tag{6.2a}$$

$$E_u(\boldsymbol{k}_1, \boldsymbol{k}_2) = \mathbb{E}\left\{\langle \tilde{\boldsymbol{u}}(\boldsymbol{k}_1, \boldsymbol{k}_2, y),\ \tilde{\boldsymbol{u}}(\boldsymbol{k}_1, \boldsymbol{k}_2, y)\rangle_y\right\}, \tag{6.2b}$$

with the inner product $\langle \cdot\ ,\ \cdot \rangle_y$ defined previously in equation (4.14). Utilizing the convolution form of the non-linear forcing given in equation (2.19), it can be shown that:

$$\boldsymbol{f}(\boldsymbol{k}_3, y) = \sum_{\boldsymbol{k}_1} \boldsymbol{f}(\boldsymbol{k}_1, \boldsymbol{k}_3 - \boldsymbol{k}_1, y), \tag{6.3a}$$

$$\tilde{\boldsymbol{u}}(\boldsymbol{k}_3, y) = \sum_{\boldsymbol{k}_1} \tilde{\boldsymbol{u}}(\boldsymbol{k}_1, \boldsymbol{k}_3 - \boldsymbol{k}_1, y). \tag{6.3b}$$

The relationships of these quantities are visually represented by the diagram in Figure 6.2. In the blue box 1, all quantities are the DNS velocity Fourier modes and their gradients. The different pairs of $(\boldsymbol{k}_1, \boldsymbol{k}_2)$ are all triadically compatible with the selected $\boldsymbol{k}_3$ with $\boldsymbol{k}_1 + \boldsymbol{k}_2 = \boldsymbol{k}_3$. Each pair non-linearly interacts and generates a forcing $\boldsymbol{f}(\boldsymbol{k}_1, \boldsymbol{k}_2, y)$, defined in equation (6.1a) and is located within the red box

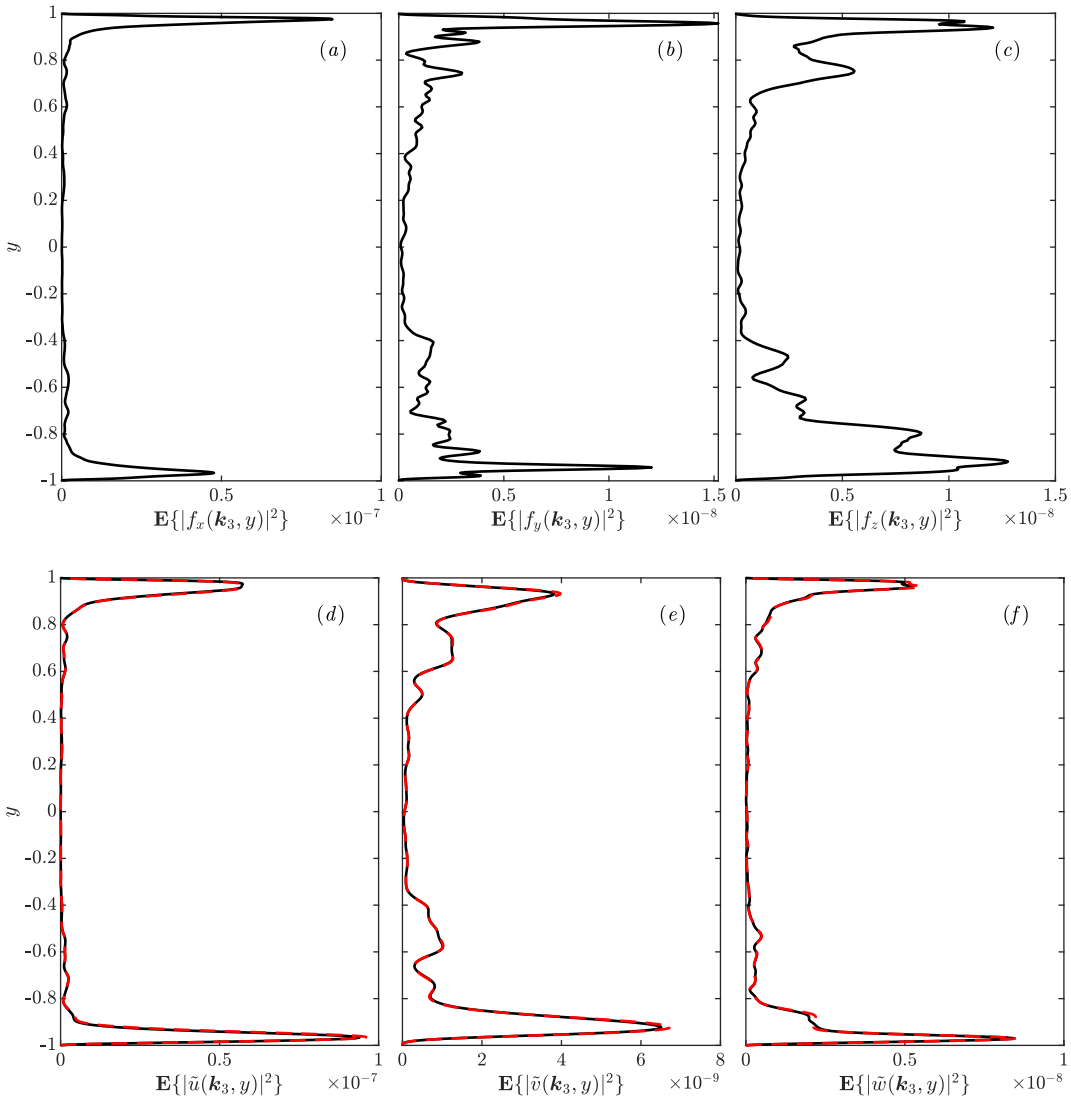

Figure 6.1: Spectral energy of Fourier modes for $\boldsymbol{k}_3 = \boldsymbol{k}_1 + \boldsymbol{k}_2 = [4,\ 28,\ 2.492]$ averaged over all temporal segments. The top row (a - c) are the three components of $\mathbb{E}\left\{|\boldsymbol{f}(\boldsymbol{k}_3,y)|^2\right\}$, the energy of the forcing Fourier modes. The black solid lines in bottom row (d - f) are the three components of $\mathbb{E}\left\{|\tilde{\boldsymbol{u}}(\boldsymbol{k}_3,y)|^2\right\}$, the energy of the velocity Fourier modes corrected for the effect of the window function, and the red dashed lines are for $\mathbb{E}\left\{|\mathcal{H}(\boldsymbol{k}_3,y)\boldsymbol{f}(\boldsymbol{k}_3,y)|^2\right\}$.

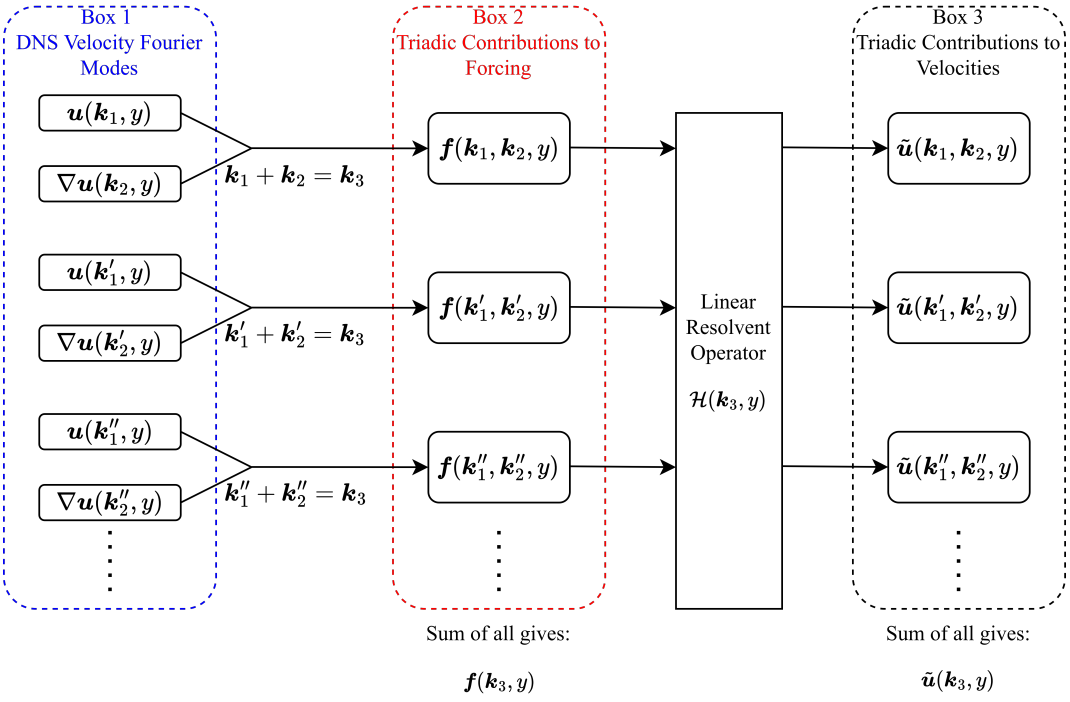

Figure 6.2: Diagram for the triadic interactions showing individual contributions toward the forcing and velocity Fourier modes by interactions between $\boldsymbol{k}_1$ and $\boldsymbol{k}_2$ that are triadically compatible with $\boldsymbol{k}_3$.

2. Equation (6.3a) indicates that the sum of everything in the red box 2 gives $\boldsymbol{f}(\boldsymbol{k}_3, y)$, the DNS forcing Fourier mode at $\boldsymbol{k}_3$. Multiplying $\boldsymbol{f}(\boldsymbol{k}_1, \boldsymbol{k}_2, y)$ by the linear resolvent operator at $\boldsymbol{k}_3$ gives the triadic contributions to the velocities by this pair of $(\boldsymbol{k}_1, \boldsymbol{k}_2)$, denoted as $\tilde{\boldsymbol{u}}(\boldsymbol{k}_1, \boldsymbol{k}_2, y)$, and defined in equation (6.1b). And finally, equation (6.3b) indicates that the sum of everything in black box 3 gives $\tilde{\boldsymbol{u}}(\boldsymbol{k}_3, y)$, the DNS velocity Fourier mode at $\boldsymbol{k}_3$ corrected for the effect of the window function.

6.2 3-dimensional Analyses of Forcing and Response Coefficients

In the previous chapter, the triadic interactions are studied using the two-dimensional forcing and response coefficients: P_{k_x}, P_{k_z}, P_ω, R_{k_x}, R_{k_z}, and R_ω, where the streamwise, spanwise, and temporal interactions are each studied separately. In this section, with a fixed $\boldsymbol{k}_3$, the original 6-dimensional forcing and response coefficients $P(\boldsymbol{k}_1, \boldsymbol{k}_2)$ and $R(\boldsymbol{k}_1, \boldsymbol{k}_2)$ defined in equations (5.1) and (5.6) collapse into 3-dimensional quantities, which can be computed and stored with reasonable resources, and can reveal additional information about the spatio-temporal nature of the non-linear interactions.

The magnitude of the forcing and response coefficients are plotted in Figure 6.3 with log scale color bars. First of all, it can be observed that the majority of the high-value markers reside towards the center, indicating that the large-scale structures have dominant contributions as observed in the last chapter. However, the largest magnitude in the figures are 2.2×10^{-10} for P, and 2.0×10^{-9} for R. These small values are the result of the low energy for this $\boldsymbol{k}_3$ mode. Individual near wall cycle modes are expected to have low energy levels, and the energy of this selected mode of $\boldsymbol{k}_3 = [4,\ 28,\ 2.492]$ is 1.3×10^{-8}. As a result, the largest magnitude of R, 2.0×10^{-9} is in fact 15% of the energy level, and is a major contributor towards this representative mode of the near wall cycle. It should also be pointed out that this chapter is directed towards studying the spatio-temporal nature of the forcing and response coefficients and not for studying the most important triadic interactions in the entire flow. As a result, this mode of $\boldsymbol{k}_3 = [4,\ 28,\ 2.492]$, with low energy level, is selected to represent the near wall cycle. For studying the most important triadic interactions in the entire flow, a $\boldsymbol{k}_3$ mode representative of the large scale structures should be selected. Results for triadic contributions towards a representative large scale is included in Appendix B.1.

Additionally, it can be observed that most of the high-value markers reside near a single plane with an almost constant $c_1 = \omega_1/k_{x1}$. This is especially evident in Figure 6.4, where both the forcing and response coefficients are summed in k_{z1} and plotted as contour plots in the $k_{x1} - \omega_1$ plane. In Figure 6.4, three different wavespeeds c_1 are also plotted: the dash-dotted lines for $c_1 = \omega_1/k_{x1} = 1$, where the wavespeed matches the center-line velocity; the dashed lines for $c_1 = c_3 = 0.63$, the wavespeed of the selected $\boldsymbol{k}_3$; and the dotted lines for $c_1 = 0.3$ ($c_1^+ = 6$). It can be observed that most of the energetic regions are bounded between $c_1^+ = 6$ and $c_1 = 1$, centering roughly around $c_1 = c_3 = 0.63$. This indicates that the main contributing triads are located roughly around $c_1 = c_2 = c_3$. Note that although the figures only show the lines with $c_1 = c_3$, they are identical to the $c_2 = c_3$ lines, as it can be proved that $c_1 = c_3$ if and only if $c_2 = c_3$ using the triadic compatibility constraint.

To understand the reason behind this phenomenon that triadic interactions located closely around $c_1 = c_2 = c_3$ contribute the most, we start by examining the energy of the forcing and response generated by the triads $\boldsymbol{k}_1$ and $\boldsymbol{k}_2 = \boldsymbol{k}_3 - \boldsymbol{k}_1$. In Figure 6.5($a$), the energy $E_f(\boldsymbol{k}_1, \boldsymbol{k}_2)$ and 6.5(b), the energy $E_u(\boldsymbol{k}_1, \boldsymbol{k}_2)$ is summed in k_{z1} and plotted in $k_{x1} - \omega_1$ plane similar to Figure 6.4 with the same wavespeeds

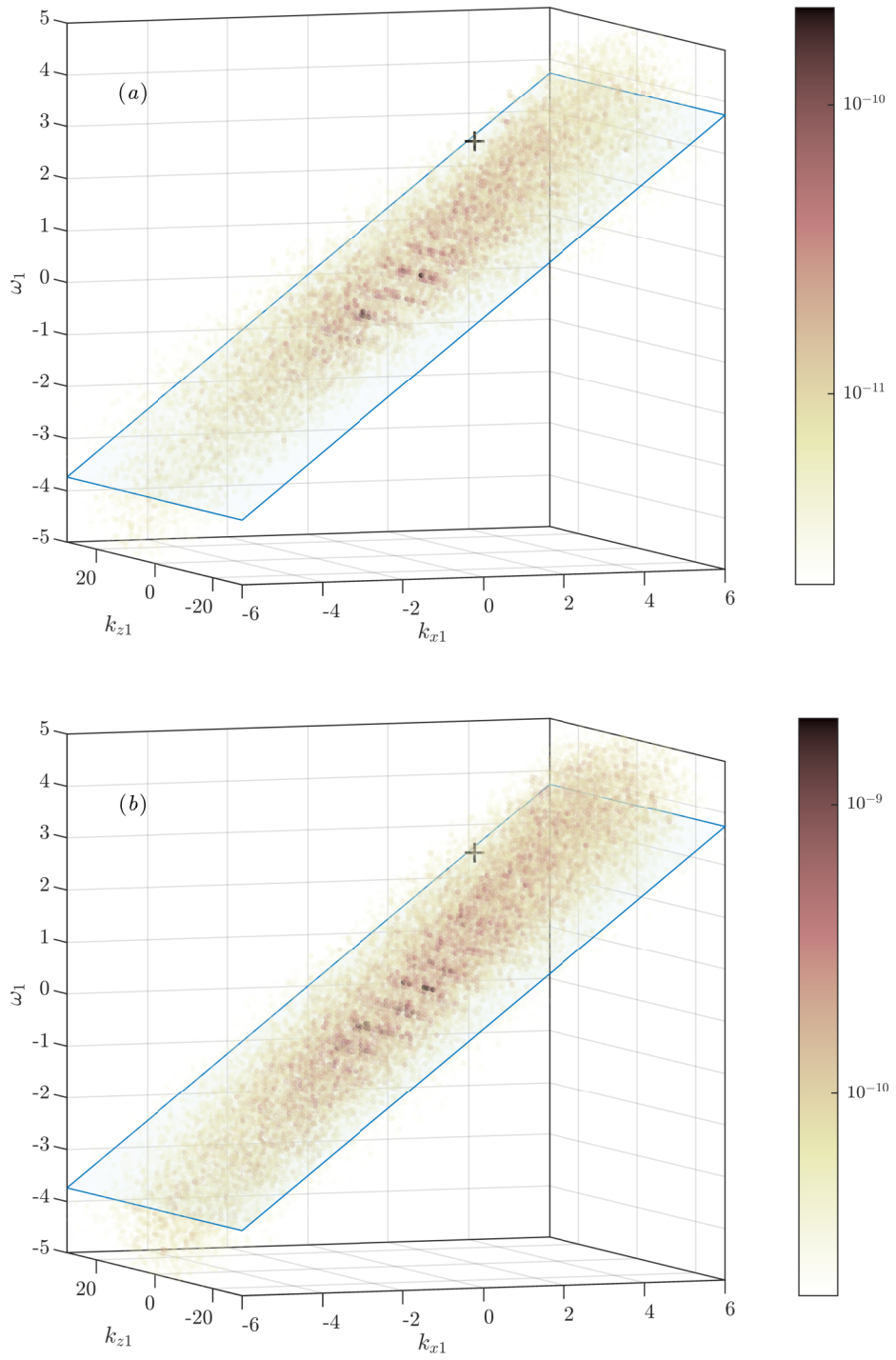

Figure 6.3: Magnitude of (a) $P(\boldsymbol{k}_1, \boldsymbol{k}_3 - \boldsymbol{k}_1)$, the forcing coefficients and (b) $R(\boldsymbol{k}_1, \boldsymbol{k}_3 - \boldsymbol{k}_1)$, the response coefficients as functions of $\boldsymbol{k}_1 = [k_{x1}, k_{z1}, \omega_1]$ with log scale color bars for $\boldsymbol{k}_3 = \boldsymbol{k}_1 + \boldsymbol{k}_2 = [4,\ 28,\ 2.492]$. The opacity of each marker is also linearly proportional to $\log_{10}$ of the magnitudes. Points with magnitude less than 1% of the peak values are not plotted. The + markers in both figures denote the location of $\boldsymbol{k}_3$, and the blue planes mark the location of $c_1 = \omega_1/k_{x1} = c_3 = 0.62$.

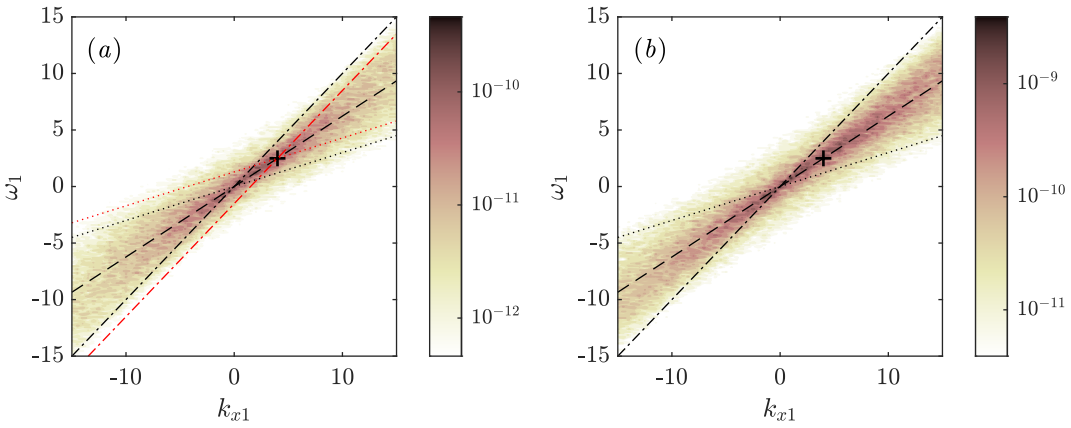

Figure 6.4: Magnitude of (a) $\sum_{k_{z1}} P(\boldsymbol{k}_1, \boldsymbol{k}_3 - \boldsymbol{k}_1)$, the forcing coefficients summed in k_{z1} and plotted as functions of k_{x1} and ω_1 for $\boldsymbol{k}_3 = [4,\ 28,\ 2.492]$, and (b) $\sum_{k_{z1}} R(\boldsymbol{k}_1, \boldsymbol{k}_3 - \boldsymbol{k}_1)$, the response coefficients. The black dash-dotted lines in both figures mark the wavespeed $c_1 = \omega/k_x = 1$; the black dashed lines for $c_1 = c_2 = c_3 = 0.63$, the wavespeed of the selected $\boldsymbol{k}_3$; and the black dotted lines for $c_1 = 0.3$ ($c_1^+ = 6$). The + markers in both figures denote the locations of $\boldsymbol{k}_3$. Subplot (a) includes an additional set of red lines, with the red dash-dotted line for $c_2 = 1$ and red dotted line for $c_2 = 0.3$ ($c_2^+ = 6$).

marked. In Figure 6.5(c), $E_u(\boldsymbol{k})$, the y-integrated turbulent kinetic energy of the DNS velocity Fourier modes, with definition given in equation (4.13), is summed in k_z and plotted in $k_x - \omega$ plane. Comparing the three figures, it can be observed that while the energetic regions of the DNS velocity Fourier modes are located much closer to $c = 1$, the energetic regions of the triadically generated forcing $E_f(\boldsymbol{k}_1, \boldsymbol{k}_2)$ are located much closer to $c_1 = c_2 = c_3$, and the triadically generated response $E_u(\boldsymbol{k}_1, \boldsymbol{k}_2)$ almost exactly on $c_1 = c_2 = c_3$.

However, the triadically generated forcing $\boldsymbol{f}(\boldsymbol{k}_1, \boldsymbol{k}_2, y)$ is the product between the DNS velocity Fourier modes at $\boldsymbol{k}_1$ and the gradient of DNS velocity Fourier modes at $\boldsymbol{k}_2$. In Figure 6.6, three sets of contours are plotted together with two sets of axes. In Figure 6.7, a set of exaggerated illustrations are plotted to highlight the features of Figure 6.6. First of all, each point in the Figures 6.6 and 6.7 represents a particular triadic interaction that contributes to the selected $\boldsymbol{k}_3$, with k_{x1} and ω_1 given on the bottom and left axes, and k_{x2} and ω_2 given on the top and right axes. The top and right axes for k_{x2} and ω_2 are flipped and shifted so that the triadic compatibility constraint is satisfied for all points in the figures. For example, in Figure 6.7(a), the point with $[k_{x1}, \omega_1] = [0, 0]$, $[k_{x2}, \omega_2] = [k_{x3}, \omega_3]$, representing the origin of the $k_{x1} - \omega_1$ axes, is marked with the black X, and the point with $[k_{x1}, \omega_1] = [k_{x3}, \omega_3]$,

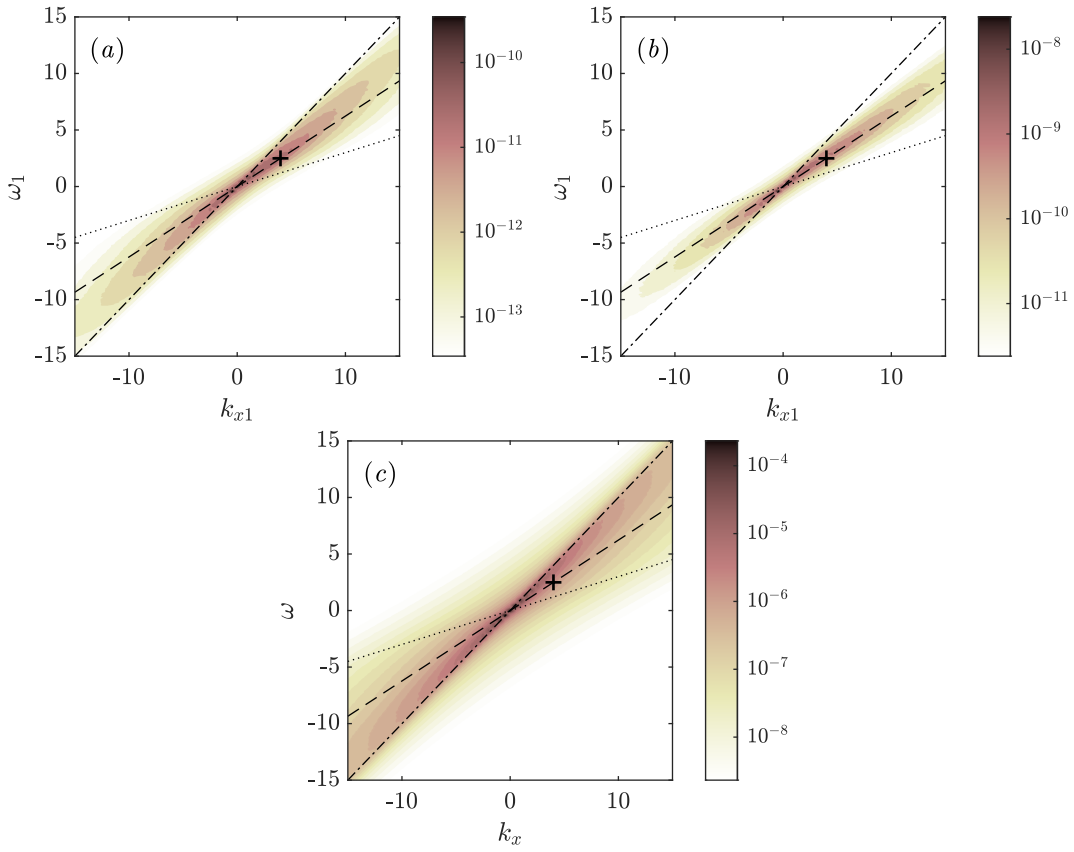

Figure 6.5: Contour plots of (a) $\sum_{k_{z1}} E_f(\boldsymbol{k}_1, \boldsymbol{k}_3 - \boldsymbol{k}_1)$, the forcing energy and (b) $\sum_{k_{z1}} E_u(\boldsymbol{k}_1, \boldsymbol{k}_3 - \boldsymbol{k}_1)$, the response energy generated by the interactions between $\boldsymbol{k}_1$ and $\boldsymbol{k}_3 - \boldsymbol{k}_1$ summed in k_{z1} and plotted as a function of k_{x1} and ω_1 for $\boldsymbol{k}_3 = [4,\ 28,\ 2.492]$. Subplot (c) is the contour of $\sum_{k_z} E_u(\boldsymbol{k})$, the y integrated kinetic energy of the DNS Fourier modes summed in k_z and plotted as a function of k_x and ω. The three lines mark the same wavespeeds as Figure 6.4: dash-dotted lines for $c_1 = 1$, dashed lines for $c_1 = c_2 = c_3 = 0.63$, and dotted lines for $c_1^+ = 6$.

$[k_{x2}, \omega_2] = [0, 0]$, representing the origin of the $k_{x2} - \omega_2$ axes, is marked with the red X. Both points lie on the line with $c_1 = c_2 = c_3$ plotted in blue dotted line and are triadically compatible with $\boldsymbol{k}_3$. The shift in the k_{x2}, ω_2 axes are marked with the arrows. In Figures 6.6 and 6.7(b), the black dashed contour lines are the energy of the DNS velocity Fourier modes at $\boldsymbol{k}_1$, and the red dashed contour lines are the energy at $\boldsymbol{k}_2$. They are both the same data as plotted in Figure 6.5(c), with the red ones shifted to the right by k_{x3} and to the top by ω_3 (the flipping of k_{x2} and ω_2 together does not change the red contour since the energy is symmetric about the origin). As seen from Figure 6.5(c), $E_u(\boldsymbol{k})$ has a peak roughly aligned with $c = 1$, which are plotted in the illustration Figure 6.7(b) with the black and red dotted lines. Finally, the blue dash-dotted contour lines in Figure 6.6 and the illustrating

Figure 6.7(c) represent the energy of the triadically generated forcing $\boldsymbol{f}(\boldsymbol{k}_1, \boldsymbol{k}_2, y)$, which is the same data from Figure 6.5(a), and can be seen to align closely to the line of $c_1 = c_2 = c_3$. For all three contour plots in Figure 6.6, the plotted contour lines are 1% of the peak value of each data set.

From Figure 6.5(c), it can be observed that the contour lines are denser near the middle and more sparse away from the center, suggesting that the energy of the Fourier modes changes more rapidly near the center. Therefore, at the bottom left corner of Figure 6.6, where it is closer to the center of the black contour ($\boldsymbol{k}_1 = 0$), and further from the center of the red contour ($\boldsymbol{k}_2 = 0$), the peak in $E_f(\boldsymbol{k}_1, \boldsymbol{k}_2)$ tends to align more with the black contours to take full advantage of larger energy from $\boldsymbol{u}(\boldsymbol{k}_1, y)$, while receiving little penalty from moving even further from the center of the red contours. As a result, the blue contours for $E_f(\boldsymbol{k}_1, \boldsymbol{k}_2)$ can be seen to align more with the black contours near the bottom left, and similarly align more with the red contours near the top right. The amount of right and top shift of red contour lines from the black is given by k_{x3} and ω_3, or in other words shifted along the line of $c_1 = c_2 = c_3$. This results in the energy of the generated forcing $E_f(\boldsymbol{k}_1, \boldsymbol{k}_3 - \boldsymbol{k}_1)$ having a peak much more closely aligned with the line of $c_1 = c_2 = c_3$ as observed in Figure 6.5(a). Additionally, the response energy is further tilted towards $c_1 = c_2 = c_3$ as observed in Figure 6.5(b), which is due to the effect of the linear resolvent operator, and would be interesting topics for future studies.

Finally, it should be noted that although the forcing and response coefficients P and R in Figure 6.4 seem to be largely bounded by $c_1 = 1$ and $c_1^+ = 6$, these two lines are only meant to be considered as references instead of bounds. This is especially true when around $k_{x1} = 0$, where the interpretation of the wavespeed fails, and a non-negligible amount of energy lies outside of the two lines. Additionally, the presence of c_2 as demonstrated in Figure 6.4(a) with the red lines also complicates this matter, as it provides another set of references. Lastly, the large-scale modes near $k_x = 0$ are also the most energetic modes, resulting in a higher level of energy overall, as evident by the non-negligible energy outside of the two reference lines in Figure 6.5(c).

In conclusion, although the triadic compatibility constraint of $\boldsymbol{k}_1 + \boldsymbol{k}_2 = \boldsymbol{k}_3$ does not impose any requirement on the relationship between wavespeeds c_1, c_2, and c_3, the quadratic nature of the non-linear forcing causes triads with three similar wavespeeds to contribute more towards both the forcing and response Fourier modes.

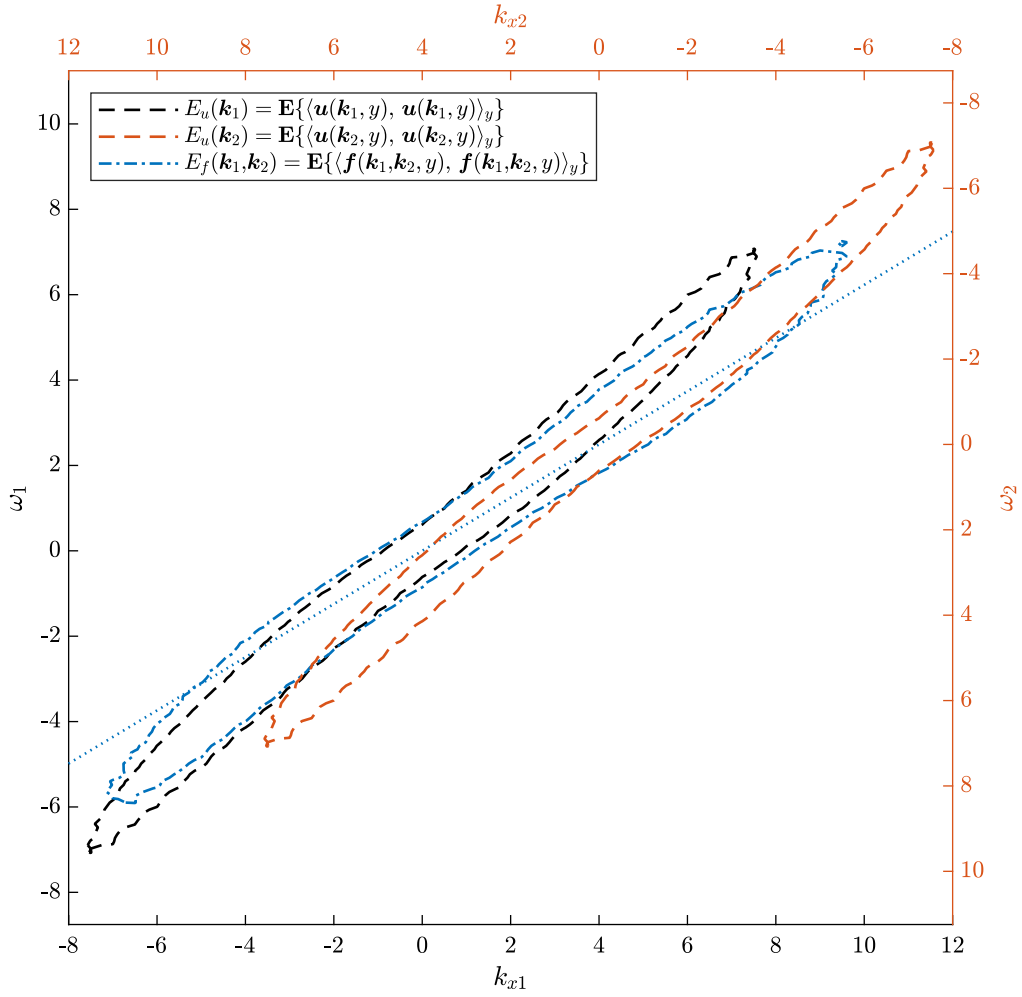

Figure 6.6: Contour lines for the y-integrated energy of $\boldsymbol{u}(\boldsymbol{k}_1, y)$ in black dashed line, energy of $\boldsymbol{u}(\boldsymbol{k}_2, y)$ in red dashed lines, and $E_f(\boldsymbol{k}_1, \boldsymbol{k}_2)$, the energy of the triadically generated forcing from interactions between $\boldsymbol{k}_1$ and $\boldsymbol{k}_2$ in blue dotted lines. All points in the figure have k_{x1} and ω_1 given by the bottom and left axes, and k_{x2} and ω_2 given by the top and right axes, all of which are triadically compatible with $\boldsymbol{k}_3 = [4,\ 28,\ 2.492]$.

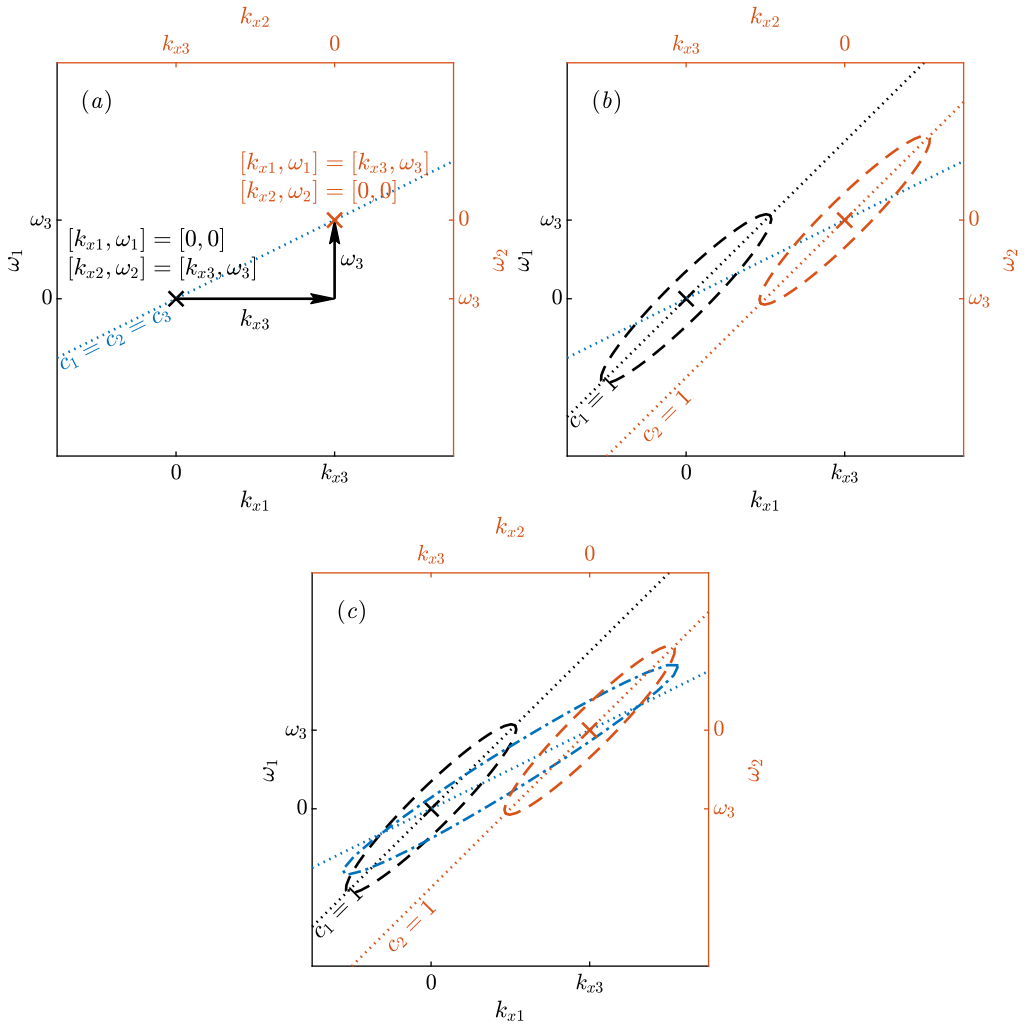

Figure 6.7: Exaggerated illustrations of the features in Figure 6.6. Subplot (a) illustrates the shift of the $k_{x2}-\omega_2$ axes along the line $c_1 = c_2 = c_3$, and the origin of the two sets of axes are marked with X. Subplot (b) illustrates the energy of the DNS velocity Fourier modes at $\boldsymbol{k}_1$ and $\boldsymbol{k}_2$, plotted in the black and red contour lines, and each aligned roughly with $c_1 = 1$ (black dotted line) and $c_2 = 1$ (red dotted line). Subplot (c) illustrates the energy of the triadically generated forcing $E_f(\boldsymbol{k}_1, \boldsymbol{k}_2)$, plotted in blue dotted lines, showing a close alignment with $c_1 = c_2 = c_3$.

This result is likely true for most (if not all) cases (with a representative large scale mode shown in appendix B.1), with future work needed to verify this for other $\boldsymbol{k}_3$ triplets. In addition, the shape of the triadically generated forcing and the linear resolvent operator might also play a role in this phenomenon and would be interesting topics for future studies.

6.3 Effect of the Linear Resolvent Operator

In this section, we will analyze individual triadic interactions to examine the effect of the linear resolvent operator. The resolvent operator at $\boldsymbol{k}_3$ can be decomposed using the SVD in equation (2.17) to obtain the response and forcing resolvent modes at $\boldsymbol{k}_3$, denoted as $\psi_q(\boldsymbol{k}_3, y)$ and $\phi_q(\boldsymbol{k}_3, y)$ respectively, and the singular values $\sigma_q(\boldsymbol{k}_3)$, which show the amplification by the resolvent operator at each mode. The non-linear weights $\chi_q(\boldsymbol{k}_3)$ obtained by projecting the forcing Fourier modes $\boldsymbol{f}(\boldsymbol{k}_3, y)$ onto the resolvent forcing modes $\phi_q(\boldsymbol{k}_3, y)$ are defined as:

$$\chi_q(\boldsymbol{k}_3) = \left\langle \phi_q(\boldsymbol{k}_3, y),\ \boldsymbol{f}(\boldsymbol{k}_3, y) \right\rangle_y . \tag{6.4}$$

Similarly, individual triadic contributions to the forcing, $\boldsymbol{f}(\boldsymbol{k}_1, \boldsymbol{k}_2, y)$, can also be projected and $\chi_q(\boldsymbol{k}_1, \boldsymbol{k}_2)$ defined as:

$$\chi_q(\boldsymbol{k}_1, \boldsymbol{k}_2) = \left\langle \phi_q(\boldsymbol{k}_1 + \boldsymbol{k}_2, y),\ \boldsymbol{f}(\boldsymbol{k}_1, \boldsymbol{k}_2, y) \right\rangle_y . \tag{6.5}$$

The Fourier forcing and response modes can therefore be reconstructed using the following as a result of the orthonormality of the response and forcing resolvent modes:

$$\boldsymbol{f}(\boldsymbol{k}_3, y) = \sum_q \chi_q(\boldsymbol{k}_3)\phi_q(\boldsymbol{k}_3, y), \tag{6.6a}$$

$$\tilde{\boldsymbol{u}}(\boldsymbol{k}_3, y) = \sum_q \chi_q(\boldsymbol{k}_3)\sigma_q(\boldsymbol{k}_3)\psi_q(\boldsymbol{k}_3, y). \tag{6.6b}$$

And similarly, for the individual triadic contributions to the forcing and response, the reconstruction is given by:

$$\boldsymbol{f}(\boldsymbol{k}_1, \boldsymbol{k}_2, y) = \sum_q \chi_q(\boldsymbol{k}_1, \boldsymbol{k}_2)\phi_q(\boldsymbol{k}_1 + \boldsymbol{k}_2, y), \tag{6.7a}$$

$$\tilde{\boldsymbol{u}}(\boldsymbol{k}_1, \boldsymbol{k}_2, y) = \sum_q \chi_q(\boldsymbol{k}_1, \boldsymbol{k}_2)\sigma_q(\boldsymbol{k}_1 + \boldsymbol{k}_2)\psi_q(\boldsymbol{k}_1 + \boldsymbol{k}_2, y). \tag{6.7b}$$

Finally, the following property can also be obtained from equation (6.3a):

$$\chi_q(\boldsymbol{k}_3) = \sum_{\boldsymbol{k}_1} \chi_q(\boldsymbol{k}_1, \boldsymbol{k}_3 - \boldsymbol{k}_1). \tag{6.8}$$

It can be seen that $\chi_q(\boldsymbol{k}_3)$ describes the amount of the q-th resolvent forcing mode contained in the DNS forcing Fourier mode at $\boldsymbol{k}_3$, while $\chi_q(\boldsymbol{k}_1, \boldsymbol{k}_3 - \boldsymbol{k}_1)$ is the amount contributed towards the q-th resolvent forcing mode by the interaction between $\boldsymbol{k}_1$ and $\boldsymbol{k}_2 = \boldsymbol{k}_3 - \boldsymbol{k}_1$. Similarly $\sigma_q(\boldsymbol{k}_3)\chi_q(\boldsymbol{k}_3)$ describes the amount of the q-th resolvent response mode contained in the DNS velocity Fourier mode at $\boldsymbol{k}_3$, while $\sigma_q(\boldsymbol{k}_3)\chi_q(\boldsymbol{k}_1, \boldsymbol{k}_3 - \boldsymbol{k}_1)$ is the amount contributed towards the q-th resolvent response mode by the interaction between $\boldsymbol{k}_1$ and $\boldsymbol{k}_2$.

It should be noted that velocity and forcing Fourier modes $\boldsymbol{f}(\boldsymbol{k}_3, y)$ and $\tilde{\boldsymbol{u}}(\boldsymbol{k}_3, y)$, and the resulting triadically generated forcing and response modes $\boldsymbol{f}(\boldsymbol{k}_1, \boldsymbol{k}_2, y)$ and $\tilde{\boldsymbol{u}}(\boldsymbol{k}_1, \boldsymbol{k}_2, y)$ all have variations across different temporal segments. As a result, both $\chi_q(\boldsymbol{k}_3)$ and $\chi_q(\boldsymbol{k}_1, \boldsymbol{k}_2)$ also vary across different temporal segments. Therefore, we will be analyzing the power spectral density of these quantities, such as $\mathbb{E}\left\{\left|\chi_q(\boldsymbol{k}_3)\right|^2\right\}$ and $\mathbb{E}\left\{\left|\chi_q(\boldsymbol{k}_1, \boldsymbol{k}_2)\right|^2\right\}$, which are averaged across all available temporal segments. This is similar to the analysis performed in Towne et al. (2018) and Morra et al. (2021), where the cross spectral density is used to describe the non-linear weights.

Substituting equations (6.6a)-(6.7b) into the definitions of $P(\boldsymbol{k}_1, \boldsymbol{k}_2)$ in equation (5.1) and $R(\boldsymbol{k}_1, \boldsymbol{k}_2)$ in equation (5.6), and using the orthonormality of the resolvent modes, we can obtain:

$$P(\boldsymbol{k}_1, \boldsymbol{k}_2) = \sum_q \mathbb{E}\left\{\chi_q^*(\boldsymbol{k}_1 + \boldsymbol{k}_2)\chi_q(\boldsymbol{k}_1, \boldsymbol{k}_2)\right\}, \tag{6.9a}$$

$$R(\boldsymbol{k}_1, \boldsymbol{k}_2) = \sum_q \sigma_q^2(\boldsymbol{k}_1 + \boldsymbol{k}_2)\mathbb{E}\left\{\chi_q^*(\boldsymbol{k}_1 + \boldsymbol{k}_2)\chi_q(\boldsymbol{k}_1, \boldsymbol{k}_2)\right\}, \tag{6.9b}$$

note that σ_q can be moved outside of the expected value operator as these are quantities computed from the deterministic resolvent operator that remains unchanged. From these, we clearly see the effect of the resolvent operator included in the definition of $R(\boldsymbol{k}_1, \boldsymbol{k}_2)$ shown as the weight σ_q^2 for each q. The linear resolvent operator amplifies the different forcing modes differently, and the effect is captured in the response coefficients $R(\boldsymbol{k}_1, \boldsymbol{k}_2)$. The energy of the forcing and response generated by the interactions between $\boldsymbol{k}_1$ and $\boldsymbol{k}_2$, defined in equations (6.2a) and (6.2b) can also be rewritten in terms of σ_q and χ_q:

$$E_f(\boldsymbol{k}_1, \boldsymbol{k}_2) = \sum_q \mathbb{E}\left\{\left|\chi_q(\boldsymbol{k}_1, \boldsymbol{k}_2)\right|^2\right\}, \tag{6.10a}$$

$$E_u(\boldsymbol{k}_1, \boldsymbol{k}_2) = \sum_q \sigma_q^2(\boldsymbol{k}_1 + \boldsymbol{k}_2)\mathbb{E}\left\{\left|\chi_q(\boldsymbol{k}_1, \boldsymbol{k}_2)\right|^2\right\}. \tag{6.10b}$$

To analyze the effect of the linear resolvent operator, we start by examining the singular values $\sigma_q(\boldsymbol{k}_3)$ of the resolvent, the non-linear weights $\mathbb{E}\left\{\left|\chi_q(\boldsymbol{k}_3)\right|^2\right\}$, and their product $\mathbb{E}\left\{\left|\sigma_q(\boldsymbol{k}_3)\chi_q(\boldsymbol{k}_3)\right|^2\right\}$ in Figure 6.8. It can be observed from Figure 6.8(a) that the first two singular values are larger than the rest, showing that the linear resolvent operator predominately amplifies the first two modes and is low-rank at this $\boldsymbol{k}_3$. Figure 6.8(b) shows that the non-linear weights $\chi_q(\boldsymbol{k}_3)$ are roughly the same order of magnitude throughout, with the first few modes on the smaller side. This shows that the first few modes contribute only a small portion of the forcing Fourier mode at this $\boldsymbol{k}_3$. However, due to the strong amplification of the linear resolvent operator, these first few modes contribute significantly towards the velocity Fourier modes, as evident in Figure 6.8(c), where it is shown that the first two modes have the largest $\left|\sigma_q\chi_q\right|$. In all, this shows that the forcing Fourier mode receives contributions from a wide range of resolvent forcing modes, while the velocity Fourier mode is dominated mainly by the first few resolvent response modes due to the low-rank nature of the resolvent. This result is consistent with the work of Morra et al. (2021), where it is shown that the forcing has significant projection onto the sub-optimal resolvent forcing modes. In fact, the authors showed that the projections onto the first few optimal forcing modes are smaller than the rest, as also observed here. On the other hand, the bulk of the velocity responses is shown to be well approximated using a rank-2 approximation with the first two resolvent modes, which can also be observed in this study.

Next, we dissect the forcing and velocity Fourier modes into contributions from individual pairs of $\boldsymbol{k}_1$ and $\boldsymbol{k}_2$ that are triadically compatible with $\boldsymbol{k}_3 = [4,\ 28,\ 2.492]$. In this section, three triads are selected for demonstration purposes to showcase the effect of the linear resolvent operator, with their $\boldsymbol{k}_1$, $\boldsymbol{k}_2$, $|P(\boldsymbol{k}_1, \boldsymbol{k}_1)|$, $|R(\boldsymbol{k}_1, \boldsymbol{k}_1)|$, $E_f(\boldsymbol{k}_1, \boldsymbol{k}_1)$, $E_u(\boldsymbol{k}_1, \boldsymbol{k}_1)$ listed in table 6.1. Triad 1 is selected for generating both strong forcing and response. Triad 2 generates a relatively large response from a small forcing, and triad 3, being the opposite, generates a small response even though it has a large forcing.

The triadically generated forcing and velocity responses for the three triads listed in table 6.1 are plotted with blue, red, and yellow respectively in Figure 6.9 for the energy of each component. The non-linear weights $\mathbb{E}\left\{\left|\chi_q(\boldsymbol{k}_3)\right|^2\right\}$, and $\mathbb{E}\left\{\left|\sigma_q(\boldsymbol{k}_3)\chi_q(\boldsymbol{k}_3)\right|^2\right\}$ are plotted in Figure 6.10 using the same color scheme.

Starting with triad 1, which has the highest $E_u(\boldsymbol{k}_1, \boldsymbol{k}_2)$ and $E_f(\boldsymbol{k}_1, \boldsymbol{k}_2)$ in all triads

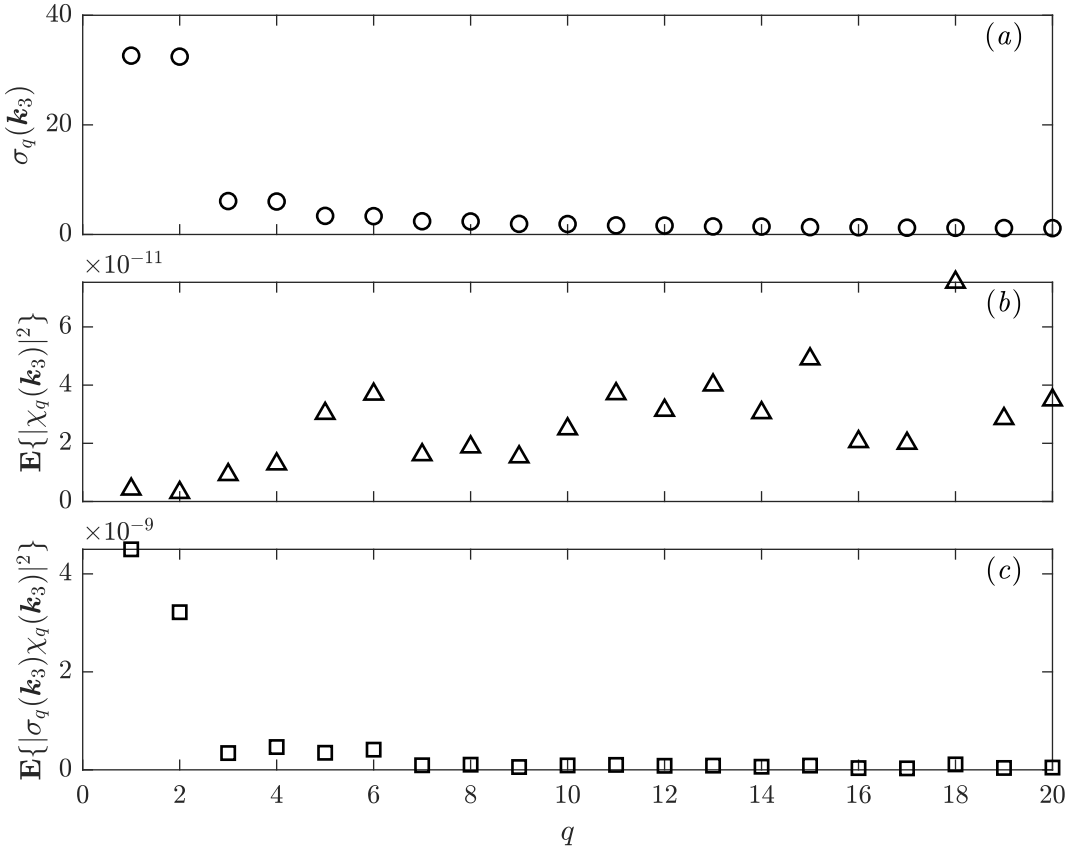

Figure 6.8: Plots of (a) the resolvent singular values $\sigma_q(\boldsymbol{k}_3)$, ($b$) the power spectral density of the non-linear weights $\chi_q(\boldsymbol{k}_3)$, obtained by taking the inner product between the resolvent forcing modes and the DNS forcing Fourier mode, and (c) the product of the two as a function or the resolvent mode number q.

Table 6.1: Three selected triads that contribute to $\boldsymbol{k}_3 = \boldsymbol{k}_1 + \boldsymbol{k}_2 = [4,\ 28,\ 2.492]$, with the magnitude of the forcing and response coefficients $|P(\boldsymbol{k}_1, \boldsymbol{k}_2)|$, $|R(\boldsymbol{k}_1, \boldsymbol{k}_2)|$ and the energy of the triadically generated forcing and response $E_f(\boldsymbol{k}_1, \boldsymbol{k}_2)$, $E_u(\boldsymbol{k}_1, \boldsymbol{k}_2)$.

Triad	$\boldsymbol{k}_1$	$\boldsymbol{k}_2$	$\lvert P(\boldsymbol{k}_1, \boldsymbol{k}_2)\rvert$	$\lvert R(\boldsymbol{k}_1, \boldsymbol{k}_2)\rvert$	$E_f(\boldsymbol{k}_1, \boldsymbol{k}_2)$	$E_u(\boldsymbol{k}_1, \boldsymbol{k}_2)$
1	[−0.5, 2, −0.415]	[4.5, 26, 2.907]	1.2×10^{-10}	1.2×10^{-9}	7.5×10^{-11}	6.4×10^{-9}
2	[0.5, −4, 0.415]	[3.5, 32, 2.077]	1.5×10^{-11}	1.9×10^{-9}	2.2×10^{-11}	2.0×10^{-9}
3	[−0.5, 4, −0.415]	[4.5, 24, 2.907]	1.4×10^{-10}	4.3×10^{-10}	3.6×10^{-11}	1.2×10^{-9}

contributing to $\boldsymbol{k}_3 = \boldsymbol{k}_1 + \boldsymbol{k}_2 = [4,\ 28,\ 2.492]$, it can be seen from Figure 6.9 that this triad indeed results in a very strong forcing $\boldsymbol{f}(\boldsymbol{k}_1, \boldsymbol{k}_2, y)$ and response $\tilde{\boldsymbol{u}}(\boldsymbol{k}_1, \boldsymbol{k}_2, y)$. In addition, this triad has large values of $\chi_q(\boldsymbol{k}_1, \boldsymbol{k}_2)$ and $\sigma_q(\boldsymbol{k}_1 + \boldsymbol{k}_2)\chi_q(\boldsymbol{k}_1, \boldsymbol{k}_2)$ for the low mode numbers q, which shows significant contributions to both the forcing and response Fourier modes. Large $\sigma_q(\boldsymbol{k}_1 + \boldsymbol{k}_2)\chi_q(\boldsymbol{k}_1, \boldsymbol{k}_2)$ for modes $q = 1, 2$, combined with large values of $\sigma_q(\boldsymbol{k}_3)\chi_q(\boldsymbol{k}_3)$ seen in Figure 6.8(c) also results in

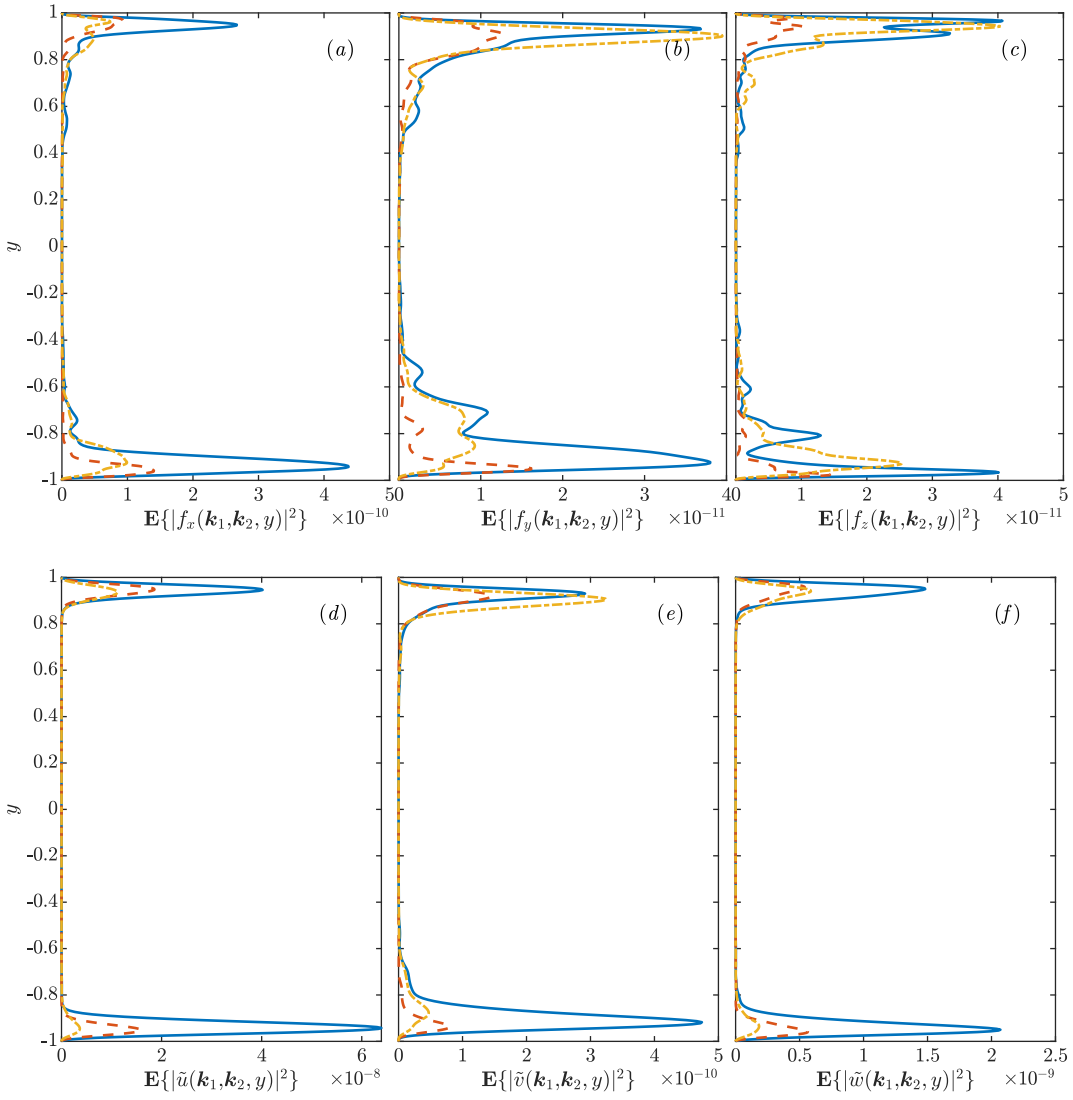

Figure 6.9: Energy of the forcing $\mathbb{E}\left\{|\boldsymbol{f}(\boldsymbol{k}_1,\boldsymbol{k}_2,y)|^2\right\}$ (top row) and velocity responses $\mathbb{E}\left\{|\tilde{\boldsymbol{u}}(\boldsymbol{k}_1,\boldsymbol{k}_2,y)|^2\right\}$ (bottom row) generated by the triadic interactions between $\boldsymbol{k}_1$ and $\boldsymbol{k}_2$ averaged over all temporal segments. Blue solid lines are for triad 1 in table 6.1, red dashed lines for triad 2, and yellow dash-dotted lines for triad 3. All 3 triads contribute partially to the DNS forcing and velocity Fourier modes at $\boldsymbol{k}_3 = \boldsymbol{k}_1 + \boldsymbol{k}_2 = [4,\ 28,\ 2.492]$.

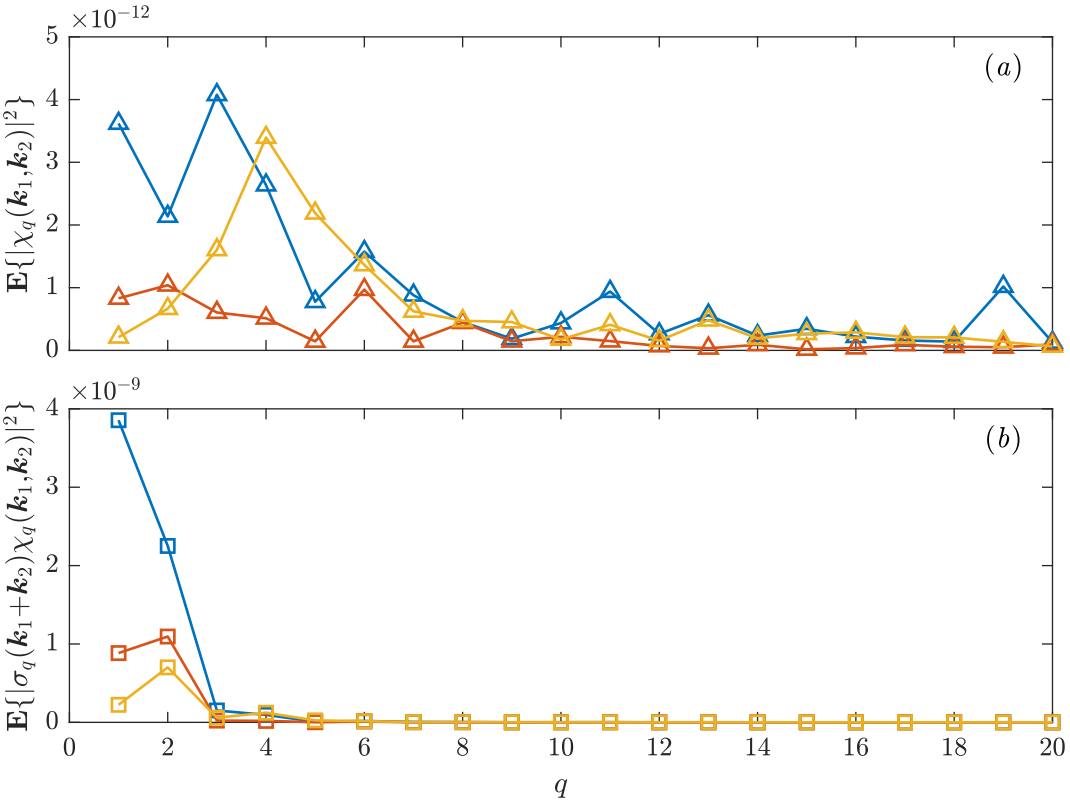

Figure 6.10: Plots of (a) non-linear weights $\mathbb{E}\left\{\left|\chi_q(\boldsymbol{k}_1,\boldsymbol{k}_2)\right|^2\right\}$ of triadic interactions between $\boldsymbol{k}_1$ and $\boldsymbol{k}_2$, and (b) the non-linear weights multiplied by the resolvent singular values $\mathbb{E}\left\{\left|\sigma_q(\boldsymbol{k}_1+\boldsymbol{k}_2)\chi_q(\boldsymbol{k}_1,\boldsymbol{k}_2)\right|^2\right\}$ as a function of the resolvent mode number q. Blue markers are for triad 1 in table 6.1, red markers for triad 2, and yellow markers for triad 3.

large R values, indicating a significant contribution to the velocity Fourier modes.

On the other hand, the comparison between triads 2 and 3 highlights the effect of the linear resolvent operator. Triad 2 has a E_f that is slightly smaller than triad 3, showing that triad 2 generates a weaker forcing than triad 3, evident in the top row of Figure 6.9, where the red lines (triad 2) have smaller amplitudes than the yellow lines (triad 3) in general. In addition, triad 2 also has a P that is a few times smaller, indicating a smaller contribution towards the forcing Fourier mode. However, triad 2 has larger E_u, showing a stronger response seen in the bottom row of Figure 6.9, and also a much larger R, showing more contributions towards the velocity Fourier mode. This effect of generating a stronger response with a weaker forcing is the result of the linear resolvent operator. Observing Figure 6.10(a), it can be seen that triad 2 (red) has much larger χ_q for resolvent modes 1 and 2, where large amplification from the resolvent operator is present (large σ_q in Figure 6.8).

This becomes more evident in Figure 6.10(b), where triad 2 has a much larger $\sigma_q \chi_q$ than triad 3, resulting in a strong velocity response. The large values for $q = 1, 2$ in both Figure 6.10(b) and Figure 6.8(c) resulted in the large R value for triad 2, as R is the product of the two as seen in equation (6.9b). In summary, although triad 2 generates a weaker forcing, it makes up for it by having a shape in y that projects strongly onto the first two resolvent modes, therefore taking full advantage of the strong resolvent amplification, and generates a stronger velocity response than triad 3. This ties back to the previous observations for the full response and forcing modes at $\boldsymbol{k}_3$ and the work of Morra et al. (2021). The full forcing is shown to project significantly onto sub-optimal modes, while the full response is relatively low-rank. By performing separate analysis on different triads, we have highlighted that the triadically generated forcing and response also behave similarly. Although some triadically generated forcing projects significantly onto sub-optimal resolvent forcing modes, the response is mainly concentrated on the first 2 modes.

6.4 Conclusion and Future Directions

In this chapter, by examining the triadic contributions to a single $\boldsymbol{k}_3 = [4, 28, 2.492]$, a representative triplet for the near wall cycle, we demonstrated two important mechanisms. First of all, although no relationships are imposed on the wavespeeds c_1, c_2, and c_3 by the triadic compatibility constraint, triadic interactions around $c_1 = c_2 = c_3$ tend to contribute more mainly due to the quadratic nature of the non-linear forcing. This allows for a sparsification of the important triadic interactions within the flow. Secondly, we highlighted the effect of the linear resolvent operator, where the low-rank nature of the resolvent results in an amplification of certain forcing shapes much more than others. As a result, certain triadic interactions can take advantage of this strong amplification and generate a stronger response even with a weak forcing. This also highlights the different perspectives offered by the response coefficients R, which includes the action of the linear resolvent operator, compared to the forcing coefficient P and the more traditional bispectrum analyses discussed in Chapter 5.

For future work, there are certainly more mechanisms behind that can be analyzed, such as the role of the linear resolvent operator in contributing towards the concentration of R near the plane with $c_1 = c_2 = c_3$. It will also be valuable to verify if these results presented here are generally applicable to all modes in the channel flow besides the one studied here, and if they are applicable to different types of flows. Finally, it would be valuable to explore the potential modeling and

computational benefits that can result from this sparsification of important triadic interactions within the flow. For example, this sparsity of important triadic interactions in the temporal frequency could be useful for future GQL algorithms. For the large scales, high energy modes and modes that take part in important triadic interactions all have low ω, while the small scales reside at higher frequencies. This separation of frequency enables the small scales to treat the resolved large scales as quasi-steady, only utilizing an updated large scale every few time steps. This could lead to an algorithm where the large scales, with fully non-linear equations, use a larger time step (resolving only lower frequencies), and the small scales, with linear equations, use smaller time steps to resolve the necessary high frequencies, essentially performing a GQL reduction in time in addition to GQL in space.

Chapter 7

CONCLUSIONS AND FUTURE WORK

This thesis has contributed to both the linear and non-linear analyses of mainly the large-scale structures in wall-bounded turbulence. This chapter summarizes the key contributions and directions for future research.

First, the resolvent analysis was applied to a flow over spanwise periodic roughness in Chapter 2, to model the streamwise constant large-scale structures manifested as counter-rotating rolls within this flow. Building on the work of Fan et al. (2024) and Chavarin and Luhar (2020), we enhanced the resolvent with the eddy viscosity and a crude model for the boundary geometry. To our knowledge, this is the first analysis to incorporate both eddy viscosity and boundary geometry models into the resolvent, and the streamwise constant modes have also not been widely studied using the resolvent analysis. We utilized the experimental data to examine both the predictive and data compression capabilities of the resolvent and illustrated the improvements by the additional models. Starting with just the streamwise velocity data, the standard resolvent modes are able to approximately predict the location, shape, and direction of the counter-rotating large-scale structures seen in the spanwise and wall-normal velocities while under-predicting the magnitude. The inclusion of the eddy viscosity improves the magnitude prediction and generates modes that can more efficiently represent all three components of the velocity data. Experimental data for all three velocity components are then utilized in the modeling, to study the data compression capabilities. Utilizing 0.18% of the original degree of freedom, the resolvent modes with eddy viscosity are able to represent the structures of the counter-rotating rolls. The 2D resolvent combining both eddy viscosity and a crude boundary geometry is able to further improve the agreement with the experimental data. This study provides a low-order model for the streamwise constant structures in the flow and can be used as a basis for future studies to explore other mechanisms in the flow such as the meandering of the secondary waves and the effect of the spanwise wavelength of the surface.

Next, we developed a novel framework to quantitatively analyze the triadic non-linear contributions to both the forcing and the response in a turbulent channel in Chapter 5. Building upon previous studies that focused on the transfer of energy

between modes, we incorporated the linear resolvent operator into this study to provide the missing link from energy transfer into (or out of) a mode to the changes in the spectral turbulent kinetic energy of this mode. This provides a new and more complete description of the effect of triadic interactions on the resulting turbulent kinetic energy at each wavenumber-frequency triplet. The coefficients highlight the importance of interactions involving large-scale structures, which is shown to be mainly driven by the interactions between large scales, while interactions between small scales are also non-negligible energy extraction mechanisms. For the small scales, it is revealed that the triadic interactions involving large scales contribute significantly, consistent with the coherence revealed by amplitude modulation studies. The importance of the large scales provides a natural connection to the modeling assumptions of the QL and GQL analyses. A detailed study of the regions of triadic interactions permitted under QL and GQL reductions revealed that they are efficiently capturing important triadic interactions in the flow, and the inclusion of small amounts of wavenumbers into the GQL large-scale base flow quickly captures most of the important triadic interactions. Additionally, a detailed analysis of regions of neglected triadic interactions in GQL is also performed. It is revealed that as Λ increases, although more triadic interactions are included, certain interactions can still be lost. The relative importance between the lost and newly included triadic interactions could cause non-monotonic performance for the small scales, and may also have an effect on the resolved large scales in GQL. For future research, the methods presented here can be applied to more complex flows and could assist in the understanding of the underlying non-linear mechanisms behind less understood flows. It can also be used with QL and GQL analyses to further quantify the underlying effect of the truncation of permitted interactions under QL/GQL.

Finally, in Chapter 6, by performing spatio-temporal analyses of the triadic contributions to a single mode representative of the near wall cycle, we demonstrated the spatio-temporal nature of the triadic interactions and the effect of the resolvent operator. In this study, it is shown that although no relationships are imposed on the wavespeeds between the three triplets in a triad, the important triadic interactions are localized in temporal frequencies around a plane where all three wavespeeds are the same. This is mainly due to the quadratic nature of the non-linear forcing and allows for a sparsification of the important triadic interactions within the flow. It is valuable for future work to explore the potential modeling and computational benefits that can result from this. We also demonstrated the effect of the linear resolvent operator. It is observed that although the forcing has significant projection

onto sub-optimal resolvent modes, the velocity response is still dominated by the optimal resolvent response modes due to the linear amplification by the low-rank nature of the resolvent. As a result, certain triadic interactions are demonstrated to be able to utilize this strong amplification and generate a stronger response even with a weak forcing. This again underscores the different perspectives offered by the inclusion of the linear resolvent operator into the analyses of the non-linear triadic interactions.

Overall, this thesis presented methods that enable useful low-cost linear modeling of large-scale structures, and tools for detailed quantitative analysis of triadic non-linear interactions. We hope this will provide useful tools for future modeling and computational research, especially in identifying improved modeling of the nonlinearity, and future research on extending the capabilities of quasi-linear, generalized quasi-linear, and resolvent analyses.

BIBLIOGRAPHY

Amaral, F. R., Cavalieri, A.V.G., Martini, E., Jordan, P., and Towne, A. (Nov. 2021). "Resolvent-based estimation of turbulent channel flow using wall measurements". en. *J. Fluid Mech.* 927, A17. ISSN: 0022-1120, 1469-7645. DOI: 10.1017/jfm.2021.764.

Barthel, B. (2022). "On the variational principles of linear and nonlinear resolvent analysis". en. PhD thesis. California Institute of Technology.

Barthel, B., Gomez, S., and McKeon, B. J. (Jan. 2022). "Variational formulation of resolvent analysis". en. *Phys. Rev. Fluids* 7.1, p. 013905. ISSN: 2469-990X. DOI: 10.1103/PhysRevFluids.7.013905.

Bechert, D. W., Bruse, M., Hage, W., Van Der Hoeven, J. G. T., and Hoppe, G. (May 1997). "Experiments on drag-reducing surfaces and their optimization with an adjustable geometry". *J. Fluid Mech.* 338, pp. 59–87. ISSN: 1469-7645, 0022-1120.

Chauhan, K. A., Monkewitz, P. A., and Nagib, H. M. (Mar. 2009). "Criteria for assessing experiments in zero pressure gradient boundary layers". *Fluid Dyn. Res.* 41.2, p. 021404. ISSN: 1873-7005.

Chavarin, A. and Luhar, M. (Feb. 2020). "Resolvent Analysis for Turbulent Channel Flow with Riblets". en. *AIAA Journal* 58.2, pp. 589–599. ISSN: 0001-1452, 1533-385X. DOI: 10.2514/1.J058205.

Cheung, L. C. and Zaki, T. (2014). "An exact representation of the nonlinear triad interaction terms in spectral space". *J. Fluid Mech.* 748, pp. 175–188.

Cho, M., Hwang, Y., and Choi, H. (Nov. 2018). "Scale interactions and spectral energy transfer in turbulent channel flow". en. *J. Fluid Mech.* 854, pp. 474–504. ISSN: 0022-1120, 1469-7645. DOI: 10.1017/jfm.2018.643.

del Álamo, J. C. and Jiménez, J. (2006). "Linear energy amplification in turbulent channels". *J. Fluid Mech.* 559, p. 205.

Duff, I. S., Erisman, A. M., and Reid, J. K. (Jan. 2017). *Direct Methods for Sparse Matrices*. en. DOI: 10.1093/acprof:oso/9780198508380.001.0001. Oxford University Press. ISBN: 978-0-19-174642-0. DOI: 10.1093/acprof:oso/9780198508380.001.0001. URL: https://academic.oup.com/book/27908.

Duvvuri, S. and McKeon, B. J. (Mar. 2015). "Triadic scale interactions in a turbulent boundary layer". en. *J. Fluid Mech.* 767. ISSN: 0022-1120, 1469-7645. DOI: 10.1017/jfm.2015.79.

Fan, Y., Kozul, M., Li, W., and Sandberg, R. D. (Mar. 2024). "Eddy-viscosity-improved resolvent analysis of compressible turbulent boundary layers". en. *J. Fluid Mech.* 983, A46. ISSN: 0022-1120, 1469-7645.

Farrell, B. F. and Ioannou, P. J. (Nov. 1993). "Stochastic forcing of the linearized Navier–Stokes equations". en. *Phys. Fluids A: Fluid Dyn.* 5.11, pp. 2600–2609. ISSN: 0899-8213. DOI: 10.1063/1.858894.

Farrell, B. F. and Ioannou, P. J. (Oct. 2007). "Structure and Spacing of Jets in Barotropic Turbulence". en. *J. Atmos. Sci.* 64.10, pp. 3652–3665. ISSN: 1520-0469, 0022-4928. DOI: 10.1175/JAS4016.1.

Farrell, B. F. and Ioannou, P. J. (Oct. 2012). "Dynamics of streamwise rolls and streaks in turbulent wall-bounded shear flow". en. *J. Fluid Mech.* 708, pp. 149–196. ISSN: 0022-1120, 1469-7645. DOI: 10.1017/jfm.2012.300.

Farrell, B. F., Ioannou, P. J., Jiménez, J., Constantinou, N. C., Lozano-Durán, A., and Nikolaidis, M. (Dec. 2016). "A statistical state dynamics-based study of the structure and mechanism of large-scale motions in plane Poiseuille flow". en. *J. Fluid Mech.* 809, pp. 290–315. ISSN: 0022-1120, 1469-7645. DOI: 10.1017/jfm.2016.661.

Flores, O. and Jiménez, J. (Nov. 2006). "Effect of wall-boundary disturbances on turbulent channel flows". *J. Fluid Mech.* 566, pp. 357–376. ISSN: 1469-7645, 0022-1120. DOI: 10.1017/S0022112006001534.

Gayme, D. F., McKeon, B. J., Bamieh, B., Papachristodoulou, A., and Doyle, J. C. (June 2011). "Amplification and nonlinear mechanisms in plane Couette flow". en. *Phys. Fluids* 23.6, p. 065108. ISSN: 1070-6631, 1089-7666. DOI: 10.1063/1.3599701.

Gayme, D. F., McKeon, B. J., Papachristodoulou, A., Bamieh, B., and Doyle, J. C. (Dec. 2010). "A streamwise constant model of turbulence in plane Couette flow". en. *J. Fluid Mech.* 665, pp. 99–119. ISSN: 0022-1120, 1469-7645. DOI: 10.1017/S0022112010003861.

Gomez, S. (2024). "Linear Amplification in Nonequilibrium Turbulent Boundary Layers". en. phd. California Institute of Technology. DOI: 10.7907/hn98-c285. URL: https://resolver.caltech.edu/CaltechTHESIS:08312023-005517217.

Gómez, F., Blackburn, H. M., Rudman, M., McKeon, B. J., Luhar, M., Moarref, R., and Sharma, A. S. (2014). "On the origin of frequency sparsity in direct numerical simulations of turbulent pipe flow". *Phys. Fluids* 26.10, p. 101703.

Gómez, F., Blackburn, H. M., Rudman, M., Sharma, A. S., and McKeon, B. J. (July 2016). "A reduced-order model of three-dimensional unsteady flow in a cavity based on the resolvent operator". en. *J. Fluid Mech.* 798, R2. ISSN: 0022-1120, 1469-7645. DOI: 10.1017/jfm.2016.339.

Hernández, C. G., Yang, Q., and Hwang, Y. (Apr. 2022a). "Generalised quasilinear approximations of turbulent channel flow. Part 1. Streamwise nonlinear energy transfer". en. *J. Fluid Mech.* 936, A33. ISSN: 0022-1120, 1469-7645. DOI: 10.1017/jfm.2022.59.

Hernández, C. G., Yang, Q., and Hwang, Y. (Aug. 2022b). "Generalised quasi-linear approximations of turbulent channel flow. Part 2. Spanwise triadic scale interactions". en. *J. Fluid Mech.* 944, A34. ISSN: 0022-1120, 1469-7645. DOI: 10.1017/jfm.2022.499.

Hou, Y., Somandepalli, V. S. R., and Mungal, M. G. (Apr. 2006). "A technique to determine total shear stress and polymer stress profiles in drag reduced boundary layer flows". en. *Exp. Fluids* 40.4, pp. 589–600. ISSN: 0723-4864, 1432-1114.

Huang, Y., Hutchins, N., and McKeon, B. J. (2024). "Reduced Order Mddeling of Flow Over Spanwise Periodic Rough Surfaces". International Mechanical Engineering Congress and Exposition 2024 (accepted).

Huynh, D. P., Huang, Y., and McKeon, B. J. (May 2021). "Experiments and Modeling of a Compliant Wall Response to a Turbulent Boundary Layer with Dynamic Roughness Forcing". *Fluids* 6.55, p. 173. DOI: 10.3390/fluids6050173. URL: https://www.mdpi.com/2311-5521/6/5/173.

Hwang, Y. and Cossu, C. (2010). "Linear non-normal energy amplification of harmonic and stochastic forcing in the turbulent channel flow". *J. Fluid Mech.* 664, pp. 51–73.

Illingworth, S. J., Monty, J. P., and Marusic, I. (May 2018). "Estimating large-scale structures in wall turbulence using linear models". en. *J. Fluid Mech.* 842, pp. 146–162. ISSN: 0022-1120, 1469-7645.

Jiménez, J. (Jan. 2012). "Cascades in Wall-Bounded Turbulence". en. *Ann. Rev. Fluid Mech.* 44.1, pp. 27–45. ISSN: 0066-4189, 1545-4479. DOI: 10.1146/annurev-fluid-120710-101039.

Jiménez, J. (Oct. 2013). "Near-wall turbulence". en. *Phys. Fluids* 25.10, p. 101302. ISSN: 1070-6631, 1089-7666. DOI: 10.1063/1.4824988.

Jiménez, J. (May 2018). "Coherent structures in wall-bounded turbulence". en. *J. Fluid Mech.* 842, P1. ISSN: 0022-1120, 1469-7645. DOI: 10.1017/jfm.2018.144.

Jovanović, M. R. and Bamieh, B. (June 2005). "Componentwise energy amplification in channel flows". en. *J. Fluid Mech.* 534, pp. 145–183. ISSN: 0022-1120, 1469-7645. DOI: 10.1017/S0022112005004295.

Kamal, O., Rigas, G., Lakebrink, M. T., and Colonius, T. (2020). "Application of the One-Way Navier-Stokes (OWNS) Equations to Hypersonic Boundary Layers". *AIAA AVIATION 2020 FORUM*. DOI: 10.2514/6.2020-2986.

Karban, U., Martini, E., Cavalieri, A. V. G., and Jordan, P. (2023). "Modal decomposition of nonlinear interactions in wall turbulence". *arXiv 2301.01078*. DOI: 10.48550/ARXIV.2301.01078. URL: https://arxiv.org/abs/2301.01078.

Khadra, K., Angot, P., Parneix, S., and Caltagirone, J. (2000). "Fictitious domain approach for numerical modelling of Navier–Stokes equations". en. *International Journal for Numerical Methods in Fluids* 34.8, pp. 651–684. ISSN: 1097-0363.

Kim, J. and Lim, J. (Aug. 2000). "A linear process in wall-bounded turbulent shear flows". *Phys. Fluids* 12.8, pp. 1885–1888. ISSN: 1070-6631. DOI: 10.1063/1.870437.

Lee, M. and Moser, R. (2015). "Direct numerical simulation of turbulent channel flow up to $Re_\tau \approx 5200$". *J. Fluid Mech.* 774, pp. 395–415. DOI: 10.1017/jfm.2015.268.

Lii, K. S., Rosenblatt, M., and Van Atta, C. (Sept. 1976). "Bispectral measurements in turbulence". en. *J. Fluid Mech.* 77.1, pp. 45–62. ISSN: 0022-1120, 1469-7645. DOI: 10.1017/S0022112076001122.

Luhar, M., Sharma, A. S., and McKeon, B. J. (June 2014). "Opposition control within the resolvent analysis framework". en. *J. Fluid Mech.* 749, pp. 597–626. ISSN: 0022-1120, 1469-7645. DOI: 10.1017/jfm.2014.209.

Luhar, M., Sharma, A. S., and McKeon, B. J. (Apr. 2015). "A framework for studying the effect of compliant surfaces on wall turbulence". en. *J. Fluid Mech.* 768, pp. 415–441. ISSN: 0022-1120, 1469-7645. DOI: 10.1017/jfm.2015.85.

Lumley, J. L. (1970). *Stochastic Tools in Turbulence*. en. Academic Press.

Marati, N., Casciola, C. M., and Piva, R. (2004). "Energy cascade and spatial fluxes in wall turbulence." *J. Fluid Mech.* 521, pp. 191–215.

Marston, J. B., Chini, G. P., and Tobias, S. M. (May 2016). "Generalized Quasilinear Approximation: Application to Zonal Jets". en. *Phys. Rev. Lett.* 116.21, p. 214501. ISSN: 0031-9007, 1079-7114. DOI: 10.1103/PhysRevLett.116.214501.

Marusic, I., Chandran, D., Rouhi, A., Fu, M. K., Wine, D., Holloway, B., Chung, D., and Smits, A. J. (Oct. 2021). "An energy-efficient pathway to turbulent drag reduction". en. *Nat. Commun.* 12.11, p. 5805. ISSN: 2041-1723. DOI: 10.1038/s41467-021-26128-8.

Marusic, I., Mathis, R., and Hutchins, N. (July 2010a). "Predictive Model for Wall-Bounded Turbulent Flow". *Science* 329.5988, p. 193. ISSN: 0036-8075, 1095-9203.

Marusic, I., McKeon, B. J., Monkewitz, P. A., Nagib, H. M., Smits, A. J., and Sreenivasan, K. R. (June 2010b). "Wall-bounded turbulent flows at high Reynolds numbers: Recent advances and key issues". en. *Phys. Fluids* 22.6, p. 065103. ISSN: 1070-6631, 1089-7666. DOI: 10.1063/1.3453711.

MATLAB (2023). *version 9.14.0 (R2023a)*. Natick, Massachusetts: The MathWorks Inc.

Mattsson, K. and Nordström, J. (Sept. 2004). "Summation by parts operators for finite difference approximations of second derivatives". en. *J. Comput. Phys.* 199.2, pp. 503–540. ISSN: 00219991. DOI: 10.1016/j.jcp.2004.03.001.

McKeon, B. J. (Apr. 2017). "The engine behind (wall) turbulence: perspectives on scale interactions". *J. Fluid Mech.* 817. ISSN: 0022-1120, 1469-7645.

McKeon, B. J. and Sharma, A. S. (Sept. 2010). "A critical-layer framework for turbulent pipe flow". *J. Fluid Mech.* 658, pp. 336–382. ISSN: 0022-1120.

McMullen, R. M. (2020). "Aspects of Reduced-Order Modeling of Turbulent Channel Flows: From Linear Mechanisms to Data-Driven Approaches". en. phd. California Institute of Technology. DOI: 10.7907/wayx-eh75. URL: https://resolver.caltech.edu/CaltechTHESIS:05282020-161209039.

McMullen, R. M., Rosenberg, K., and McKeon, B. J. (Aug. 2020). "Interaction of forced Orr-Sommerfeld and Squire modes in a low-order representation of turbulent channel flow". en. *Phys. Rev. Fluids* 5.8, p. 084607. ISSN: 2469-990X. DOI: 10.1103/PhysRevFluids.5.084607.

Moarref, R., Jovanović, M. R., Tropp, J. A., Sharma, A. S., and McKeon, B. J. (May 2014). "A low-order decomposition of turbulent channel flow via resolvent analysis and convex optimization". *Phys. Fluids* 26.5, p. 051701. ISSN: 1070-6631, 1089-7666.

Moarref, R., Sharma, A. S., Tropp, J. A., and McKeon, B. J. (Nov. 2013). "Model-based scaling of the streamwise energy density in high-Reynolds-number turbulent channels". *J. Fluid Mech.* 734, pp. 275–316. ISSN: 0022-1120, 1469-7645.

Morra, P., Nogueira, P. A. S., Cavalieri, A. V. G., and Henningson, D. S. (Jan. 2021). "The colour of forcing statistics in resolvent analyses of turbulent channel flows". *J. Fluid Mech.* 907, A24. ISSN: 0022-1120, 1469-7645. DOI: 10.1017/jfm.2020.802.

Nogueira, P. A. S., Morra, P., Martini, E., Cavalieri, A. V. G., and Henningson, D. S. (Feb. 2021). "Forcing statistics in resolvent analysis: application in minimal turbulent Couette flow". en. *J. Fluid Mech.* 908, A32. ISSN: 0022-1120, 1469-7645. DOI: 10.1017/jfm.2020.918.

Padovan, A., Otto, S. E., and Rowley, C. W. (Oct. 2020). "Analysis of amplification mechanisms and cross-frequency interactions in nonlinear flows via the harmonic resolvent". *J. Fluid Mech.* 900, A14. ISSN: 0022-1120, 1469-7645. DOI: 10.1017/jfm.2020.497.

Parks, T. W. and Burrus, C. S. (1987). *Digital filter design*. en. Topics in digital signal processing. New York: Wiley. ISBN: 978-0-471-82896-9.

Pickering, E., Rigas, G., Schmidt, O. T., Sipp, D., and Colonius, T. (June 2021). "Optimal eddy viscosity for resolvent-based models of coherent structures in turbulent jets". en. *J. Fluid Mech.* 917, A29. ISSN: 0022-1120, 1469-7645. DOI: 10.1017/jfm.2021.232.

Reynolds, W. C. and Hussain, A. K. M. F. (July 1972). "The mechanics of an organized wave in turbulent shear flow. Part 3. Theoretical models and comparisons with experiments". en. *J. Fluid Mech.* 54.2, pp. 263–288. ISSN: 0022-1120, 1469-7645. DOI: 10.1017/S0022112072000679.

Reynolds, W. C. and Tiederman, W. G. (Feb. 1967). "Stability of turbulent channel flow, with application to Malkus's theory". en. *J. Fluid Mech.* 27.2, pp. 253–272. ISSN: 1469-7645, 0022-1120.

Ribeiro, J. H. M., Yeh, C., and Taira, K. (Mar. 2020). "Randomized resolvent analysis". en. *Phys. Rev. Fluids* 5.3, p. 033902. ISSN: 2469-990X. DOI: 10.1103/PhysRevFluids.5.033902.

Rigas, G., Sipp, D., and Colonius, T. (Mar. 2021). "Nonlinear input/output analysis: application to boundary layer transition". en. *J. Fluid Mech.* 911, A15. ISSN: 0022-1120, 1469-7645. DOI: 10.1017/jfm.2020.982.

Rosenberg, K. (2018). "Resolvent-Based Modeling of Flows in a Channel". phd. California Institute of Technology. URL: https://resolver.caltech.edu/CaltechTHESIS:06012018-114927289.

Rosenberg, K. and McKeon, B. J. (Aug. 2019a). "Computing exact coherent states in channels starting from the laminar profile: A resolvent-based approach". *Phys. Rev. E* 100.2, p. 021101. DOI: 10.1103/PhysRevE.100.021101.

Rosenberg, K. and McKeon, B. J. (Jan. 2019b). "Efficient representation of exact coherent states of the Navier–Stokes equations using resolvent analysis". en. *Fluid Dyn. Res.* 51.1, p. 011401. ISSN: 1873-7005. DOI: 10.1088/1873-7005/aab1ab.

Schmid, P. J. (Aug. 2010). "Dynamic mode decomposition of numerical and experimental data". en. *J. Fluid Mech.* 656, pp. 5–28. ISSN: 0022-1120, 1469-7645. DOI: 10.1017/S0022112010001217.

Schmid, P. J. and Brandt, L. (Mar. 2014). "Analysis of Fluid Systems: Stability, Receptivity, Sensitivity". en. *Appl. Mech. Rev.* 66.2, p. 024803. ISSN: 0003-6900, 2379-0407. DOI: 10.1115/1.4026375.

Schmid, P. J. and Henningson, D. S. (2001). *Stability and Transition in Shear Flows*. Vol. 142. Applied Mathematical Sciences. New York, NY: Springer. ISBN: 978-1-4612-6564-1. DOI: 10.1007/978-1-4613-0185-1.

Schmidt, O. T. (Dec. 2020). "Bispectral mode decomposition of nonlinear flows". en. *Nonlinear Dyn.* 102.4, pp. 2479–2501. ISSN: 0924-090X, 1573-269X. DOI: 10.1007/s11071-020-06037-z.

Schmidt, O. T., Towne, A., Rigas, G., Colonius, T., and Brès, G. A. (Nov. 2018). "Spectral analysis of jet turbulence". en. *J. Fluid Mech.* 855, pp. 953–982. ISSN: 0022-1120, 1469-7645. DOI: 10.1017/jfm.2018.675.

Schultz, M. P., Bendick, J. A., Holm, E. R., and Hertel, W. M. (Jan. 2011). "Economic impact of biofouling on a naval surface ship". *Biofouling* 27.1, pp. 87–98. ISSN: 1029-2454.

Sharma, A. S., Moarref, R., and McKeon, B. J. (Mar. 2017). "Scaling and interaction of self-similar modes in models of high Reynolds number wall turbulence". *Philosophical Transactions of the Royal Society A: Mathematical, Physical and Engineering Sciences* 375.2089, p. 20160089. DOI: 10.1098/rsta.2016.0089.

Sipp, D. and Marquet, O. (Sept. 2013). "Characterization of noise amplifiers with global singular modes: the case of the leading-edge flat-plate boundary layer". en. *Theor. Comput. Fluid Dyn.* 27.5, pp. 617–635. ISSN: 0935-4964, 1432-2250. DOI: 10.1007/s00162-012-0265-y.

Smits, A. J. and Marusic, I. (Sept. 2013). "Wall-bounded turbulence". en. *Physics Today* 66.9, pp. 25–30. ISSN: 0031-9228, 1945-0699. DOI: 10.1063/PT.3.2114.

Smits, A. J., McKeon, B. J., and Marusic, I. (2011). "High–Reynolds Number Wall Turbulence". *Annu. Rev. Fluid Mech.* 43.1, pp. 353–375.

Symon, S., Illingworth, S. J., and Marusic, I. (Mar. 2021). "Energy transfer in turbulent channel flows and implications for resolvent modelling". *J. Fluid Mech.* 911, A3. ISSN: 0022-1120, 1469-7645.

Taira, K., Brunton, S. L., Dawson, Scott T. M., Rowley, C. W., Colonius, T., McKeon, B. J., Schmidt, O. T., Gordeyev, S., Theofilis, V., and Ukeiley, L. S. (Dec. 2017). "Modal Analysis of Fluid Flows: An Overview". en. *AIAA Journal* 55.12, pp. 4013–4041. ISSN: 0001-1452, 1533-385X. DOI: 10.2514/1.J056060.

Thomas, V. L., Farrell, B. F., Ioannou, P. J., and Gayme, D. F. (Oct. 2015). "A minimal model of self-sustaining turbulence". en. *Phys. Fluids* 27.10, p. 105104. ISSN: 1070-6631, 1089-7666. DOI: 10.1063/1.4931776.

Toedtli, S., Luhar, M., and McKeon, B. J. (July 2019). "Predicting the response of turbulent channel flow to varying-phase opposition control: Resolvent analysis as a tool for flow control design". *Phys. Rev. Fluids* 4.7, p. 073905. DOI: 10.1103/PhysRevFluids.4.073905.

Toedtli, S., Yu, C., and McKeon, B. J. (Oct. 2020). "On the origin of drag increase in varying-phase opposition control". en. *International Journal of Heat and Fluid Flow* 85, p. 108651. ISSN: 0142727X. DOI: 10.1016/j.ijheatfluidflow.2020.108651.

Towne, A., Lozano-Durán, A., and Yang, X. (Jan. 2020). "Resolvent-based estimation of space–time flow statistics". en. *J. Fluid Mech.* 883, A17. ISSN: 0022-1120, 1469-7645.

Towne, A., Rigas, G., Kamal, O., Pickering, E., and Colonius, T. (Oct. 2022). "Efficient global resolvent analysis via the one-way Navier–Stokes equations". en. *J. Fluid Mech.* 948, A9. ISSN: 0022-1120, 1469-7645. DOI: 10.1017/jfm.2022.647.

Towne, A., Schmidt, O. T., and Colonius, T. (July 2018). "Spectral proper orthogonal decomposition and its relationship to dynamic mode decomposition and resolvent analysis". en. *J. Fluid Mech.* 847, pp. 821–867. ISSN: 0022-1120, 1469-7645. DOI: 10.1017/jfm.2018.283.

Trefethen, L. N., Trefethen, A. E., Reddy, S. C., and Driscoll, T. A. (1993). "Hydrodynamic Stability Without Eigenvalues". *Science* 261.5121, pp. 578–584. ISSN: 0036-8075.

Wang, J., Koley, S., and Katz, J. (Sept. 2020). “On the interaction of a compliant wall with a turbulent boundary layer”. en. *J. Fluid Mech.* 899. ISSN: 0022-1120, 1469-7645. DOI: 10.1017/jfm.2020.446.

Wangsawijaya, D. D., Baidya, R., Chung, D., Marusic, I., and Hutchins, N. (July 2020). “The effect of spanwise wavelength of surface heterogeneity on turbulent secondary flows”. *J. Fluid Mech.* 894. ISSN: 0022-1120, 1469-7645.

Welch, P. (June 1967). “The use of fast Fourier transform for the estimation of power spectra: A method based on time averaging over short, modified periodograms”. en. *IEEE Trans. Audio Electroacoust.* 15.2, pp. 70–73. ISSN: 0018-9278. DOI: 10.1109/TAU.1967.1161901.

World Oil Outlook (2018). The Organization of the Petroleum Exporting Countries. URL: https://woo.opec.org/chapter.html?chapterNr=3&chartID=59.

Yeh, C. and Taira, K. (May 2019). “Resolvent-analysis-based design of airfoil separation control”. en. *J. Fluid Mech.* 867, pp. 572–610. ISSN: 0022-1120, 1469-7645. DOI: 10.1017/jfm.2019.163.

Zare, A., Jovanović, M. R., and Georgiou, T. T. (Feb. 2017). “Colour of turbulence”. en. *J. Fluid Mech.* 812, pp. 636–680. ISSN: 0022-1120, 1469-7645. DOI: 10.1017/jfm.2016.682.

Appendix A

ADDITIONAL DERIVATIONS

A.1 Derivation of the Spectral Turbulence Kinetic Energy (TKE) Equation

In Chapter 3, we define the spectral turbulence kinetic energy (TKE) as $e(\boldsymbol{k}, y) = |u(\boldsymbol{k}, y)|^2 + |v(\boldsymbol{k}, y)|^2 + |w(\boldsymbol{k}, y)|^2$, which is the energy of a Fourier modes at given $\boldsymbol{k}$. Due to the Hermitian symmetry of the Fourier modes, we have $e(\boldsymbol{k}, y) = e(-\boldsymbol{k}, y)$. Starting with the Fourier transformed NSE:

$$\left[-i\omega + ik_x\overline{U}(y) + \frac{k^2}{Re} - \frac{1}{Re}\frac{d^2}{dy^2}\right] u(\boldsymbol{k}, y) \; + \overline{U}'(y)v(\boldsymbol{k}, y) + ik_x p(\boldsymbol{k}, y) = f_x(\boldsymbol{k}, y), \tag{A.1}$$

$$\left[-i\omega + ik_x\overline{U}(y) + \frac{k^2}{Re} - \frac{1}{Re}\frac{d^2}{dy^2}\right] v(\boldsymbol{k}, y) \qquad\qquad + \frac{d}{dy}p(\boldsymbol{k}, y) = f_y(\boldsymbol{k}, y), \tag{A.2}$$

$$\left[-i\omega + ik_x\overline{U}(y) + \frac{k^2}{Re} - \frac{1}{Re}\frac{d^2}{dy^2}\right] w(\boldsymbol{k}, y) \qquad\qquad + ik_z p(\boldsymbol{k}, y) = f_z(\boldsymbol{k}, y), \tag{A.3}$$

with $\overline{U}'(y) = \frac{d\overline{U}(y)}{dy}$. Multiply the three equations with $u^*(\boldsymbol{k}, y)$, $v^*(\boldsymbol{k}, y)$, $w^*(\boldsymbol{k}, y)$, take the sum, and utilize continuity to obtain:

$$\left[-i\omega + ik_x\overline{U}(y) + \frac{k^2}{Re}\right] e(\boldsymbol{k}, y) + u^*(\boldsymbol{k}, y)v(\boldsymbol{k}, y)\overline{U}'(y) + \frac{d}{dy}\left[v^*(\boldsymbol{k}, y)p(\boldsymbol{k}, y)\right]$$
$$- \frac{1}{Re}\left[u_i^*(\boldsymbol{k}, y)\frac{d^2}{dy^2}u_i(\boldsymbol{k}, y)\right] = u_i^*(\boldsymbol{k}, y)f_i(\boldsymbol{k}, y), \tag{A.4}$$

where the summation notation is used with the subscript i. We then add it with the equation for $e(-\boldsymbol{k}, y)$, and utilized $e(\boldsymbol{k}, y) = e(-\boldsymbol{k}, y)$ and the symmetry of Fourier modes $u^*(\boldsymbol{k}, y) = u(-\boldsymbol{k}, y)$ to obtain:

$$\underbrace{\mathrm{Re}\left\{u^*(\boldsymbol{k}, y)v(\boldsymbol{k}, y)\overline{U}'(y)\right\}}_{\text{Production}} + \underbrace{\frac{k^2}{Re}e(\boldsymbol{k}, y) + \frac{1}{Re}\frac{d}{dy}u_i^*(\boldsymbol{k}, y)\frac{d}{dy}u_i(\boldsymbol{k}, y)}_{\text{Viscous Dissipation}}$$
$$+ \underbrace{\mathrm{Re}\left\{\frac{d}{dy}\left[v^*(\boldsymbol{k}, y)p(\boldsymbol{k}, y)\right]\right\}}_{\text{Pressure Transport}} - \underbrace{\frac{1}{2}\frac{1}{Re}\frac{d^2}{dy^2}e(\boldsymbol{k}, y)}_{\text{Viscous Transport}} = \underbrace{\mathrm{Re}\left\{u_i^*(\boldsymbol{k}, y)f_i(\boldsymbol{k}, y)\right\}}_{\text{Turbulent Transport}}, \tag{A.5}$$

where Re $\{\cdot\}$ indicates the real part. This resembles the form in Cho et al. (2018), which is written for the modes Fourier transformed in z only, while we provide the results for the modes Fourier transformed in x, z, t.

A.2 Importance of Linear Phase Response for Temporal Filtering

In this section, we will show that phase distortion in the pass band can be avoided with a linear phase low pass filter. Since the stop band frequencies have significantly lower amplitude response, it is sufficient to limit the analysis to only the pass band of the filter, with a transfer function $A(\omega)e^{i\phi(\omega)}$, where $A(\omega)$ is the amplitude, and $\phi(\omega) = -k\omega$ is the linear phase response of the filter.

Denote a pre-filtered signal containing frequencies only in the pass band as $q(t)$, with Fourier coefficient $\hat{q}(\omega)$ and the filtered signal $q_f(t)$ and $\hat{q}_f(\omega)$, the filtered signal is related to the unfiltered by the filter transfer function:

$$\hat{q}_f(\omega) = A(\omega)\hat{q}(\omega)e^{i\phi(\omega)} = A(\omega)\hat{q}(\omega)e^{-ik\omega}. \tag{A.6}$$

Utilizing the approximation of $A(\omega) \approx 1$ in the filter pass band and the Fourier transform pair, we obtain:

$$q_f(t) = \int \hat{q}_f(\omega)e^{i\omega t}d\omega \approx \int \hat{q}(\omega)e^{i\omega t - ik\omega}d\omega = q(t-k), \tag{A.7}$$

which shows that the filtered signal is a time delayed copy of the original signal with no phase distortion in the pass band. This constant time delay can be easily corrected in post-processing, and the next section shows that the time delay does not affect the computation of the interaction coefficients. More rigorous analyses of linear-phase filters can be found in digital filter textbooks such as Parks and Burrus, 1987.

A.3 Validity of the Application of the Welch Method

In this section, we will (non-rigorously) show that the Welch method can be correctly applied to the computation of $P(\boldsymbol{k}_1, \boldsymbol{k}_2)$ and $R(\boldsymbol{k}_1, \boldsymbol{k}_2)$. For simplicity, we will neglect all spatial coordinates as those do not affect the temporal Fourier analysis, and redefine P and R for this analysis as:

$$P(\omega_1, \omega_2) = \hat{f}^*(\omega_1 + \omega_2)\hat{u}_1(\omega_1)\hat{u}_2(\omega_2), \tag{A.8}$$

$$R(\omega_1, \omega_2) = \hat{u}_1^*(\omega_1 + \omega_2)\mathcal{H}(\omega_1 + \omega_2)\hat{u}_1(\omega_1)\hat{u}_2(\omega_2), \tag{A.9}$$

where $\hat{u}_1(\omega)$ is the Fourier coefficient of $u_1(t)$, a proxy for the velocity, $\hat{u}_2(\omega)$ is the Fourier coefficient of $u_2(t)$, a proxy for the velocity gradient, and $\hat{f}(\omega)$ is the Fourier coefficient of $f(t) = u_1(t)u_2(t)$.

The three signals are then shifted in time by a constant Δt, resulting in their Fourier coefficients shifted in phase:

$$u_1'(t) = u_1(t + \Delta t) \implies \hat{u}_1'(\omega) = \hat{u}_1(\omega) e^{i\omega\Delta t}, \tag{A.10}$$

with u_2 and f following the same relation. $P'(\omega_1, \omega_2)$ can therefore be defined for the time shifted signals:

$$\begin{aligned} P'(\omega_1, \omega_2) &= \hat{f}'^{*}(\omega_1 + \omega_2)\hat{u}_1'(\omega_1)\hat{u}_2'(\omega_2) \\ &= \left[\hat{f}(\omega_1 + \omega_2) e^{i(\omega_1+\omega_2)\Delta t}\right]^* \left[\hat{u}_1(\omega_1) e^{i\omega_1\Delta t}\right] \left[\hat{u}_2(\omega_2) e^{i\omega_2\Delta t}\right] \\ &= P(\omega_1, \omega_2) \end{aligned} \tag{A.11}$$

which shows that $P(\omega_1, \omega_2)$ is invariant with respect to any time shifts of the signals. With the resolvent operator $\mathcal{H}(\omega)$ also invariant with respect to time shifts, a similar analysis can be applied to $R(\omega_1, \omega_2)$ as well, reaching the same conclusion.

Since the two coefficients are invariant with respect to time shifts, the full time series can be segmented, the coefficients computed for each segment, before taking the average across multiple segments for improved convergence. More rigorously, we are assuming wide-sense stationarity extended to the third order statistics, where the triple correlation depends only on the time differences, similar to the auto-correlation in second order statistics.

Appendix B

ADDITIONAL RESULTS

B.1 Triadic Contributions to a Representative Large Scale

In Chapter 6, we presented the results of triadic contributions to a single $\boldsymbol{k}_3$ representative of the near wall cycle and showed that the active triadic interactions are very localized around the plane with $c_1 = c_2 = c_3$. In this section, we will show the same results for a $\boldsymbol{k}_3$ representative of a large-scale structure.

In this section, the selected triplet is $\boldsymbol{k}_3 = [0.5,\ 4,\ 0.415]$. $k_x = 0.5$ is selected as it is the largest streamwise mode that is not streamwise constant. $k_z = 4$ and $\omega = 0.415$ are selected for being the most energetic mode with $k_x = 0.5$. The resulting magnitude of the forcing and response coefficients are plotted in Figure B.1 with log scale color bars in the same format as Figure 6.3. In Figure B.2, both the forcing and response coefficients are summed in k_{z1} and plotted as contour plots in the $k_{x1} - \omega_1$ plane in the same format as Figure 6.4. In Figure B.2, three different wavespeeds c_1 are also plotted: the dash-dotted lines for $c_1 = \omega_1/k_{x1} = 1$, where the wavespeed matches the center-line velocity; the dashed lines for $c_1 = c_2 = c_3 = 0.83$, the wavespeed of the selected $\boldsymbol{k}_3$; and the dotted lines for $c_1 = 0.3$ ($c_1^+ = 6$). Similar to the case for the NWC in Chapter 6, from the two figures, it can be observed that the main contributing triads are also concentrated roughly around $c_1 = c_2 = c_3$.

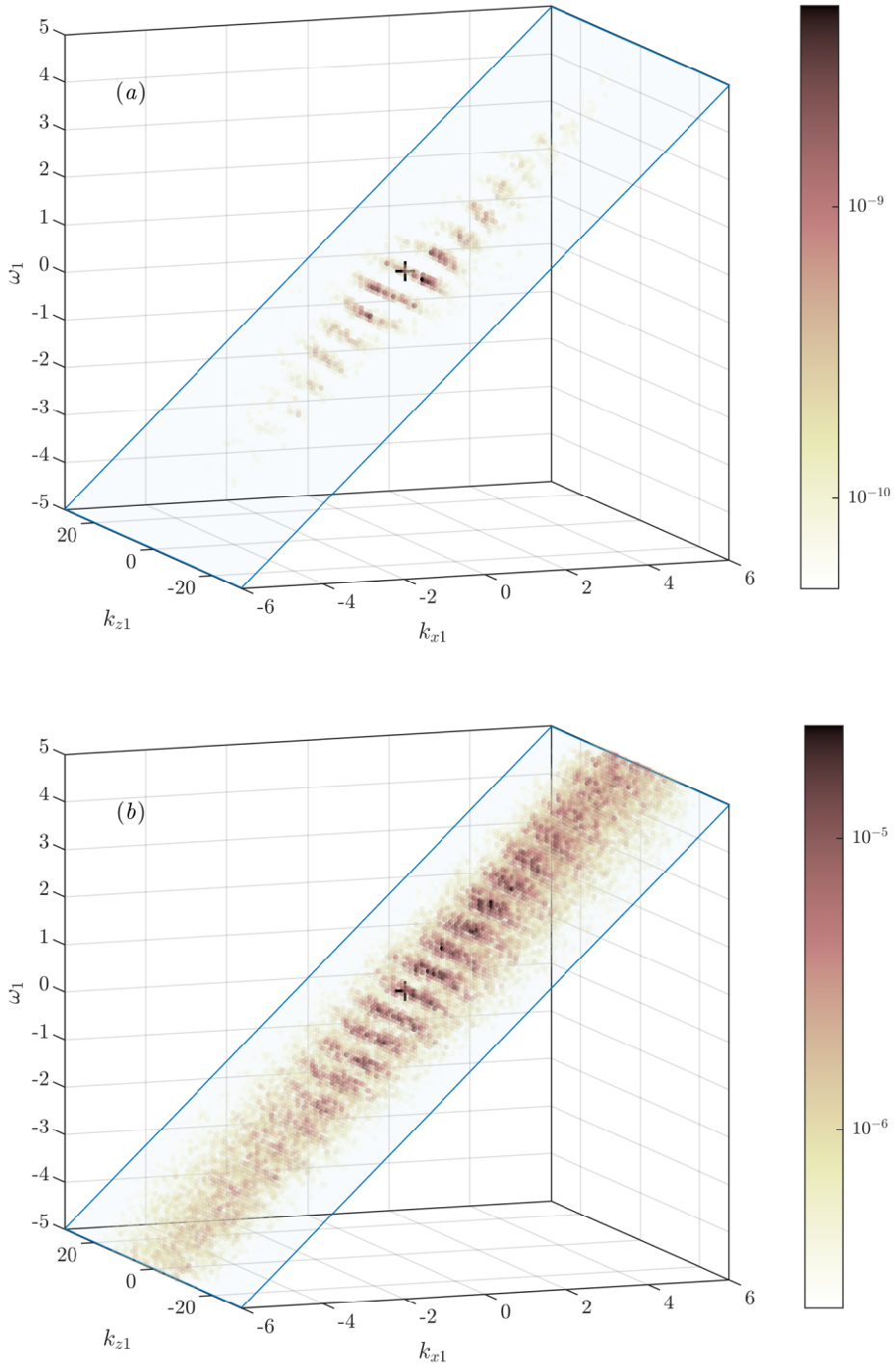

Figure B.1: Magnitude of (a) $P(\boldsymbol{k}_1, \boldsymbol{k}_3 - \boldsymbol{k}_1)$, the forcing coefficients and (b) $R(\boldsymbol{k}_1, \boldsymbol{k}_3 - \boldsymbol{k}_1)$, the response coefficients as functions of $\boldsymbol{k}_1 = [k_{x1}, k_{z1}, \omega_1]$ with log scale color bars for $\boldsymbol{k}_3 = \boldsymbol{k}_1 + \boldsymbol{k}_2 = [0.5,\ 4,\ 0.415]$. The opacity of each marker is also linearly proportional to $\log_{10}$ of the magnitudes. Points with magnitude less than 1% of the peak values are not plotted. The + markers in both figures denote the location of $\boldsymbol{k}_3$, and the blue planes mark the location of $c_1 = \omega_1/k_{x1} = c_3 = 0.83$.

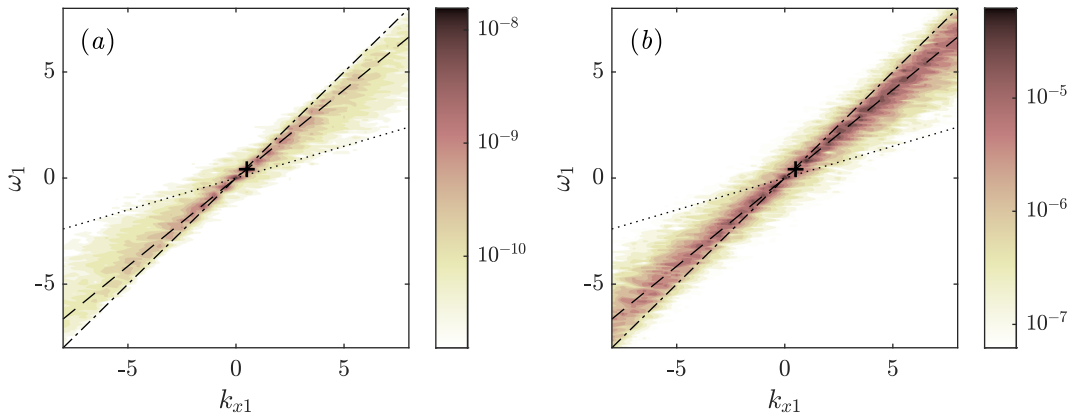

Figure B.2: Magnitude of (a) $\sum_{k_{z1}} P(\boldsymbol{k}_1, \boldsymbol{k}_3 - \boldsymbol{k}_1)$, the forcing coefficients summed in k_{z1} and plotted as functions of k_{x1} and ω_1 for $\boldsymbol{k}_3 = [0.5,\ 4,\ 0.415]$, and (b) $\sum_{k_{z1}} R(\boldsymbol{k}_1, \boldsymbol{k}_3 - \boldsymbol{k}_1)$, the response coefficients. The dash-dotted lines in both figures mark the wavespeed $c_1 = \omega/k_x = 1$; the dashed lines for $c_1 = c_2 = c_3 = 0.83$, the wavespeed of the selected $\boldsymbol{k}_3$; and the dotted lines for $c_1 = 0.3$ ($c_1^+ = 6$). The + markers in both figures denote the locations of $\boldsymbol{k}_3$.

Appendix C

VARIATIONS OF FORCING AND RESPONSE COEFFICIENTS

In Chapter 5, we presented the two-dimensional forcing and response coefficients P_{k_x}, P_{k_z}, P_ω, R_{k_x}, R_{k_z}, and R_ω computed by taking the average over all temporal segments. In this appendix, we will analyze the variation of these coefficients over the different temporal segments to determine the robustness of the identified features.

For each of the two-dimensional coefficients, we start by defining the coefficients for the i^{th} temporal segment with a superscript i. For example, the streamwise response coefficient at the i^{th} temporal segment is denoted as $R^i_{k_x}$. Therefore, R_{k_x} defined in equation (5.7a) can be rewritten as the average of the results from all temporal segments:

$$R_{k_x}(k_{x1}, k_{x2}) = \frac{1}{N_{seg}} \sum_{i=1}^{N_{seg}} R^i_{k_x}(k_{x1}, k_{x2}), \tag{C.1}$$

where $N_{seg} = 5$ is the number of available temporal segments.

For each of the 2D coefficients, we will first plot the results from each temporal segment and compare with the averaged result for both the magnitudes and the phases in formats similar to Figures 5.3-5.5 and Figure 5.6.

Next, to quantify the variations of the magnitude, we define ϵ, the standard deviation of the magnitude of the coefficient normalized by the average magnitude, to provide a relative quantification of the variations over different temporal segments. For example, for R_{k_x}, $\epsilon_{R_{k_x}}$ is defined as:

$$\epsilon_{R_{k_x}}(k_{x1}, k_{x2}) = \frac{std\left(\left|R^i_{k_x}\right|\right)}{mean\left(\left|R^i_{k_x}\right|\right)}. \tag{C.2}$$

This can be defined for all six two-dimensional forcing and response coefficients. A small magnitude of ϵ (much smaller than 1) indicates small variation relative to the mean, or in other words, the identified features in the forcing or response coefficients are robust. A large magnitude of ϵ ($\sim$ 1 or larger that 1) indicates a variation level comparable to the mean, which is the result of high variations in the magnitude of the forcing or response coefficients, and would require further analysis. Similarly,

the deviation of the phase can be quantified using α, the standard deviation of the phase across the five temporal segments:

$$\alpha_{R_{k_x}}(k_{x1}, k_{x2}) = std\left(\left|\angle R^i_{k_x}\right|\right) \tag{C.3}$$

C.1 Magnitude Variations of the Forcing Coefficients

We start by comparing the magnitude of the forcing coefficients for the five temporal segments and the averaged coefficient in Figure C.1-C.3. In these three figures, subplots (a) - (e) are the results from individual temporal segments 1 - 5, and subplots (f) are the results of the average over all five temporal segments. In Figures C.4-C.6, the normalized standard deviations, $\epsilon_{P_{k_x}}$, $\epsilon_{P_{k_z}}$, and ϵ_{P_ω} are plotted for the three forcing coefficients. In each figure, subplot (a) is the result for integrating over the entire y range, while subplots (b)-(d) are the results for three different y ranges, same as the results presented in Chapter 5. In all three figures, ϵ are plotted in log scale, sharing the same colorbar from 10^{-2} (small relative variance) to 1 (large relative variance).

From the six set of figures, it can be observed that the magnitude of all three forcing coefficients exhibits almost identical structures with only small variations in the numerical values across all five temporal segments. One of the two notable exceptions is the teardrop shaped region at high k_{z2} and k_{z3} values for P_{k_z}, which can be observed in Figures C.2 and C.5. This region is previously identified as a region not well converged, and the observations here provide additional evidence. Additionally, the high wavenumber region in P_{k_x} for $y^+ \in (200, 550)$ displays high relative variations as observed in Figure C.4 (d). This region corresponds to the small magnitude region of P_{k_x} as shown in Figures 5.3 (d), and the normalization with this small magnitude causes the observed high $\epsilon_{P_{k_x}}$. Apart from these two exceptions, the overall structures of the forcing coefficients are robust and consistent across the different temporal segments, and the main conclusions regarding the importance of triadic interactions involving large scale structures remain valid.

C.2 Magnitude Variations of the Response Coefficients

Next, the magnitude of the response coefficients for the five temporal segments and the averaged coefficients for the streamwise response coefficients R_{k_x}, the spanwise response coefficients R_{k_z}, and the temporal response coefficients R_ω are compared in Figures C.7 - C.9. Similarly, in the three figures, subplots (a) - (e) are the results from individual temporal segments 1 - 5, and subplots (f) are the results of the average over all five temporal segments. Additionally, the normalized standard

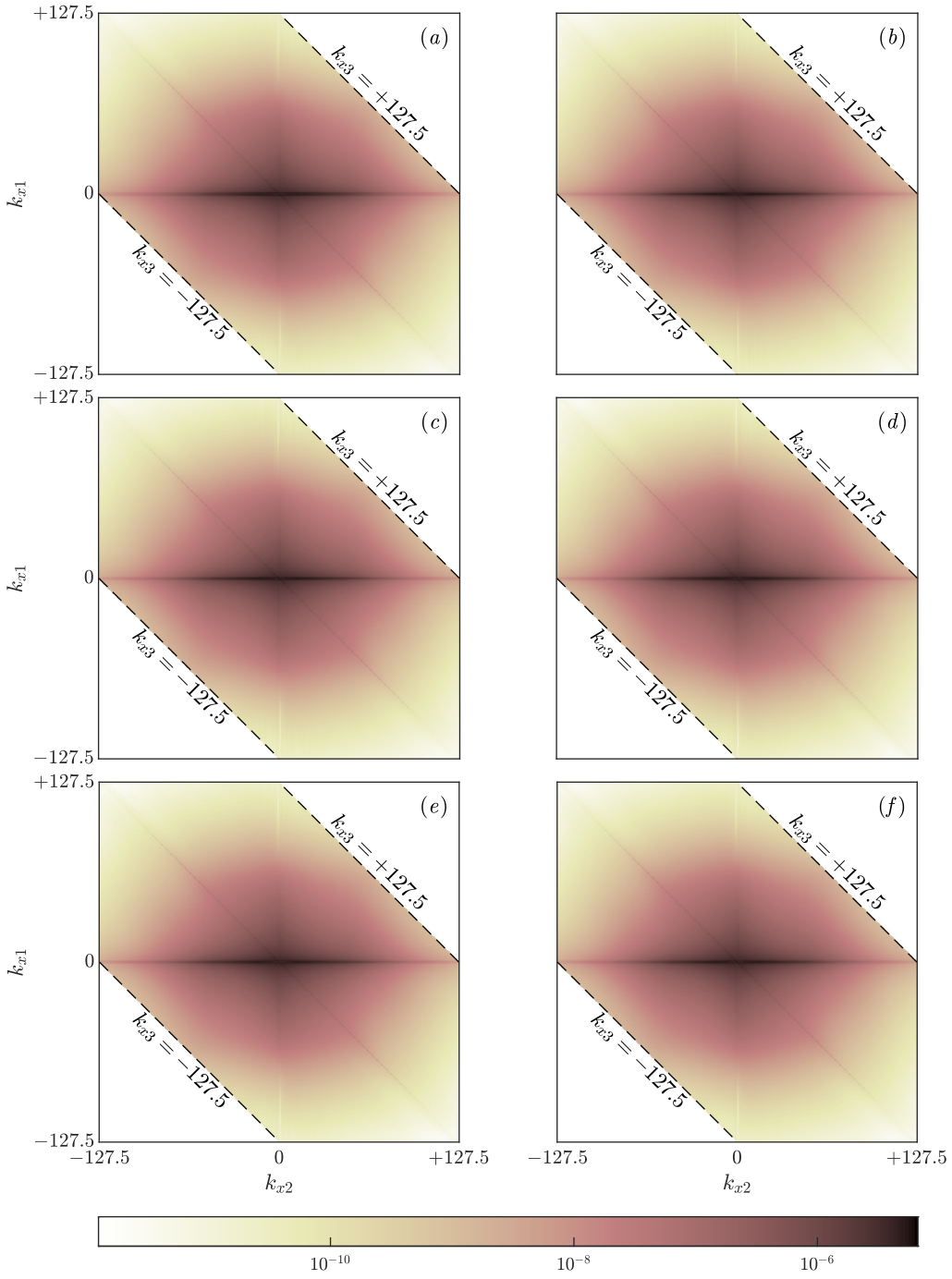

Figure C.1: Comparison of the magnitude of the streamwise forcing coefficient $\left|P_{k_x}\right|$ between (*a*-*e*) the five individual temporal segments and (*f*) the average over all five temporal segments. The figure formats are the same as Figure 5.3, with k_{x1} on the vertical axis and k_{x2} on the horizontal axis. All six subplots share the same log scale colorbar at the bottom of the figure.

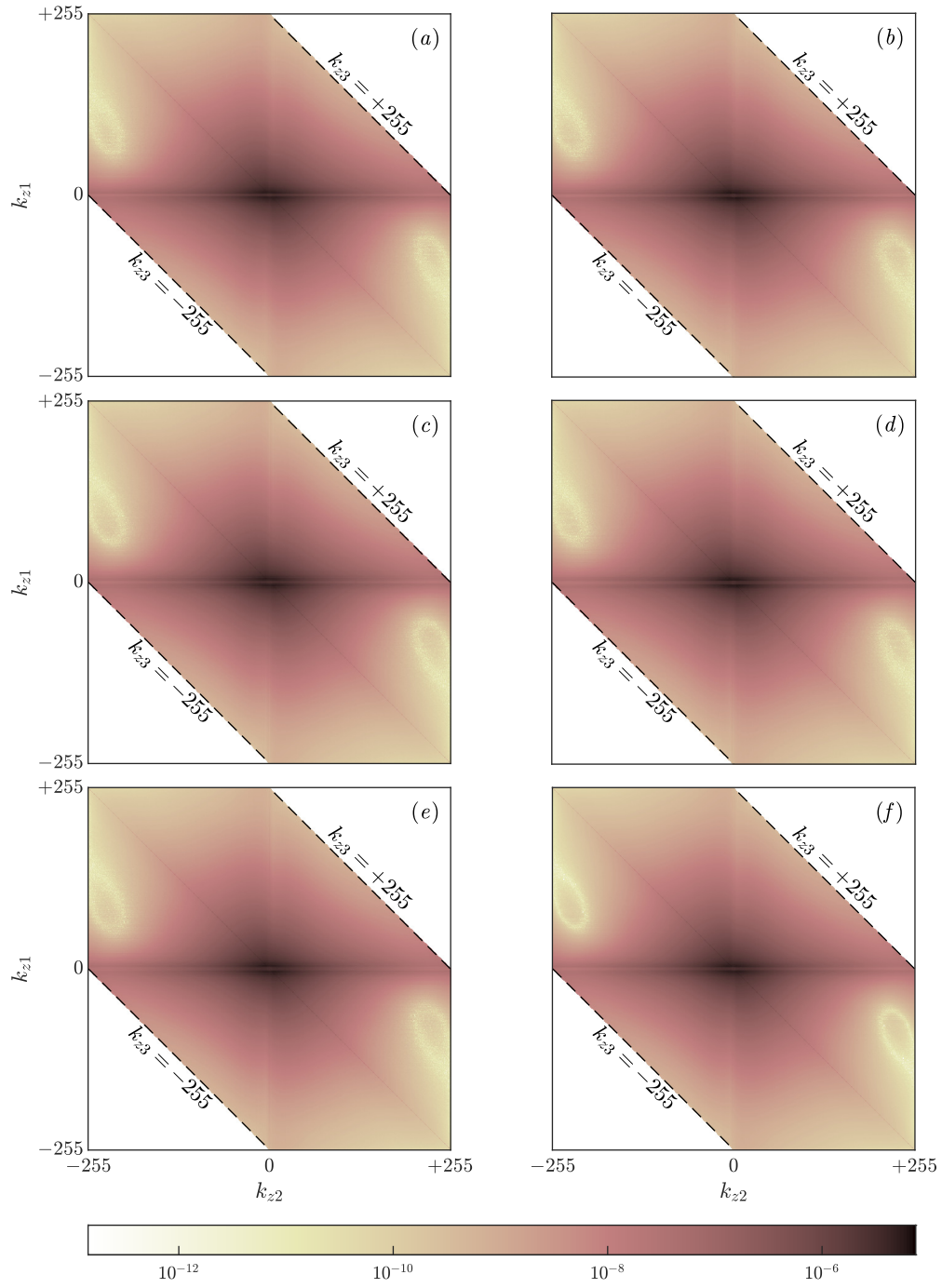

Figure C.2: Comparison of the magnitude of the spanwise forcing coefficient $\left|P_{k_z}\right|$ between (*a*-*e*) the five individual temporal segments and (*f*) the average over all five temporal segments. The figure formats are the same as Figure 5.4, with k_{z1} on the vertical axis and k_{z2} on the horizontal axis. All six subplots share the same log scale colorbar at the bottom of the figure.

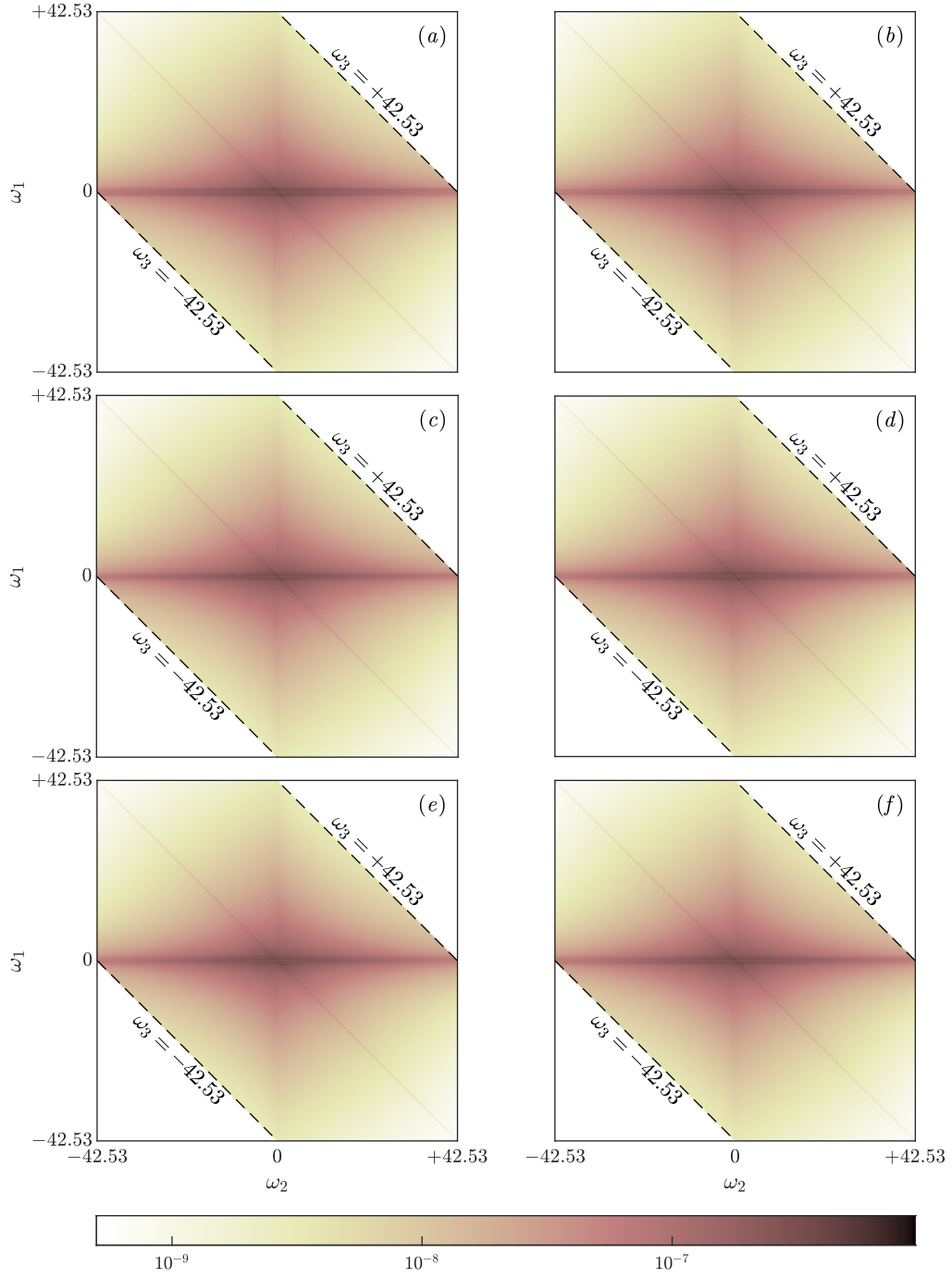

Figure C.3: Comparison of the magnitude of the temporal forcing coefficient $|P_\omega|$ between (*a*-*e*) the five individual temporal segments and (*f*) the average over all five temporal segments. The figure formats are the same as Figure 5.5, with ω_1 on the vertical axis and ω_2 on the horizontal axis. All six subplots share the same log scale colorbar at the bottom of the figure.

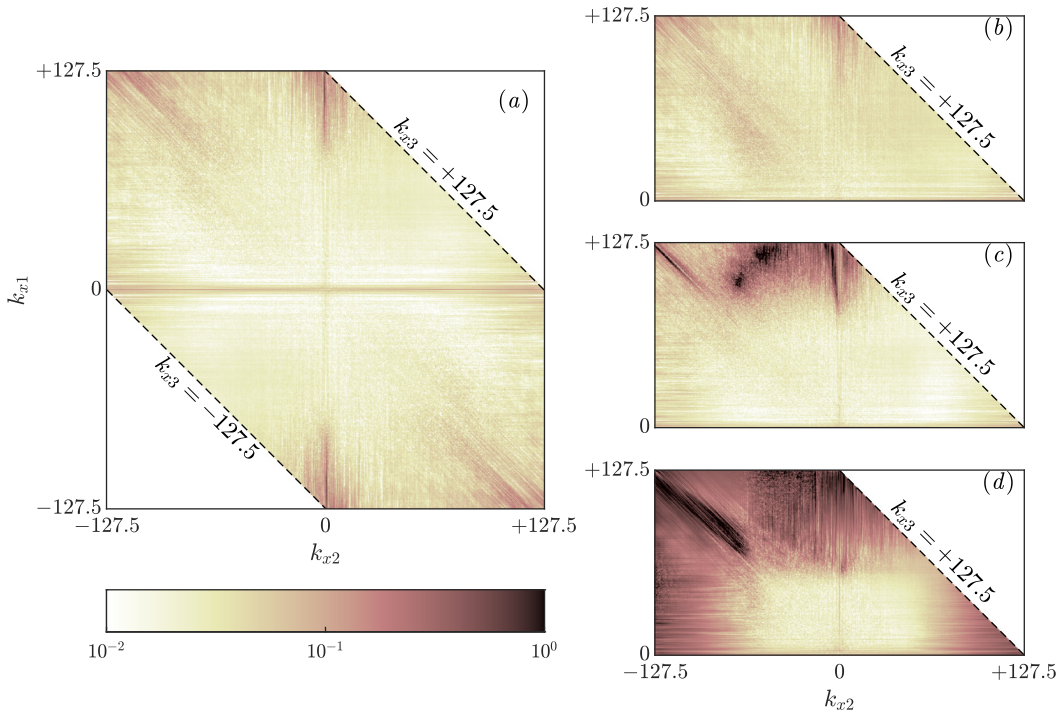

Figure C.4: Heatmaps of $\epsilon_{P_{k_x}}$, the standard deviation of $\left|P_{k_x}(k_{x1}, k_{x2})\right|$ normalized by the average of $\left|P_{k_x}\right|$. Subplots (a - d) share the same logarithmic colorbar, and the y-integration limits for the inner product in equation (4.14) are: (a) all y^+; (b) $y^+ \in (0, 30)$; (c) $y^+ \in (30, 200)$; and (d) $y^+ \in (200, 550)$. The streamwise wavenumber for the velocity fields, k_{x1}, is on the vertical axis; k_{x2} for the velocity gradient is on the horizontal axis; $k_{x3} = k_{x1} + k_{x2}$ for the resulting forcing and response is constant along lines with slopes of -1, same as the figures presented in Chapter 5.

deviation, $\epsilon_{R_{k_x}}$, $\epsilon_{R_{k_z}}$, and ϵ_{R_ω} are plotted in Figure C.10-C.12 for the magnitudes of the response coefficients.

From Figures C.7 - C.9, it can be observed that the overall structures of the figures are relatively robust across the different temporal segments, with the high magnitude regions located at the same locations throughout all temporal segments. However, the normalized standard deviations show that the variations of the numerical values are non-negligible. Nevertheless, since all conclusions in Chapter 5 are drawn from the overall distribution of the high magnitude regions of the response coefficients, which are shown to be robust across different temporal segments, these conclusions remain valid despite the observed variations.

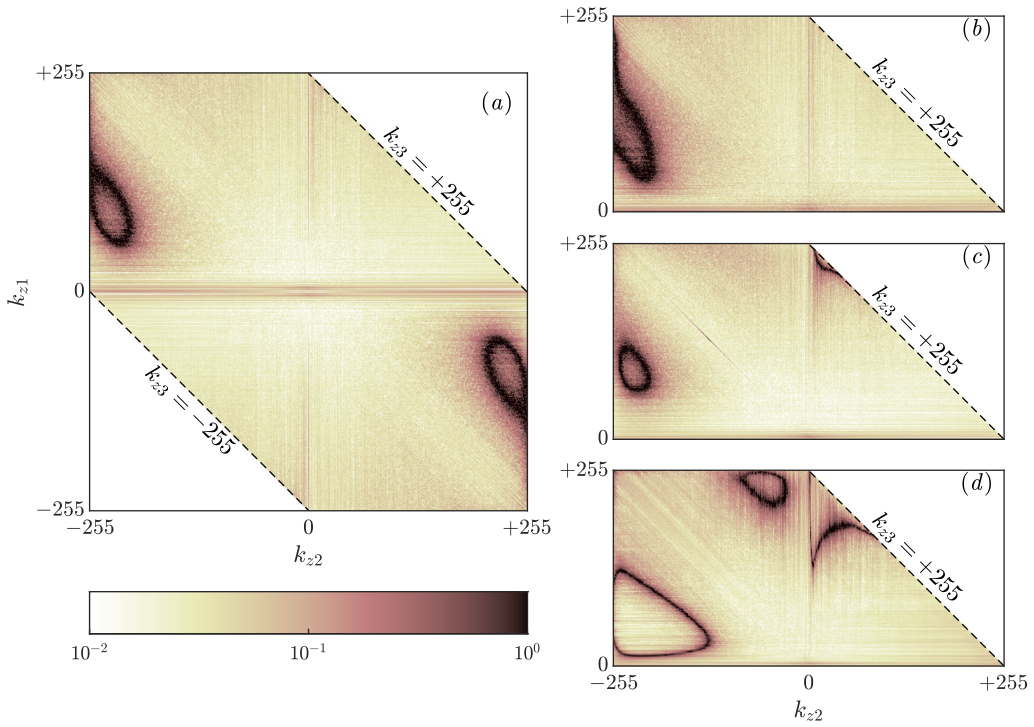

Figure C.5: Heatmaps of $\epsilon_{P_{k_z}}$, the standard deviation of $\left|P_{k_z}(k_{z1}, k_{z2})\right|$ normalized by the average of $\left|P_{k_z}\right|$ in the same format as Figure C.4.

C.3 Phase Variations of the Response Coefficients

Finally, the phase of the response coefficients are compared between the results from the five individual temporal segments and the results from the average of all five segments in Figures C.13-C.15, and the standard deviations of the phase angles across all five temporal segments are plotted in Figure C.16. From these figures, it can be observed that the overall structures of the phase of the response coefficients remain robust across different temporal segments. Additionally, the strongly constructive and strongly destructive regions have small standard deviations.

Between the constructive and destructive regions, fuzzy transition regions can be observed. These transition regions have relatively high standard deviations and some salt-and-pepper like variations. The fuzziness in these transition regions are reduced by the averaging across all five temporal segments as observed in subplots (f) of Figures C.13-C.15. The results in the transition regions might not be fully converged, and future studies focusing on these transition regions would require more data to ensure the convergence and robustness of features in the transition region.

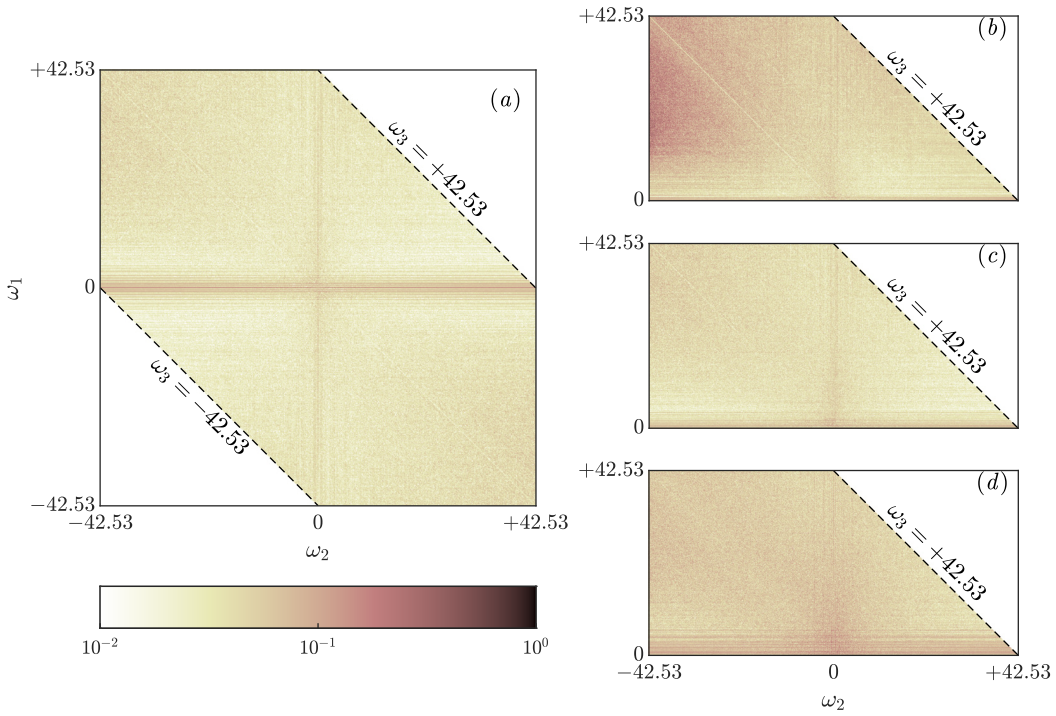

Figure C.6: Heatmaps of ϵ_{P_ω}, the standard deviation of $|P_\omega(\omega_1, \omega_2)|$ normalized by the average of $|P_\omega|$ in the same format as Figure C.4.

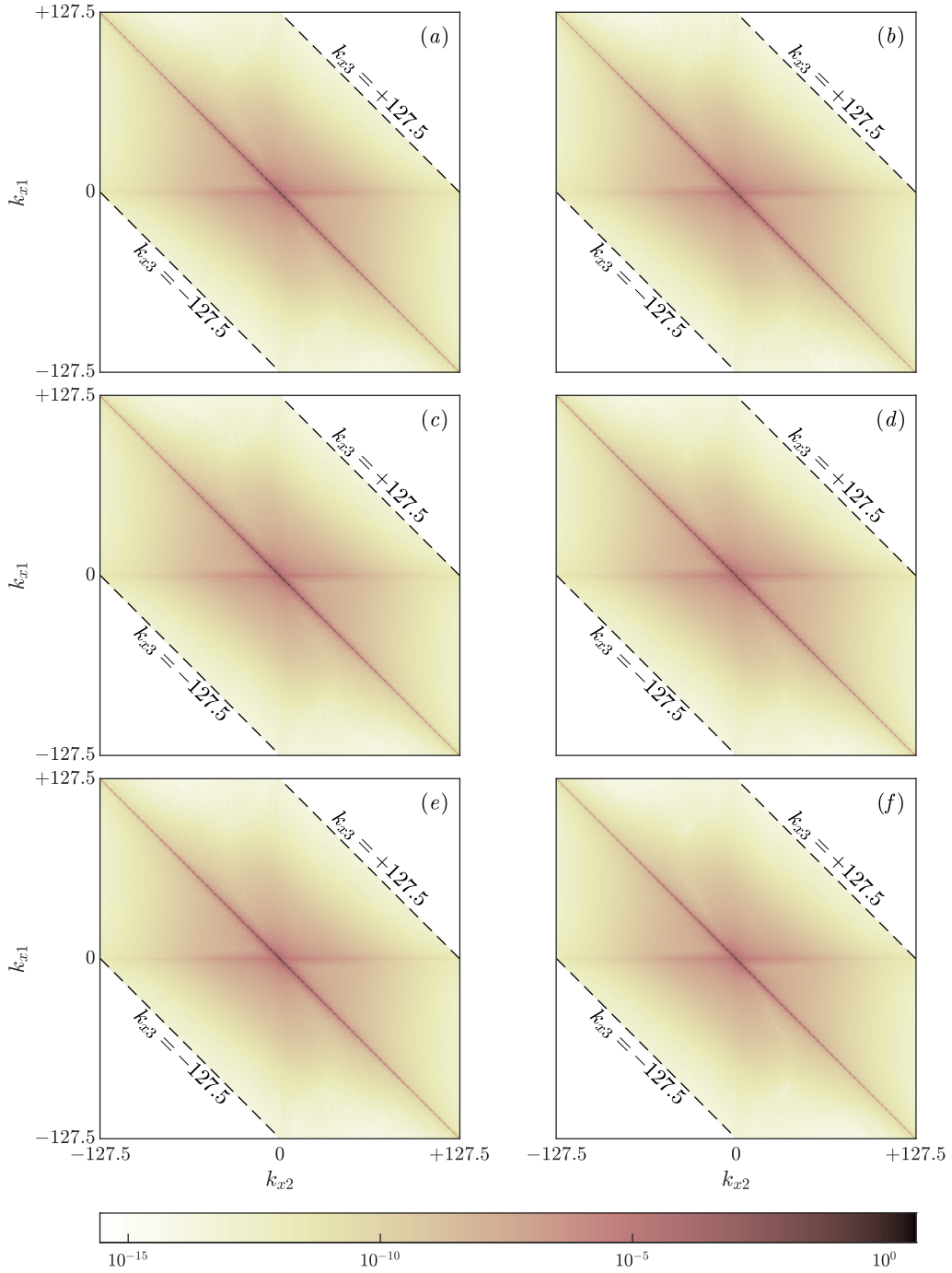

Figure C.7: Comparison of the magnitude of the streamwise response coefficient $\left|R_{k_x}\right|$ between (*a-e*) the five individual temporal segments and (*f*) the average over all five temporal segments. The figure formats are the same as Figure 5.3, with k_{x1} on the vertical axis and k_{x2} on the horizontal axis. All six subplots share the same log scale colorbar at the bottom of the figure.

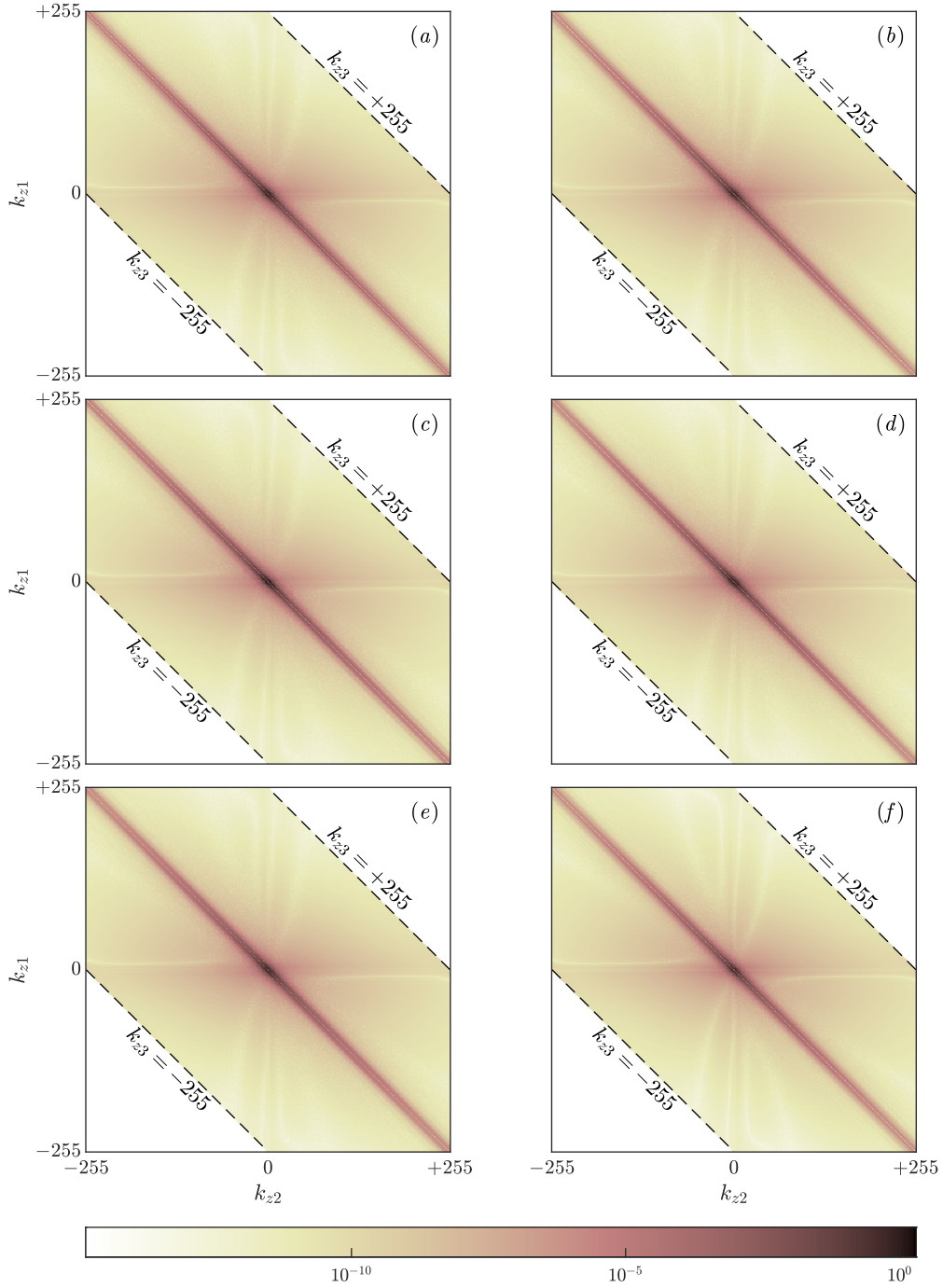

Figure C.8: Comparison of the magnitude of the spanwise response coefficient $\left|R_{k_z}\right|$ between (*a*-*e*) the five individual temporal segments and (*f*) the average over all five temporal segments. The figure formats are the same as Figure 5.4, with k_{z1} on the vertical axis and k_{z2} on the horizontal axis. All six subplots share the same log scale colorbar at the bottom of the figure.

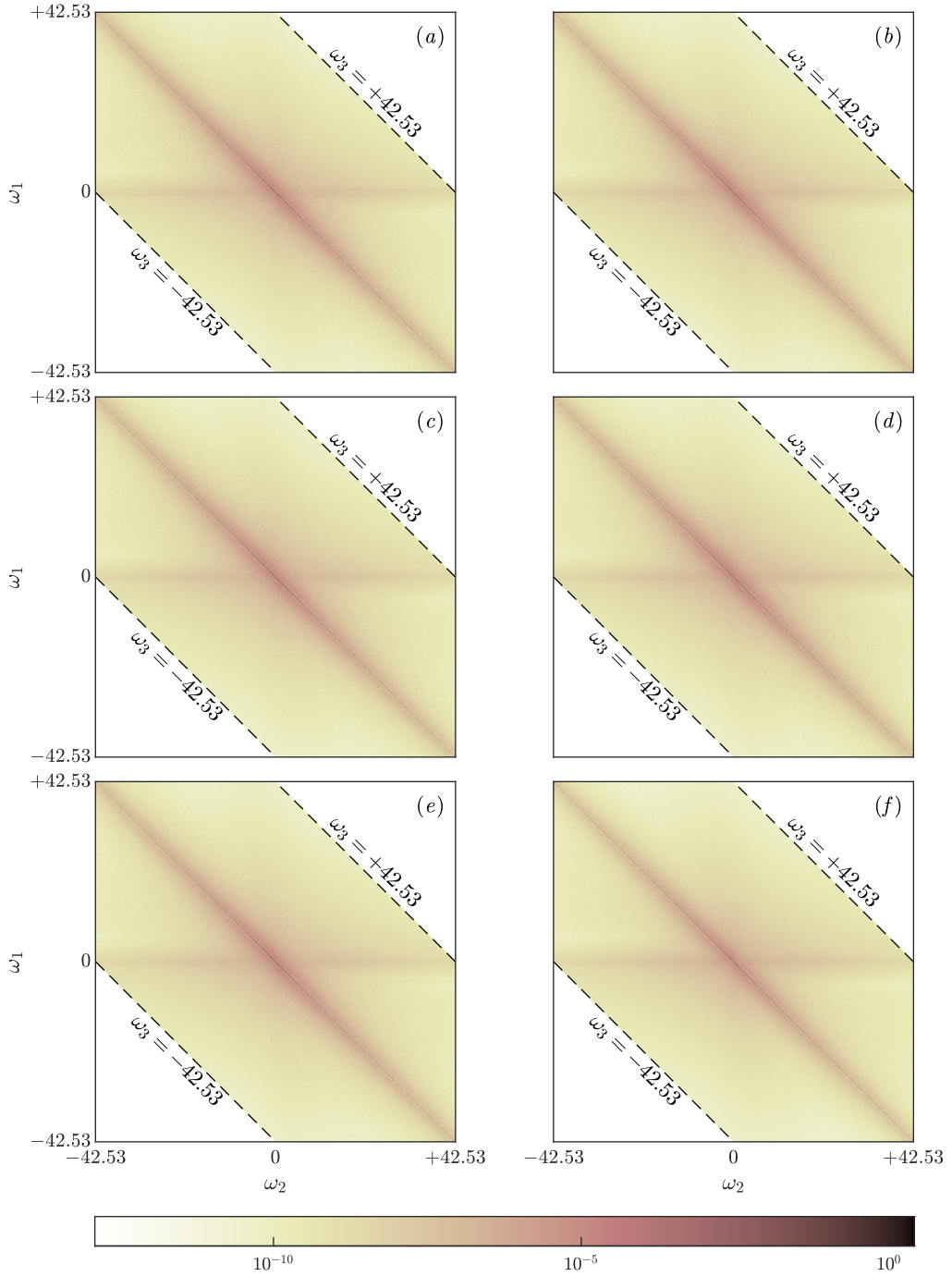

Figure C.9: Comparison of the magnitude of the temporal response coefficient $|R_\omega|$ between (*a*-*e*) the five individual temporal segments and (*f*) the average over all five temporal segments. The figure formats are the same as Figure 5.5, with ω_1 on the vertical axis and ω_2 on the horizontal axis. All six subplots share the same log scale colorbar at the bottom of the figure.

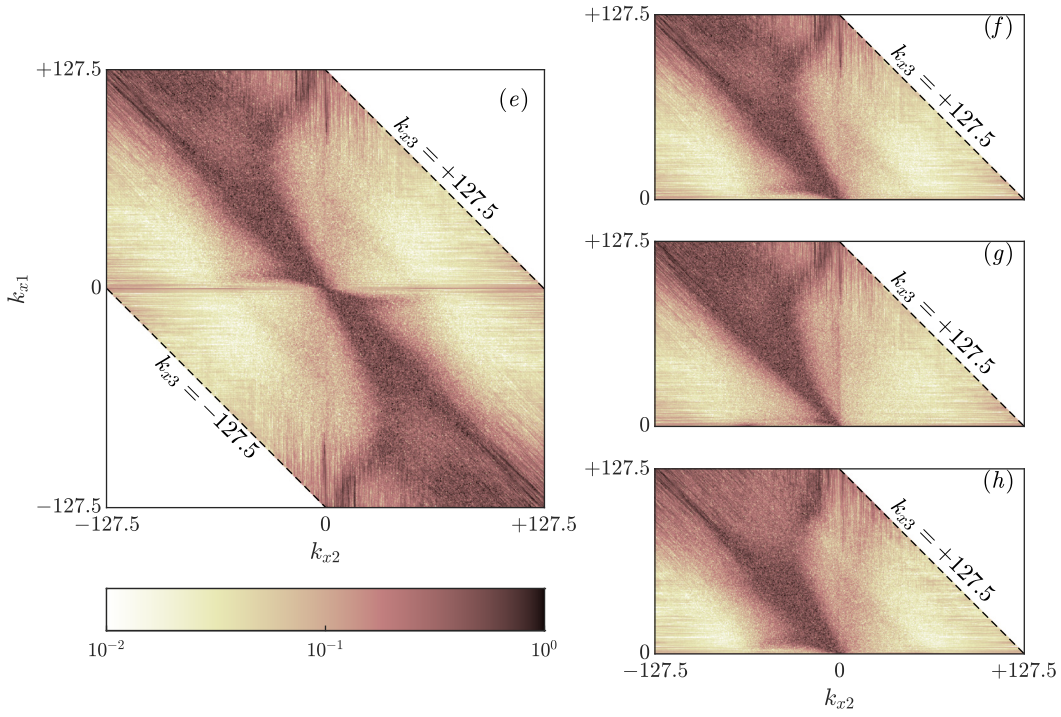

Figure C.10: Heatmaps of $\epsilon_{R_{k_x}}$, the standard deviation of $\left|R_{k_x}(k_{x1}, k_{x2})\right|$ normalized by the average of $\left|R_{k_x}\right|$. Subplots (*a* - *d*) share the same logarithmic colorbar, and the y-integration limits for the inner product in equation (4.14) are: (*a*) all y^+; (*b*) $y^+ \in (0, 30)$; (*c*) $y^+ \in (30, 200)$; and (*d*) $y^+ \in (200, 550)$. The streamwise wavenumber for the velocity fields, k_{x1}, is on the vertical axis; k_{x2} for the velocity gradient is on the horizontal axis; $k_{x3} = k_{x1} + k_{x2}$ for the resulting forcing and response is constant along lines with slopes of -1, same as the figures presented in Chapter 5.

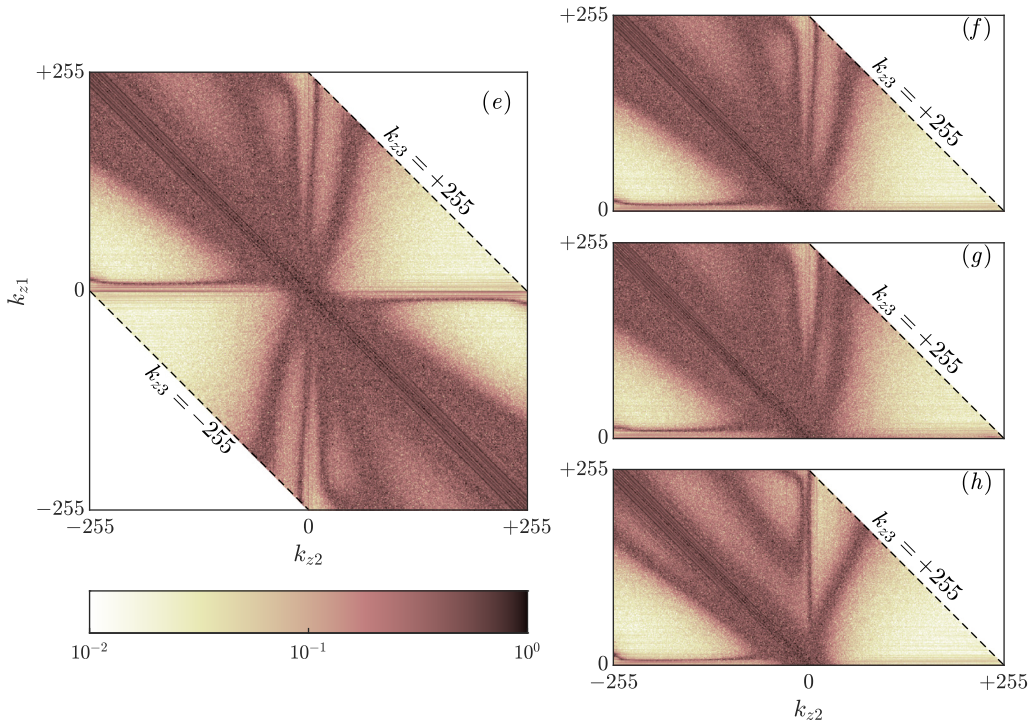

Figure C.11: Heatmaps of $\epsilon_{R_{k_z}}$, the standard deviation of $\left|R_{k_z}(k_{z1}, k_{z2})\right|$ normalized by the average of $\left|R_{k_z}\right|$ in the same format as Figure C.10.

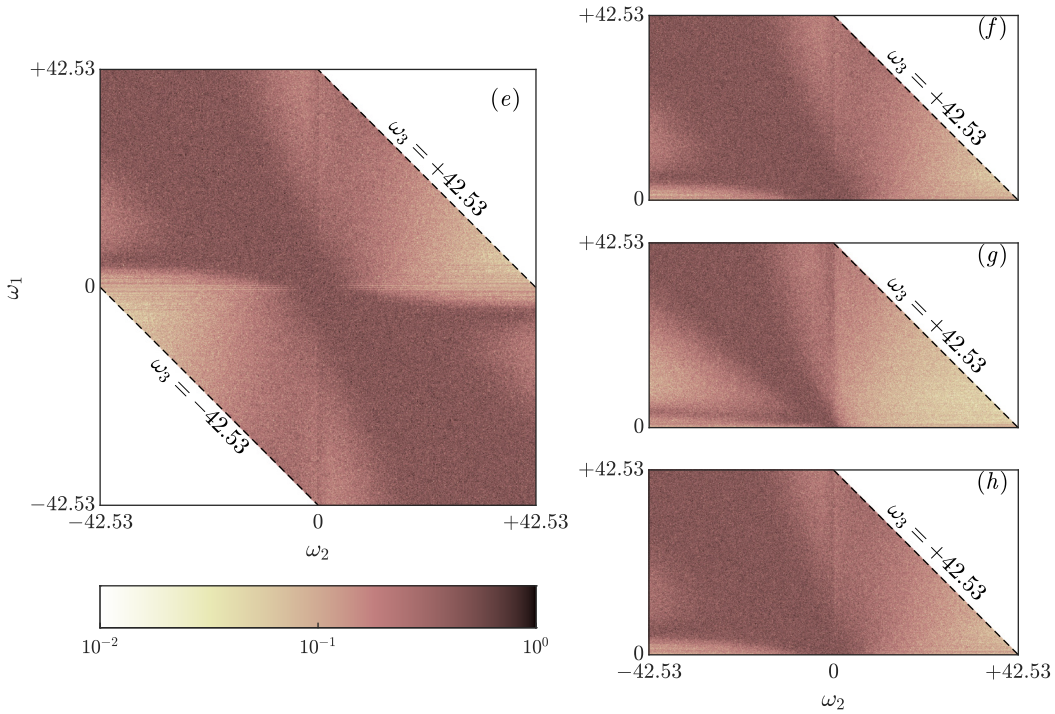

Figure C.12: Heatmaps of ϵ_{R_ω}, the standard deviation of $|R_\omega(\omega_1, \omega_2)|$ normalized by the average of $|R_\omega|$ in the same format as Figure C.10.

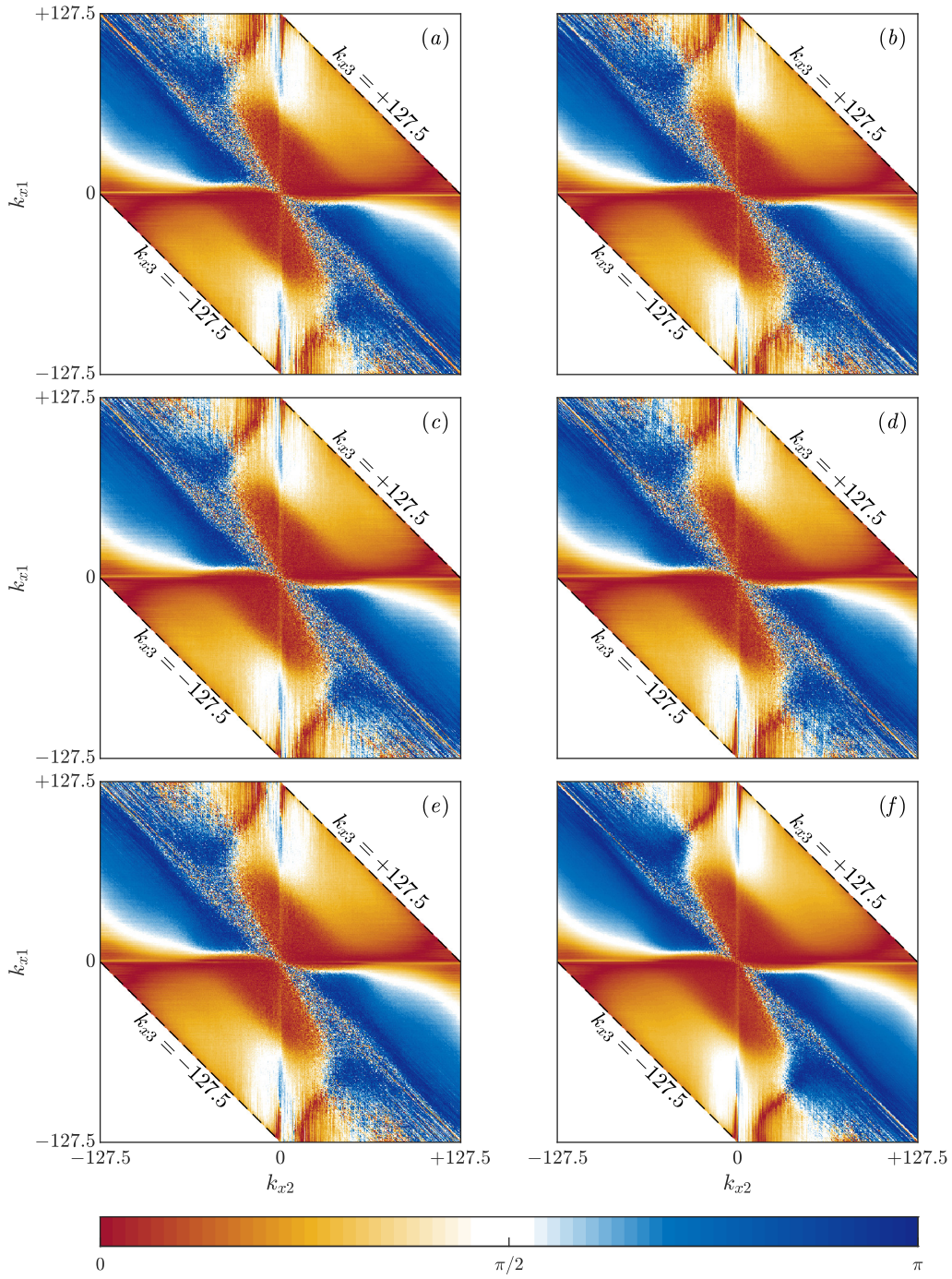

Figure C.13: Comparison of the phase of the streamwise response coefficient $\angle R_{k_x}$ between (*a*-*e*) the five individual temporal segments and (*f*) the average over all five temporal segments. The figure formats are the same as Figure 5.6, with k_{x1} on the vertical axis and k_{x2} on the horizontal axis. All six subplots share the same linear scale colorbar at the bottom of the figure spanning from 0 (constructive interference) to π (destructive interference).

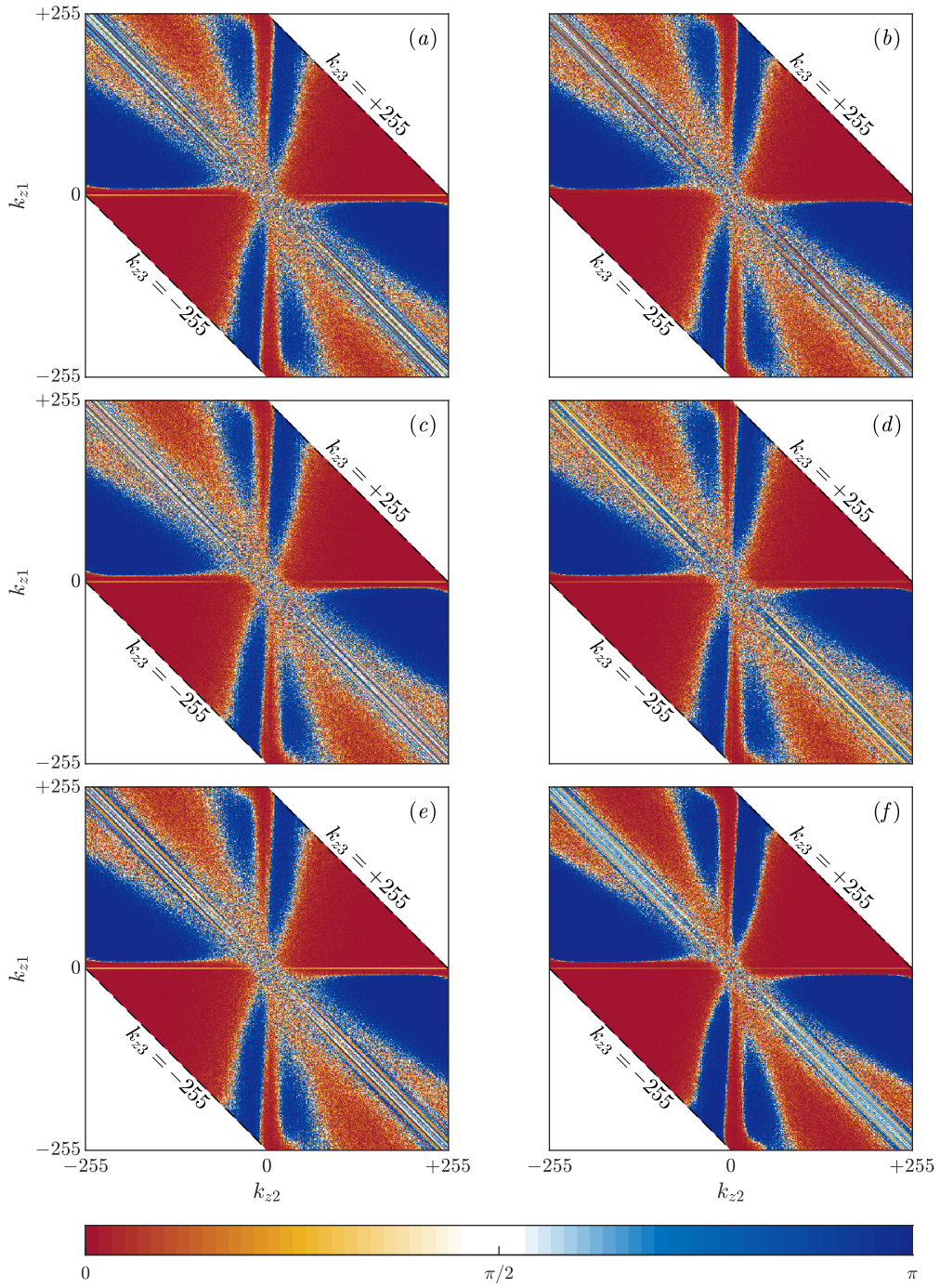

Figure C.14: Comparison of the phase of the spanwise response coefficient $\angle R_{k_z}$ between (*a*-*e*) the five individual temporal segments and (*f*) the average over all five temporal segments. The figure formats are the same as Figure 5.6, with k_{z1} on the vertical axis and k_{z2} on the horizontal axis. All six subplots share the same linear scale colorbar at the bottom of the figure spanning from 0 (constructive interference) to π (destructive interference).

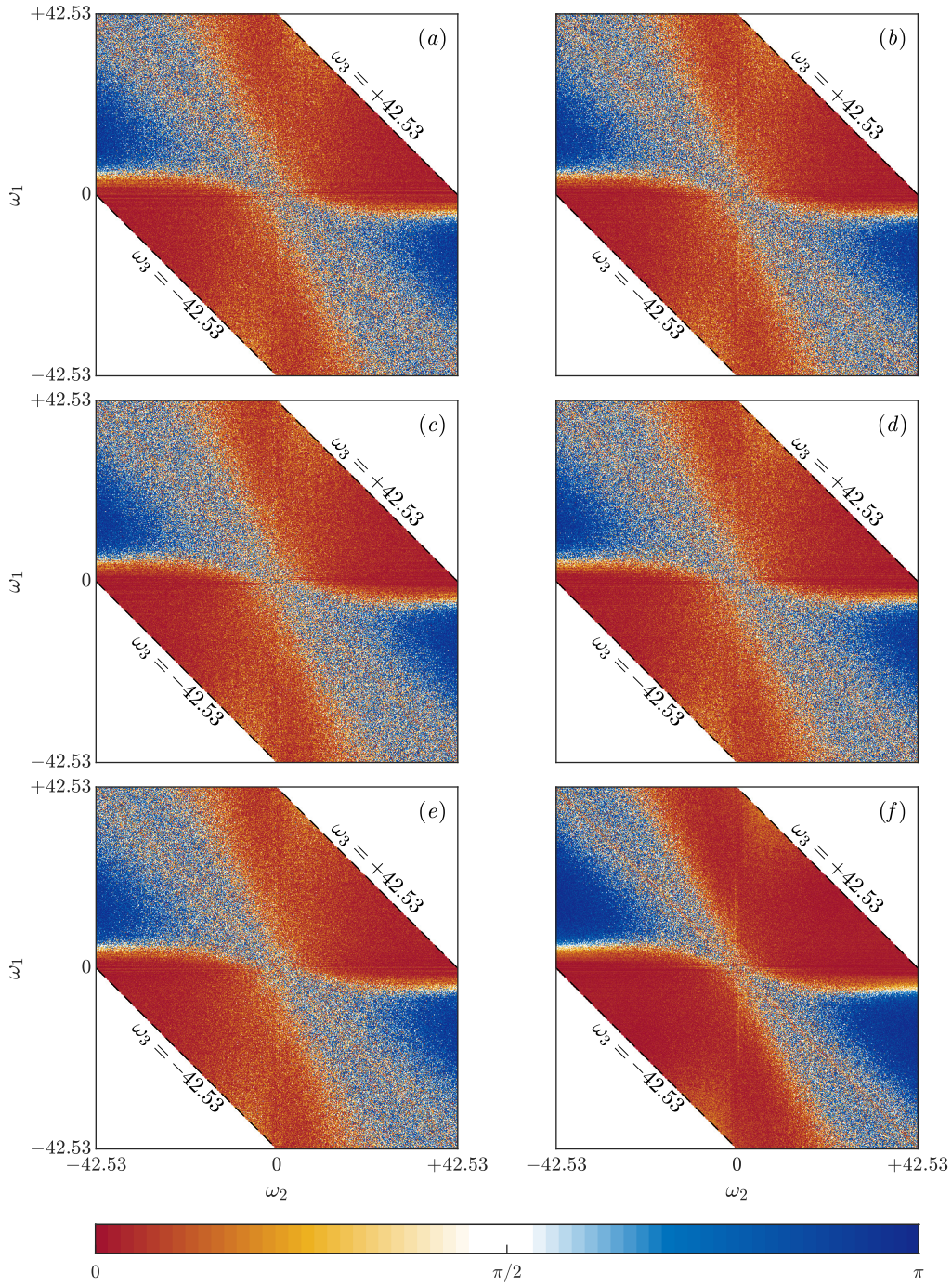

Figure C.15: Comparison of the phase of the temporal frequency response coefficient $\angle R_\omega$ between (*a*-*e*) the five individual temporal segments and (*f*) the average over all five temporal segments. The figure formats are the same as Figure 5.6, with ω_1 on the vertical axis and ω_2 on the horizontal axis. All six subplots share the same linear scale colorbar at the bottom of the figure spanning from 0 (constructive interference) to π (destructive interference).

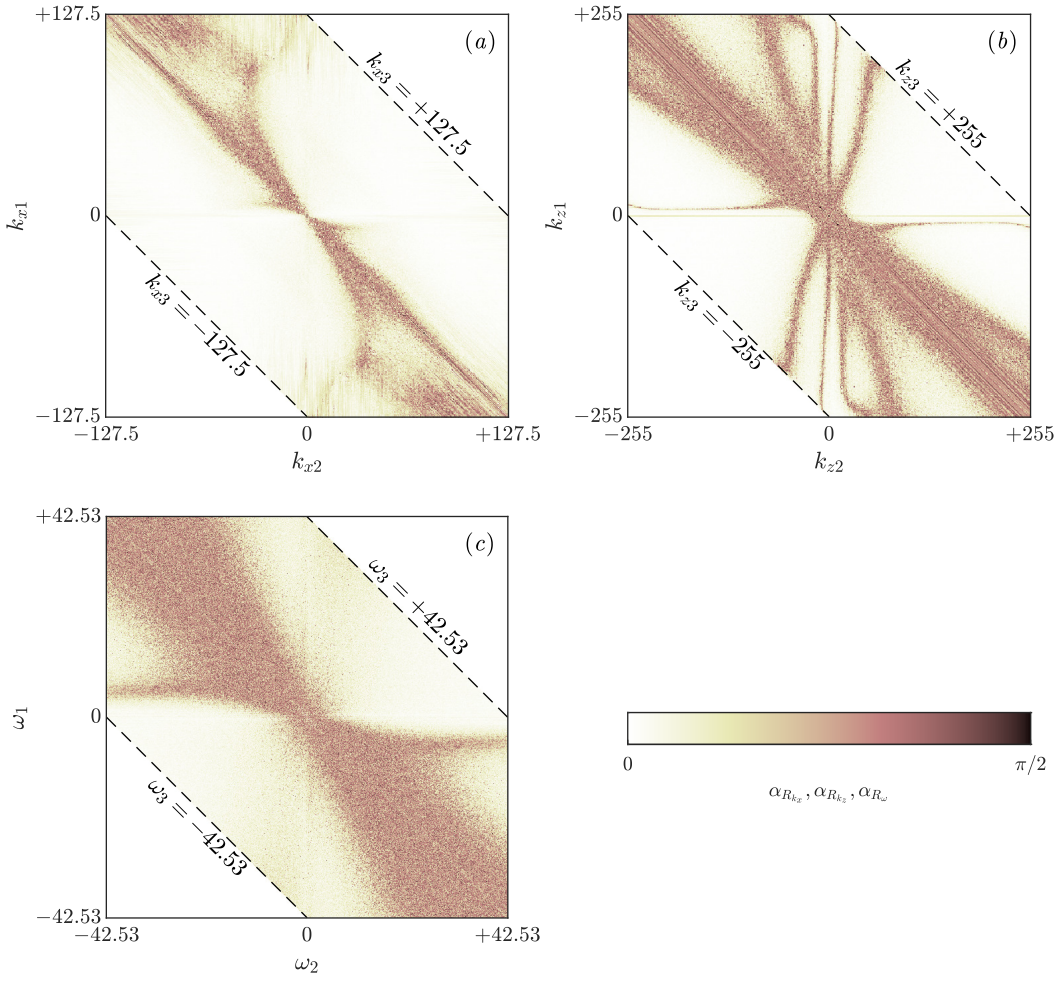

Figure C.16: Standard deviation of the phase of the response coefficients across the five temporal segments: (*a*) $\alpha_{R_{k_x}}$, (*b*) $\alpha_{R_{k_z}}$, and (*c*) α_{R_ω},

Appendix D

NUMERICAL ALGORITHMS

The DNS data sizes in Fourier space are N_{k_x} N_{k_z}, N_ω for the streamwise, spanwise wavenumbers and temporal frequencies, and the number of temporal segments is N_{seg}. In physical space, the data sizes are N_x, N_y, N_z, N_t for the three spatial coordinates and time. An additional subscripts p indicates that the dimension is distributed across the more than 100 CPU cores utilized for the computations. Additionally, nine weight matrices $\boldsymbol{W}$ are utilized for the computations: three different y integration ranges for each of the three velocity components.

The full data set is too big to completely fit in available memory; therefore an outermost sequential loop is required, so that the code reads and operates only on a partial data set within a given iteration. Internally, parallel loops are required within the outermost sequential loop to utilize all the available CPU cores.

The computation of $\boldsymbol{h}(\boldsymbol{k}, y)$ defined in equation (5.12), involving the resolvent operator, and a Fourier transform in time, requires all data in y and t. Therefore, the outermost loop of algorithm 1 is selected to be k_z, with internal parallelization on k_x. For the computation of $V(\boldsymbol{k})$, defined in equation (4.12) and R_{k_x}, R_{k_z}, R_ω using equations (5.14a)-(5.14c), Fourier transforms in x, z and t are utilized and therefore leaving y as the only available dimension for the outermost loop. However, these computations also utilize the first derivatives in y, and we elect to pre-compute and store the y derivatives to use later in these computations. The algorithms 2-6 for $V(\boldsymbol{k})$, and R_{k_x}, R_{k_z}, R_ω, internally switches between different dimensions for parallelization, with high-level overviews given below.

In these overviews, "master" is the master core, a single CPU core that assigns tasks to "slaves", which are all other CPU cores. The data dimensions, for example $[N_{k_x,p} \times N_y \times N_t] \times 2$ indicates the presence of 2 variables with size $[N_{k_x,p} \times N_y \times N_t]$, and $N_{k_x,p}$ indicates that the total N_{k_x} streamwise wavenumbers are distributed across all available CPU cores.

Algorithm 1: Computing $\boldsymbol{h}(\boldsymbol{k})$

for $i_{k_z} = 1 : N_{k_z}$ **do**
  Master reads $v(t), \omega_2(t)$ for current k_z
  Master distributes data in k_x to all salves ▷ $[N_{k_x,p} \times N_y \times N_t] \times 2$
  for $i_{k_x} = 1 : N_{k_x,p}$ **do** ▷ Parallel Loop
    Compute $\Delta, \mathcal{L}_{OS}, \mathcal{L}_{SQ}$ for current (k_x, k_z)
    Compute $\frac{\partial v}{\partial y}(t), u(t), w(t)$ ▷ $[N_y \times N_t] \times 3$
    Segment, apply window function $w(t)$, FFT in t, truncate $\omega \rightarrow \hat{\boldsymbol{u}}$ ▷ $[N_y \times N_\omega \times N_{seg}] \times 3$
    Segment, apply window function $\frac{\mathrm{d}}{\mathrm{d}t} w(t)$, FFT in t, truncate $\omega \rightarrow \hat{\boldsymbol{s}}$ ▷ $[N_y \times N_\omega \times N_{seg}] \times 3$
    for $i_\omega = 1 : N_\omega$ **do**
      Compute $\mathcal{H}'(\boldsymbol{k})$ for current $\boldsymbol{k}$
      for $i_{seg} = 1 : N_{seg}$ **do**
        Compute $\tilde{\boldsymbol{u}} = \hat{\boldsymbol{u}} - \boldsymbol{A}(k_x, k_z)\mathcal{H}'(\boldsymbol{k})\boldsymbol{B}(k_x, k_z)\hat{\boldsymbol{s}}$
        Compute $E_u(\boldsymbol{k}) = \tilde{u}^* \boldsymbol{W} \tilde{u}$, $E_v(\boldsymbol{k}), E_w(\boldsymbol{k})$ ▷ $[N_{k_x,p} \times N_\omega \times N_{seg}] \times 3$
        Compute $\boldsymbol{h}(\boldsymbol{k}) = \tilde{\boldsymbol{u}}^*(\boldsymbol{k})\boldsymbol{W}\boldsymbol{A}(k_x, k_z)\mathcal{H}'(\boldsymbol{k})\boldsymbol{B}(k_x, k_z)$ with 9 different $\boldsymbol{W}$ ▷ $[3N_y \times N_{k_x,p} \times N_\omega \times N_{seg}] \times 9$
      end
    end
  end
  Master collects data in k_x from slaves
  Master saves $\boldsymbol{h}(\boldsymbol{k})$, with each (y, seg) in a separate file ▷ $[N_{k_x} \times N_{k_z} \times 3 \times N_\omega] \times 9$
  Master saves $E_u(\boldsymbol{k})$, $E_v(\boldsymbol{k})$, $E_w(\boldsymbol{k})$, with each seg in a separate file ▷ $[N_{k_x} \times N_\omega \times N_{k_z}] \times 3$
end

Algorithm 2: Computing $V(\boldsymbol{k})$

for $i_y = 1 : N_y$ **do**
  Master reads $v(t), \omega_2(t), \frac{\partial \boldsymbol{u}}{\partial y}(t)$ for current y
  Master distributes data in t to each slave ▷ $[N_{k_x} \times N_{k_z} \times N_{t,p}] \times 5$
  for $i_t = 1 : N_{t,p}$ **do** ▷ Parallel Loop
    Compute u, w at current (y, t), 1D mean subtract for u ▷ $[N_{k_x} \times N_{k_z}] \times 2$
    Compute $\boldsymbol{f}$ at current (y, t), 1D mean subtract for f_x ▷ $[N_{k_x} \times N_{k_z} \times N_{t,p}] \times 3$
  end
  Exchange $\boldsymbol{f}$ from partial t to partial k_z ▷ $[N_{k_x} \times N_{k_z,p} \times N_t] \times 3$
  for $i_{k_z} = 1 : N_{k_z,p}$ **do** ▷ Parallel Loop
    Segment, apply window function $w(t)$, FFT in t, truncate $\omega \rightarrow \hat{\boldsymbol{f}}$ ▷ $[N_{k_x} \times N_{k_z,p} \times N_\omega \times N_{seg}] \times 3$
  end
  for $i_{seg} = 1 : N_{seg}$ **do**
    Exchange $\boldsymbol{f}$ from partial k_z to partial ω ▷ $[N_{k_x} \times N_{k_z} \times N_{\omega,p}] \times 3$
    Read $\boldsymbol{h}_u, \boldsymbol{h}_v, \boldsymbol{h}_w$ at current (y, seg) ▷ $[N_{k_x} \times N_{k_z} \times 3 \times N_{\omega,p}] \times 3$
    for $i_\omega = 1 : N_{\omega,p}$ **do** ▷ Parallel Loop
      Compute V_u, V_v, V_w ▷ point-wise multiplication
    end
  end
  Cumulatively sum V_u, V_v, V_w in y ▷ $[N_{k_x} \times N_{k_z} \times N_{\omega,p} \times N_{seg}] \times 3$ ▷ Weight matrix already in $\boldsymbol{h}$
end
Save data

Algorithm 3: Computing R_{k_x}, R_{k_z} and R_ω

for $i_y = 1 : N_y$ **do**
  Master reads $v(t), \omega_2(t), \frac{\partial \boldsymbol{u}}{\partial y}(t)$ for current y
  Master distributes data in t to each slave ▷ $[N_{k_x} \times N_{k_z} \times N_{t,p}] \times 5$
  for $i_t = 1 : N_{t,p}$ **do** ▷ Parallel Loop
    Compute $u(t), w(t)$ at current y, 1D mean subtract for u ▷ $[N_{k_x} \times N_{k_z} \times N_{t,p}] \times 2$
  end
  Master reads $\boldsymbol{h}$ at current y, and distributes data in ω to each slave ▷ $[N_{k_x} \times N_{k_z} \times 3 \times N_{\omega,p} \times N_{seg} \times 9]$
  Compute R_{k_x} using subroutine *compute_Rkx*
  Compute R_{k_z} using subroutine *compute_Rkz*
  Compute R_ω using subroutine *compute_Rom*
end
Cumulatively sum R_{k_x}, R_{k_z}, R_ω in y ▷ Weight matrix already in $\boldsymbol{h}$
Save data

Algorithm 4: subroutine *compute_Rkx* for computing R_{k_x} at a single y plane

Inputs: $\boldsymbol{u}$, $\frac{\partial \boldsymbol{u}}{\partial y}$, size $[N_{k_x} \times N_{k_z} \times N_{t,p}] \times 6$

Inputs: $\boldsymbol{h}$, size $[N_{k_x} \times N_{k_z} \times 3 \times N_{\omega,p} \times N_{seg} \times 9]$

for $i_t = 1 : N_{t,p}$ **do** ▷ Parallel Loop
  Compute $\frac{\partial \boldsymbol{u}}{\partial z}$ for current (y, t)
  Zeropad and IFFT in z for $\boldsymbol{u}$, $\frac{\partial \boldsymbol{u}}{\partial y}$, $\frac{\partial \boldsymbol{u}}{\partial z}$ ▷ $[N_z \times N_{t,p} \times N_{k_x}] \times 9$
end
Exchange $\boldsymbol{u}$, $\frac{\partial \boldsymbol{u}}{\partial y}$, $\frac{\partial \boldsymbol{u}}{\partial z}$ from partial t to partial z ▷ $[N_{z,p} \times N_t \times N_{k_x}] \times 9$
for $i_{k_{x3}} = 1 : N_{k_x}$ **do**
  Extract $\boldsymbol{h}$ at current k_{x3} ▷ $[N_{k_z} \times 3 \times N_{\omega,p} \times N_{seg} \times 9]$
  for $i_{seg} = 1 : N_{seg}$ **do**
    for $i_\omega = 1 : N_\omega$ **do** ▷ Parallel Loop
      Zeropad and IFFT in z for $\boldsymbol{h}$ ▷ $[N_z \times N_{\omega,p} \times N_{seg}] \times 3$
    end
    Exchange $\boldsymbol{h}$ from partial ω to partial z ▷ $[N_{z,p} \times N_\omega \times N_{seg} \times 9] \times 3$
  end
  for $i_{k_{x1}} = 1 : N_{k_x}$ **do** ▷ Operate on partial z data
    $k_{x2} = k_{x3} - k_{x1}$, skip loop if k_{x2} out of range
    Compute $\boldsymbol{f}(k_{x1}, k_{x3}, z, t)$ ▷ $[N_{z,p} \times N_t] \times 3$
    ▷ negative k_x obtained with complex conjugate
    Mean subtract f_x if $k_{x3} = 0$ ▷ average in z, t and subtract
    Segment, apply window function $w(t)$, FFT in t, truncate $\omega \rightarrow \boldsymbol{f}(k_{x1}, k_{x3}, z, \omega)$
    ▷ $[N_{z,p} \times N_\omega \times N_{seg}] \times 3$
    Pointwise multiply $\boldsymbol{f}$ with $\boldsymbol{h}$ and sum in z, ω_3 ▷ $[N_{k_{x1}} \times N_{k_{x2}} \times N_{seg} \times 27]$
  end
end
Sum in z over all processors with *MPI_REDUCE*

Algorithm 5: subroutine *compute_Rkz* for computing R_{k_z} at a single y plane

Inputs: $\boldsymbol{u}$, $\frac{\partial \boldsymbol{u}}{\partial y}$, size $[N_{k_x} \times N_{k_z} \times N_{t,p}] \times 6$
Inputs: $\boldsymbol{h}$, size $[N_{k_x} \times N_{k_z} \times 3 \times N_{\omega,p} \times N_{seg} \times 9]$

1 **for** $i_t = 1 : N_{t,p}$ **do** ▷ Parallel Loop
2 Compute $\frac{\partial \boldsymbol{u}}{\partial x}$ for current (y, t)
3 Zeropad and IFFT in x for $\boldsymbol{u}$, $\frac{\partial \boldsymbol{u}}{\partial y}$, $\frac{\partial \boldsymbol{u}}{\partial x}$ ▷ $[N_x \times N_{t,p} \times N_{k_z}] \times 9$
4 **end**
5 Exchange $\boldsymbol{u}$, $\frac{\partial \boldsymbol{u}}{\partial y}$, $\frac{\partial \boldsymbol{u}}{\partial x}$ from partial t to partial x ▷ $[N_{x,p} \times N_t \times N_{k_z}] \times 9$
6 **for** $i_{k_{z3}} = 1 : N_{k_z}$ **do**
7 Extract $\boldsymbol{h}$ at current k_{z3} ▷ $[N_{k_x} \times 3 \times N_{\omega,p} \times N_{seg} \times 9]$
8 Reorganize $\boldsymbol{h}$ to get both positive and negative k_{x3} using hermitian symmetry
9 **for** $i_{seg} = 1 : N_{seg}$ **do**
10 **for** $i_\omega = 1 : N_\omega$ **do** ▷ Parallel Loop
11 Zeropad and IFFT in x for $\boldsymbol{h}$ ▷ $[N_x \times N_{\omega,p} \times N_{seg}] \times 3$
12 **end**
13 Exchange $\boldsymbol{h}$ from partial ω to partial x ▷ $[N_{x,p} \times N_\omega \times N_{seg} \times 9] \times 3$
14 **end**
15 **for** $i_{k_{z1}} = 1 : N_{k_z}$ **do** ▷ Operate on partial x data
16 $k_{z2} = k_{z3} - k_{z1}$, skip loop if k_{z2} out of range
17 Compute $\boldsymbol{f}(k_{z1}, k_{z3}, x, t)$ ▷ $[N_{x,p} \times N_t] \times 3$
▷ negative k_z obtained with complex conjugate
18 Mean subtract f_x if $k_{z3} = 0$ ▷ average in x, t and subtract
19 Segment, apply window function $w(t)$, FFT in t, truncate $\omega \longrightarrow \boldsymbol{f}(k_{z1}, k_{z3}, x, \omega)$
▷ $[N_{x,p} \times N_\omega \times N_{seg}] \times 3$
20 Pointwise multiply $\boldsymbol{f}$ with $\boldsymbol{h}$ and sum in x, ω_3 ▷ $[N_{k_{z1}} \times N_{k_{z2}} \times N_{seg} \times 27]$
21 **end**
22 **end**
23 Sum in x over all processors with *MPI_REDUCE*

Algorithm 6: subroutine *compute_Rom* for computing R_ω at a single y plane

Inputs: $\boldsymbol{u}$, $\frac{\partial \boldsymbol{u}}{\partial y}$, size $[N_{k_x} \times N_{k_z} \times N_{t,p}] \times 6$
Inputs: $\boldsymbol{h}$, size $[N_{k_x} \times N_{k_z} \times 3 \times N_{\omega,p} \times N_{seg} \times 9]$

for $i_t = 1 : N_{t,p}$ **do** ▷ Parallel Loop
  Compute $\frac{\partial \boldsymbol{u}}{\partial x}$, $\frac{\partial \boldsymbol{u}}{\partial z}$ for current (y, t)
  2D Zeropad and 2D IFFT in x, z for $\boldsymbol{u}$, $\frac{\partial \boldsymbol{u}}{\partial x}$, $\frac{\partial \boldsymbol{u}}{\partial y}$, $\frac{\partial \boldsymbol{u}}{\partial z}$ ▷ $[N_x \times N_z \times N_{t,p}] \times 12$
end
Exchange $\boldsymbol{u}$, $\frac{\partial \boldsymbol{u}}{\partial x}$, $\frac{\partial \boldsymbol{u}}{\partial y}$, $\frac{\partial \boldsymbol{u}}{\partial z}$ from partial t to partial z ▷ $[N_x \times N_{z,p} \times N_t] \times 12$
Segment, apply window function $\sqrt{w}(t)$, FFT in t, truncate ω for $\boldsymbol{u}$, $\frac{\partial \boldsymbol{u}}{\partial x}$, $\frac{\partial \boldsymbol{u}}{\partial y}$, $\frac{\partial \boldsymbol{u}}{\partial z}$ ▷ $[N_x \times N_{z,p} \times N_\omega \times N_{seg}] \times 12$
for $i_{seg} = 1 : N_{seg}$ **do**
  for $i_\omega = 1 : N_{\omega,p}$ **do** ▷ Parallel Loop
    Zeropad and IFFT in z for $\boldsymbol{h}$ ▷ $[N_{k_x} \times N_z \times N_{\omega,p} \times 9] \times 3$
  end
  Exchange $\boldsymbol{h}$ from partial ω to partial z ▷ $[N_{k_x} \times N_{z,p} \times N_\omega \times 9] \times 3$
  Reorganize $\boldsymbol{h}$ to get both positive and negative k_x using hermitian symmetry
  for $i_{\omega_3} = 1 : N_\omega$ **do** ▷ Operate on partial z data
    Extract $\boldsymbol{h}$ at current ω_3 ▷ $[N_{k_x} \times N_{z,p} \times 9] \times 3$
    Zeropad and IFFT in x for $\boldsymbol{h}$ ▷ $[N_x \times N_{z,p} \times 9] \times 3$
    for $i_{\omega_1} = 1 : N_\omega$ **do**
      $\omega_2 = \omega_3 - \omega_1$, skip loop if ω_2 out of range
      Compute $f(x, z, \omega_1, \omega_3)$ ▷ $[N_x \times N_{z,p}] \times 3$
      Mean subtract f_x if $\omega_3 = 0$ ▷ average in x, z and subtract
      Pointwise multiply $\boldsymbol{f}$ with $\boldsymbol{h}$ and sum in x, z ▷ $[N_{\omega_1} \times N_{\omega_3} \times N_{seg} \times 27]$
    end
  end
end
Sum in z over all processors with *MPI_REDUCE*